Inclusive Electroweak measurements in the muon channel with pp collisions at $\sqrt{s}$=7 TeV

by

Philip Coleman Harris

Submitted to the Department of Physics
in partial fulfillment of the requirements for the degree of

Doctor of Philosophy

at the

MASSACHUSETTS INSTITUTE OF TECHNOLOGY

September 2011

Author .....
Department of Physics
September 9, 2011

Certified by .....
Steven Nahn
Associate Professor
Thesis Supervisor

Accepted by .....
Prof. Krishna Rajagopal
Associate Department Head for Education

Inclusive Electroweak measurements in the muon channel with pp collisions at $\sqrt{s}$=7 TeV

by

Philip Coleman Harris

Submitted to the Department of Physics
on September 9, 2011, in partial fulfillment of the
requirements for the degree of
Doctor of Philosophy

Abstract

In this thesis, we perform the measurement of the production of W and Z bosons in proton-proton collisions at $\sqrt{s} = 7$ TeVwith the Large Hadron Collider (LHC). In the LHC, W and Z bosons are produced at a high rate, providing for large yields, which along with the clean signature of W boson decay into a muon and neutrino and the Z boson decay into two muons, allow for precision measurement of their production within the first year of operation. Deviation of these values from standard model predictions gives a clear indication of new physics interactions occurring at the LHC. We present the measurement of the inclusive W$\rightarrow \mu\nu$ and Z$\rightarrow \mu^+\mu^-$ cross sections along with the W boson charge ratio (W^+/W^-) and the W/Z production ratio in the muon channel using the first data corresponding to 35.9 pb^{-1} of proton proton collisions at $\sqrt{s} = 7$ TeV. Measured values of

$$\begin{aligned}
\sigma\left(pp \rightarrow \mathrm{W} \rightarrow \mu\nu\right) &= 10.30 \pm 0.03(\mathrm{stat}) \pm 0.15(\mathrm{sys}) \pm 0.41(\mathrm{lumi})\ \mathrm{nb} \\
\frac{\sigma\left(pp \rightarrow \mathrm{W}^+ \rightarrow \mu^+\nu\right)}{\sigma\left(pp \rightarrow \mathrm{W}^- \rightarrow \mu^-\nu\right)} &= 1.433 \pm 0.008(\mathrm{stat}) \pm 0.034(\mathrm{sys}) \\
\sigma\left(pp \rightarrow \mathrm{Z} \rightarrow \mu^+\mu^-\right) &= 972 \pm 11(\mathrm{stat}) \pm 23(\mathrm{sys}) \pm 39(\mathrm{lumi})\ \mathrm{pb} \\
\frac{\sigma\left(pp \rightarrow \mathrm{W} \rightarrow \mu\nu\right)}{\sigma\left(pp \rightarrow \mathrm{Z} \rightarrow \mu^+\mu^-\right)} &= 10.59 \pm 0.12(\mathrm{stat}) \pm 0.13(\mathrm{sys})
\end{aligned} \tag{1}$$

are in agreement with the most advanced NNLO predictions. These are currently the most precise Electroweak measurements at the LHC.

Thesis Supervisor: Steven Nahn
Title: Associate Professor

In Memory of Douglas G. Michael

Contents

1 Introduction **11**

1.1 Overview . . . 11
1.1.1 Gauge field theories . . . 12
1.1.2 Path integral in perturbative theory . . . 13
1.1.3 Forces at the LHC . . . 14
1.1.4 Quarks . . . 14
1.1.5 The proton . . . 15
1.1.6 Electroweak force . . . 16
1.1.7 Implications of Electroweak theory . . . 20
1.1.8 Proton collisions in the LHC . . . 21
1.2 Impact of W and Z boson cross section measurements on the LHC . . . 22
1.2.1 CMS detector performance . . . 22
1.2.2 Higher order QCD effects . . . 23
1.2.3 Parton distribution functions . . . 23
1.2.4 Sensitivity to new physics . . . 24
1.3 Outline of the measurement . . . 24
1.4 Reliance on the Z boson . . . 26
1.5 Outline of the rest of the thesis . . . 26

2 Experimental Apparatus **27**

2.1 The Large Hadron Collider . . . 27
2.2 Compact Muon Solenoid detector . . . 31
2.2.1 Muons in the CMS detector . . . 32
2.3 Tracks . . . 33
2.4 Silicon tracker . . . 35
2.4.1 Overview of the tracker . . . 35
2.4.2 Silicon particle detection in the tracker . . . 35
2.4.3 Tracker design . . . 37
2.4.4 Data Flow in the tracker . . . 38
2.4.5 Electromagnetic calorimeter . . . 42
2.4.6 Hadron calorimeter . . . 45
2.4.7 Muon chambers . . . 47
2.5 Data flow . . . 51
2.5.1 Trigger . . . 51
2.5.2 Simulation . . . 53

2.6 Summary 54

3 Luminosity **57**
3.1 Rate of collisions 58
3.2 Absolute normalization 59
3.2.1 Magnet adjustments method 60
3.2.2 Vertex reconstruction method 61
3.2.3 Comparison 62
3.3 Instantaneous luminosityin 2010 62
3.4 Summary 63

4 Event Reconstruction **65**
4.1 Reconstruction overview 65
4.2 Photons 65
4.3 Electron 66
4.4 Track reconstruction 66
4.4.1 Vertex reconstruction 68
4.5 Particle Flow ($\not\!\!E_{\mathrm{T}}$ reconstruction) 68
4.5.1 Particle Flow calorimeter clustering 68
4.5.2 Particle Flow linking 69
4.5.3 Particle Flow identification 69
4.5.4 Particle Flow energy calibration 70
4.5.5 Particle Flow $\not\!\!E_{\mathrm{T}}$ 70
4.5.6 Particle Flow jet reconstruction 71
4.6 Muon reconstruction 71
4.6.1 Muon propagators 71
4.6.2 Reconstruction in the muon chambers 72
4.6.3 Global muon reconstruction 72
4.6.4 Tracker muon reconstruction 74
4.7 Muon level one trigger 74
4.8 Muon high level trigger 76
4.8.1 Level two muons 76
4.8.2 Level three muon seeding 77
4.8.3 Level three muon reconstruction 78
4.9 Muon p_{T} resolution 78
4.10 Summary 79

5 Selection **87**
5.1 Muon trigger selection 87
5.2 Muon event selection 88
5.3 Final selection 91
5.3.1 Global Muon 91
5.3.2 Number of pixel hits 91
5.3.3 Number of tracker hits 91
5.3.4 Tracker fit quality 93

5.3.5 Number of valid hits . . . 94
5.3.6 Number of segments . . . 95
5.3.7 Impact parameter . . . 96
5.3.8 Isolation . . . 97
5.3.9 Di-muon veto . . . 100
5.4 Selection summary . . . 100

6 Muon Efficiency **101**
6.1 Z boson selection . . . 101
6.2 Efficiency calculation . . . 101
6.2.1 Efficiency calculation . . . 103
6.2.2 Fitting the efficiency . . . 103
6.3 Efficiency scale factor . . . 108
6.3.1 Track efficiency . . . 109
6.3.2 Stand-Alone muon efficiency . . . 110
6.3.3 Global muon efficiency . . . 111
6.3.4 Identification and isolation efficiency . . . 112
6.3.5 Secondary muon veto . . . 119
6.4 Systematic uncertainties . . . 120
6.4.1 Fitting bias . . . 121
6.4.2 Background systematic uncertainty . . . 121
6.4.3 Muon signal systematic uncertainty . . . 125
6.4.4 Systematic uncertainties propagation . . . 126
6.5 Summary . . . 128

7 Muon Energy Scale and Resolution **129**
7.1 Fitting Z boson mass . . . 130
7.1.1 Parametrization one: Voigtian with a crystal ball tail . . . 130
7.1.2 Parametrization two: Monte Carlo simulation convolved with a Gaussian . . . 132
7.2 Weak modes in the tracker . . . 132
7.3 Fit to energy scale corrections . . . 134
7.3.1 Scale variation in ϕ . . . 135
7.3.2 Scale variation in η . . . 137
7.3.3 Fit to resolutions . . . 138
7.4 Systematic uncertainties . . . 139
7.4.1 Fit validation . . . 140
7.4.2 Scale uncertainty . . . 141
7.4.3 Resolution uncertainty . . . 141
7.5 Extrapolation of corrections . . . 142
7.6 Summary . . . 142

8 Theoretical Modeling **145**
8.1 Acceptance . . . 145
8.1.1 Leading order W cross section . . . 146
8.2 Higher order QCD corrections . . . 148
8.2.1 Extending to higher orders . . . 149
8.2.2 Generalized cross section to all orders . . . 151
8.2.3 Parton shower Monte Carlo simulation . . . 155
8.2.4 Differential NNLO calculation . . . 158
8.2.5 Comparison with data . . . 158
8.3 Electroweak corrections . . . 164
8.3.1 Final state radiation(FSR) . . . 165
8.3.2 Electroweak corrections of $\mathcal{O}(\alpha)$ . . . 165
8.3.3 Systematic uncertainty . . . 166
8.4 Parton distribution function uncertainties . . . 167
8.4.1 Systematic uncertainty . . . 168
8.4.2 Uncertainty with CT10 . . . 169
8.4.3 Uncertainty with MSTW2008 . . . 170
8.4.4 Uncertainty with NNPDF2.0 . . . 170
8.4.5 Results . . . 171
8.5 Summary . . . 171

9 Model of $\not\!\!E_{\mathrm{T}}$ **173**
9.1 Definitions . . . 173
9.2 Samples and selections . . . 174
9.3 Recoil parametrization . . . 174
9.3.1 Gaussian recoil parametrization . . . 175
9.3.2 Unbinned method . . . 178
9.3.3 Non-Gaussian resolution . . . 180
9.3.4 Double Gaussian method . . . 181
9.3.5 Application . . . 183
9.3.6 Shape p_{T} Variation Uncertainty . . . 183
9.4 Calculation of the scale factors . . . 185
9.4.1 Scale factor variation . . . 187
9.5 Corrections at NNLO . . . 188
9.6 Additional theoretical uncertainties . . . 189
9.7 Modified cumulant fit . . . 190
9.8 Calculation flow . . . 192
9.9 Summary . . . 195

10 Backgrounds **197**
10.1 Background composition of QCD . . . 197
10.1.1 Heavy flavor decays . . . 198
10.1.2 Light flavor decays . . . 199
10.1.3 Comparison in real $\not\!\!E_{\mathrm{T}}$ . . . 200
10.2 Modeling of the $\not\!\!E_{\mathrm{T}}$ . . . 202

10.3 Extrapolation from non-isolated region 206
10.3.1 Charge dependence 209
10.4 Systematic uncertainty 211
10.5 Electroweak backgrounds 214
10.5.1 W$\rightarrow \tau\nu$ background 215
10.5.2 Z$\rightarrow \mu^+\mu^-$ background 215
10.5.3 Other backgrounds 216
10.6 Summary 216

11 Cross Section and Ratio Measurements **219**
11.1 W boson yield extraction 219
11.2 Uncertainties 221
11.2.1 Signal extraction uncertainties 222
11.2.2 Combined systematic uncertainties 225
11.3 W boson cross section 225
11.4 Z boson cross section 226
11.4.1 Selection of events 227
11.4.2 Z boson efficiency correction 227
11.4.3 Energy scale uncertainty on Z boson selection 229
11.4.4 Z boson cross section 229
11.5 W/Z boson ratio 230
11.6 Differential W boson distributions 230

12 Conclusions **235**

Chapter 1

Introduction

A guy walks into a bar with a dog. He goes over to the bartender and says "my dog can talk." The bartender, in a discouraged mood, says "there is no way that is possible." So the guy says "well if you give me a beer I will show you." As the bartender slides the beer over, the guy asks the dog "so what's above our head?" The dog says "roof." Putting his hands on his hips, the bartender exclaims "that's not very convincing." So the guy goes to the dog and asks who's the most famous baseball player of all time. The dog turns around and says "Ruth." Irritated at this point, the bartender kicks the guy and his dog out of the bar. Upon leaving, the dog turns over to the man and says "do you think I should have said DiMaggio?"

Had the bartender been more discerning, he would have understood the nature of the dog's remarks. They confirmed the man's assertion. However, the questions were, perhaps, not the most appropriate to determine the dog's abilities. Physics has long been a journey of questions and understanding. In some cases, people have had a clear confirmation of their claim and in others, they have had clear rejection. The most difficult cases are the answers in between confirmation and rejection, which is what happened to the bartender.

The only way to ameliorate a predicament of such uncertainty is to rephrase the question. For example, the bartender could have asked is there any reason the dog cannot speak.

In this document, we present a set of measurements, which lead to the assessment of the W and Z boson cross sections in the muon channel at the Large Hadron Collider (LHC). This measurement is currently the most precise electroweak measurement performed at the LHC. Throughout this document, we emphasize not just how to measure the W boson cross section, but what questions are necessary to measure it precisely.

1.1 Overview

The Large Hadron Collider (LHC) consists of a ring of super conducting magnets containing high energy circulating protons. These protons collide at an approximate rate of 40 million times a second. Each collision does not actually consist of full

proton colliding with another proton. It actually consists of a small fraction of the proton colliding with another small fraction of the other proton, with the resulting constituents of the protons typically dispersed along the beamline. In a small number of cases, an additional process can occur during the collision process resulting in a myriad of possibilities including the production of a W or Z boson.

W boson production is the largest single source of high energy leptons (electrons, its heavier partner muons, and even heavier parter tauons). There are also concrete precision calculations that predict its expected properties at the Large Hadron Collider. In this document, we present the results of the first detailed study of the W boson in the new energy regime of the LHC in the muon decay channel. Deviations in the properties of the W boson with respect to the predictions are one of the first and most powerful indications of new physics at the LHC [1].

Z boson production occurs at smaller rate compared to that of W boson production, but it leaves a very clear signature of two high energy leptons. This combination make measurements of its properties nearly as sensitive to new physics and W boson production. The combination of the two channels, single leptons and double leptons, comprise more than 80 percent of the physics measurements at the Large Hadron Collider all of which are studies of specific regions of W and Z boson production. This thesis sets the ground work for all of these measurements and provides the first test of new physics involving high energy leptons.

To understand the importance of these measurements, we must first develop the intuition that leads to the modern description of W boson and Z boson production. We will start with the very basic questions and build up to the cross section measurements. The most basic question starts with the nature of particle interactions, which may be described through the concept of gauges. The formalism for these sorts of calculations is known as gauge field theory. Calculations of interactions of gauge fields are performed with the path integral formalism. These calculations are applied to the proton and its constituents to determine W and Z boson production. Once the W and Z bosons are produced, their properties determine how they decay. The decays of the W boson into a muon and neutrino and the Z boson into two oppositely charged muons is where the measurement starts. In the sections below, we build the intuition leading to the modern concept of W and Z boson production, setting up the path to perform the measurement.

1.1.1 Gauge field theories

To understand boson production, we must first consider the origin of all the forces. At the most basic level, all processes start with a Lagrangian [2],

$$\mathcal{L} = (\delta\phi)^2 - m^2\phi^2 , \tag{1.1}$$

formulated in terms of a generic field ϕ. The left term $\delta\phi$, the kinetic term, is equivalent to the momentum and represents the kinetic energy in the field. When the geometry of the field changes, the motion in the space is modified. In curved space-time, an additional term originating from the modified geometry is added. The

modifications change the kinetic term by adding an additional force on the field ϕ, this takes the form of a Christoffel symbol [3] $\delta \rightarrow \delta + \Gamma^i$, where Γ^i is the Christoffel symbol originating from the modified space-time. Extending beyond curved space time, we may modify the kinetic term in the exact same manner with additional generalized forces. A generalized force of this form is equal to a rotation in some abstract space. Thus, the differential operators that manifest the force itself is written in terms of Lie algebras. The most general form of such a Lagrangian, the Yang-Mills Lagrangian, is written as

$$\mathcal{L} = \left((\delta + g t^a A_\mathrm{a})\phi\right)^2 - m^2\phi^2 \ , \tag{1.2}$$

where t^a is the generator of the Lie Algebra and A_a is a new force field acting on ϕ with a coupling of g. This Lagrangian describes all known physical interactions including all of the sub processes needed for W and Z boson production. These type of forces are known as gauge field theories, with the t^a as the gauge group element.

1.1.2 Path integral in perturbative theory

In order to perform calculations in gauge field theory, it is necessary to first consider the formalism of calculations using quantum mechanics. The most general of such formalisms starts with the Feynman path integral [4] expressed here as

$$\langle \phi_\mathrm{a} | e^{-iHT} | \phi_\mathrm{b} \rangle = \int \mathcal{D}\phi \exp\left[i \int_0^T d^4x \mathcal{L} \right] \ , \tag{1.3}$$

where the left side in brackets denotes the interaction probability of two fields ϕ_a and ϕ_b with any possible Hamiltonian H over a time T. The right side of the equation, denotes the integral over all paths ϕ of the integral over space of the Lagrangian $\mathcal{L}$, known as the action. This equation defines the probability of interaction for any Lagrangian $\mathcal{L}$

To perform a calculation with an interaction of a field A and a coupling g in the Lagrangian (equation 1.2), we expand the action in terms of g. This leads to an expression of the form

$$\langle \phi_\mathrm{a} | e^{-iHT} | \phi_\mathrm{b} \rangle = \int \mathcal{D}\phi \exp\left[i \int_0^T d^4x \mathcal{L}_0 \right] \left(1 + g \int d^4x t^a A_\mathrm{a} \phi^2 + g^2 \int d^4x .... \right) \ , \tag{1.4}$$

where each term on the right (*ie 1, g, g^2*) defines a calculable interaction which may be written as a Feynman diagram, one such diagram is shown in figure 1-4. For a coupling $g < 1$, the higher order terms in g are suppressed, allowing for a perturbation calculation term by term in powers of g. Such perturbative calculations define a large fraction of calculable interactions in the high energy physics. Terms of the order g are known as leading order (LO) calculations, terms of the order g^2 are referred to as next to leading order (NLO) and so on. The W and Z boson cross section calculation is presently known to next to next to leading order (NNLO).

1.1.3 Forces at the LHC

In the LHC, the production of W and Z bosons critically involves two sets of forces, the strong force and the electroweak force. The strong force binds the quarks and the gluons together through interaction of the gauge group elements $t^a \in SU(3)$. The weak force, for which the W and Z bosons are constituents, couples to the fields through the elements t^a in the gauge group $SU(2)$. For each force, the interactions occur within their respective Lie algebra. This implies there is no known mixing of the strong and the weak force.

However, because the weak and strong force both interact through $SU(N)$ gauge groups, there are certain properties that apply to both the weak and strong force. For all $SU(N)$ gauge groups the renormalization of the coupling is written as [4]

$$g^2(\mu) = g^2 \left(1 + \frac{g^2}{16\pi^2}\left(\frac{11}{3}N - \frac{2}{3}n_{\mathrm{f}}\right)\log(\mu^2)\right)^{-1} , \tag{1.5}$$

where μ is the energy scale of the coupling, N is the order of the SU group (*ie two for SU(2)*) and n_{f} is the number of fermions. The term in front of n_{f} is negative, which for a small enough number of fermions (as is true in reality) implies the coupling g gets weaker with higher energy. This is known as asymptotic freedom.

In the case of the strong force where the coupling g is large, there exists a region of small energy μ where the strong coupling $g > 1$. Thus, at low energies the coupling is too strong to permit perturbative calculations. The energy scale for which the strong coupling exceeds 1 is near the mass of the proton, at which point the quarks and gluons condense into proton form. The weak force coupling g is small enough such that perturbative calculations are permissible for all ranges.

Now, this brief introduction may appear somewhat arbitrary. Why show yang-mills theory? Why present asymptotic freedom? This, in some respects, is the crux of modern particle physics. Why is it that two random gauge groups, SU(2) and SU(3) describe most of the standard model of particle physics? The only answer to this is that we do not know why, but experiments over the past 40 years have continually led to a clearer understanding of why it is this way. With time we may be able to answer all of these questions.

1.1.4 Quarks

All collisions in the LHC start with protons interacting through the strong force. The only carriers of the strong force charge, known as color, are quarks and gluons. Gluons, the A field in equation 1.2 for $t^a \in SU(3)$, mediate the strong interactions, which occur between quarks and gluons or gluons and gluons.

In the "standard model" of particle physics (standard model), three couplets of quarks are known to exist (green columns in figure 1-2). The lightest couplet, the up and down quarks, are known to be stable and constitute protons, neutrons, and presumably all stable baryonic (strong coupled matter) matter in the universe. The additional couplets, the strange and charm, and the top and bottom, both constitute

higher states of matter, which decay eventually through the weak force to matter consisting of up and down quarks. The existence of three couplets of quarks is at present considered to be arbitrary. There is no fundamental reason why a fourth family should not exist. Additionally, the theory underlying the mass distribution of the quarks is presently unknown. The masses themselves span five orders of magnitude arranged over this spectrum with no clear systematic pattern.

1.1.5 The proton

Production of W and Z bosons starts with collisions of quarks inside the proton. The proton consists of three "valence" quarks, two up quarks and a down quark bound together by gluons. Looking at the proton in more detail, it is apparent that the proton consists of more quarks and gluons. The evolution from the three valence quarks to the detailed view consisting of a large amalgam of quarks and gluons is characterized by the energy scale with which the proton is probed. The relative fractions of each quark in the proton as a function of the momentum fraction x of the proton are known as parton distribution functions (PDF), $f(x)$. PDFs are used to describe the fraction all components in the proton including the valence quarks, the gluons, heavier quarks, and the anti-quarks. Heavy quarks and anti-quarks inside the proton originate from processes where a quark and its anti-quark partner are produced from a gluon, quarks produced in such a manner are known as "sea quarks".

The parametrization of each quark contribution in the PDF is performed empirically given a basic assumption of the quark gluon interactions. An example of such is written below as [5].

$$q(x,\mu_0) = a_0 x^{a_1}(1-x)^{a_2}\exp\left(a_3 x + a_4 x^2 + a_5\sqrt{x}\right) , \quad (1.6)$$

$$g(x,\mu_0) = q(x,\mu_0)\exp\left(-a_6 x^{-a_7}\right) , \quad (1.7)$$

where here $q(x,\mu_0)$ represents the form of the parton distribution function for the quarks and $g(x,\mu_0)$ represents the parton distribution function for the gluons at a specific energy scale μ_0. The parameters a_i are determined empirically from fits to data.

The evolution of the PDFs as a function of energy scale follows from predictions of gluon splitting and gluon radiation. This occurs inside the proton more frequently at smaller and smaller length scales, or equivalently at higher and higher energy scales. This evolution of the parton distribution as a function of μ_0 is calculated and commonly referred to as DGLAP evolution [6, 7, 8].

For LHC energies, the distribution functions for the up quark and the gluon are shown in figure 1-1. The distributions are taken from the MSTW collaboration [9] and shown for fits to data using either the LO, NLO, or NNLO calculations. The up quark distribution shows a small ridge near $\log(x) = -1$ from the contribution due to valence quarks. At low x, a large amount of quark and gluon splitting leads to large contribution to the total momentum of the proton from gluons. As one pregresses to high x, the gluon contribution rapidly falls to zero. The effect of the higher orders (LO→NNLO) leads to a small change in the distributions at small values of

x. The effect between the orders is important for best approximating the true data distributions at each order because the LO PDFs are determined from fits to data using LO calcuations. For NLO, one must use NLO pdfs, likewise NNLO PDFs for NNLO calculations. Studies have shown that this rule is is not completely true [10]. However, violations of this rule will not be further investigated in this Thesis.

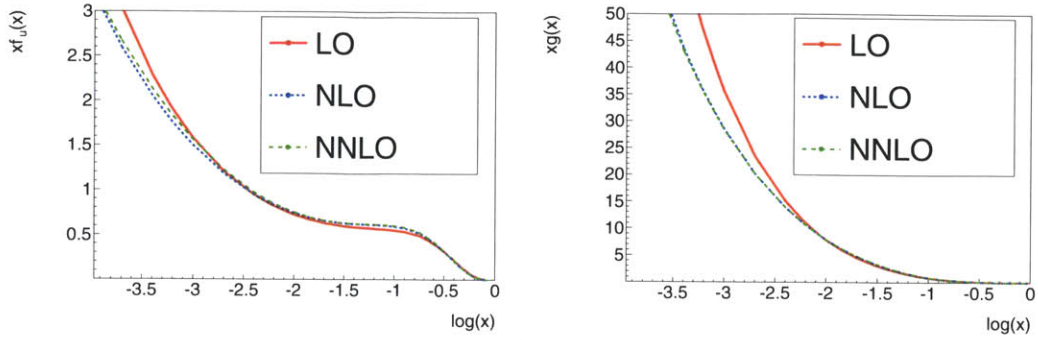

Figure 1-1: Distribution functions $xf(x)$ for the up quark (left) and the gluons (right) for $\sqrt{s} = 7$ TeV using the MSTW parton distribution functions.

1.1.6 Electroweak force

The weak force, like the strong force, follows directly from the Yang-Mills Lagrangian, where in this case the theory is governed by the $SU(2)$ Lie algebra. It is found from experiment that the weak force interacts with left handed doublet fields. Namely, the fields ϕ in equation 1.2 must be necessarily paired with another field into a doublet. It turns out again, by happenstance, that the doublets are ordered into specific quark doublets and lepton and neutrino doublets given by the vertical green or blue pairs in figure 1-2.

The W and Z bosons originate from three of the field elements A_a, which couple with the four group elements of $t^a \in SU(2)$ (expressed as the Pauli matrices) to form the $SU(2)$ extension of the Lagrangian. Expanding the terms in the differential component of Lagrangian we find the kinetic term of the Lagrangian is written as

$$\mathcal{L}_{\mathrm{kin}} = \left(\delta + \frac{g}{\sqrt{2}}\left(A_1 t^1 + A_2 t^2 + A_3 t^3 + A_0 t^0\right)\phi\right)^2 , \tag{1.8}$$

$$\mathcal{L}_{\mathrm{kin}} = \left(\delta + \frac{g}{\sqrt{2}}\left(\mathrm{W}_\mu^+ + \mathrm{W}_\mu^- + \frac{A'_\mathrm{Z}}{2}\left(t^0 - t^3\right) + \frac{A'_0}{2}\left(t^0 + t^3\right)\right)\phi\right)^2 , \tag{1.9}$$

where in the last line we have rewritten the Lagrangian into the three possible charge eigenstates. The separation into charged eigenstates is further interpreted as bosons. The two charged eigenstates $\mathrm{W}_\mu^\pm = \mathrm{W}_\mu(t^1 \mp it^2)/\sqrt{2}$ denote the two charged electroweak bosons, the W bosons [11]. The other two bosons A'_Z and A' have no charge. These second chargless bosons do not exist in the real world because another force is

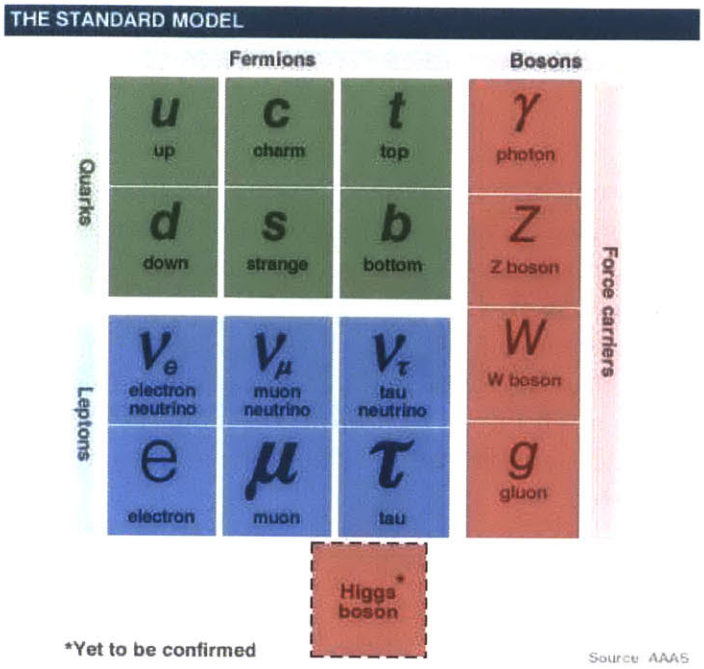

Figure 1-2: Summary of the all the particles in the standard model

present, the electromagnetic force, which is entangled with these bosons introducing terms which modify the lagrangian giving two different bosons. The additional force results from a modification of the identity element t^0, which contains the complete Lie group $U(1)$. $U(1)$ describes all electromagnetic interactions. The entanglement follows by modifying the differential, $\Delta = \delta + A_i t^i = \delta_0$, to

$$\Delta = \delta_0 + g' B t_0 \ , \tag{1.10}$$

to preserve the group structure $t^0 + t^3$ on one of the fields (this keeps it massless discussed below) and incorporate the B field, we re-write A_0 as A_μ with a coupling given by the electric charge e:

$$eA_\mu \left(t^3 + t^0\right) = \left(gA_0 + g'B\right) t^0 + A_3 t^3 \ . \tag{1.11}$$

Taking the rest of the terms and combining them into one particle, Z_μ [12], we rewrite the Δ component expanded out as

$$\begin{aligned} \Delta \ &= \ \delta - i\frac{g}{\sqrt{2}}\left(\mathrm{W}^+_\mu + \mathrm{W}^-_\mu\right) - i\frac{g}{\cos\theta_\mathrm{W}}\mathrm{Z}_\mu\left(t^3 - \sin^2\theta_\mathrm{W}\left(t^0 + t^3\right)\right) \\ &\quad -ieA_\mu\left(t^3 + t^0\right) \ , \end{aligned} \tag{1.12}$$

where the electron charge is given by

$$e \ = \ g\sin\theta_\mathrm{W} = \frac{gg'}{\sqrt{g^2 + g'^2}} \ . \tag{1.13}$$

The additional parameter θ_{W} is known as the weak mixing angle. The combination of the weak interactions $SU(2)$, with $U(1)$, give what is known as the electroweak theory.

The above theory predicts four massless bosons A_{a}. In reality it is found that the W and Z bosons have mass. To impose mass on the bosons, the mass symmetry of the massless A_{a} bosons of the Lagrangian must be broken [13]. The most well known symmetry breaking mechanism, which is widely believed to explain this phenomenon, is known as the Higgs mechanism [14]. The breaking follows by introducing an isospin doublet scalar field h to the Lagrangian. In addition to the kinetic term and the mass term, we also introduce a self interaction term, the simplest possible, which preserves $\phi \rightarrow -\phi$ symmetry is the quartic term. The full Lagrangian including the quartic interaction term is written as:

$$\mathcal{L} = ((\delta + gt^a A_{\mathrm{a}})h)^2 + \mu^2 h^2 + \lambda h^4. \tag{1.14}$$

For a quartic Lagrangian of the above form the minimum energy is found to be $h_0 = \sqrt{-\mu^2/2|\lambda|}$. For a non-zero minimum energy h_0, known as the vacuum expectation energy, the minimum must have $\mu^2 < 0$. Introducing a non-zero vacuum expectation h_0 into the standard model, we write this in doublet form as

$$h_0 = \begin{pmatrix} 0 \\ \frac{v}{\sqrt{2}} \end{pmatrix}, \tag{1.15}$$

where $v = \sqrt{-\mu^2/|\lambda|}$ is known as the Higgs vacuum expectation value (vev). The expansion of this non-zero doublet in equation 1.14 gives the Lagrangian, we write as

$$\mathcal{L} = \left((\delta + gt^a A_{\mathrm{a}})\left(h' + h_0\right)\right)^2 - \mu^2 \left(h + h_0\right)^2 + \lambda \left(h + h_0\right)^4. \tag{1.16}$$

Isolating the h_0 terms and expanding using the definition of h_0 1.15 and the definition the differential Δ 1.12:

$$\begin{aligned} \mathcal{L}_0 = & \left(\delta - \frac{ig}{\sqrt{2}}\mathrm{W}_\mu \frac{(t^1 - it^2)}{\sqrt{2}} h_0 - \frac{ig}{\sqrt{2}}\mathrm{W}_\mu \frac{(t^1 + t^2)}{\sqrt{2}} h_0 \right. \\ & -i\frac{g}{\cos\theta_{\mathrm{W}}}\mathrm{Z}_\mu \left(t^3 - \sin^2\theta_{\mathrm{W}}\left(t^0 + t^3\right)\right) h_0 \\ & \left. -ieA_\mu \left(t^0 + t^3\right) h_0\right)^2 + \mu^2 \ldots, \end{aligned} \tag{1.17}$$

$$\mathcal{L}_0 = \left(\delta + \frac{gv}{2}\left(\mathrm{W}_\mu^+ + \mathrm{W}_\mu^- + \frac{1}{\cos\theta_{\mathrm{W}}}\mathrm{Z}_\mu\right)\right)^2 + \mu^2 \ldots, \tag{1.18}$$

where the last line of the above equation is obtained by considering the zero charge eigenstate, which is written into two combinations, a combination which multiplied by h_0 (equation 1.15) is non-zero (massive combination)

$$t'_{\mathrm{Z}} = \frac{1}{2}\left(t^0 - t^3\right) = \begin{pmatrix} 0 & 0 \\ 0 & 1 \end{pmatrix} \tag{1.19}$$

and a combination which multiplied by h_0 is zero (massless combination)

$$t' = \frac{1}{2}\left(t^0 + t^3\right) = \begin{pmatrix} 1 & 0 \\ 0 & 0 \end{pmatrix}. \tag{1.20}$$

Multiplying these two combinations with the Higgs doublet h_0 gives zero for the photon and gives $\frac{v}{2}$ for the Z boson. The terms from equation 1.18 for W and Z are equivalent to the basic Lagrangian $m\phi^2$ terms, where ϕ is replaced by the W or Z boson. This defines a mass for the W and Z boson, which is given by:

$$M_{\mathrm{W}} = \frac{gv}{2}, \tag{1.21}$$

$$M_{\mathrm{Z}} = \frac{M_{\mathrm{W}}}{\cos\theta_{\mathrm{W}}}. \tag{1.22}$$

The additional field h is known as the Higgs field. Its interacts with other particles through the scalar boson known as the Higgs boson. Its existence is the "simplest" explanation that gives the W and Z boson mass. The mass of the Higgs is given by μ from the equation 1.14.

Under precision tests [15], modern electroweak theory is very robust, however the theory itself remains incomplete, since no confirmation of the Higgs boson has been performed [16, 17]. The only limit comes indirectly from WW production (figure 1-3), where a Higgs boson is requried to avoid divergence of the cross section through a theorem which bounds all wave collisions,the optical theorem. In the case of WW production, this limits the Higgs mass to $\mu < 1.2$ TeV [18].

Summary The electroweak theory follows from an $SU(2)$ Yang-Mills algebra. It predicts four distinct bosons, which are entangled with an additional $U(1)$ gauge that is responsible for the electromagnetic force, giving rise to mixed state bosons, the photon and Z boson. It is found from experiment that the additional bosons interact through the weak force with left handed leptonic or quark doublets. Additionally, it is found from experiment that three of these bosons are massive. In its simplest form, the masses of these additional bosons are generated by adding an additional boson, the Higgs boson, with non-zero vacuum expectation v. At present, the Higgs model for mass generation in the electroweak theory is confirmed only indirectly by WW boson production. Other models may exist, which give the W and Z bosons mass.

In light of the Higgs boson being a doublet, left handed doublets couple with right handed leptonic or quark singlets and the Higgs, this produces a mass term [4]. Thus, it has also been surmised for simplicity's sake that the Higgs boson couples to fermions giving them mass. If we are to believe the Higgs couples to fermions, for which there is no evidence, then tighter constraints on the Higgs from the top quark mass and the W boson mass constrain the mass to be below 200 GeV/c^2 [16]. A lower bound on the Higgs mass of 114 GeV/c^2 is determined by previous searches for the Higgs particle at the large electron positron collider (LEP) [15]. New regions between these two have been recently excluded by the Tevatron and both the ATLAS and CMS detectors at the LHC [20, 21, 22].

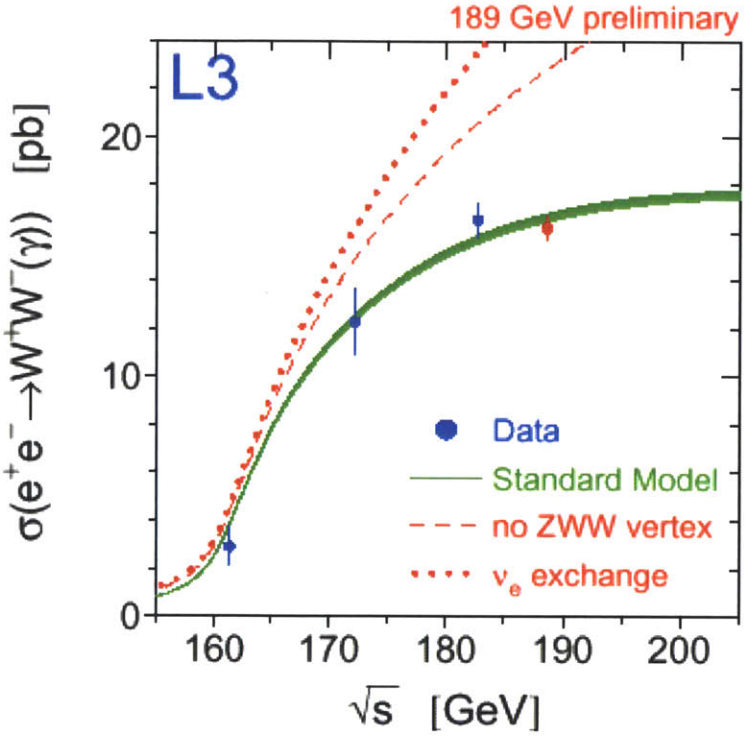

Figure 1-3: WW boson production in the large electron-positron (LEP) collider using the L3 detector [19]. The two red lines indicate the behavior of WW scattering if the W boson did not couple to Z bosons (dashed line) and if WW boson production through a neutrino exchange were not present

1.1.7 Implications of Electroweak theory

The electroweak doublet structure of the theory impose rules on the production and decay of the W boson. The W boson decays into either the quark doublets $u\bar{d}$ or $c\bar{s}$, or the three lepton doublets $e\nu_e$, $\mu\nu_\mu$ and $\tau\nu_\tau$. The third quark doublet is not kinematically allowed because the mass of the top quark is heavier than the mass of the W boson. The two quark pairs have a degeneracy of three arising from the three possible colors (from the strong theory), which amount to a total of $3+3+1+1+1 = 9$ possible decay states. Thus, the W decays $\approx 2/3$ of the time to quarks and $\approx 1/9$ of the time to a specific lepton and its corresponding neutrino.

Figure 1-4 shows the leading order diagram of W production at the LHC. The Lagrangian requires that either the lepton or the neutrino in the decay must be an anti-particle.

Further details follow from experiment, where it is found that the photon is a vector (spin 1) boson [4], consequently the W and Z bosons have spin 1. This implies that the W and Z bosons may exist in three different polarization states. The possible states are left handed, longitudinal and right handed. If the boson had no mass a lon-

gitudinal polarization would not be possible. This is why longitudinal photons exist only indirectly through interactions (*virtually*). In lepton decays, polarized W bosons decay to a lepton and a nearly massless neutrino [23]. The nearly massless neutrino constrains the lepton to be polarized on or against the W boson. If the neutrino were massive the helicity of the lepton would be less constrained and the polarization would decouple from that of the W boson. This defines specific characteristics on the shape of the decay kinematics, most notably in the lepton transverse momentum (p_{T}) [24].

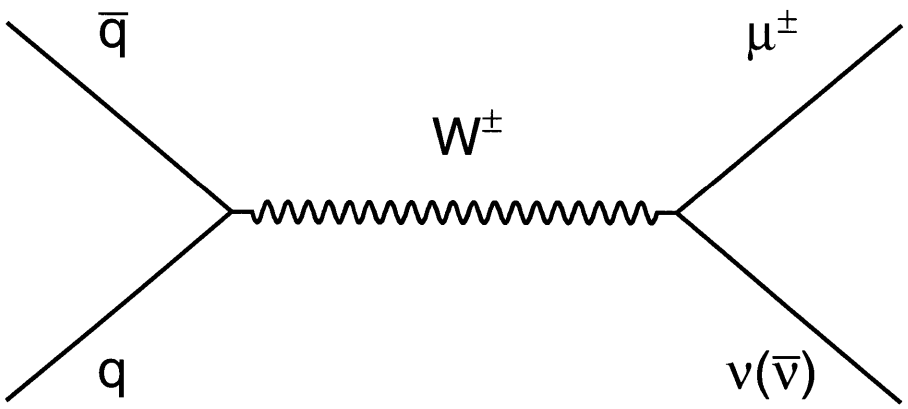

Figure 1-4: W boson production Feynman diagram at leading order

1.1.8 Proton collisions in the LHC

In the LHC, protons collide at 7 TeV, high enough to allow interactions with objects that exist with low probability inside the proton. Such interactions do occur on an everyday basis in household objects (such as smoke detectors), but at such an extremely low rate that it is impossible to study them. An example of an everyday low probability event occurs through W boson production when a quark interacts weakly by decaying to a lighter quark through a virtual W boson leading to nuclear β decay. At higher energies such as in collisions in the LHC, the increased energy allotment per interaction allows for real W and Z boson production at a very a high rate.

W and Z boson production at the LHC is, in essence, a method to probe quark distributions at small momentum fraction, x. The production itself typically arises from the interaction of a valence quark and a virtual "sea" quark that results from gluon splitting at low x. This asymmetry of this effect, one quark at high x colliding with one quark at low x, enables the W or Z boson to be produced in regions of

phase space ranging from nearly parallel to orthognal collision beamline. The latter occuring when x is nearly the same in both colliding protons.

W and Z bosons have a clean signature and the physics behind them is well understood. Modern measurements of W and Z boson production are thus, fundamentally a measurement of QCD physics and substructure of the proton. In particular, the ratio of charged W bosons and Z bosons, W^+/W^- and W/Z, put tight constraints on predictions of the parton distribution functions.

1.2 Impact of W and Z boson cross section measurements on the LHC

The measurement of the W cross section is a baseline for all high energy hadron collider experiments. Due to the fact that the W boson decays into leptons and has a cross section ten times larger than that of the Z boson, it is the largest source of leptons without additional neaby deposits from other particles (isolated leptons) in the CMS detector. Thus, it serves as a baseline for all other isolated lepton measurements at the LHC. These other studies include all electroweak physics measurements and a large number of searches for new physics. The W boson cross section measurement also tests both the parton distribution functions and precision QCD calculations.

The Z boson cross section measurement contributes more isolated leptons and provides a second region for which to search for new physics. The selection of Z bosons by requiring two leptons has almost no background; allowing for precision tests of the cross section production models.

1.2.1 CMS detector performance

Identifying the W boson requires two components: a lepton and a neutrino. Each component leaves a clear signature, which we use to calibrate and constrain the performance of the CMS detector. The high rate of W production and solid understanding of the underlying physics make it an excellent calibration source to understand the detector behavior.

A neutrino has a very small probability of interaction inside the CMS detector, consequently its existence is inferred from the sum of the other components in the event. Each parton-parton collision consists of a random fraction of the proton from $x \in (0, 1)$ with another different undetermined partonic fraction x; thus, the collision center of mass frame is unknown. However, the momentum transverse to the beamline of the colliding partons is close to zero allowing for conservation of transverse momentum before and after the collision. Conservation of transverse momentum is therefore used to infer the missing transverse energy ($\not{E}_{\mathrm{T}}$) defined as the negative vector sum of the transverse momentum of all particles emanating from the collision. In a detector, in place of taking the vector sum of all particle the various deposits each particle leaves behind are combined into objects representing the original particle and the negative vector sum of these combined deposits defines the $\not{E}_{\mathrm{T}}$ as measured in

the detector. A real neutrino, as is produced in a W decay, leaves a clear signature for which we use to calibrate the expected $\not\!\!E_{\mathrm{T}}$ compared with the measured $\not\!\!E_{\mathrm{T}}$.

In addition to improving our understanding of the performance of each detector component, the $\not\!\!E_{\mathrm{T}}$ provides a sensitive tool to study the remnants from other parts of the proton not involved during W or Z boson production (so-called underlying event) and additional collisions occurring at the same time of the W boson collision (so-called pileup collisions). The measurement of both of these collisions and its comparison with simulation improve the understanding of the simulation and calculations of the soft QCD interactions.

The lepton resulting from the W boson decay has a few distinct properties, which make it excellent to understand lepton reconstruction. The most defining characteristic is that the lepton is produced alone with no other particles nearby. This defines an isolated muon or electron with a transverse momentum near $M_{\mathrm{W}}c/2 \approx 40$ GeV/c.

1.2.2 Higher order QCD effects

The distinctive signature and the low background make the W and Z boson cross sections excellent tests of high order QCD calculations. The existing knowledge of W and Z boson production, originating from both our knowledge of QCD and also from our continual study of W and Z boson production at the Tevatron and LEP colliders provides an external constraint to difficult QCD physics calculations, which need further improvement.

Present knowledge of W and Z production is known to the Next to Next to Leading Order (NNLO) [25]. The fully differential NNLO calculation in terms of boson rapidity and p_{T} was completed in 2006 [26, 27]. For the LHC, unlike at the Tevatron, predictions for W and Z boson production are very sensitive to this highest order calculation.

At small values of p_{T} NNLO calculations of the W and Z boson cross section break down because this part of the distribution is sensitive to non-perturbative QCD effects. The parametrization of these non perturbative effects are still not well known theoretically and are presently being pursued in hopes of understanding low energy QCD interactions. This measurement will provide new constraints on low p_{T} measurements.

1.2.3 Parton distribution functions

The W boson is produced from the interaction of a valence quark with a sea quark. Furthermore, the production of a specifically charged boson (W^+ or W^-) probes a specific valence quark proton distribution. The W^+ is most sensitive to the up quark distribution $u(x)$ and the W^- boson is sensitive to the down quark distribution $d(x)$. Because collisions at the LHC are at a larger energy than ever before, the regions of the PDFs probed reaches very low momentum fractions x, where large uncertainties remain.

In the measurement of a cross section ratio the term with the largest uncertainty cancels out completely. This maximizes sensitivity to the PDFs. Different PDFs vary

as a function of rapidity, thus the most sensitive and constraining measurement of the PDFs are the differential W^+/W^- and W/Z ratio for which the inclusive ratio of both serve as a basis.

1.2.4 Sensitivity to new physics

In addition to providing insight into QCD calculations, the W and Z boson cross section and the resulting kinematic distributions, such as the $\not{E}_T$ and the boson p_T serve as cornerstones for searches for new physical processes. A large discrepancy from the standard model predicted distributions would indicate new physics processes. Several models for supersymmetric particles as well as more exotic models, such as the W′ predict a production of a new particle which would lead to missing energy, an isolated lepton and potentially jets [28]. Such a production would show up in one of the differential distributions for W boson production. In this thesis, we shall not explore limits on new physics, however hints or absences thereof can be interpreted from the results in this thesis.

In addition to these processes, one of the most important discovery channels of the Higgs boson involves W pair production (Higgs $\rightarrow W^+W^-$). Studies involving one W boson establish a baseline for the search for the Higgs boson.

1.3 Outline of the measurement

The cross section, σ, is determined by counting the number of events, N, for a total integrated beam luminosity, $\mathcal{L}$:

$$\sigma = \frac{N}{\mathcal{L}} \, . \tag{1.23}$$

To account for the fact that in a detector there is a physical limitation to the fiducial size of the detector we must apply a correction defined as

$$a = \frac{N_{\text{fiducial}}}{N_{\text{total}}} \, . \tag{1.24}$$

This term is known as the acceptance. The correction itself is determined by making an assumption that the standard model describes W production to within an uncertainty. The value shown above is determined by an event based simulation (Monte Carlo simulation). The number N_{fiducial} is then defined as the number of simulated events where the muon is within the fiducial region of the detector. The number N_{total} is the total number of events generated. At this point, we note the two different uses of simulation and generation. Generation denotes sampling events from a standard model calculation. Simulation denotes passing a generated event through a simulation of the CMS detector. Inserting the acceptance in the cross section, the formula is now written as

$$\sigma = \frac{N}{\mathcal{L}} = \frac{N_{\text{fiducial}}}{a\mathcal{L}} \, . \tag{1.25}$$

A series of identification selections are applied to the event to select out and reconstruct well identified muons from W bosons and remove backgrounds from other processes. The number of muons reconstructed and identified, N_{selected}, over the total number of muons simulated in the fiducial region is deemed the efficiency, this is defined as

$$\epsilon = \frac{N_{\text{selected}}}{N_{\text{fiducial}}} \ . \tag{1.26}$$

The efficiency in data is determined by tagging events, where a muon is known to be present and ascertaining whether or not it is found by selection algorithms. This method, known as the tag and probe method, is performed on $Z\rightarrow \mu^+\mu^-$ events. To ensure accurate reproduction of the efficiency of leptons from W bosons with the efficiencies of leptons from Z bosons, the efficiency is calculated and compared on Z events in both data and simulation. The comparison, performed in a well defined context, is used to correct the simulation of W events to reflect the true data efficiency.

The simulated efficiency is absorbed into the acceptance, such that for the scale corrected acceptance (we denote now as a') and the efficiency from simulation (denoted as ϵ_{MC}) the acceptance may be written as

$$a' = \epsilon_{\text{MC}} a \ . \tag{1.27}$$

We thus have the master cross section formula, which we write out as in terms of the acceptance a and a'

$$\sigma = \frac{N}{\mathcal{L}} = \frac{N_{\text{fiducial}}}{a\mathcal{L}} = \frac{N_{\text{selected}}}{a\epsilon_{\text{Data}}\mathcal{L}} \ , \tag{1.28}$$

$$= \frac{N\epsilon_{\text{MC}}}{a'\epsilon_{\text{Data}}\mathcal{L}} \ . \tag{1.29}$$

Each term in the rightmost term of equation 1.28 defines a chapter of this thesis. The luminosity $\mathcal{L}$ is discussed in chapter 3. It is performed by two methods, which measure the beam geometry of the large hadron collider.

The efficiency, discussed in chapter 6, is determined through the tag and probe method. The acceptance, discussed in chapter 8, is determined through comparisons of several simulations, which incorporate the most up to date knowledge of W boson production.

The number of events is written as

$$N_{\text{W/Z}} = N_{\text{selected}} - N_{\text{QCD}} - N_{\text{EWK}} \ , \tag{1.30}$$

where N_{total} is the total events passing the muon selection and identification (chapter 5), N_{QCD} is the number of predicted QCD events in the selected region (chapter 10) and N_{EWK} is the number of non-QCD and non-W boson events in the selected region (chapter 11).

1.4 Reliance on the Z boson

It is important to emphasize the reliance of the Z boson in this W boson measurement. The Z boson cross section parallels the W boson cross section in almost every aspect. The only difference is that the neutrino resulting from the W$\rightarrow \ell\nu$ decay is replaced with a lepton of the same flavor. The second lepton allows for the determination of the mass, providing a means for an extremely clean signature, for which we use as a source of leptons to calibrate the W boson performance. The clean signature enables the calibration of the detector, namely the $\not\!\!E_{\mathrm{T}}$, the lepton efficiencies and our present theoretical understanding. In the course of the W boson measurement, we will perform a simple counting cross section of the Z boson and we will end by additionally presenting the W/Z boson cross section ratio.

1.5 Outline of the rest of the thesis

In the rest of the dissertation we will present the details involved in the W and Z boson cross section measurement. We will start with a discussion of the CMS detector, the LHC accelerator (chapter 2) and the luminosity measurement (chapter 3). We will follow this with a presentation on the lepton reconstruction (chapter 4), selection and optimization (chapter 5). This is continued with the determination of the lepton energy scale (chapter 7) and the lepton efficiency (chapter 6), followed by an in-depth discussion of the theory behind the W boson cross section calculation (chapter 8). Then we will continue with a discussion of several techniques to model the $\not\!\!E_{\mathrm{T}}$ (chapter 9), followed by the full extraction of the W and Z boson yields (chapters 10 and 11). We finish with a presentation of all the results followed by the conclusion (chapter 12).

Chapter 2

Experimental Apparatus

To measure the W and Z boson production cross sections, collisions from the Large Hadron Collider (LHC) are recorded with the Compact Muon Solenoid (CMS) detector. The LHC is a particle accelerator that can perform proton-proton collisions at a number of different collider energies and instantaneous luminosities, ranging from collision energies of $\sqrt{s}$=980 GeV to 14 TeV. In this document, the first set of collisions at an energy run of $\sqrt{s}$ = 7 TeV are used.

Around the LHC are four different detectors, ATLAS, CMS, LHCb, and ALICE (figure 2-1). The two detectors, CMS and ATLAS, are considered to be "all-purpose" detectors which are designed to measure all production mechanisms that may occur in the LHC.

2.1 The Large Hadron Collider

The LHC accelerator complex, shown in figure 2-1, consists of a series of different accelerators which increase the proton energy stepwise per ring going up to the highest energy ring. A diagram of the acceleration chain is shown in figure 2-2. The beam starts with a bottle of hydrogen. Exiting the bottle, electrons are stripped from the hydrogen atom leaving protons, which are directed to a linear accelerator (LINAC) that accelerates the protons up to 50 MeV. The protons from the LINAC are then put into a booster, which accelerates the protons up to 1.4 GeV kinetic energy and inserts them into the Proton Synchrotron (PS). The protons leave the PS at an energy of 25 GeV and are then inserted into the Super Proton Synchrotron (SPS). The SPS finally injects beams at 450 GeV into the LHC ring. It is in the LHC ring, where the final acceleration of the beam up to the desired energy is performed.

The accelerator complex is capable of accelerating both protons and heavy ions through a lead linear accelerator and ion collector which are attached to the PS. The intended design of the LHC will reach $\sqrt{s}$ = 5.5 TeV /nucleon in heavy ion collisions and $\sqrt{s}$ = 14 TeV in proton collisions. Stability in the tuning of the magnets of the LHC has descoped the intended energy of the LHC, thus it is expected that the LHC magnets will attain an final energy below 14 TeV , but above 10 TeV . Presently, the LHC accelerator is capable of accelerating protons up to a center of

mass energy of $\sqrt{s} = 7$ TeV and heavy ions up to an energy of $\sqrt{s} = 2.2$ TeV/nucleon.

At nominal running, the LHC ring needs to be filled by 12 cycles of the SPS. Each cycle of the SPS requires 3-4 cycles of the PS. For a cycling time of 21.6 seconds and 3.6 seconds for the SPS and PS respectively, the filling time of the LHC ring is about four minutes per beam [29]. Taking into account time for analysis the accelerator can be completely filled in a minimum time of 16 minutes. Following the filling of the beam, the energy of the beam is accelerated up to the desired energy. The ramping of the magnets typically takes 20 minutes to go either up or down. Consequently, the total time to fill the beam and accelerate it is on the order of 70 minutes (with additional checks). Successfully filling the beam is not gauranteed, failures of the filling can lead to delays which may extend the 70 minutes to 6 hours, depending on the characteristics of the beam.

The magnets that compose the LHC are superconducting NbTi wire magnets, which operate at a temperature of the formation of the helium super-fluid, 1.7 K. In the LHC there are eight completely connected super cooled sectors. Each sector alone is the world's largest super cooled volume. The combined eight sectors span a ring of circumference 26.7 km, where on one side are the Jura mountains and the other side is the Geneva airport. The depth of the ring ranges from 50 m near the Geneva airport to 175 m along the Jura mountains. Before and after the collision points along the beam are straight sections. There are eight straight sections in total, allowing eight possible interaction points.

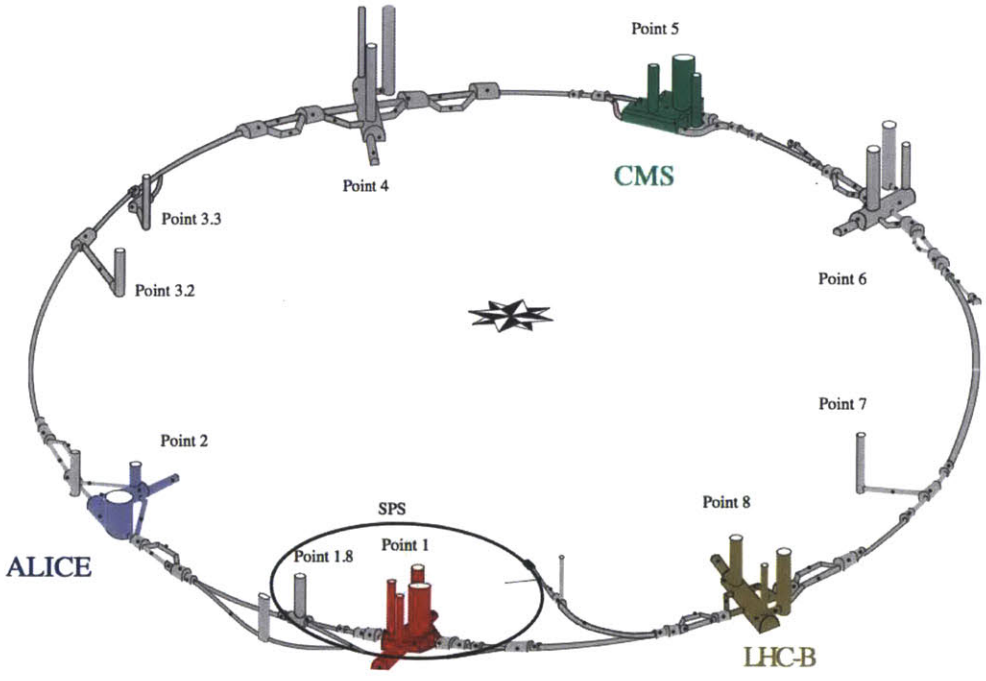

Figure 2-1: LHC and its different collider halls

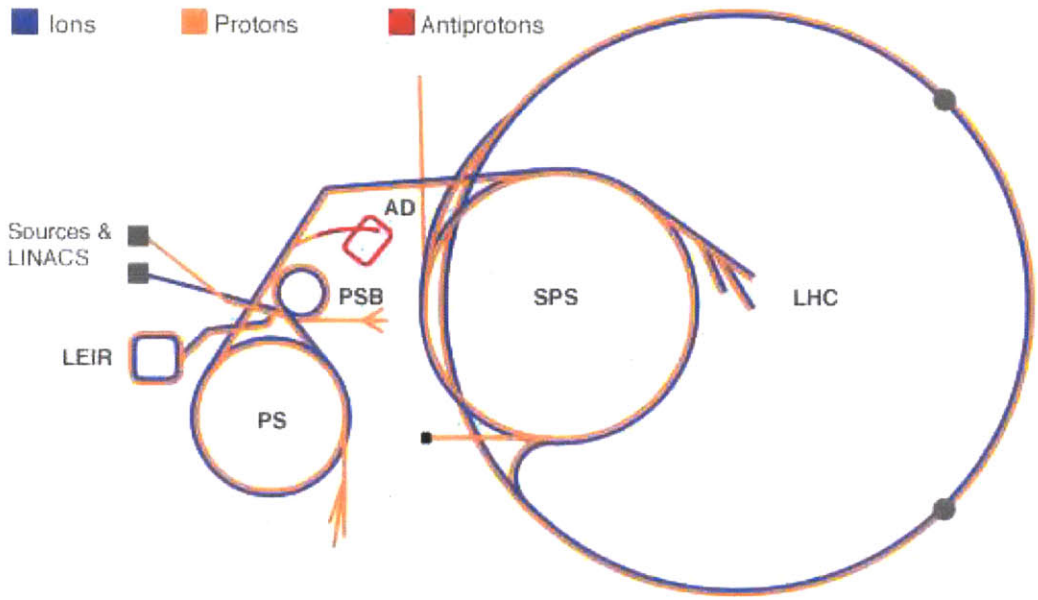

Figure 2-2: LHC Accelerator complex [30]

The two crucial parameters of the accelerator are the beam energy and the instantaneous luminosity. These two parameters drive the capability of physics studies at the LHC. The beam energy is determined by the magnetic field of the ring. The magnets in the LHC are designed to reach a magnitude of 8.33 T. This yields an energy of 7 TeV per beam. The other crucial factor, the instantaneous luminosity, is determined by the initial amount of protons injected into the beam and by the separation of this beam into separate clusters of protons, known as bunches. The collisions of an two bunches is referred to as a bunch crossing. The instantaneous luminosity of all of the bunches, $\mathcal{L}$, is expressed as

$$\mathcal{L} = \frac{N_{\mathrm{b}}^2 n_{\mathrm{b}} \nu_{\mathrm{rev}} \gamma_{\mathrm{r}}}{4\pi \epsilon_{\mathrm{n}} \beta^*} F \ , \tag{2.1}$$

where,

- n_{b} is the number of bunches per beam,
- N_{b} is the number of particles per bunch (assumed to be equal per bunch),
- ν_{rev} is revolution frequency,
- γ_{r} is the energy of the beam,
- ϵ_{n} is the beam emittance,
- β^* is the beta function at the collision point, and

- F is a geometrical factor arising from the crossing angle at interaction.

The formula for F is written as [29]:

$$F = \left(1 + \left(\frac{\theta_c \sigma_z}{2\sigma^*}\right)^2\right)^{-1/2} , \tag{2.2}$$

where θ_c is the crossing angle, σ_z is the RMS length in z of the proton bunch, and σ^* is the RMS width of the beam.

The beam size emittance ϵ_n is the width of the beam in the collision region. This combined with the bunch shape profile along the beam (beta function β^*) determine the collision size. The interaction region is adjusted by the magnets nearby the collision hall. Specific configurations of the magnets lead to resonances, which lead to a blow up of the emittance. Careful tuning of these parameters leads to an emittance around tens of microns and a β^* function of 0.5 m [31]. The most important component in the instantaneous luminosity is N_b, the number of particles per bunch, this combined with the collision area $4\pi\epsilon\beta$ define the collision density.

In the LHC, the bunches are separated by a minimum of 25 ns [29]. This yields 2808 bunches per beam. In the 2010 running the full 2808 bunches were not utilized, instead the inter bunch spacing was separated by more than 100 ns.

The number of particles is limited by the electrostatic repulsion inside the beam. This limitation is written as a limit on the density of the protons[29]

$$N_b < \frac{0.2\pi\epsilon_n}{r_p} , \tag{2.3}$$

where r_b is the Bohr radius of the proton. The lifetime of the beam follows predominantly from the rate of non-linear collisions, the rate of collisions with residual gas in the beam, and scattering due to interacting beams (IBS). The maximum number of protons per beam N_b is determined to be 1.15×10^{11} [29].

In optimal conditions, the instantaneous lifetime of the beam is written:

$$\tau = \frac{N_b}{L\sigma_{tot}k} , \tag{2.4}$$

where the term k is the number of interaction points in the LHC, 2 through 4. Inserting the instantaneous luminosity and solving for the set of equations we obtain the lifetime from non-linear collisions τ_{beam} as

$$\tau_{beam} = \left(\sqrt{e} - 1\right)\tau . \tag{2.5}$$

When all additional effects are taken into account the beam lifetime is estimated at $\tau_{beam} = 14.9$ h. This combined with the turn around time to deliver the beam, renders the length of a typical running period of the LHC (known as a fill) to about one day.

Overall the combination of the high density of protons, the 15 h/day rate of running, the carefully tuned beam parameters and the high energy γ_E, lead to a proton

collider that is unparalleled by any other machine. The instantaneous luminosity is the highest of any proton collider in the world. The design energy is the highest by nearly an order of magnitude.

2.2 Compact Muon Solenoid detector

The acronym, CMS, stands for Compact Muon Solenoid. The word compact designates the high detector density combined with its small detector size. At 21 m by 15 m, the detector size is not very small compared to a human, but small in comparison to its competitor experiment ATLAS. The words muon solenoid designate that a distinct characteristic of CMS, the extremely large solenoid, which gives excellent measurements of muon momenta.

The CMS detector is an onion-like cylindrical structure with each layer extending concentrically about the previous layer. Several basic variables are used to describe the orientation of the CMS detector. The axis for which the beam runs along is known as the beam axis or the z axis. The angle around the z axis is known as ϕ. The zenith angle (starting from horizontal in the direction of the Jura mountains and progressing towards the zenith counter-clockwise) is denoted θ. However, it is written in terms of the variable $\eta = -\log\left(\tan\left(\frac{\theta}{2}\right)\right)$, known as the pseudorapidity. The variable η is used in lieu of θ because it approximates a variable rapidity, which describes well the distribution of particles in protons, where the center of mass is ill-defined. In such collisions rapidity differences between particles are lorentz invariant [4]. Rapidity is defined as

$$y = \log\left(\frac{E + p_Z}{E - p_z}\right) , \tag{2.6}$$

where E and p_Z are the energy and z-momentum of the particle. For low mass particles, such as the muon or the pion, the difference between η and rapidity is typically below one thousandth. Proton collisions remnants are produced uniformly in η; this motivates much of the design of CMS. Closer to the beam line at high η, the detector components are smaller so their respective $\Delta\eta$ sizes are similar to those transverse to the beam (η=0).

One of the most distinctive features of CMS is the world's largest superconducting solenoid. The solenoid cylinder runs parallel to the beam axis, at an inner radius of $r = 3$ m around the beam line. The solenoid generates a field of 3.8 T. It is calibrated through a series of NMR sensors located throughout the solenoid. The B field is known to be uniform to an accuracy of 10^{-3} [32]. The solenoid allows for extremely precise measurements of the transverse momenta of particles. The shape of the solenoid constrains the rest of the design of CMS to be cylindrical. Each detector is a concentric cylinder, consisting of a barrel region at low η, which is tube like and a set of circular discs on either end of the cylinder (at high η) known as the endcaps.

The full fiduciality of the CMS detector is 100% in ϕ from $-\pi < \phi < \pi$ and covers a range in η of $|\eta| < 5$ (or $0.013 < |\theta| < \pi - 0.013$). The range in η is extended out to $|\eta| < 6.6$ (or $0.003 < |\theta| < \pi - 0.003$) if the zero-degree calorimeter is used.

2.2.1 Muons in the CMS detector

To illustrate how the general CMS detector functions, consider the passage of muon through the CMS detector. A muon has a sufficiently long lifetime and low interaction rate with matter (so called minimum ionizing particle) such that for muons with a momentum > 3 GeV/c pass through the whole CMS detector, thereby interacting with each sub component of the CMS detector. To aid in visualizing this passage consider figure 2-3 which shows a slice of CMS with its different sub-components. A muon passing through the detector is indicated by the blue line evident throughout the whole slice.

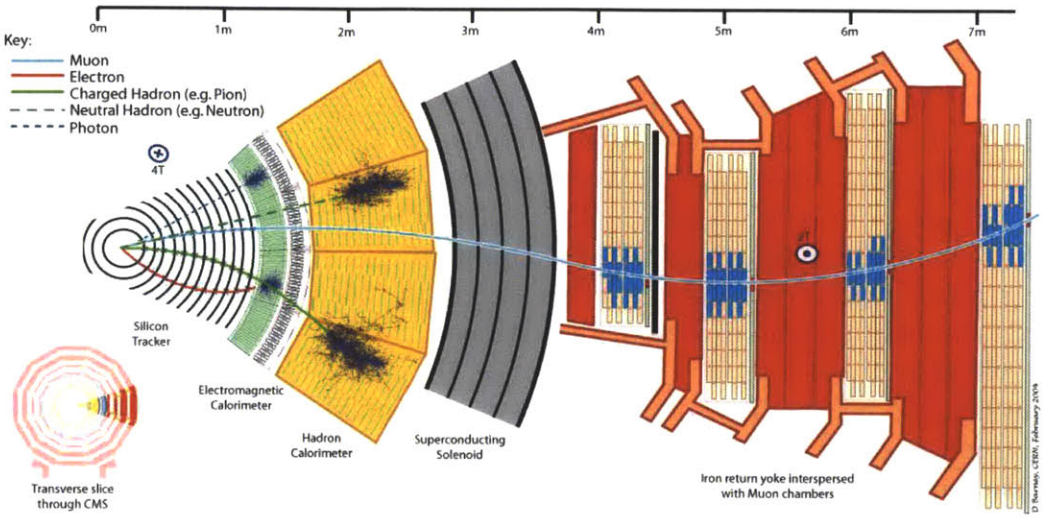

Figure 2-3: Transverse slice of the CMS detector depicting the various sub detectors. Different particle types will pass through these different components leaving depositions in each component. The behavior of the five standard particle types: muons, electrons, photons, charged hadrons, and neutral hadrons is shown in the figure. Identification of the individual particles is performed by combining the deposits in all of the different detectors and classifying given the measured deposits.

Muon production starts at the collision vertex of CMS, a region that is about 5 cm along the z axis and within a few hundred microns of the defined origin in the $r-\phi$ plane. From the collision vertex, the muon continues through the CMS detector curving along its path. This curving is caused by the large solenoid. Inside the solenoid a nearly uniform 3.8 T magnetic field propagates along the z axis allowing for the curving of charged particles transverse to the z axis. Outside the solenoid, inside a series of steel layers that are attached to the muon chambers, the magnet provides a nearly uniform 2 T return field. The return field is in the opposite direction of the B field in the solenoid. Thus, inducing the muons to curve inside the steel, in the *opposite* ϕ direction it curved inside the solenoid.

The muon first enters the inner most tracking detector known as the silicon pixel detector. This detector consists of three layers of tiny 100 micron by 150 micron

silicon rectangles which record ionized depositions originating from charged particles. Following the silicon pixel detector, the muon will pass through up to 14 additional layers of silicon arranged in long strips (3-4 cm long) with a width (pitch) of 80-220 μm. The strips record the location and energy of the ionized deposit. These pixels and strips comprise the CMS tracker, which is the single largest precision silicon imaging device. By comparison, the silicon detector on ATLAS has a surface area of roughly one quarter that of CMS.

Abaft the CMS tracker, the muon enters the electromagnetic calorimeter (ECAL). The electromagnetic calorimeter consists of a clear Lead-Tungstenate ($PbWO_4$) crystal. This material has an extremely high density and small Moliere radius providing percent level resolution of electromagnetic showers. The crystals are speicially designed to have a high level of radiation hardness.

After the CMS electromagnetic calorimeter, the muon will pass through the hadronic calorimeter (HCAL), a sub detector consisting of a series of layers of brass sandwiched between scintillation panels. The high density of brass combined with scintillation counters are used to infer energy deposits coming from nuclear interactions of neutral and charged hadrons, and the minimum ionization signal from muons.

By the end of the hadronic calorimeter, the only remaining standard model particles originating from the collision which have not decayed are muons and neutrinos. Both pass through a series of gas chambers with spatial resolution of 300 μm. These chambers, known as the muon chambers, allow for both a clear identification of a muon (separating it from all other particles) in addition to information on the muon direction and transverse momentum (p_{T}). These chambers are responsible for "triggering" events with muons, or in other words notifying the data acquisition system to record the event for further data analysis.

A triggered event goes through two filtering steps before it is sent to the CMS storage manager. The CMS storage manager acts as a buffer finally forwarding the data to be reconstructed in a series of computing systems. It is only after full reconstruction that an analysis of a physical process, such as the W boson cross section, is performed. Data taking and decisions performed at the moment where the data taking rate may still be modified by the detector readout is referred to as the online environment. This occurs before the CMS storage manager. Decisions and data taking afterward are performed in the offline environment.

2.3 Tracks

Track reconstruction is crucial to nearly all physics analyses in CMS. A track is defined as an aligned set of individual deposits in any detector, know as hits. Hits, when combined into a track, correspond to a single charged particle. Reconstruction of tracks starts by considering the Lorentz force imposed on a charged particle in a

B-field with momentum p [33].

$$\begin{aligned}
\frac{d\vec{p}}{dt} &= q\vec{v} \times \vec{B}(r) \ , && (2.7)\\
m\frac{dv_{\mathrm{y}}}{dt} &= -qv_{\mathrm{x}}B_{\mathrm{z}}|_{\mathrm{x}\leftrightarrow\mathrm{y}} \ , && (2.8)\\
\frac{p\cos\theta v_{\mathrm{x}}}{r} &= -qv_{\mathrm{x}}B_{\mathrm{z}} \ , && (2.9)\\
\frac{1}{r} &= \frac{q}{p\cos\theta}B_{\mathrm{z}} \ , && (2.10)\\
&= \frac{q}{p_{\mathrm{T}}}B_{\mathrm{z}} \ . && (2.11)
\end{aligned}$$

Here, r is the radial distance about the z axis ($1/r$ is the curvature) , q is the charge, t the time and $\vec{v}$ the velocity or a particle of mass m. On the second line we have replaced the formula to correspond with a B-field completely oriented in the z direction. On the third line we have written this in terms of the transverse projection of the momentum $p_{\mathrm{T}} = p\cos\theta$ in the $r-\phi$ plane. From equation 2.7 one obtains five independent parameters, which completely describe the helical B-field trajectory x, y, z, θ, and q/p. A minimum of three hits is necessary to determine a helix parametrization.

The dominant factor controlling the momentum resolution stems from the determination of the curvature in the transverse plane (the p_{T}). The total momentum resolution is then determined by rescaling the p_{T} measurement by the angle θ. The resolution in an ideal form is written as [34]:

$$\sigma_{p_{\mathrm{T}}} \sim \sqrt{\frac{1}{N}}\frac{\sigma_{\mathrm{x}}p_{\mathrm{T}}}{0.3B_{\mathrm{z}}R^2} \ , \qquad (2.12)$$

where N is the number of hits and R is the radial distance from the first hit to the last hit and σ_{x} is the transverse resolution. The two key components in this formula are the transverse resolution σ_{x} and the radial distance R. The resolution, $\sigma_{\mathrm{p_T}}$ improves by minimizing σ_{x}. Silicon detectors have an extremely small transverse x resolution σ_{x} of near 50 μm . This factor was the main motivation for the choice of building a large silicon tracking detector. Resolution is further reduced by increasing the radial distance R away from the first hit to the last hit, which is done for muons by incorporating both hits from the tracker and the muon chambers.

Additional effects which modify a track trajectory in the course of its propagation result from energy loss and multiple scattering of the particle. Particle energy loss and multiple scattering induces a smearing of the angle of the particle and additionally an increase in the curvature of the particle. The energy loss for a charged particle heavier than electrons is written by the Bethe-Bloch formula as [35, 36]

$$-\frac{dE}{dx} = \frac{C}{\beta^2} \times \left(\log\left(\frac{2m_{\mathrm{e}}c^2\beta^2\gamma}{I\left(1-\beta^2\right)}\right) - \beta^2 - \delta\left(\beta\right)\right) \ , \qquad (2.13)$$

where C is a constant, β is the speed of the particle, γ is the boost of the particle, I is the mean excitation energy and $\delta(\beta)$ is a density correlated effect. For a muon or pion with a momentum of 10 GeV/c, this induces an energy loss over density of 1.5 MeV cm^2/g. The multiple scattering of particles occurs by coulombic scattering, which distributes the angles as a Gaussian with a width θ_0 defined as

$$\theta_0 = \frac{13.6 \text{ MeV}}{vp} q\sqrt{x/X_0}\left(1 + 0.038 \log\left(x/X^0\right)\right) \ , \tag{2.14}$$

where 13.6 MeVis the constant (Rydberg energy), v is the velocity of the particle, p is the momentum of the particle, q the charge of particle passing through, x/X^0 the length of the passage of a particle x in terms of a measure of the interaction density known as the radiation length, X^0

2.4 Silicon tracker

2.4.1 Overview of the tracker

The silicon tracker is designed to measure and reconstruct all charged tracks emanating from the collision vertex [37] . The CMS silicon strip tracker consists of an array of finely granulated silicon-strip pitch on top of a silicon bulk. The pitch of the strips varies from 80 μm for the central region of the tracker, where the track density is high, up to a width of 200 μm for the outer regions of the tracker. The variation in the width is designed to minimize costs while preserving good track resolution. The CMS pixel detector consists of 100×150 μm pixels [37] . The use of pixels in the detector enhances the momentum resolution (resolution in the transverse plane), reduces the allowed track hit combinations, and improves the track direction determination. The latter improves the z reconstruction resolution of the tracks. Improved z resolution enhances the ability to combine track intersections into interaction vertices, leading to improved vertex reconstruction. The improved vertex reconstruction enables the separation of displaced vertices from long lived particles and the separation of two collisions occurring at the same time (so called pileup events). An overview of the different track layers inside the tracker is shown in figure 2-4.

2.4.2 Silicon particle detection in the tracker

The silicon detection system in both the pixel and strips works through a p-n junction. Figure 2-5 schematizes the two layouts used for measuring an ionized deposit. The p-n junction is reversed biased *ie* a voltage applied to it against the direction of flow of charge in the p-n junction. The voltage is large enough such that no free holes or electrons are present in the silicon (fully depleted). When a charged particle passes through the silicon it leaves a trail of ionized holes and electrons that drift to sensors where the silicon is readout.

The junction is designed by placing p^+ (SiO_2) doped strips on a n doped bulk or with n^+ doped pixels on p doped bulk[37], both are signified by the dark lines on

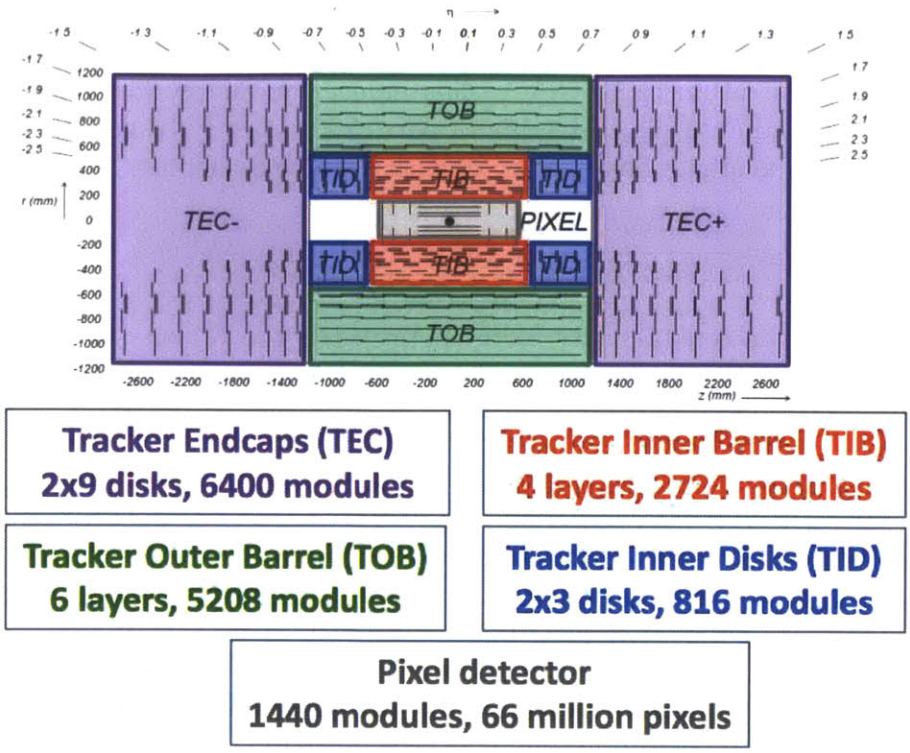

Figure 2-4: Overview of the CMS tracker. The beamline goes through the $r = 0$ coordinate, interactions occur approximately at the center of the detector indicated by a black dot. The five different sub components of the CMS tracker are shown in the figure.

top of 2-5. The differences in junction design result from the necessity for increased sensitivity in the pixels because of the small size of the pixels [37] . Along the strips and pixels are thin aluminum sensors, which read in the ionization deposits, and pass it to an amplifier and a readout system. On the opposite end is an aluminum plate (bottom of figure 2-5), which produces the voltage bias necessary to generate the depletion region.

Over years, particles originating from the proton collisions will cause the silicon to deteriorate. This occurs through two types of effects: ionization damage, which leads to oxide deposits, and non-ionization damage, which lead to defects in the silicon. Both these effects reduce the signal significance either by increasing the noise current or reducing the size of the depletion region.

To counter these effects the silicon is doped in such a way that the depletion voltage deceases over time (beneficial annealing), causing an improved signal by reducing the noise level [37, 39] . After more radiation damage, the depletion voltage increases until no depletion region exists (reverse annealing). Due to its proximity to the beamline the radiation fluence is highest near the pixel detector leading to a shortend lifetime. Radiation damage is limited by decreasing the temperature on the silicon device. In the CMS detector, the temperature of the silicon will progressively be lowered down to

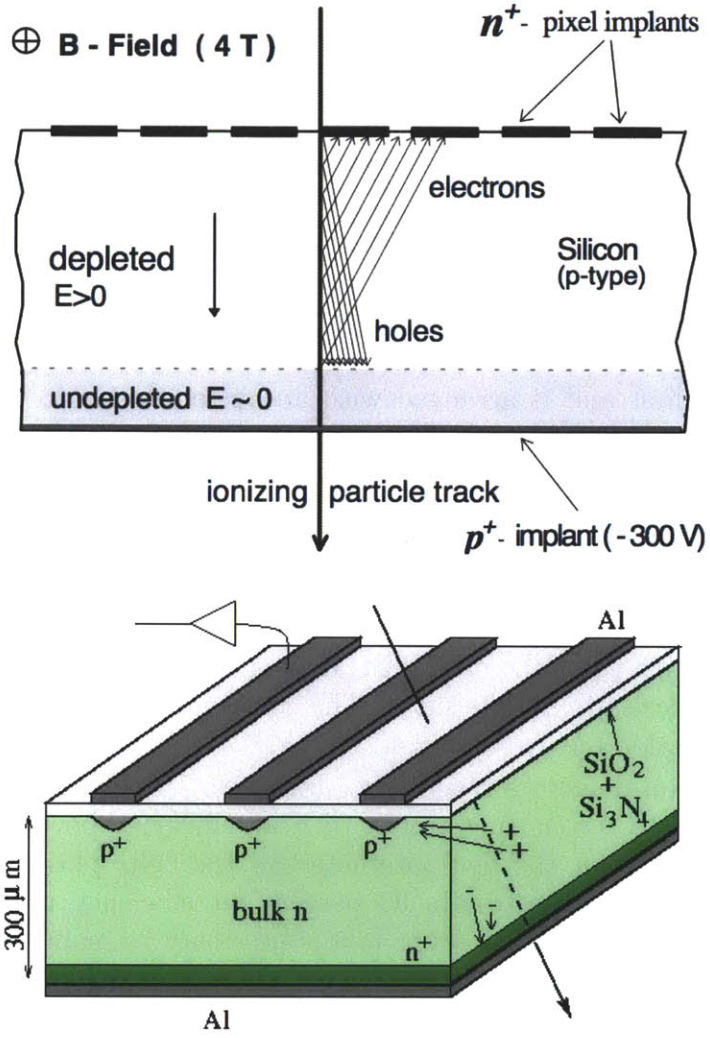

Figure 2-5: Example of the silicon design for the CMS Pixels (top) and the CMS silicon detector (bottom). Charge tracks go through the depletion region leaving electron hole pairs which drift to the (n^+) junction for negatively charge components and the (p^+) junction for positively charge components [37, 38]

-10 degrees centigrade. With the planned lowering of the temperature, the expected lifetime of the silicon strips in the LHC environment is nearly 10 years. The lifetime of the pixel detectors is smaller due to the sensitivity of the design and its proximity to the collision vertex. The expected lifetime of the pixels is only a few years [37] .

2.4.3 Tracker design

The pixel detector is divided into barrel pixels, consisting of three layers running parallel along the interaction direction, and forward pixels, consisting of two layers on both ends of the barrel oriented transversely from the beamline axis. The barrel

pixels cover a range of $0 < |\eta| < 1.5$. The forward pixels cover the range of $1.5 < |\eta| < 2.5$. The radii of the barrel pixels extend from 6 cm to 15 cm from the collision vertex. The forward pixels range from $z = \pm 34.5$ cm to $z = \pm 46.5$ cm for each layer respectively [37] .

The silicon strip tracker, shown in figure 2-4, is divided into four regions: the tracker inner barrel (TIB), tracker inner disks (TID), tracker outer barrel (TOB), and the tracker endcaps (TEC). The TIB, red part of figure 2-4, consists of four concentric cylindrical layers of modules ranging from a radii of 25 to 50 cm, the first and second of these layers are double layered. The double layering provides for the determination of the z coordinate. This follows from the fact that the second layer lies on top of the first and is arranged with an angle relative to the other layer of 100 μrad [37] . The TID, blue part 2-4, consists of three layers extending out to 70 cm in z, each layer is divided into three concentric rings of which the first two are double sided. The TOB, green in 2-4, consists of six layers of concentric cylinders of less finely granulated silicon extending from a radius of 56 cm to 116 cm. As with the TIB, the first two layers of TOB are double sided. The TECs, purple in 2-4, each consist of 9 disks extending from a region of $\pm$ 124 cm to $\pm$ 280 cm along the z direction [37] . Like the TID, each TEC disk is divided into concentric wheels, of which two inner wheels are double sided. The combination of all subdetectors allows for track reconstruction out to $|\eta| < 2.4$.

In general, silicon detectors reconstruct hits with an efficiency near 90 percent. In order to be able to reconstruct tracks with an efficiency beyond 99.9 percent, a minimum of three hits for the five parameters of the helix plus an additional four hits to account for the approximate 90 percent hit efficiency is necessary. Thus, an expected minimum number of seven hits is necessary to maintain high efficiency. Figure 2-6 show the expected number of layers where at least one or two hits can be reconstructed. The expected number of layers is on the order of ten, for nearly the whole range of the CMS tracker, ensuring high track reconstruction efficiency.

The large number of silicon layers leads to a large amount of material. This material induces energy loss, and a higher probability of photon conversions into e^+e^-. The rate of energy loss is significant enough to shift the measured energy scale of the calorimeters by more than 10 percent [40] . The expected amount of energy loss due to the material as a function of η is shown in figure 2-6. At maximum, the energy loss from material is nearly two radiation lengths.

2.4.4 Data Flow in the tracker

Figure 2-7 shows the required detector electronics to send data recorded from a deposit on a silicon wafer to the a data collection device, known as the front end driver (FED). After the FED, the signal is sent to a large computing cluster where data is combined with the rest of the CMS detector to eventually form a fully reconstructed event. The flow of this data is similar for both the pixel and strip detectors. The difference between the two systems is that the pixel detector signals are zero suppressed, *ie* signals are only sent if they are above a designated threshold [37] .

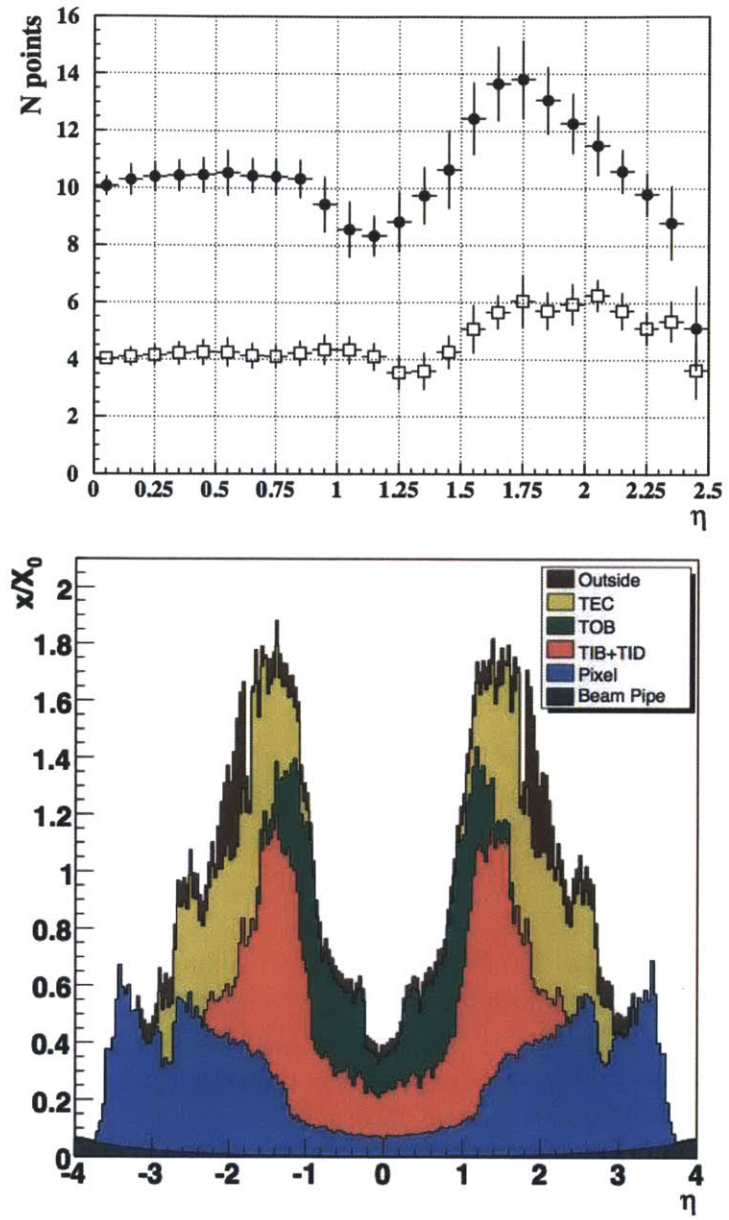

Figure 2-6: The expected number of measurement points (number of hits) as a function of η of the silicon strips (top). The open points are the double sided hits and the closed points are the total amount of measurements. Overview of the total tracker material thickness in units of radiation length X_0 over the whole η range of the CMS detector (bottom).

Tracker data flow

The signal starts from a deposit on the silicon detector, this is processed through a chip, known as the APV. The APV chip is capable of storing an analog pulse shape

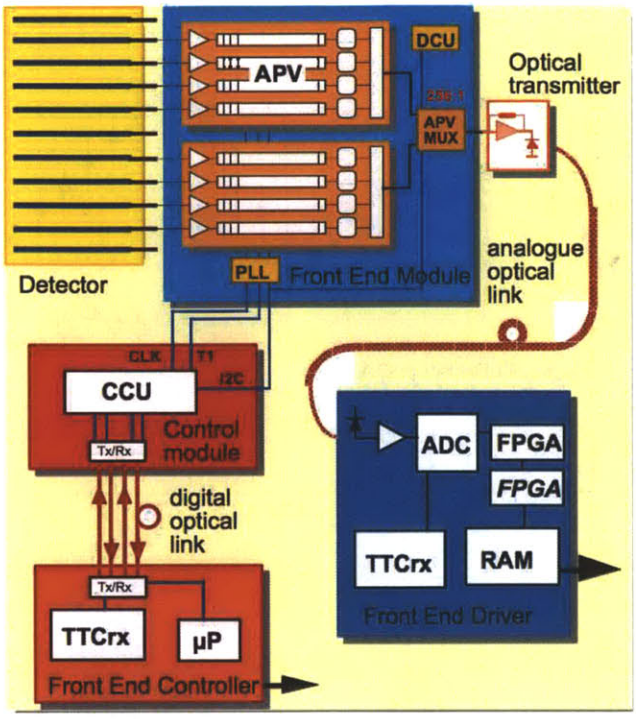

Figure 2-7: Schematic view of the flow of tracker readout and control electronics.[37]. The actual CMS detector is located in the top right of the diagram. Data flows from the detector through the APV to the Front End Driver located on the bottom right.

from 128 strips of silicon for 200 separate bunch crossings [41]. These are processed along a chain, amplifying them and deconvoluting the readout effects so that a sharp signal is obtained. The difficulty of reading out the CMS tracker results from its size, which is composed of 80,000 APV chips. This in turn equates to $128 \times 80,000 \approx 9 \times 10^6$ strips which must be read out at the interaction rate of 40MHz. To perform the readout several signals from an APV are concatenated together passed into a fiber, which is bundled with 96 other fibers and delivered to the FED [39].

Most of the information in the tracker is not relevant for physics reconstruction. A single minimum ionizing particle will only be sampled by $\approx$80 of the 9×10^6 strips. The 80 strip signals summed over at maximum several hundred particles emanating from the collision produce a per event occupancy of 0.5-3.0% (depending on the instantaneous luminosity). The reduction of data from that of the whole tracker to the few hits above a threshold is performed by the FED (zero suppression). Following zero suppression the pixel and strip data is concatenated and delivered to CMS DAQ for further filtering and eventual storage.

To control the tracker, a series of tiered systems exist (figure 2-7), which are used to synchronize the timing of the tracker, deliver settings to the readout, monitor detector behavior, and send trigger commands to induce data taking [39]. The tiered systems consists of a controlling device, known as the front end controller (FEC orange in 2-7), which delivers signals to a digital optical hybrid (DOH), that processes the

signal and delivers the processed signal to control modules known as the CCU (red in figure 2-7). The time synchronization is done through a series of phase locked loops (PLLs orange located on the blue in figure 2-7). The monitoring of the devices is done through special readout components on each device known as detector control units (DCUs).

This system, the tracker control system, is designed to instigate data taking if an event is determined to be studied. This occurs when a level one trigger fires and notifies the tracker. Upon receiving a level one trigger, the trigger signal, and a global clock are passed to the FEC [39] , which subsequently transmits the ordered signal of the two components to the DOHs. The DOHs then distribute this clock along the CCU chain. Each CCU then distributes this to the PLL where it is properly delayed and delivered to the APV chip.

The APV chip is capable of transmitting 10 signals per every 200 events. When the 10 signal buffer is exceeded the APV chip goes into an error state. In order to prevent this from happening the detector is equipped with an APV emulator (APVe) that simulates the trigger occupancy and throttles the rate of data taking based on the APV occupancy [39] .

Calibration In order to synchronize the behavior of the tracking system a series of calibration tests are performed. These tests consists of voltage scans and synchronizations of the different components of the tracker. Figure 2-8 shows one such calibration test. In this instance, the individual signal response times from the APV chips are recorded. The recorded times are read out and delays are adjusted to deliver triggers on time. To fully calibrate the tracker for collision data taking, a minimum of five more tests are required [42] . These tests are responsible for measuring the noise of the silicon and other components, calibration of the optical signal transmission, calibration of the APV chip, and synchronization with the rest of the CMS detector. As with the timing calibration, each test requires a per module (single point in figure 2-8) measurement of its individual properties.

Tracker alignment

In order to optimize the momentum resolution of the reconstructed tracks, the exact positions of the various detector sub components must be measured. To measure the positions and monitor movement a laser alignment system is used [43] . Following the laser alignment, the exact positions are determined by an alignment algorithm, which minimizes the track χ^2 by reconstructing a large collection of tracks and individually adjusting each of the 15,000 modules in the tracker so the the global track χ^2 is minimized.

Tracker performance

The individual ionization deposits of a charged particle in the silicon layers of the tracker are combined into tracks. The $\sim$100 μm size of the silicon in the tracker leads to a precise measurement of the track momentum resolution. Figure 2-9 shows the

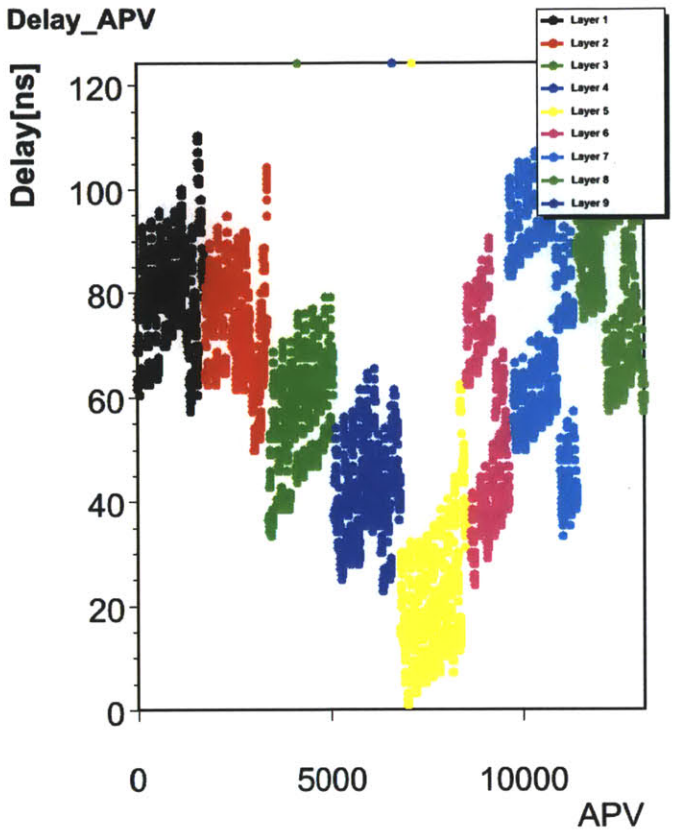

Figure 2-8: Performance of the timing of the TEC plus sub detector of the CMS tracker. The individual color indicate the different layers within the TEC plus detector. The individual points correspond to a specific tracker silicon readout module (blue in figure 2-7).

track resolution for muons reconstructed in different sub detectors. The track reconstructed in the tracker is indicated by the dotted-dashed blue line. The reconstructed resolution for muons with a $p_{\mathrm{T}} < 50$ GeV/c is below one percent.

A futher example of the performenace comes from tracks that cluster about an interaction point at the center of the detector producing an interaction vertex. Due to their small size in two dimensions, the pixel detectors allow for a very precise determination of the interaction vertex. For W boson events, the uncertainty on the resolution measurement is typically around 20 μm.

2.4.5 Electromagnetic calorimeter

The electromagnetic calorimeter (ECAL) consists of a set of $PbWO_4$ crystals. These crystals are arranged concentrically about the vertex with an inner boundary defined by the end of the tracker. The crystals are used to measure the the energy of the

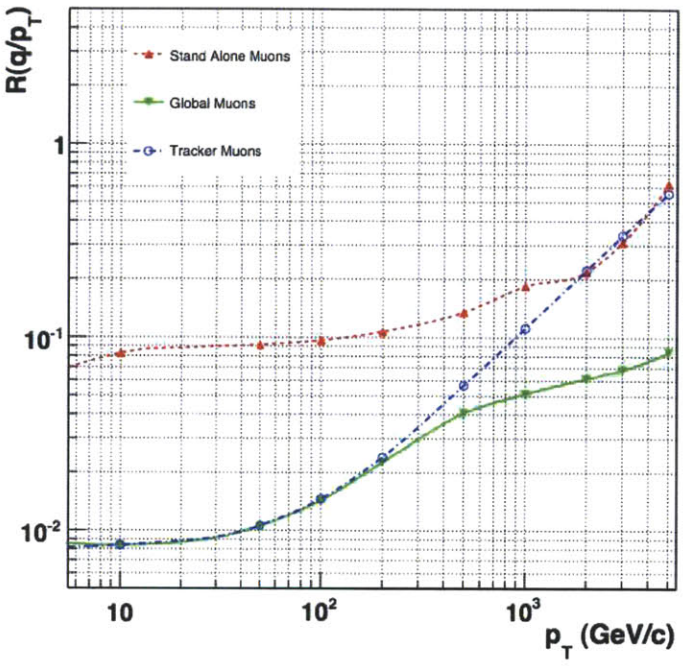

Figure 2-9: Track reconstruction resolution in terms of transverse momentum fraction defined as $R(q/p_{\mathrm{T}})$ using the silicon tracker (blue), the muon chambers (red) and the combined muon chambers and silicon tracker [44]

electrons and photons impinging on the detector by simultaneously inducing electromagnetic showers and reading out the resulting light output produced in the shower. The showers are induced due to high density (8.28 g/cm^2) and short radiation length (2.1 cm) of the $PbWO_4$ material [34]. As the shower propagates along the detector, a large number of low energy photons are produced (on the order of 10^5). Because the ECAL crystal is transparent, these photons travel to one end of the crystal where they are amplified by an avalanche photo diode [37]. A series of crystals is shown in figure 2-10.

Figure 2-11 shows the layout of the ECAL as a function of η. The ECAL is split into two regions, the barrel and endcap. The ECAL barrel runs from $0 \leq |\eta| < 1.479$ [37]. The endcaps run from $1.479 < |\eta| < 3.0$ [37]. The region between the endcap and barrel, although covered, has a degraded resolution and lower reconstruction efficiency due to the fact that the coverage is split between the barrel and endcaps. In the barrel, each crystal is designed to cover a region approximately 0.0174×0.0174 in $\eta - \phi$ space. In the endcap, the covered region goes from 0.0174×0.0174 to 0.05×0.05 in η-ϕ space. Due to the different physical size of $\delta\eta$ at high and low values, the crystals at high η have a worse resolution.

The typical size of the crystals is about 2.5 cm by 2.5cm by 23 cm. The transverse size, 2.5 cm, is on the order of 1 Moliere radius [34], thus a single electromagnetic shower originating from an electron or photon is contained primarily within one crys-

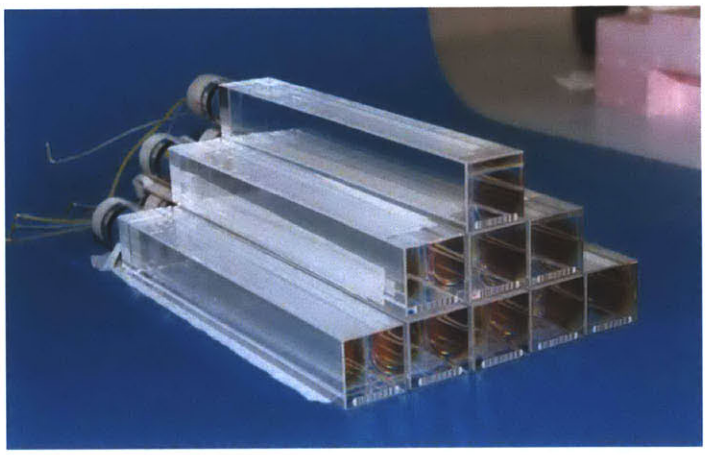

Figure 2-10: Series of CMS electromagnetic calorimeter crystals. Crystals are 23cm in length, 2.5 cm in height, and 2.5cm in width [45]. The wires on the far end are attached to the APD.

tal. Separation of small showers is more difficult; the separation becomes even more difficult at high η where the phase space density makes it difficult to separate photons that are nearby each other. In order to differentiate photons that are nearby one another, an additional series of layers of lead and silicon strips are installed directly in front of the endcap crystals. These layers are known as the CMS silicon preshower[46]. The additional lead induces the start of electromagnetic shower and the silicon strips measure the shower energy deposits and their position. The silicon strips resolve showered photons separated by a minimum of 2 mm.

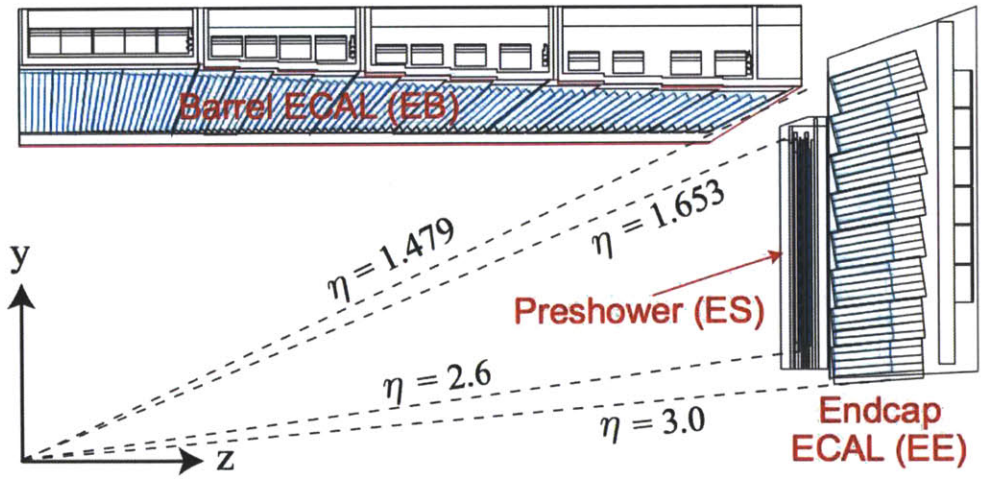

Figure 2-11: Cross section of the CMS ECAL as a function of positive $|\eta|$ for a fixed ϕ. The crystals are arranged projectively about the collision vertex. A transition region between barrel and endcap occurs at $\eta = 1.5$.

The ECAL resolution is determined from test beam studies to be [47].

$$\frac{\sigma(E)}{E} = \frac{2.8\%}{\sqrt{E(\text{GeV})}} \oplus \frac{12\%}{E(\text{GeV})} \oplus 0.3\% \ , \tag{2.15}$$

where the first term is the stochastic (nominal) energy term, which is determined by the number of photons produced per shower. The second term results from noise from the detector readout and photon excitations in the crystal. The third term is the constant term caused by limitations in the detection. This implies sub-percentage resolution from energies beyond 20 GeV. In the CMS detector, however, the test beam level precision is not obtained because of several effects. The largest effect results from a gradual decrease in the gain as function of radiation damage. With radiation, the ECAL crystals lose their transparency, thereby leading to a reduced signal. Continual monitoring of the transparency is performed through a laser. The variation in the transparency is then translated to a per-crystal correction, which approximates the variation. The second largest effect results from the variation in resolution and transparency from crystal to crystal. These variations result from impurities during production. A third, smaller, effect results from variations in gain due to temperature variations throughout the detector.

In order to correct for the effect of mis-modeling an inter-calibration of detector components is performed by requiring a well tagged π^0 decay leaving deposits in two separate crystals. At present, the inter-calibration is capable of giving 1% energy resolution accuracy in the ECAL barrel and 3% in the ECAL endcaps[47].

2.4.6 Hadron calorimeter

The CMS hadron calorimeter (HCAL) is designed to measure the neutral and charged hadronic showers originating from quark and gluon fragmentation and hadronization. It is designed to be almost completely hermetic, such that all showers within the HCAL dimensions are well contained. The HCAL is arranged in towers of dimension 0.087×0.087 in $\eta - \phi$ with radial length of 1.2m. Bounding the inner end of the HCAL is the ECAL. On the outer end the HCAL straddles the solenoid (figure 2-12).

The HCAL is divided into four different regions: the barrel (HB), $0 < |\eta| < 1.3$, the endcap (HE) from $1.3 < |\eta| < 3.0$, the forward calorimeters (HF) from $3 < |\eta| < 5$ and the outer calorimeters (HO) from $0 < |\eta| < 0.8$ [37]. The HB and the HE consist of layers of brass interlaced with scintillator. The HF consists of quartz fibers embedded within steel absorbers. The HF utilizes two sets of fibers of length 165 cm and 143 cm to separate electromagnetic and hadronic showers respectively [37]. The electromagnetic fiber is used to compensate for the fact that there is no ECAL beyond the region of $3 < |\eta|$. The outer calorimeter, the HO, is an additional scintillating calorimeter located outside the solenoid. It is used to capture energy from the tail of showers which pass through the solenoid. Each scintillator is attached to a hexagonal array of hybrid photo diodes (HPD) [48] through a wavelength shifting fiber.

In the HB, HE, and HO, the readout of each scintillator is combined to produce either a single or double energy readout for each hadronic tower. The sampling

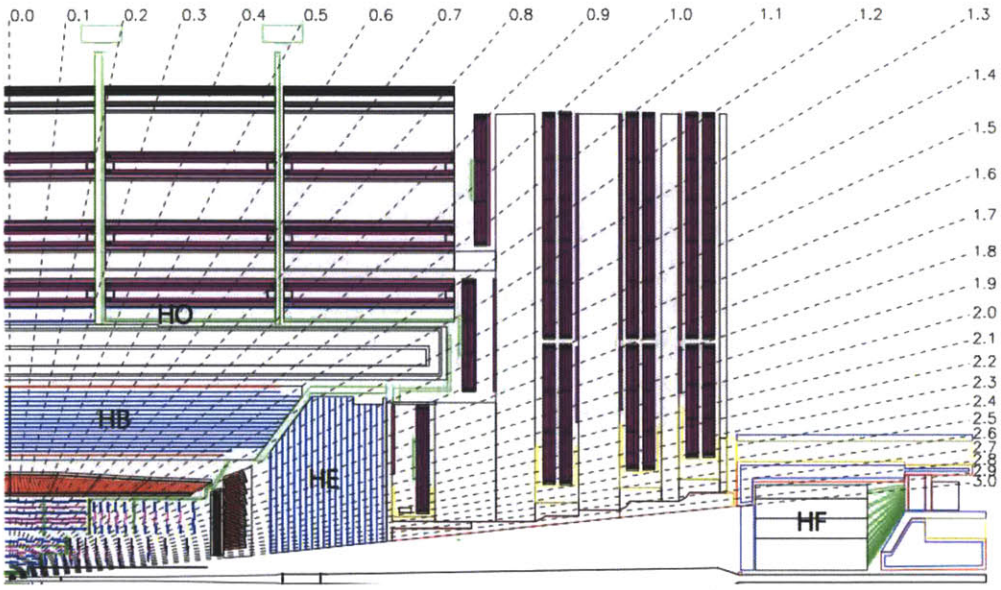

Figure 2-12: Diagram of the CMS HCAL, the blue layers designate the HB and the HE. Upwards from the HB is the solenoid followed by the HO. The HF is located in the far right.

fraction is such that a single photo electron is read from the hybrid photo diode for a 0.7 MeV energy deposit. Poisson statistics determine the resolution yielding a non-linear energy response for deposits less that 20 GeV(right of figure 2-13). The calibration of the HCAL response is done through two methods. One method uses single pions, which leave a single well measured track in the silicon tracker and then stop in the HCAL through a hadronic shower. The result of the single pion barrel calibration is shown in figure 2-13. The second method clusters energy deposits from the HCAL with the ECAL and the tracks to form a jet. The combination of the different sub components enhances the energy resolution by using each sub detector deposit. Jets are calibrated by balancing jets with other jets and photons.

The resolution shape depends strongly on the type of particle showering in the detector. The measured energy response of neutral hadrons is different from that of charged hadrons; thus, the resolution shape of a jet measured in the HCAL depends on the relative charged and neutral composition [34]. Different resolutions exist for the different calorimetry in the endcaps, barrel, and forward region. To quote a more appropriate number for the scale of the resolution shape and its uncertainty, we consider the calorimeter jet resolution. A calorimeter jet clusters the deposits in the HCAL and ECAL by a specific algorithm (chapter 5). This leads to a single object, which represents a high energy quark or gluon and its resulting quark and

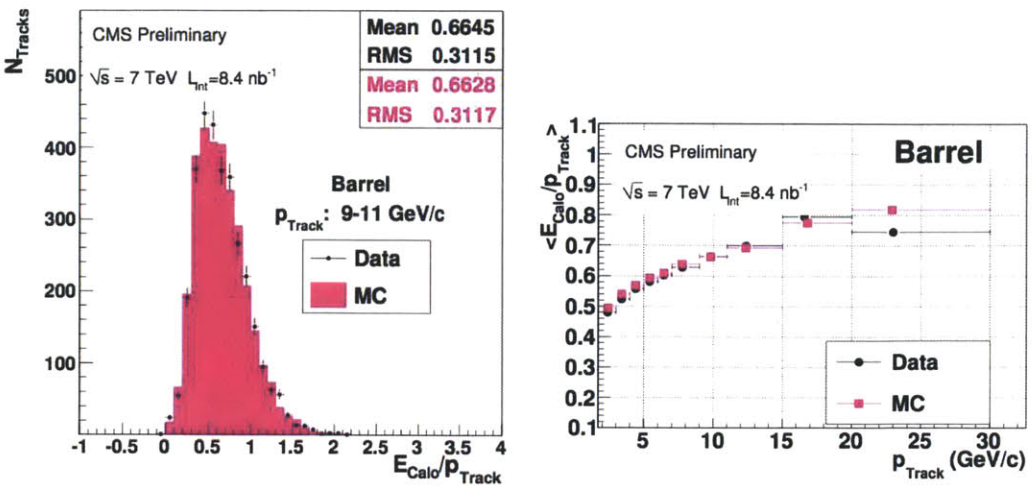

Figure 2-13: Single Charged Pion response distribution for a given pion energy range (left) and average response per energy over the whole range (right) [49]

gluon fragmentation. The overall p_{T} resolution for such a jet is written as [50].

$$\frac{\sigma(p_{\mathrm{T}})}{p_{\mathrm{T}}} = \sqrt{sign\,(N)\cdot\left(\frac{N}{p_{\mathrm{T}}}\right)^2 + S^2\cdot p_{\mathrm{T}}^{M-1} + C^2}\,. \tag{2.16}$$

The term N is known as the noise term, it dominates the resolution for low energy deposits. The value of N is on the order of 4 GeV for HB and HE and -4 GeV for HF. The term S is the stochastic term, which scales by the Poisson uncertainty of the energy deposit. It is found to be on the order of $0.7-1.1$ going from small η to high η. The term M is a correction to the stochastic term. It ranges from $-0.1 \rightarrow 0.2$. The final term, C, the constant term represents the intrinsic resolution limit originating mainly from effects of imperfect calibrations. This term is found to be close to zero.

The resulting resolution is depicted figure 2-14. Typical resolutions of jets with a $p_{\mathrm{T}} > 50$ GeV/c are near 10% of the total jet energy.

2.4.7 Muon chambers

As with the tracker, the CMS muon chambers are designed to reconstruct tracks of ionizing particles. Because of their location on the exterior of CMS, the muon chambers only detect ionizing particles which escape the rest of the CMS detector. This is almost exclusively muons. Muon chambers are clustered together into a set of muon chambers known as a station. Four stations of chambers are layered around CMS in a similar configuration to the layers of the silicon tracker.

Within each station is an arrangement of tracking detectors. Consisting of up to 12 layers utilizing one of two different detector technologies, either cathode strip chambers or a drift tubes. Resistive plate chambers are placed on either end of the

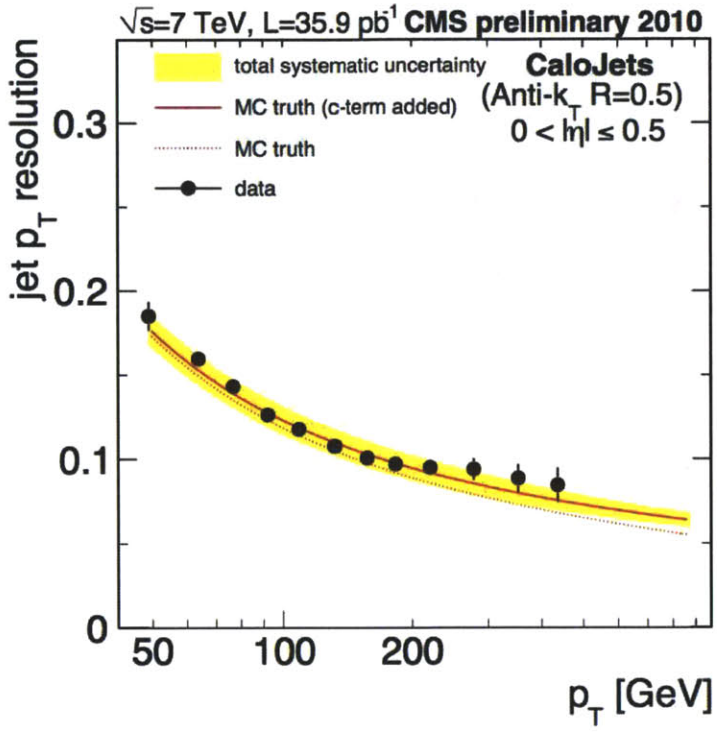

Figure 2-14: Calorimeter Jet Resolution as a function of jet p_{T} [50]. The dotted red line shows the prediction if no constant C term (equation 2.16) is present in the simulation. The solid red line shows the prediction if a C term is present. The black points correspond to the measured jet resolution from jet balancing. The yellow band is the systematic uncertainty from jet balancing.

first two muon stations and on the near end of the last two stations. Figure 2-15 shows a cross section of muon chambers. The low η region, $|\eta| < 1.04$, is composed of drift tubes (DT green in figure 2-15). The endcap region of the muons is composed of cathode strip chambers (CSC blue in figure 2-15). The RPCs (red in figure 2-15) extend from a range of $|\eta| < 1.6$.

Drift Tubes

The drift tubes consist of a wire inside a tube-like structure filled with 85% Ar and 15% CO_2. A muon going through the detector will leave an ionization trail, which will then drift to the wire and avalanche inducing a voltage. Figure 2-16 shows an example of a single drift tube element [37]. The drift time and the position of each wire constrain the location of the closest ionization deposit to an annulus of distance R from the center of the detector wire. Depeding on the wire orientation, this corresponds to either a coordinate in ϕ or θ. Figure 2-17 shows a DT station (referred to as a "super layer"). In each station are eight layers of wires oriented along the ϕ plane and four layers of wires oriented along the θ plane. Hits on the ϕ

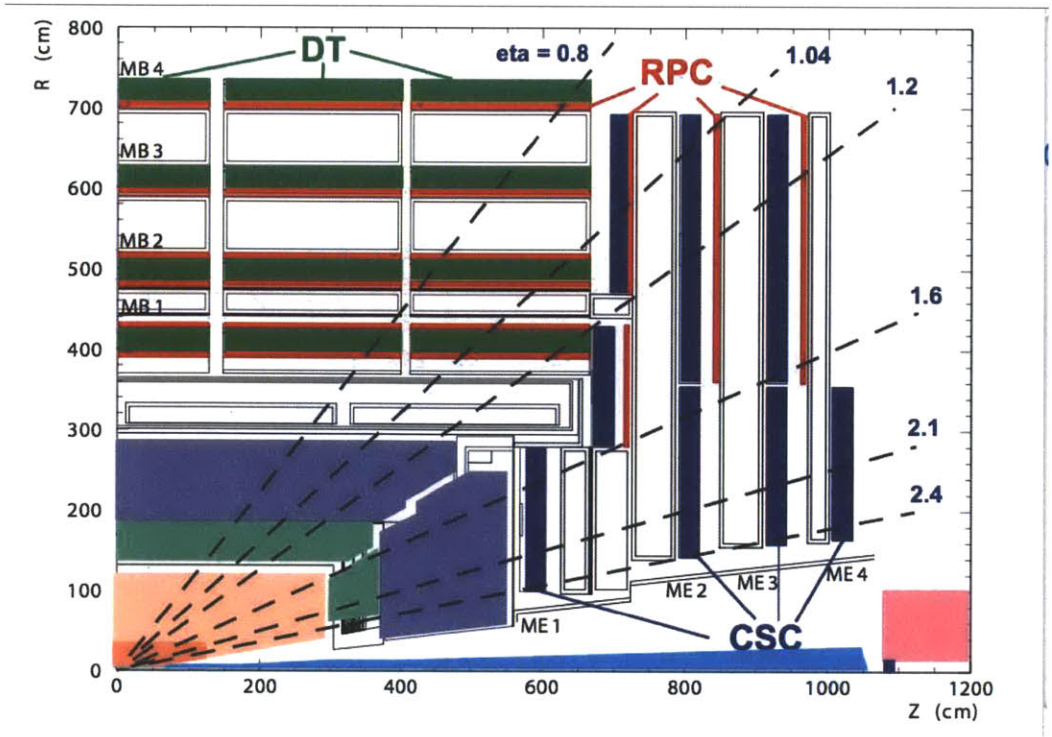

Figure 2-15: Cross section of the muon chambers in the $r - z$ plane [51]. The three different detection technologies RPC, DT, and CSC are denoted respectively by the red, green, and blue colors on outside of the muon chambers. Each colored object of the CSC or DT chambers denote a station. Stations are oriented in layers labelled as MB for the DT region and ME for the CSC regions.

and θ planes are reconstructed independently and then connected together to form a short track known as a "segment". An ambiguity arises in the position of the hit about the annulus of the wire, because the drift constrains a hit to an annulus about the wire. This ambiguity is resolved by taking the point which minimizes the χ^2 of the segment. With four separate stations of drift tubes, up to four reconstructed segments per muon are possible.

Cathode Strip Chambers

The second tracking elements of the muon chambers are the cathode strip chambers. Ionized particles of a muon passing through the detector drift field get amplified through an avalanche along a wire inducing a voltage on both the wire and a series of strips located near by the wire. Figure 2-18 shows an example of a cathode strip operation [37]. The resulting positive ion drift from the avalanche along the wire induce a charge on a set of negatively charged strips know as the cathode. The induced charge distribution determines a position (the $r - \phi$ coordinate) in the form of a four bit Gatti function [52]. The centroid of the Gatti is unfolded and converted into a hit. The wires run orthogonally to the strips, thus avalanches along the wires

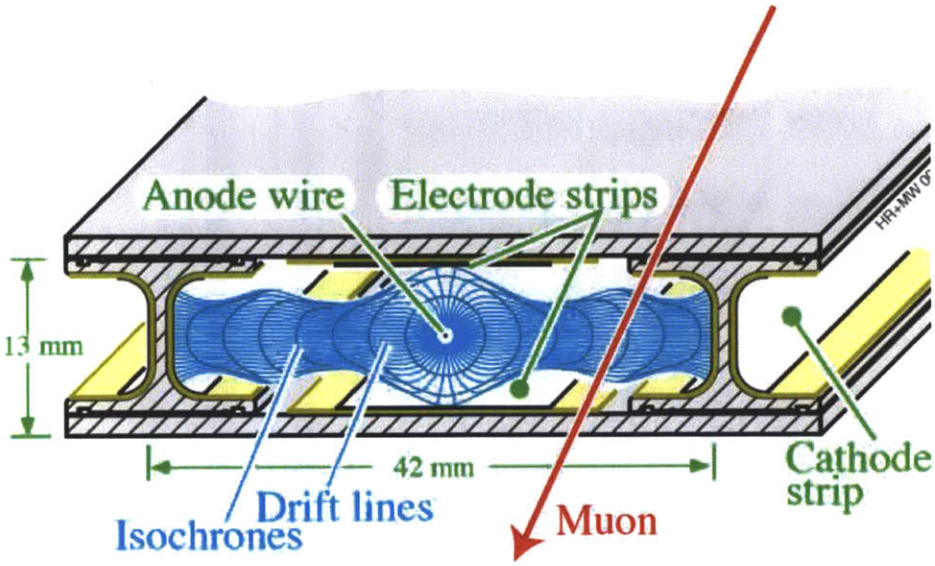

Figure 2-16: Example of a single drift tube element. The red line indicates the passage of a muon through this drift tube element.

inside the cathode strip chambers determine a position in the $r - \theta$ coordinate. The combination of the wire position and the strip position determine a three dimensional hit position. Figure 2-19 illustrates the passage of a muon through one CSC station. In one station there are three strip layers and three wire layers. The combination of these positions into a short track form a three dimensional muon segment. Up to 4 reconstructed segments per muon are possible because there are four stations of CSC chambers.

Resistive Plate Chambers

The resistive plate chambers consist of two layers of a highly resistive material known as Bakelite separated by a 2 mm gap. In a RPC, a large voltage differential (typically 5 kV) is placed across the gap in order to induce a semi-proportional discharge from the passing of an ionizing muon. This large discharge develops rapidly leaving a clear signal. This discharge is significantly larger than a proportional avalanche in the drift chambers, imposing a limitation on the position resolution to a few cm. The time for the discharge to develop is a few ns, much faster than the $\mathcal{O}(10\text{ns})$ it takes for a DT or CSC signal. Figure 2-20 illustrates the passage of a muon through a RPC chamber. In each RPC chamber, the r position and the ϕ position are recorded leaving the third dimension θ unconstratined. There are up to six $r - \phi$ hits possible in the barrel and four in the endcaps.

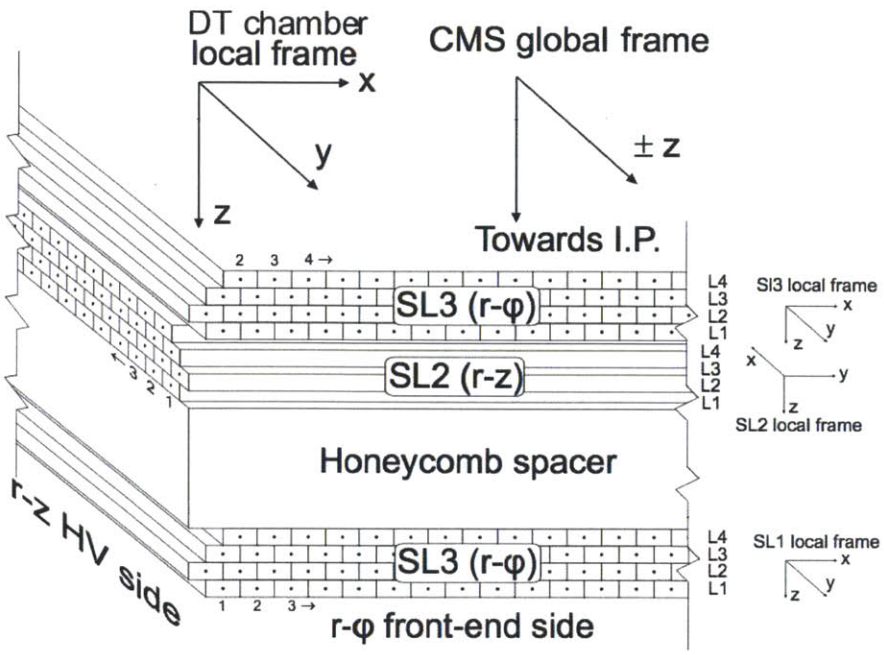

Figure 2-17: Illustration of DT station. DT chambers are separated into three clusters of chambers the top and bottom clusters are oriented in the $r-\phi$ plane and the middle cluster is oriented in the $r-z$ plane.

Muon reconstruction

The combination of segments from individual stations to a single muon is performed through an iterative tracking algorithm discussed in chapter 4. The final result is determined by a simultaneous fit of all hits in each muon station to a helical shape given an assumed energy loss model. The muon resolution that results from the final fit is shown in figure 2-21.

2.5 Data flow

Data which is read out of the CMS detector must be filtered and eventually stored. This is performed through a series of data fileters known as the trigger.

2.5.1 Trigger

Perhaps the most vital component of any hadron collider detector is the trigger. With a 40 MHz rate of collisions, the data output of the whole CMS detector is nearly 50 TB/s. In order to filter the events to a sustainable level, and keep events of great interest, events are partially read out and selected. This process of partially reading out events and selecting interesting events is known as the trigger. The CMS trigger

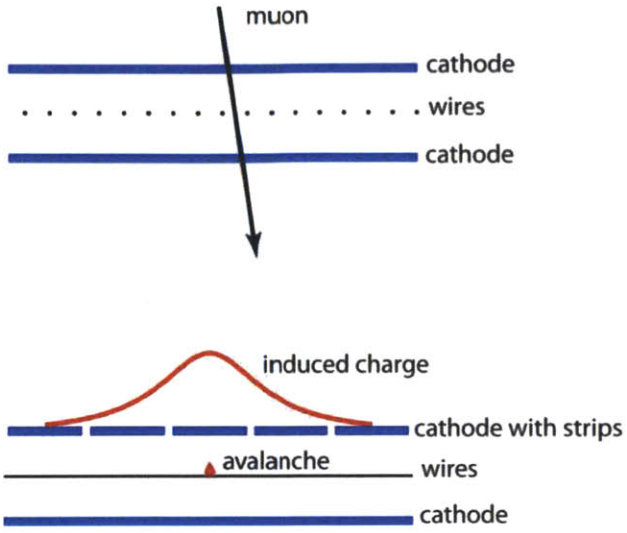

Figure 2-18: Illustration of the CSC detector operation. A muon passing through the CSC chambers leaves ionization which is amplified along the wire through an electron avalanche. Following the avalanche, drifting positive ions from the avalanche induce a position on the cathode strips.

is divided into two levels, a hardware level trigger, known as the level one trigger, and a software level trigger, known as the high level trigger (HLT).

Level one trigger

The level one trigger is implemented through a custom set of hardwired electronics which use programmable logic to assess the degree to which the event contains interesting physics. It is compartmentalized into individual detector triggers, a fast muon track reconstruction trigger (level one Muon trigger), an electromagnetic deposit trigger (the e/γ trigger), a fast jet reconstruction trigger (level one Jet), a vector sum of calorimeter deposits trigger (level one $\not\!\!E_{\mathrm{T}}$ trigger), and a scalar sum of calorimeter deposits trigger ($\mathrm{H_T}$ trigger). These triggers can be used individually or in concert with other components to select events which are passed to the high level trigger.

The level one trigger is designed to make a decision within 4 μs of an event occurring. This is limited by the total amount of data the readout buffers can store at any given time (200 events). This small latency forces the design of extremely high speed custom electronics, which are capable of partial event reconstruction at the μs level.

High level trigger

Events that are accepted by the level one trigger are then passed to the HLT. The high level trigger is completely implemented in software and run on a large computer farm. In the HLT, a complete, although cursory, event reconstruction is performed.

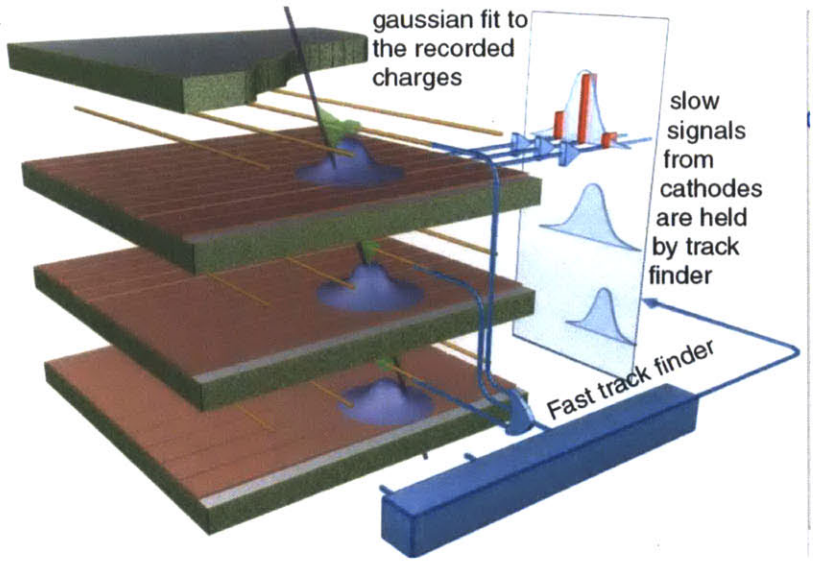

Figure 2-19: CSC layer and online readout system. The black line indicates a muon, which leaves a track identified by three layers of strips and three wire layers.

The high level trigger is designed to make a decision within one second of an event occurring. The final decision rate for recording events is 100 Hz.

The requirement to reconstruct an event and determine it is useful within one second imposes limits on the amount of reconstruction. This is most evident in the track reconstruction, which is performed by selecting hits near locations seeded by pixel hits, muon hits, or ECAL deposits and not performed on all hits in the event as it is done later on in the final reconstruction.

2.5.2 Simulation

To enhance understanding of the data a detailed simulation is constructed so as to replicate as precise as possible the behavior of physics events in CMS. The simulation is performed by a Monte Carlo generator (MC), which constructs a simulated event by randomly sampling event kinematics from the matrix element of a specified "hard scatter". The produced constituents typically consists of a collection of leptons, photons, quarks, and gluons. The strong interacting components (quarks and gluons) are further "hadronized" to form mesons and baryons [54, 55]. These hadronized particles along with the leptons yield the final products of the "generated" event. These are passed into a simulation of the CMS detector, which simulates the interaction of particles produced by the generator in the detector, leading to energy depositions. These simulated energy deposits are then passed through standard data reconstruction so as to closely mimic true proton proton collisions. The final product of the simulation is a data set specifying the Monte Carlo simulated process as it is expected to apper in the CMS detector. Details about the simulation of W and Z boson processes are discussed further in chapter 8.

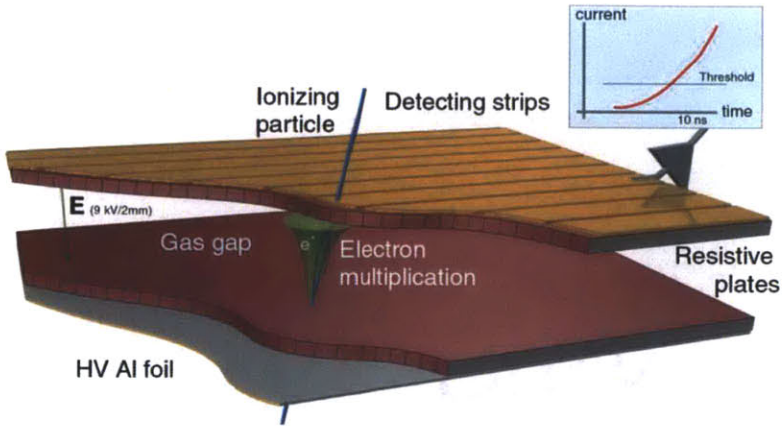

Figure 2-20: Individual RPC layer, The graph at the top right denotes the fast rise time of the RPC signal. The strips are arranged along the θ axis, yielding $r - \phi$ spatial resolution.

2.6 Summary

In this section, a description of the CMS detector and the LHC are presented. The LHC is the highest energy proton proton collider in the world. The CMS detector is a precision hadron collider detector with excellent tracking and calorimetry. Its design will motivate the choice of event selections, which allow for the precision measurement of the W and Z boson cross section.

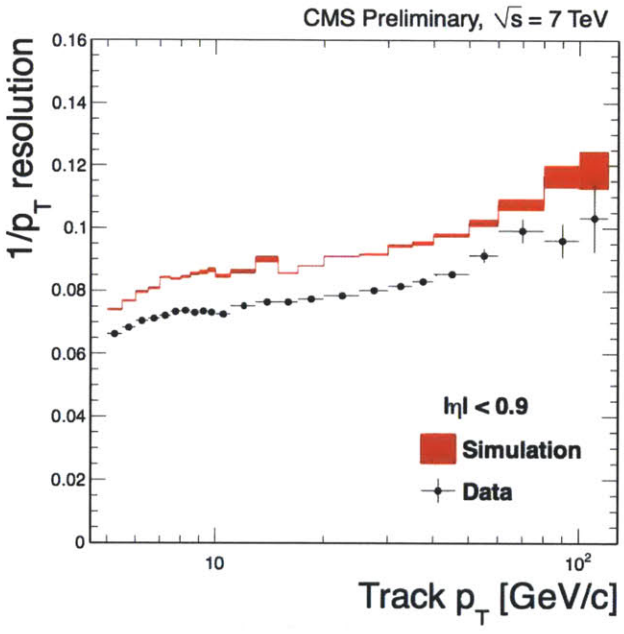

Figure 2-21: Comparison of the resolution of a muon reconstructed in the muon chambers between data (points) and Monte Carlo simulation (red band) as function of p_{T}. [53]

Chapter 3

Luminosity

A precise measurement of the instantaneous luminosity is critical for determining the W and Z boson cross section. It contributes the single largest uncertainty to the cross section measurement. In order to measure the instantaneous luminosity one must:

- Measure the rate of collisions r_{C}
- Normalize the collision rate to an absolute cross section σ_{lumi}

The rate of collisions, r_{C}, is used to determine the total amount of collected data. The normalization of the collisions is used to translate the rate into a physically meaningful value. Normalizing effectively measures the cross section of the process used in the rate determination. Following normalization, the rate r_{C} which is measured in events/second, is expressed as the instantaneous luminosity

$$\mathcal{L} = r_{\mathrm{C}}/\sigma_{\mathrm{lumi}} , \tag{3.1}$$

in units of $\mathrm{pb}^{-1}/\mathrm{s}$.

Instantaneous luminosity of a beam is written using the formula in equation 2.1. The unit pb stands for pico barn, a barn is a unit of area comparable to the size of heavy atomic nucleus, 10^{-28} cm^2. Collision rates are typically measured by the minimum effective area probed per set of collision or in other words the minimum cross section probed. The minimum size probed goes down with each collision. For a single collision this is about one mb^{-1} for N collisions this is about N^{-1} mb^{-1}. Rather than storing instantaneous luminosity in terms of collisions per second. Instantaneous luminosity is quoted by the effective area probed per second pb^{-1}.

Collision rates are determined by counting the rates of any process which have a known cross section, this includes W and Z boson production. In this section we present the instantaneous luminosity measurement as determined by the rate of soft inelastic collisions. If no new physics is present in the W or Z production channels, comparison of the W and Z boson cross section measurements with the predicted measurement will act as a cross check of this instantaneous luminosity measurement.

3.1 Rate of collisions

The rate of collisions is determined by four methods, three of which utilize the forward HCAL calorimeters (HF). Use of the HF maximizes the total fraction of all recorded collisions used in the instantaneous luminosity measurement. Two of the HF techniques are run "online" and two are run "offline". The offline measurements are treated as a cross check of the final instantaneous luminosity measurement. Finally, due to non-linearities in the HF energy response only the regions $3.5 < |\eta| < 4.2$ are used.

The first of the four methods, the so called "zero-counting" technique, is performed in the online environment. This technique calculates the mean number of interactions given the fraction of HF towers where zero interactions occur. For a Poisson distribution with mean, μ, the probability distribution of the expected number of events $p(n)$ is given by

$$p(n) = \frac{\mu^n e^{-\mu}}{n!} . \tag{3.2}$$

Thus, by determining the probability of zero interactions $p(0)$ the average number of interactions is found to be

$$\mu = -\log(p(0)) . \tag{3.3}$$

To perform this method $p(0)$ is calculated from the fraction of 864 HF towers that are empty [56]. This determines the value of μ per recorded event, which thus determines r_{C}. This technique has the advantage that it does not rely directly on energy scale calibrations of the HF; it requires only the act of triggering a recorded deposit above a threshold. This is the default method used to determine the instantaneous luminosity.

The second method exploits the linear relationship of the average transverse energy (E_{T}) per tower with the total instantaneous luminosity by recording the total energy deposit per HF tower [56]. This method leads to a straightforward and simple calculation of the instantaneous luminosity, however it suffers from mis-calibrations and non-linearities in the response of the HF. Nonetheless, both methods produce a consistent total instantaneous luminosity measurement (within four percent).

The third method, performed offline on a small, well understood dataset, is used as cross check of the first default method. This method is performed by measuring the incidence of deposits per tower in the HF detector. Unlike the first method, the deposits are cleaned by requiring them to be > 1 GeV and within 8 ns of the proton-proton collision time. These two selections remove noise effects in the HF further improving the measurement. The difference between the online and offline HF incidence based measurements is within 0.9 percent [57]. This implies an accurancy of the default method to within one percent.

The fourth method, also performed offline, is determined by counting the number of events with at least one reconstructed vertex with two tracks associated to it. For low instantaneous luminosities where multiple collisions per bunch are not expected, this technique provides a non HF based cross check of the other HF techniques. The

final result is found to differ from the default instantaneous luminosity by 3.7 percent [58]. This result is a final independent cross check of the HF counting technique. Deviations between this method and the default method define a conservative uncertainty band for which instantaneous luminosity measurements is compared to.

Figure 3-1 shows a comparison of the instantaneous luminosity for the third technique and the fourth technique. The instantaneous luminosity calculation is linear over the four orders of magnitude shown. The slope of a fit of the two instantaneous luminosities compared to one another is 1.027 indicating a deviation in the instantaneous luminosity readings of 2.7 percent between the two techniques [56].

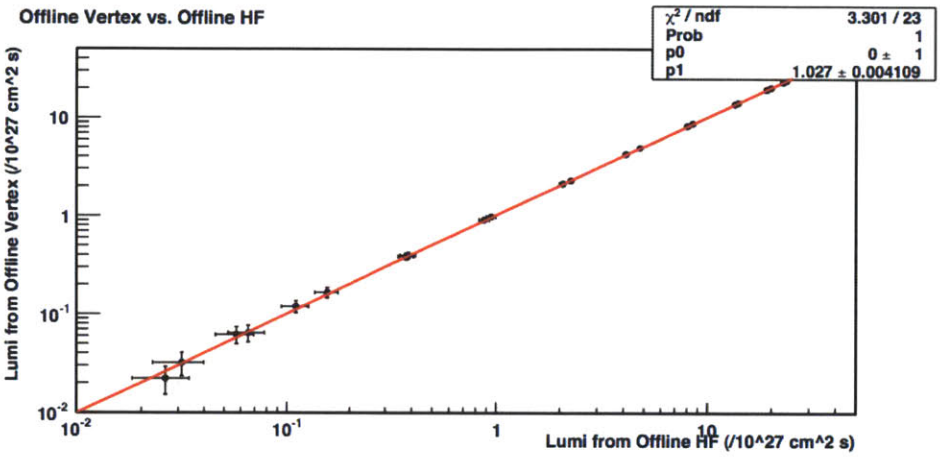

Figure 3-1: Comparison of the instantaneous luminosity rate using the two offline techniques. The y-axis indicates the instantaneous luminosity measuring the rate of vertex reconstruction (fourth technique) and the x-axis indicates the instantaneous luminosity measurement using the offline HF technique (third technique).

3.2 Absolute normalization

The absolute normalization determines a value σ_{lumi} which translates the rate of collisions to the physically meaningful definition of instantaneous luminosity given in inverse barns per second. The absolute normalization, σ_{lumi} of the collision rate requires a measurement of the cross section of the process used in the default instantaneous luminosity method. To measure the true cross section, a Van De Meer scan is utilized. It is performed by scanning over the x and y distributions of the two beams, moving the position of each beam in a stepwise manner and recording the rate. The instantaneous luminosity is obtained from equation 3.1 and the widths of each beam

distribution using the general instantaneous luminosity formula:

$$\mathcal{L} = \frac{r_c}{\sigma_{\text{lumi}}} , \tag{3.4}$$

$$= N_1 N_2 \nu_{\text{rev}} \int \rho_1(x)\rho_2(x-\Delta x)dx \int \rho_1(y)\rho_2(y-\Delta y)dy , \tag{3.5}$$

where in the top case we have written $\mathcal{L}$ in terms of the parameters that define the instantaneous luminosity measurement in CMS. In the bottom equation, we have written $\mathcal{L}$ in terms of the number of particles per beam N_i, the revolution frequency ν_{rev} and an integral over the two beam density distributions, ρ_i, in the two coordinates transverse to the beam: x and y. The separations of Δx and Δy define a offset between the central points of the two beams. Integrating over Δx and Δy of both equations 3.4 and 3.5:

$$\int d\Delta x d\Delta y \mathcal{L} = \frac{1}{\sigma_{\text{lumi}}} \int d\Delta x d\Delta y \left(r_c\left(\Delta x, \Delta y\right)\right) , \tag{3.6}$$

$$= N_1 N_2 \nu_{\text{orb}} , \tag{3.7}$$

and solving for the absolute normalization, σ_{lumi}, by inverting equation 3.6

$$\sigma_{\text{lumi}} = \frac{\int d\Delta x \left(r_c\left(\Delta x, \Delta y_0\right)\right) \int d\Delta y \left(r_c\left(\Delta x_0, \Delta y\right)\right)}{\nu N_1 N_2 r_c\left(\Delta x_0 . \Delta y_0\right)} . \tag{3.8}$$

This implies that σ_{lumi} may be determined by measuring the number of protons per bunch N_i, the frequency of the collisions, ν, and the beam width distribution defined by the measured rate of collisions for a specific beam separation Δx and Δy , $r_c(\Delta x, \Delta y)$.

To obtain $r_c(\Delta x, \Delta y)$ a scan of the beam profiles is performed by incrementally adjusting the current on the beam magnets around the collision points, so that one or both beams move some distance Δx or Δy, and then measuring the collision rate. The distance Δx or Δy of each incremental adjustment is determined utilizing two different methods:

1. Take Δx and Δy from calculations based on the magnet adjustments
2. Take Δx and Δy by reconstructing the interaction vertex position of each collision

The individual methods are presented in the sections below.

3.2.1 Magnet adjustments method

In this method several assumptions are made [57]

1. The central position of the two beams is known ($\Delta x_0, \Delta y_0$ = 0,0).
2. The beam profiles of the two colliding beams are the same

3. The length scale of Δx is linearly correlated with the magnet current readings.

4. The convolution of the two displaced beam distributions is a double Gaussian (sum of two Gaussian with mean zero)

This third assumption is checked in a specific region by the vertex reconstruction and found to be within 1 percent of the true length scale [57].

The scan is performed by adjusting the magnet current and measuring the collision rate. Translation of the magnet current to the length scale Δx yields a distribution of the rate of the convolutions of the two beams as a function of Δx. Fitting the combined distribution to a double Gaussian gives a set parameters describing $r_c(\Delta x, \Delta y)$. For double Gaussians normalized to one, the integral terms in equation 3.8 are removed giving σ_{lumi} as

$$\sigma_{\text{lumi}} = \frac{1}{\nu N_1 N_2 r_c\,(0,0)}\ , \tag{3.9}$$

$$= \frac{\sqrt{2\pi}}{\nu N_1 N_2 \left(f\sigma_1^{-1} + \sigma_2^{-1}(1-f)\right)}\ , \tag{3.10}$$

where σ_1 and σ_2 denote the two widths of the beam and f is the relative fraction of one of the Gaussians within the double Gaussian. A fit of the double Gaussians to the rate as a function of Δx is shown in figure 3-2.

3.2.2 Vertex reconstruction method

In place of relying on magnetic current measurements to determine the positions Δx or Δy, the reconstructed vertex position is used. Use of the vertex position removes the assumptions that the position adjustments are distributed about zero, the colliding beams have the same profile, and the magnetic adjustments of the beams vary the separation of the beams by a known amount.

To perform this measurement a second scan is performed where one beam is moved at a time. First the beam in $+z$ (beam 1) is moved and then the beam in $-z$ (beam 2) is moved. Moving the beams separately allows for the determination of the beam density profiles $\rho(x)$ separately for the $+z$ and $-z$ beams. To see how this is obtained consider first the distribution of the rate along the x axis given a measured vertex position x for a fixed separation Δx :

$$r_c\,(x|\sigma_{\text{res}}) = \rho_1\,(x-\Delta x)\,\rho_2\,(x) \otimes G\,(x,\sigma_{\text{res}})\ , \tag{3.11}$$

where we have convolved the beam profile distributions $\rho_1\rho_2$ with a Gaussian $G(x,\sigma_{\text{res}})$ with resolution given by the vertex reconstruction resolution σ_{res}. Uniformly adjusting beam 1 stepwise over a values Δx_i and measuring the rate versus reconstructed

position x gives:

$$r_c(x|\sigma_{res}) = \sum_i \rho_1(x - \Delta x_i)\,\rho_2(x) \otimes G(x, \sigma_{res}) \ , \quad (3.12)$$

$$\approx \rho_2(x) \otimes G(x, \sigma_{res}) \ , \quad (3.13)$$

where we have noted that $\int \rho_1(x)dx = 1$. For a sufficient number of steps the approximation in equation 3.13 is within 0.5% of equality [58]. Assuming the x and y coordinates are not correlated ($\rho_1(x,y) = \rho_1(x)\,\rho_1(y)$), this method is used to obtain the x and y profiles of both beam 1 and beam 2. The true beam shape is then determined by a two dimensional fit to the collision rate $r_c(x|\sigma_{res})$ where one axis is the reconstructed vertex position (*ie beam position*) and the other axis is the vertex position resolution σ_{res}. This two dimensional fit assumes a double Gaussian convolved with a Gaussian with resolution σ_{res} determined by its position on the second axis. Figure 3-2 shows the result of the fit to the x axis of both $\pm z$ beams. The fit model describes the beam profile shape well. This allows for the determination of the instantaneous luminosity normalization from equation 3.9 by integrating over the two beam profiles

$$r_c(0,0) = \int dxdy\rho_1(x,y)\,\rho_2(x,y) \ , \quad (3.14)$$

$$\sigma_{lumi} = \frac{1}{\nu N_1 N_2 r_c(0,0)} \ . \quad (3.15)$$

3.2.3 Comparison

Comparing the two methods yields a value of the instantaneous luminosity consistent within 2.5 percent[58]. This difference is quoted as a systematic uncertainty on the instantaneous luminosity measurement. The second largest uncertainty, 1.7 percent, results from the uncertainty of the measurement of the bunch densities N_1 and N_2 obtained from dedicated bunch current devices (known as the fast BCT and the DC BCT). Combining the 2.5 percent difference with the 1.7 percent uncertainty and additional smaller uncertainties yields a total systematic uncertainty of 3.6 percent [59]. The final systematic uncertainty is conservatively quoted as four percent.

3.3 Instantaneous luminosityin 2010

The data used in this thesis was performed with the complete 2010 dataset. Over the course of the 2010 running LHC delivered 47 pb^{-1} of integrated luminosity. CMS recorded 43 pb^{-1} of this data yielding a 92% efficient data taking rate [57]. Some fraction of the instantaneous luminosity was further flagged as bad due to noisy detectors, missing detector components, or mis-calibrations in the CMS detector. This yielded 35.9 pb^{-1} of physics quality data used in this analysis. Figure 3.3 shows the history of instantaneous luminosity over 2010 [57]. The instantaneous luminosity rate ranged over three orders of magnitude.

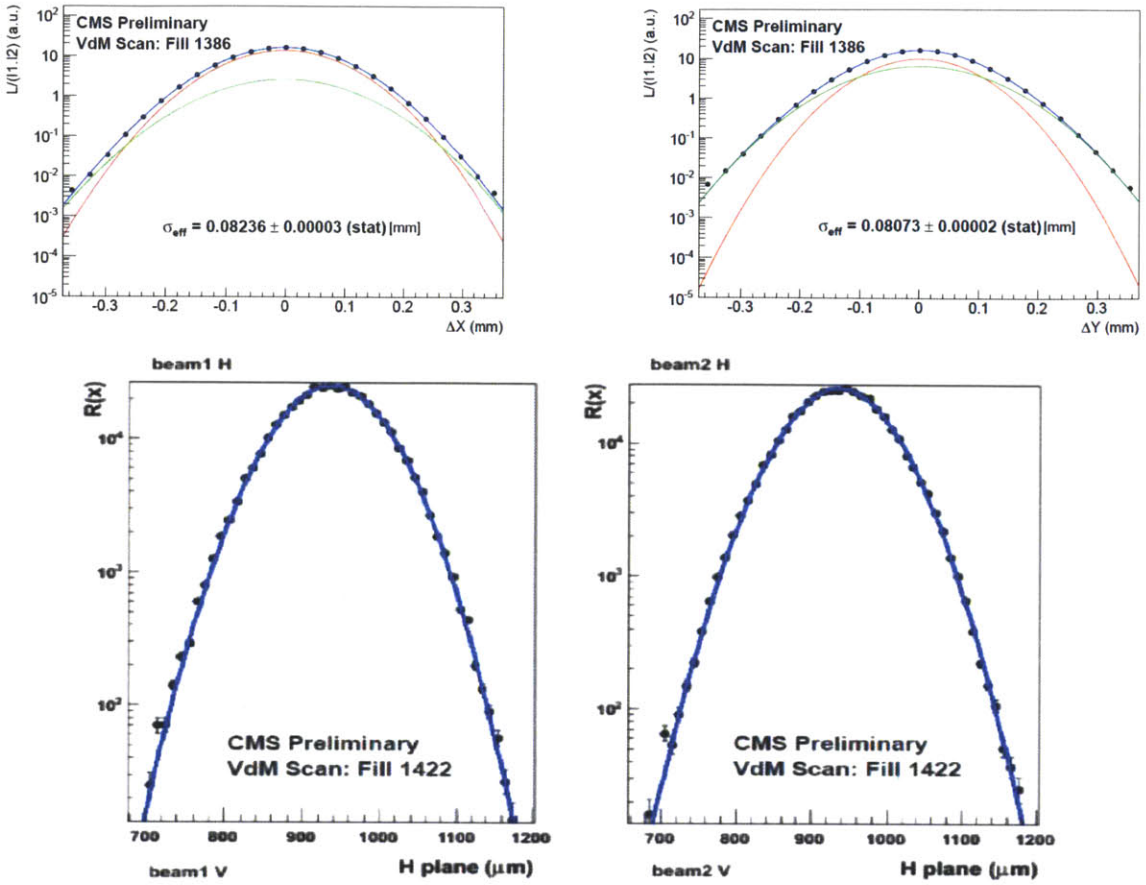

Figure 3-2: Fit to the beam shape to a double Gaussian model using the magnet current position method (top) for the horizontal (top left) and vertical (top right) planes using a double Gaussian model. Projected two dimensional fit of of the rate per vertex position versus the vertex position resolution on the vertex position plane, where the beam 1 position is moved (bottom left) and beam 2 position is moved (bottom right). [59]

3.4 Summary

The instantaneous luminosity in the CMS is determined by reading out the number of hits in the HCAL forward detector (HF). Absolute normalization of the instanteous luminosity is performed by measuring the beam widths of a Van De Meer scan using two different techniques. The final integrated luminosity after a good runs selection is quoted in the cross section measurement to be

$$\mathcal{L} \;=\; 35.9 \pm 1.44 \text{ pb}^{-1} \,. \tag{3.16}$$

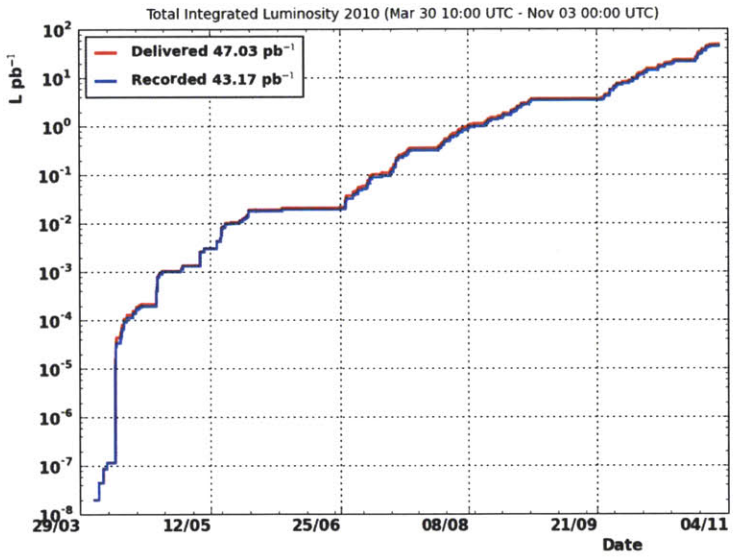

Figure 3-3: History of total integrated luminosity recorded by the CMS detector over 2010 running. [57]

Chapter 4

Event Reconstruction

Event selection, triggering and reconstruction are the cornerstones of any hadron collider analysis. Reconstruction starts with hits in the detector (chapter 2), which get reconstructed into basic physics objects. For the W and Z cross section measurements, we require well isolated muons and missing transverse energy $\not\!\!E_{\mathrm{T}}$. The reconstruction of these two objects will be the focus of this chapter.

4.1 Reconstruction overview

The sub-detectors of CMS each play a different, but critical role in reconstruction the fundamental physics objects. The main objects are:

1. Photon
2. Electron
3. Charged Particle
4. Jet
5. $\not\!\!E_{\mathrm{T}}$
6. Muon

We describe the reconstruction of these objects in the following sections.

4.2 Photons

A photon is reconstructed by selecting an electromagnetic deposit and requiring the deposit to be absent of a nearby track. If a track were matched to the deposit, this would indicate with high likelihood an electron. This is made more difficult because the large amount of silicon material induces, with high probability, the photon to convert into and electron and positron pair. In this instance, tracks exist nearby ECAL deposits. The inclusion of the these events is performed through a series of techniques after basic photon reconstruction [60].

4.3 Electron

Electron reconstruction is similar to track reconstruction (described below), however, in this case the electrons are seeded by an ECAL deposit with a transverse energy >4 GeV known as a super cluster [61]. From the seed, a search for a matching pair of hits in the pixel chambers is performed. If a match is found, additional hits along the probable path of the electrons are incorporated into a track. Because of the high rate of bremstrahlung radiation emanating from an electron, hits are matched to a track given a set of possible energy loss models. The energy loss models are added in weights (a "Gaussian sum filter" algorithm) and fitted with the super cluster energy to determine an electron.

4.4 Track reconstruction

Track reconstruction is performed by combining hits deposited on the silicon tracker in a pattern so that a full track is reconstructed. This is done through five iterative steps. Each iteration is designed to incorporate increasingly less likely hit patterns into reconstructed tracks by utilizing hits not previously assigned to a track. The final two iterations remove the vertex constraint allowing for tracks resulting from long lived particles such as Λ baryons and K_S mesons to be reconstructed.

The seeding of the first iteration is performed by looking for a triplet or pair of hits in the pixel detector. The hit combinations are required to roughly point to the vertex. At high $|\eta|$, where the pixel detector is not present, seeding is modified to incorporate tracker hits. This extends the tracking out to a region of $|\eta| < 2.5$.

Following the seeding, the trajectory from the seed is used to propagate the track to each subsequent layer. An illustration of this procedure is described in figure 4.4. At each layer, the compatible hits are incorporated into the track when the incremental χ^2 is below the threshold. With each new included hit, a Kalman filter is used to modify the track parameters. The modified track is subsequently propagated to the next silicon layer. In the case of multiple hits, multiple tracks are propagated through to the last layers. Ambiguities, between two tracks with shared hits greater than 50%, are resolved after the full track reconstruction [62].

Following propagation through tracker, fully propagated tracks are refit along the whole path yielding the final set of helical parameters. A significant fraction of reconstructed tracks do not correspond to any particle passing through the detector. These tracks are removed by basic requirements on:

- χ^2/NDF of the fitted track,
- transverse distance d_0 (known as impact parameter) to the mean collision point (known as the beamspot),
- Δz to the closest primary vertex,
- significance $d_0/\delta d_0$ of d_0 given a fitted uncertainty δd_0 with respect to the beam spot, and

- significance $\Delta z/\delta z$ of Δz with respect to the closest primary vertex given a fitted uncertainty δd_z.

Table 4.4 lists example quality requirements of track reconstruction. At each step of the iteration of the track reconstruction, the listed parameters are loosened with each step. In order improve track reconstruction efficiency, a propagator taking

Parameter	Requirement
χ^2/NDF	$< 0.9n$
d_0 to the beamspot	$< (0.3n)^4 \sigma_{d_0}(p_T)$
Δz to closest primary vertex	$< (0.35n)^4 \sigma_{Z_0}(p_T, \eta)$
$d_0/\delta d_0$ to the beamspot	$< (0.4n)^4$
$\Delta z/\delta z$ to the beamspot	$< (0.4n)^4$

Table 4.1: Track selection requirements for all tracks with a given p_T, η, and n matched layers. Here $\sigma_{d_0}(p_T)$ and $\sigma_{Z_0}(p_T, \eta)$ are resolution functions, which describe the impact parameter, d_0, and the z positions of the vertex, Z_0, respectively

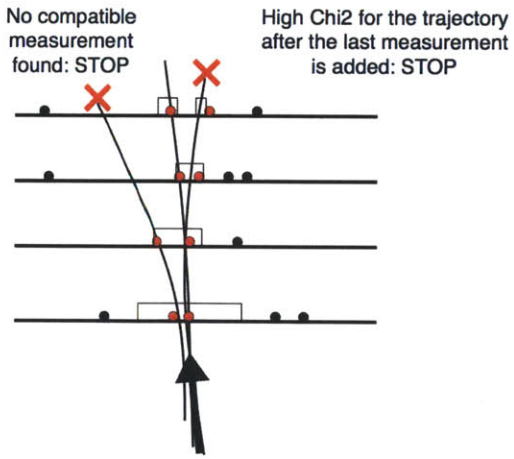

Figure 4-1: Example of the iterative Kalman filter procedure on track reconstruction [63]

into account a parametrized material distribution of the CMS detector is used to predict the energy loss. The energy loss of propagating particles is predicted on the assumption that each track corresponds to a π meson. In the tracking fit, this is implemented with the aid of the Runge-Kutta based iterative propagator [64]. The Runge-Kutta propagator incorporates both the detector material model and the variation in the magnetic field at high $|\eta|$. The track reconstruction produces tracks with one percent transverse momentum resolution for $p_T < 100$ GeV/c.

4.4.1 Vertex reconstruction

In addition to the basic track reconstruction, a crucial aspect to CMS tracking is the clustering of tracks at the origin into a set of vertices. Vertex reconstruction is performed through an annealing algorithm whereby each track is assigned to every vertex with a probability determined by the distance to each vertex. This is iterated several times recomputing weights for each vertex with each iteration. Vertices with at least two tracks with a final weight probability above 90% are kept for further analysis. The vertex resolution in CMS is capable of reaching a precision of 20 μm in the transverse plane and 100 μm in the z-plane [65, 66].

4.5 Particle Flow ($\not\!\!E_{\mathrm{T}}$ reconstruction)

Missing transverse energy reconstruction in the CMS detector takes advantage of an all inclusive form of reconstruction known as particle flow reconstruction. Particle flow reconstruction takes into account information from both tracks and calorimeter deposits. The tracks and calorimeter deposits are combined into a single object, incorporating the optimal resolutions for both tracking and calorimetry. In order to comprehensively understand particle flow $\not\!\!E_{\mathrm{T}}$ reconstruction, we first describe the steps to form particle flow objects in the CMS detector.

4.5.1 Particle Flow calorimeter clustering

Particle flow reconstruction is designed to augment the energy measurements determined by the tracks. In order to do this, one must cleanly ascribe tracks to calorimeter deposits. For this to happen, particle flow relies on a custom technique for the clustering of calorimeter deposits. The clustering proceeds by

1. Treating all deposits above a specified threshold as a seed

2. Allowing seeds to grow by adding adjacent clusters above a lowered threshold

3. Clusters which merged are separated

The last step, separating two merged clusters is determined by applying a weight factor to the energy of a specific cluster to each of the merged clusters and separating the total energy in the deposit by the relative fraction of the weight factors. The weight factor is given by $E\exp\left(-d_{\mathrm{iJ}}^2/2R^2\right)$ where E is the energy, R is a pre-determined distance, which depends on the detector, and d_{iJ} is the distance from the center of the specified cluster to the deposit. The center is determined iteratively by first taking the seed cluster, then computing the energy-weighted geometrical center, and finally iterating so as to define a clear distribution for each particle flow cluster.

4.5.2 Particle Flow linking

Following the clustering, the tracks and the clusters are linked together into one object. This step is the most critical step of particle flow reconstruction because it removes double counting of deposits which creates an artificial energy imbalance.

The linking is performed by propagating tracks through the CMS detector, starting from the last hit in the tracker, through the ECAL Pre-Shower, the ECAL and then to the HCAL. In the ECAL this propagation is performed until the track position reaches the average longitudinal position of a expected electron shower. In the HCAL, this is propagated to a position of one nuclear interaction length λ_I in the shower. In the instance where the propagated track goes through an existing calorimeter cluster in η and ϕ, the components are linked together. When the propagation goes through a crack or gap in the calorimeter window, the cluster size is enlarged up to twice its existing size.

4.5.3 Particle Flow identification

The identification of each particle starts with the most evident objects and progressively goes down to the more ambiguous objects. Following the identification of each particle the deposits associated with that particle are removed, thereby simplifying further identification of other particles. The particle identification order is:

1. Muons
2. Electrons
3. Charged Particles
4. Neutral Particles

Muon identification follows directly by classifying particles which match the global muon reconstruction (section 4.6). The electron identification is determined from a modified electron reconstruction where seeding requirements are loosened to incorporate tracks with bremstrahlung-like deposits in the ECAL. After electron reconstruction, the remaining deposits with a track link are classified as charged hadronic deposits and in some occasions refit to incorporate both calorimeter and track deposits. For rare instances where there is a small calorimeter deposit compared to that of the track p_T, the track is classified as a muon. (provided the p_T fit uncertainty is $< 25\%$). In the instance where the associated track p_T to calorimeter energy deposit E satisfies $p_T < E - \sigma($ where σ is the calorimeter energy resolution), the candidate is classified as either a neutral particle or photon depending on whether the deposit is in the HCAL or ECAL respectively.

Figure 4-2 shows a jet with $p_T = 65$ GeV/c. In this jet are 4 particles [67], two charged pions, one K_L^0 meson, and one π^0 meson. This results in two tracks, 3 ECAL deposits and two HCAL deposits. From the linking algorithm, the two charged tracks are linked to both HCAL deposits and one track is linked to an ECAL deposit. The iterative procedure of identifying follows as

1. K_L^0 meson produces one ECAL deposit with no overlap $\rightarrow$ classify this as a particle

2. ECAL cluster from π^0 meson not linked to a track $\rightarrow$ classify this as a particle

3. Both HCAL deposits linked to both tracks $\rightarrow$ remove link to farthest track

4. One ECAL deposit linked to charged track $\rightarrow$ classify track plus ECAL plus HCAL as one particle

5. Classify remaining track plus HCAL as a particle

From this iterative example, we are able to decompose jets and other complicated objects into all of the individual particles. This method is capable of consistently classifying more than 95 percent of the total energy deposits in the event[67]. The classified particles will be referred to as particle flow candidates.

4.5.4 Particle Flow energy calibration

Energy scale calibration of the ECAL and HCAL particle flow deposits is performed in data. For the ECAL, each crystal is inter-calibrated by requiring two photons from a π^0 meson decay to have a combined mass consistent with that of the π^0 [47]. For the HCAL, the calibration of the particle flow clusters is determined by selecting objects with a set of well reconstructed tracks associated to it. The sum of the track p_T is then compared to the sum of the calorimeter E_T and tuned to correspond to a one to one p_T to E_T ratio (figure 4-3) [67].

4.5.5 Particle Flow $\not\!\!E_T$

Following the reconstruction of the particle flow candidates, jet and $\not\!\!E_T$ reconstruction is performed on the particle flow candidates. In the case of the $\not\!\!E_T$ this is performed by taking the negative vector sum of all of the particle flow candidates,

$$\vec{\not\!\!E}_T = -\sum_{\text{candidates}} \vec{p_T} \, . \tag{4.1}$$

This has the advantage of excluding calorimeter spikes or additional noise, which may be read in with one detector, but does not cluster to create a particle. Figure 4-4 shows a comparison of the particle flow $\not\!\!E_T$ resolution with the $\not\!\!E_T$ resolution defined by two more traditional methods, summing calorimeter deposits (calo $\not\!\!E_T$) and summing calorimeter deposits corrected with track deposits (tc $\not\!\!E_T$). Comparing with these two methods, we observe first that correction by track deposits reduces the resolution by a factor of two and going to particle flow $\not\!\!E_T$ reduces the $\not\!\!E_T$ resolution further by 20 percent.

4.5.6 Particle Flow jet reconstruction

Jet reconstruction takes advantage of particle flow candidates, by clustering candidates in place of typical calorimeter deposits. Jet reconstruction is performed with the anti-k_{T} algorithm which clusters Jets within a distance d_{ij} of the hardest particle, where d_{ij} is defined as [69]

$$d_{\mathrm{ij}} = min(1/k_{\mathrm{Ti}}, 1/k_{\mathrm{Tj}}) \frac{\sqrt{\Delta\phi^2 + \Delta\eta^2}}{R} \ , \tag{4.2}$$

and $R = 0.4$ is the cone size for which all deposits with $\sqrt{\Delta\eta^2 + \Delta\phi^2}$ less than R are clustered to form the jet. This reconstruction retains infrared and collinear safety and in the instance of hard jets is nearly equivalent to more traditional jet reconstruction performed by counting all energy deposits within a specified cone [69].

4.6 Muon reconstruction

The muon reconstruction is essentially track reconstruction with a matching to the muon chambers. This is made difficult by the rather complicated material and B-field variation between the muon chambers and the tracker. To seed the reconstruction of a muon, deposits in either the tracker or the muon chambers are utilized. Seeding in the separate detectors defines two types of muons, those seeded by deposits in the tracker and propagated outwards (tracker muons) and those seeded by deposits in the muon chambers and propagated inwards (global muons).

4.6.1 Muon propagators

In CMS, there are three methods of trajectory propagation. The three propagators use different material models of the CMS detector. For each step of the propagation, the material induces an energy loss given by equation 2.13 (Bethe-Bloch). This is used to adjust the curvature κ in the B field by iteratively recalculating κ through the two steps below:

$$-\frac{dE}{dx} = f(E) \ , \tag{4.3}$$

$$\kappa = F(B/p_{\mathrm{T}}) \ . \tag{4.4}$$

This is performed with a Runge-Kutta iterative method, which allows for modification of the expected trajectory parameters. For tracks inside the tracker volume the material is introduced at each layer, with stepwise propagation occurring from layer to layer. Outside of the tracker volume a special propagator known as the stepping-helix propagator is used, this propagator incorporates an energy loss model given by either energy loss in the iron of the magnetic yoke, or a value which approximates the energy loss in the support material between the iron (5.3% that of iron) [70]. The

energy loss function in the iron is given for momentum p by

$$\frac{dE}{dx} = -\left(11.4 + 0.96|\log(2.8p)| + 0.033p\left(1 - p^{-1/3}\right)\right) \text{MeV/cm}. \quad (4.5)$$

The permissible fluctuations in the energy loss model for which a hit may still be incorporated into a track are determined from MC simulation in iron. The value used is $(\Delta E)^2 / x\,(1 + p \cdot 10^{-3})$ where ΔE is the predicted energy loss, x the propagated distance from the last incorporated hit and p the momentum. Multiple scattering effects are accounted for in a similar manner to the energy loss using the standard scattering formula [34] given by

$$\theta_0 = \frac{13.6MeV}{p}\sqrt{x/X_0}\,(1 + 0.38\log(x/X_0)) \ . \quad (4.6)$$

4.6.2 Reconstruction in the muon chambers

Muon reconstruction is seeded from either a level one trigger firing (discussed in section 4.7) or hit pattern in the muon chambers. The hit pattern in the muon chambers starts first with segment reconstruction in the local muon chambers (chapter 2.4.7). The seeding is performed by clustering one or more segments together based on geometrical criteria. The initial p_T of the reconstructed segment is taken to be

$$p_T = A - \frac{B}{\Delta\phi} \ , \quad (4.7)$$

where A and B are constants depending on the position of the segment. The angle $\Delta\phi$ is defined as either the closest hit on the segment with respect to the collision vertex position or in the endcap as the difference in angles of two segments in two of the three closest chambers.

Following the seeding, the track is propagated through the muon chambers using the stepping-helix propagator. Hits, which when included into the track give an additional χ^2 below a specified value, are incorporated into the track and the track parameters are updated through a Kalman filter. The final track fit is performed using the hits within the muon chambers where a tighter χ^2 cut is imposed. All tracks with at least two measurements, for which one must be a segment in the DT or CSCs, yields a reconstructed muon in the muon chambers, known as a Stand-Alone Muon.

4.6.3 Global muon reconstruction

A global or tracker muon involves the combination of both a track in the tracker and a Stand-Alone muon in the muon chambers.

Global Muon reconstruction starts with a Stand-Alone muon and then determines a set of tracks for which a possible track muon link may exist. To obtain the set of possible tracks, all tracks in the tracker that are compatible in a rectangular region

in $\eta - \phi$ space and which pass a criteria selection of seven different parameters given by:

- Distance of closest approach to the collision point
- Δz of the muon and the track near the region of origin
- ΔR (in η and ϕ) of the track to the muon near the region of origin
- Direction of the two tracks at the origin
- $\Delta\phi$ of the track and the muon as determined given the uncertainty of ϕ in the Stand-Alone muon fit.
- $\Delta\eta$ of the track and the muon as determined given the uncertainty of η in the Stand-Alone muon fit.
- minimum allowable p_{T} of tracks

The matching of track to Stand-Alone muon is performed by first propagating the selected tracks to the front surface of the muon chambers and then matching by iteratively comparing several quantities:

- χ^2 of the two tracks as defined by:

$$\chi^2 = (\vec{p_1} - \vec{p_2})^T (C_1 + C_2) (\vec{p_1} - \vec{p_2}) \ , \tag{4.8}$$

  where $\vec{p_{\mathrm{i}}}$ is the momentum of the track or muon and C_{i} is its respective covariance matrix.

- Track position along the surface of the muon $\vec{d} = (x, y)$ with respect to the track

$$d = \sqrt{(x_1 - x_2)^2 + (y_1 - y_2)^2} \ . \tag{4.9}$$

  Distance requirements range from $2 - 15$ cm depending on the quality of the muon.

- Local position $\chi^2 < 20$ where

$$\chi^2 = (\vec{d_1} - \vec{d_2})^T (C_{\mathrm{d1}} + C_{\mathrm{d2}}) (\vec{d_1} - \vec{d_2}) \ . \tag{4.10}$$

- Angular matching $\Delta R < 0.1 - 1.0$ of the *position* vectors between the track and muon

$$\Delta R = \sqrt{\Delta\eta^2 + \Delta\phi^2} \ . \tag{4.11}$$

- Angular matching ΔR of the *momentum* vectors between the track and the muon, when propagated back to the closest approach of the primary vertex.

Tracks sufficiently well matched are promoted to the final step of the global muon reconstruction, the global muon fit.

The global muon fit is performed by refitting all of the hits along the path of the linked track muon system. This fit, like the other track fits, is performed through an iterative propagation and Kalman filter of the associated hits. Hits which increase the χ^2 of the track, are removed from the track. In the instance where multiple tracks are matched to the muon, all track plus muon combinations are fit and the combination with the lowest χ^2 is chosen.

4.6.4 Tracker muon reconstruction

In tracker muon reconstruction, the seeding starts in the tracker by selecting all tracks with a momentum $p > 2.5$ GeV. The seed tracks are propagated into the muon chambers. All tracks with a hit in the muon chambers associated to the track are considered tracker muons. The association is defined as a hit (or segment) within 3 cm or 4σ of the projected track surface, where σ incorporates both the segment and energy loss uncertainty. In the instance where multiple tracks are compatible with a hit in the muon chambers (as is the case in jets), the closest track in Δx of the local coordinates is chosen. This requirement is relatively loose and leads to high reconstruction efficiency of muons at the expense of a high fake muon reconstruction rate. The fake muon reconstruction rate is compensated by identification cuts after muon reconstruction.

4.7 Muon level one trigger

The level one trigger performs the same action as Stand-Alone muon reconstruction; however, due to the fact that the level one trigger must be able to reconstruct and identify muons within a period of 200 bunch crossings (4μs), the reconstruction is performed in an extremely optimized way. In order to perform such a fast reconstruction, custom application specific integrated circuits (ASICs) and field programmable gate arrays (FPGAs) are utilized extensively to enable the decision making.

Figure 4-5 shows the reconstruction chain of the level one trigger. Reconstruction starts with local segment reconstruction performed independently in each station of the three different muon sub-detectors (DT, RPC, and CSC). Segment reconstruction is followed by track finding where segments in a specific sub detector from each station are combined to produce a track. The best tracks are promoted to the global muon trigger, which combines and sorts the tracks yielding the four best muon candidates.

Figure 4-6 shows the measured cross sections of muons in the level one and high level trigger. Current 2011 running corresponds to 3000 nb^{-1}/h of integrated luminosity per hour. This is approximately 1 nb^{-1}/s, which from figure 4-6 translates to a trigger rate of 5000Hz for muons with momentum > 10 GeV/c.

DT Level one reconstruction

Local reconstruction is performed by dividing a DT muon station into three parts, the two $r-\phi$ oriented layers of detectors and the one $r-\theta$ oriented detector layer (figure 2-18). In each of the thee parts a set of three or more hits in four of the individual DT layers is required. In $r-\phi$, this forms a segment which is paired with a segment from the other $r-\phi$ part of the DT layer through a look up table. This segment in $r-\theta$ is then combined with the $r-\phi$ segment producing a segment in the whole muon chamber. Segments which point closest to the vertex are promoted to the track finding step.

A schematic of the DT track finder is shown in figure 4-7. The DT track finder takes as input all segments within a given 30^0 angle in the $r-\phi$ plane. The segments are then sorted and combined through a look up table, which takes into account the approximate motion of a muon given the magnetic field, p_{T}, and ϕ coordinates of the segment. Segments which loosely match in $\Delta\phi$ are promoted. The two highest p_{T} muons that pass a quality requirement on the segment alignment are promoted to the global muon trigger. The p_{T} determination is performed discretely through a look up table. Selection requirements on the p_{T} are tuned to correspond with 90% efficiency rate above a specified p_{T} threshold (*ie* 90 percent of all muons with true $p_{\mathrm{T}} > 10$ GeV/$c$have L1 trigger $p_{\mathrm{T}} > 10$ GeV/c).

CSC level one reconstruction

The local reconstruction in a CSC is similar to that of the DT chamber. In the CSC, the timing of the muons is driven by the anode wires. The cathode strips are used, *in situ*, to constrain the ϕ coordinate. As with the DT level one trigger, hits are compared to templated hit patterns and the two best segments are promoted to the CSC track finder. The CSC track finder combines all segments within a division of six 60° wedges on either end of the interaction point. The segments in each individual wedge are combined through the help of look up tables. Candidates which pass requirements specified through the look up tables are promoted to tracks. The two best tracks in each 60° wedge are passed to the global muon trigger.

RPC level one reconstruction

A schematic of the RPC trigger is found in figure 4-8. In the RPCs, there are either one or two detector layers per DT or CSC station. Hits from these detectors are passed to an RPC track finder, which combines the hits in a designated hourglass shaped region (gray region in figure 4-8), one hit per layer. The resulting hit configurations with at least 3 hits are then matched to one of the $\approx$80 possible hit patterns by the Pattern Comparator Trigger (PACT), yielding an RPC muon. Following reconstruction, muons reconstructed twice in overlapping hourglass regions are removed (known as ghost busting), the best 4 muon candidates are delivered to the global muon trigger.

Global muon trigger

The global muon trigger matches the different muon candidates by performing a matching in η and ϕ. Where two systems cover the detector, muon candidates which are reconstructed in two of the three systems are considered good candidates and promoted to the final level one trigger. Before promotion, the global muon trigger removes muons multiply reconstructed in the transition region between the DT and CSCs. In some instances, lower quality muons reconstructed poorly may be selected; however in this analysis these trigger objects are not selected. Finally, a calorimeter bit corresponding to a minimum ionizing equivalence is matched to the level one muon.

4.8 Muon high level trigger

The muon high level trigger is separated into two separate components: level two (L2) muon reconstruction and level three (L3) muon reconstruction. Level two muon reconstruction is performed with only the muon chambers. Level three muon reconstruction combines track and muon information. The seeding for both these components comes from the results of the level one muon trigger, thereby avoiding any instance of trigger volunteer originating from either the muon or the other components in the event.

4.8.1 Level two muons

The level two reconstruction is seeded by level one trigger candidates. Candidates identified as halo muons originating from beam interactions outside of the interaction point are removed from the seeding. The remaining candidates are then propagated to the innermost surface of the muon chambers.

Level two reconstruction starts by performing offline segment reconstruction on all hits in the muon chambers. Reconstruction of level two muons is then performed by propagating the seeded candidates through the muon chambers incorporating any segments with an incremental $\chi^2 < 1000$ on the modified track parameters. Segments with an incremental $\chi^2 < 25$ on the modified track parameters are deemed compatible and incorporated into the fit using the same Kalman filtering and propagation used in offline Stand-Alone muon reconstruction. A muon with at least one compatible DT or CSC segment and an additional hit or segment is declared a successful candidate. Successful candidates are refit from outwards to inward replacing the segments with the muon hits. All hits with an incremental $\chi^2 < 25$ on the muon track are used in final fit to determined the track parameters.

Concurrently with the level 2 muon reconstruction, calorimeter deposits are clustered forming calorimeter towers. In the ECAL, unpacking and clustering is performed for a region of $(0.3, 0.3)$ in $(\Delta\eta, \Delta\phi)$ about the level one muon seed, while in the HCAL the full deposits are unpacked and clustered. Deposits within a cone $\Delta R = \sqrt{\Delta\eta^2 + \Delta\phi^2} < 0.24$ with respect to the level two muon are summed together. This defines a variable known as isolation, which is used to reject muons resulting from decays in jets.

4.8.2 Level three muon seeding

The level three reconstruction follows a similar procedure to global muon reconstruction. In global muon reconstruction, Stand-Alone muons are used to seed a muon in both the muon chambers and ther tracker. In level three reconstruction, muons are seeded by level two muons and combined with a track in the silicon tracker. In order to perform the seeding three different techniques are used:

- Outside-in state based seeding
- Outside-in hit based seeding
- Inside-out hit based seeding

The three techniques are applied sequentially following the order above. In the instance where a candidate passes the selection, the next stage of the seeding is not performed. This method of seeding and reconstructing is known as the Cascade Algorithm [71].

The first seeding technique, the outside in state based seeding, relies on the direction and p_{T} of the level two muon propagated to the outer surface of the tracker (defined to be the first module with an incremental $\chi^2 < 20$ when added with the level two track). The projected momentum and direction ("state") at the surface of the tracker are used as a seed to look for compatible track hits.

The second seeding technique, the outside in hit based seeding, is performed by modifying the level two muon track with hits in the tracker that are compatible with the propagated muons. Hits are deemed compatible when the incrementalχ^2 of the track with respect to the hit is within 15. Once a compatible hit is found on a layer, the algorithm stops searching for hits beyond that layer.

The third seeding technique is performed by matching muons to pixel triplets and pixel pair plus primary vertex tracklets. Reconstruction of these tracklets, unlike track reconstruction, can be performed within the time constraint of the high level trigger. The matching with the tracklets is determined by requirements on

- Δz: difference of the z coordinate at the distance of closet approach to the primary vetex of the the two tracks
- ΔR: difference in the minimum distance to the primary vertex
- Track direction
- $\Delta\phi$: difference in ϕ at the distrance of closet approach to the primary vetex of the two tracks
- $\Delta\eta$: difference in η at the distrance of closet approach to the primary vetex of the two tracks

Candidates that pass the selection requirement are then filtered to remove duplicate matches and passed on to full level three muon reconstruction.

During the 2010 running, different seeding algorithms on level three muons were employed. The algorithm shown here (cascade seeding) was only used for the last 33 pb^{-1} of data. Before that a different seeding configuration four percent less efficient was used.

4.8.3 Level three muon reconstruction

Level three muon reconstruction is essentially track reconstruction with a specified seed. This track reconstruction is performed in the high level trigger environment, thus access to all of the silicon hits is not readily available and a dynamic unpacking of hits is performed. A selected good level three muon must have five hits where an incremental χ^2 on the modified track parameters including the hit is < 30 and a good level three muon must be matched to a level two muon.

Isolation on level three muons is calculated by taking the calorimeter based isolation from level two muons and combining it with a the sum of the p_{T} of pixel based tracks where for each track compared to the muon:

- the vertex $\delta r < 0.1$ cm,
- the vertex $\Delta z < 0.2$ cm,
- distance $0.01 < \sqrt{\Delta\eta^2 + \Delta\phi^2} < 0.24$,
- track $p_{\text{T}} > 2$ GeV/c, and
- distance with respect to the vertex is $\delta r < 250$ μm.

4.9 Muon p_{T} resolution

The reconstruction in either the muon chambers or the tracker lead to different resolution in both the track parameters and the vertexing. From equation 2.12, the uncertainty on the transverse momentum is determined from measuring the resolution of the sagitta s. Additionally, the resolution is degraded by the amount of medium for which the muon has scattered through and improved by both the resolution and number of hits in the reconstruction.

At extremely high p_{T}, muon tracks in the tracker are essentially straight, making a measurement of the muon p_{T} particularly difficult. The measurement of these muons is thus optimal if one relies on the larger distance (lever arm) provided by the muon chambers to measure the momentum. For muons with a $p_{\text{T}} < 200$ GeV/c, the momentum resolution is dominated by the measurements in the tracker, where multiple scattering outside of the tracking volume is large enough ($x/X^0 \approx 40$) such that the additional smearing imposed on the muon outside of the volume is larger than the resolution of the measured p_{T}.

Figure 4-9 shows the reconstructed resolution for muons as a function of the type of muon and p_{T} of the muon. The transition region where tracker plus muon combined fit improves resolution is visible in the plots at 200 GeV/c. In this analysis,

we choose to exclusively use track p_{T} for which we expect less that 1% of events above $p_{\mathrm{T}} > 200$ GeV/c. Modifying the p_{T} choice to incorporate the track plus muon chamber fits leads to inconsistencies further on in the analysis.

4.10 Summary

In this section, the reconstruction of muon objects and the $\not\!\!E_{\mathrm{T}}$ has been presented. These two objects are used to select both W and Z boson events. The muon will be used to trigger events and select out isolated well identified muons coming from W and Z boson events. The $\not\!\!E_{\mathrm{T}}$ will be used in the final separation of W boson events from other backgrounds.

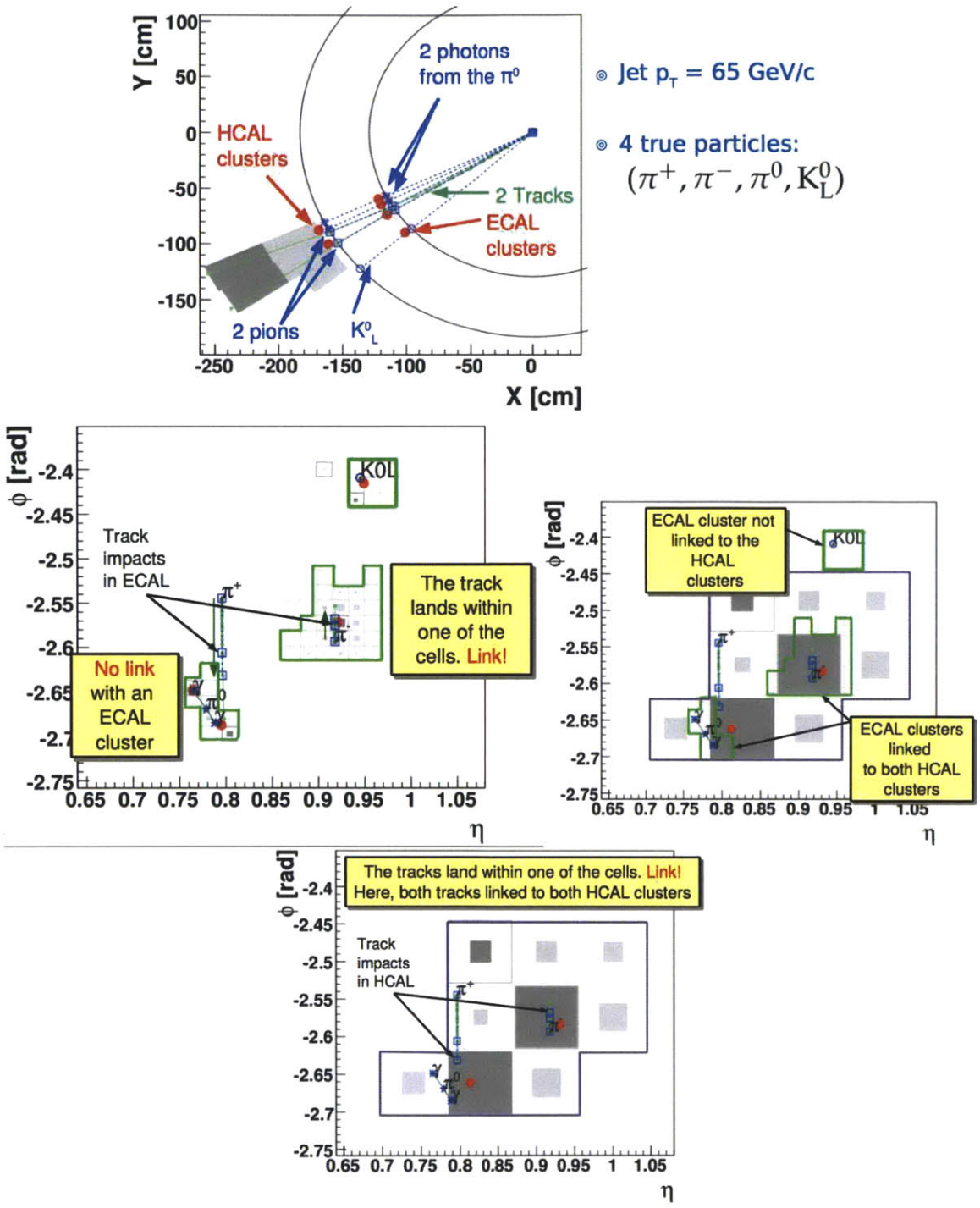

Figure 4-2: Example of a jet with $p_{\mathrm{T}} = 65\mathrm{GeV}/c$. The top diagram is an overview of the event in the r-ϕ plane. The concentric rings denote the ECAL (inner) and the HCAL (outer). The gray components denote the ECAL (light gray) and the HCAL (dark gray) deposits. The colored lines denote the particle flow clustering, green for ECAL, blue for tracks, purple for HCAL. The second from top plot shows the linking between the HCAL and the ECAL. The bottom left shows the linking between tracks and ECAL. The bottom right plot shows the linking between the tracks and the HCAL.

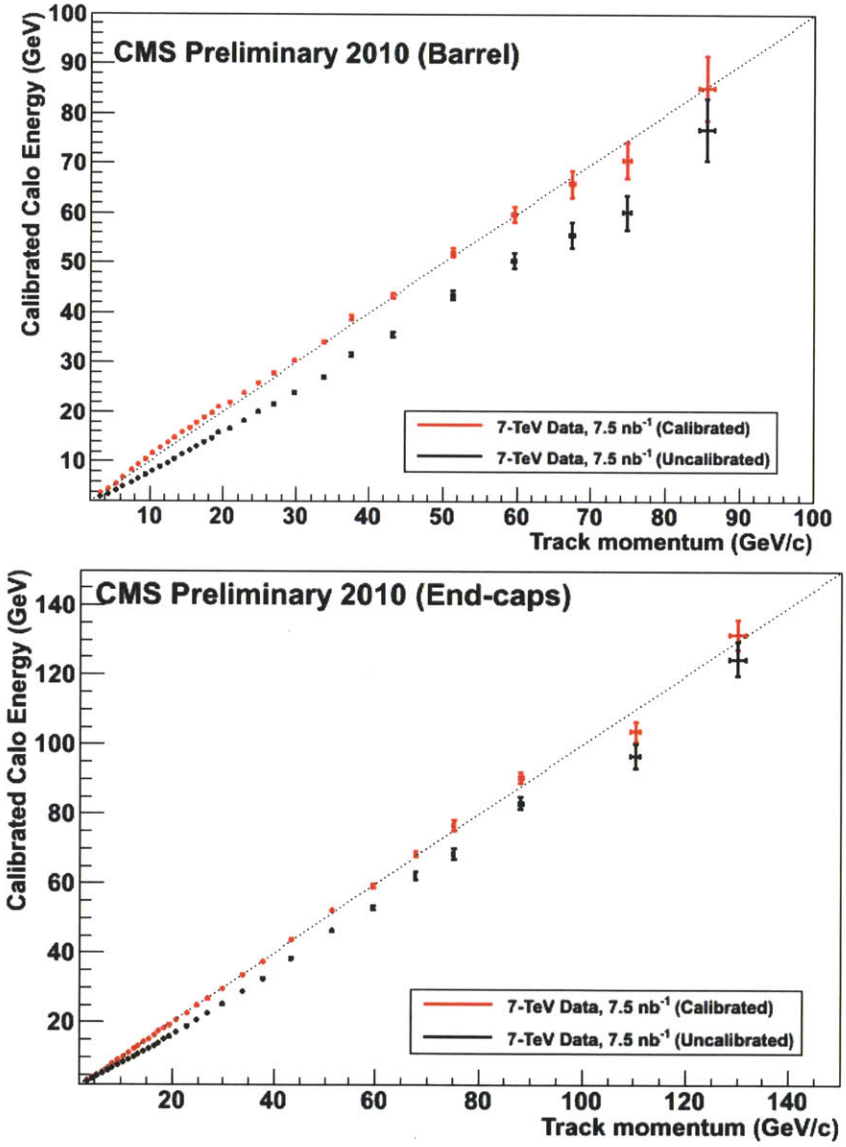

Figure 4-3: Calibration of particle flow reconstructed calorimeter energy for Barrel (top) and Endcaps (bottom). Calibration is performed by matching the momentum of a track with the measured deposits.

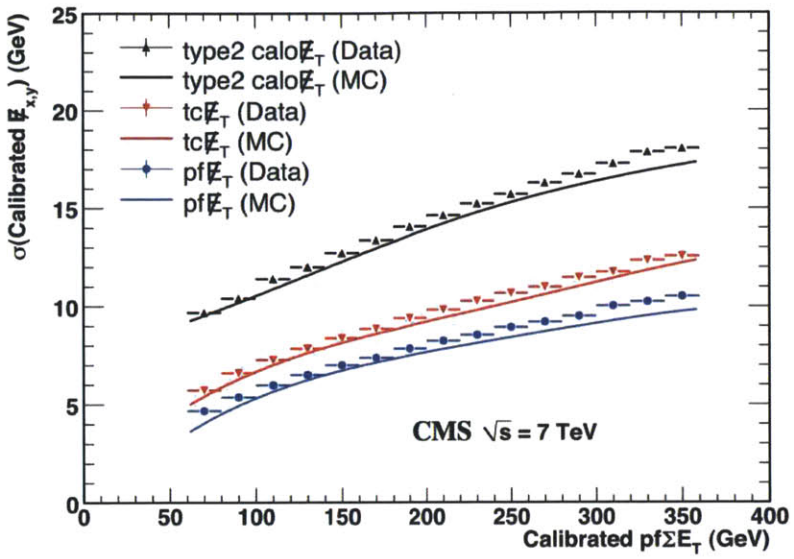

Figure 4-4: Comparison of the resolutions using three different $\not\!\!E_{\mathrm{T}}$ calculations for both simulation (MC) and data as a function of the total energy seen in the event, assessed with the particle flow algorithm. The black components denote Calo $\not\!\!E_{\mathrm{T}}$, which is obtained by the vector sum over calorimeter deposits in equation 4.1. The red line (tc $\not\!\!E_{\mathrm{T}}$) is obtained by correcting calo $\not\!\!E_{\mathrm{T}}$ with track deposits. The blue line is the default particle flow $\not\!\!E_{\mathrm{T}}$ [68]

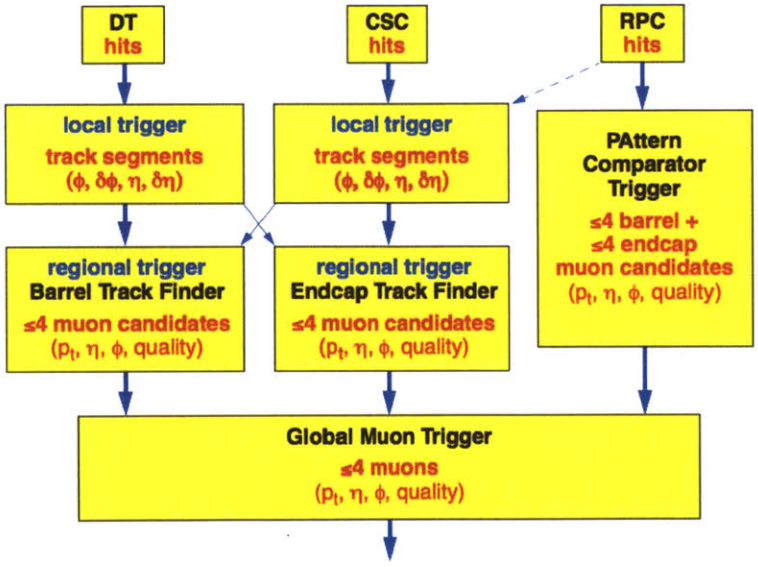

Figure 4-5: Schematic flow for Muon Level One reconstruction. Muon reconstruction is performed in separate chambers and combined when the individual segments arrive to the global muon trigger.

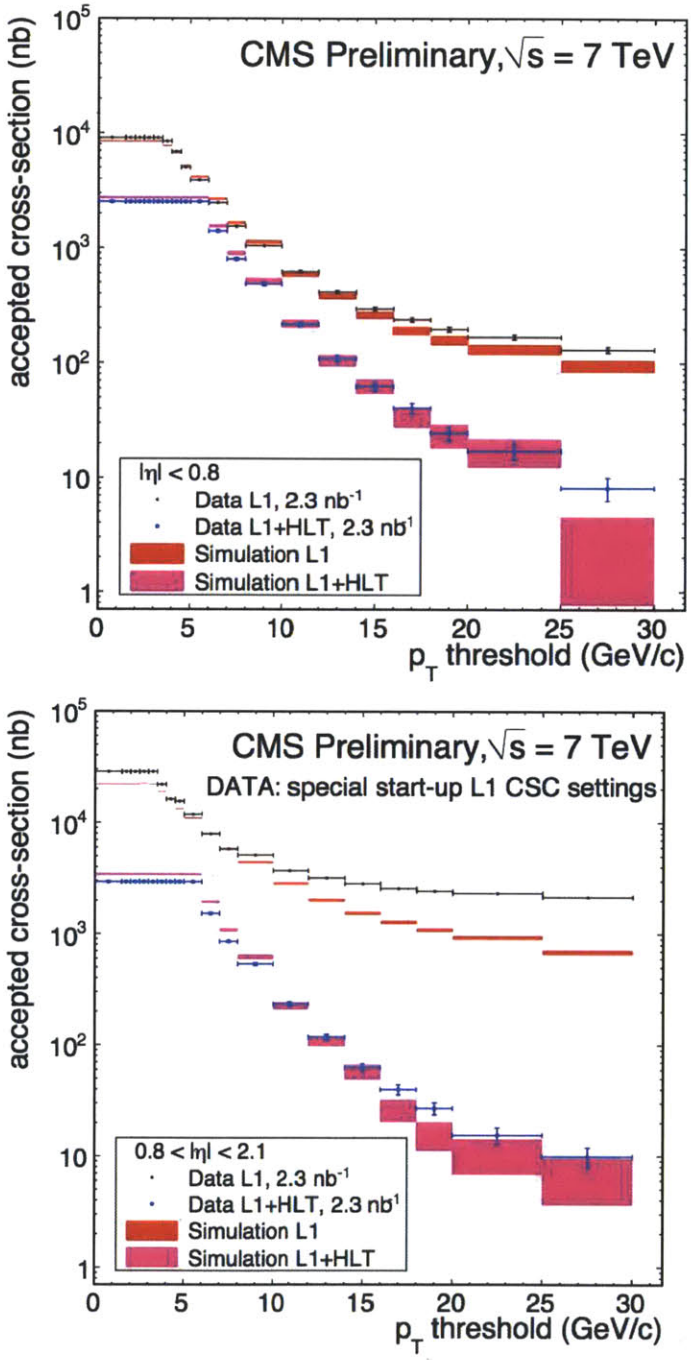

Figure 4-6: Cross sections for the level one and high level triggers for central muons (top) and for endcap muons (bottom). Typical luminosity rates are 1 nb^{-1}/s

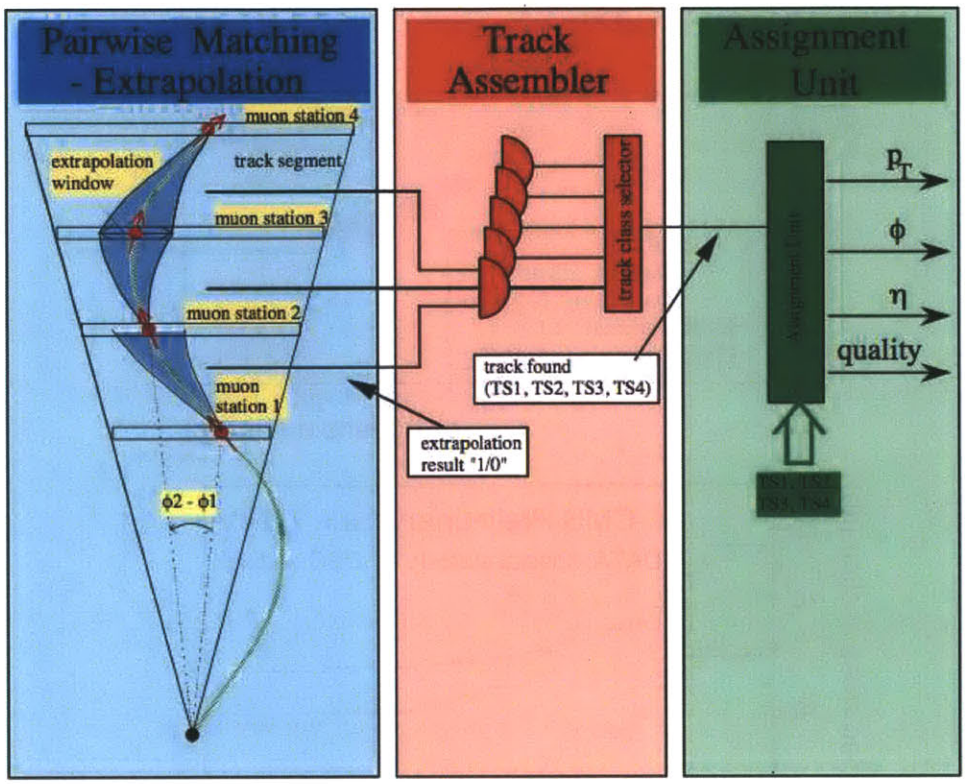

Figure 4-7: Schematic flow for fast muon track reconstruction in the drift tubes using the DT track finder. Hits are individually reconstructed on the left and then connected through a series of look up tables using the angles ϕ_1 and ϕ_2 shown in the diagram. Tracks are then combined in the assembler (center) and assigned track parameters in the assignment unit (right).

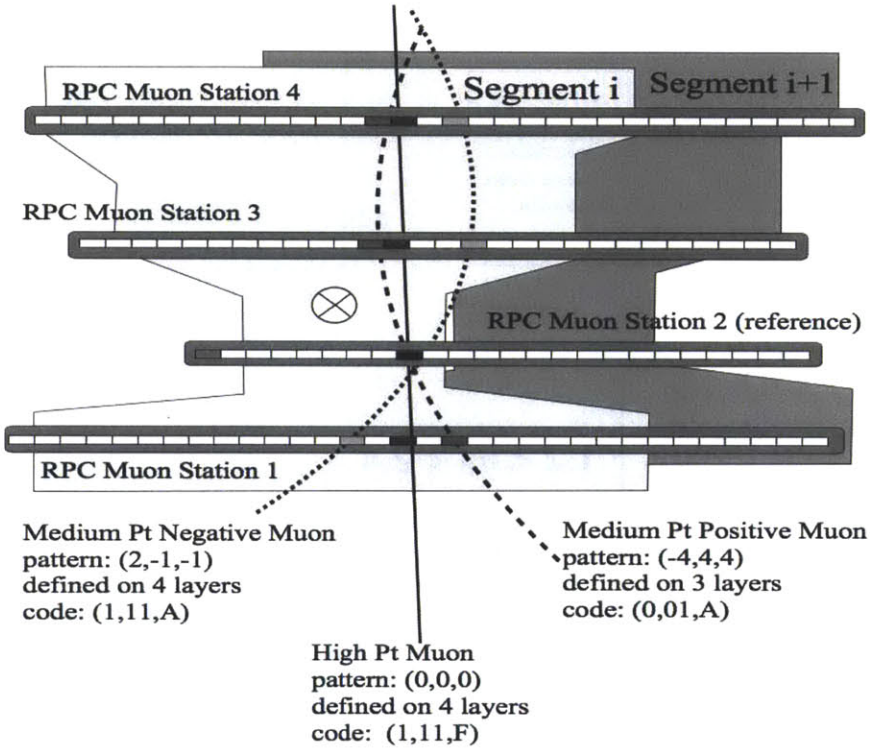

Figure 4-8: Diagram illustrating the reconstruction of level one RPC muons. Muons are seeded by hits in station two and then allowed to follow hit configurations within the the gray hourglass region determined by a look up table.

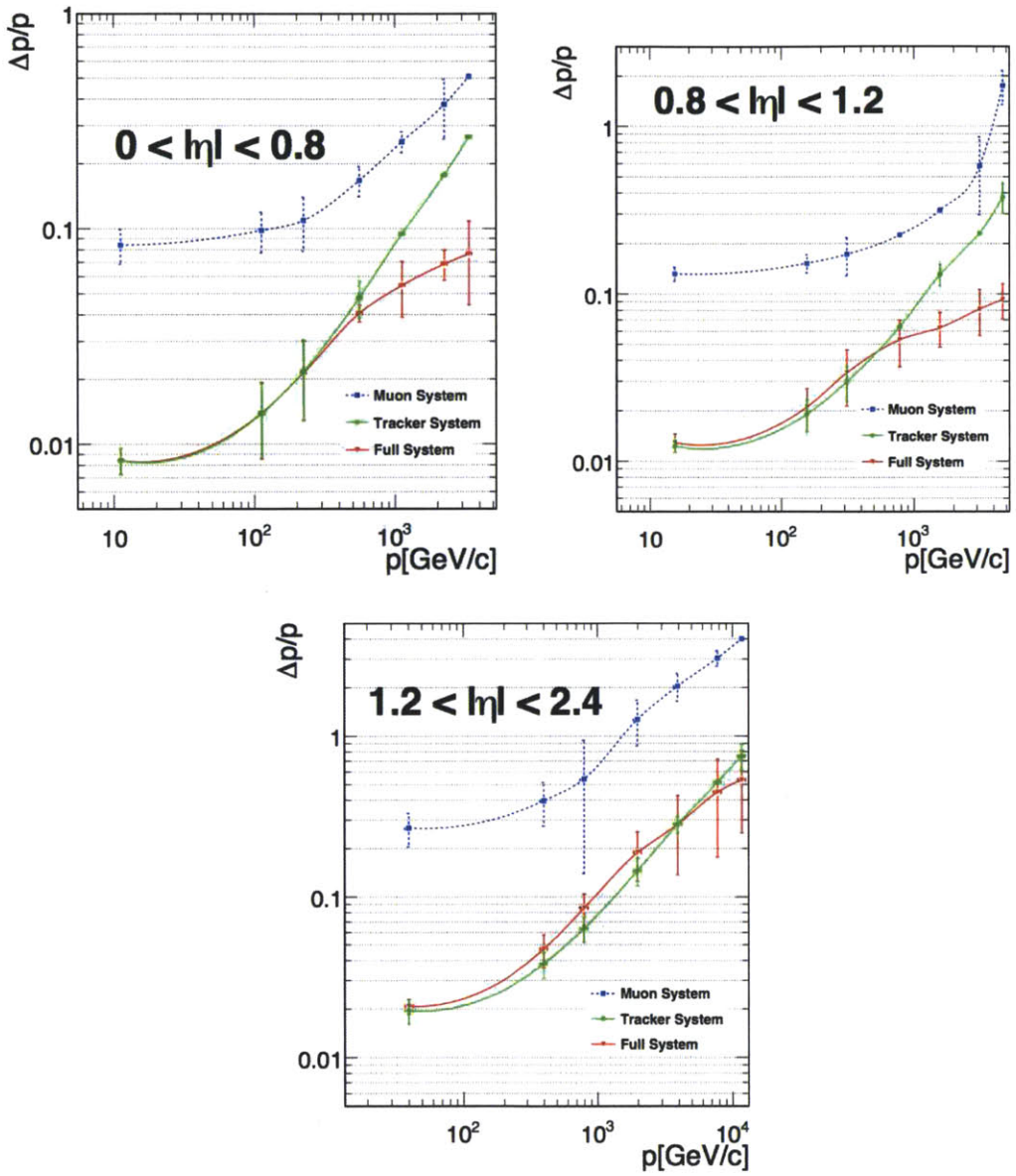

Figure 4-9: Muon p_{T} fractional resolution as a function of momentum p for the barrel region (top left), which is composed of muons exclusively reconstructed the DTs, the transition region (top right), which is composed of muons reconstructed partly in the DTs and CSCs, and endcap region (bottom) composed of muons reconstructed in the CSCs.

Chapter 5

Selection

The separation of W and Z boson events from backgrounds is performed by requirements on the quality of the muons. The selection removes a large faction of background events with minimal loss of W and Z boson events. In this section we present a muon selection optimized for the cross section measurement. The final selection amounts to a remaining signal and background yield such that, after selection, the W boson yield is extracted with minimal uncertainty.

5.1 Muon trigger selection

The muon trigger filters events to a sustainble data recording rate for further event analysis. This is performed by apply p_{T} threshold on the muon trigger objects. Events that fall below this threshold are recorded at a fraction of their total rate (known as prescaling). The maximum sustainable trigger p_{T} thresholds during data taking were 10 GeV/c for the level one trigger and 15 GeV/c for the high level trigger[72]. Each trigger used in these measurements has a well defined name in the CMS trigger nomenclature. The level one trigger used is known as

`L1_SingleMu10`

and the high level trigger is given by

`HLT_Mu15`

The high level trigger leads to a rate of online reconstruction smaller than 7 Hz in 2010 data. This trigger did not exist throughout the course of 2010 running. In place of this trigger was a high level trigger with a nine GeV/c threshold. This trigger was seeded by a seven GeV/c level one trigger. In order to minimize the variation in the yield as a function of the trigger thresholds, an offline selection of $p_{\mathrm{T}} > 15$ GeV/c was imposed on all HLT level three triggered muons. A final p_{T} cut of 25 GeV/c is imposed on the fully recontructed muon p_{T}, thus keeping the influence of p_{T} mis-reconstruction to a minimum.

5.2 Muon event selection

In this analysis, two kinematic cuts are imposed: an η cut on the muon, selecting all events with a muon having $|\eta| < 2.1$, and p_{T} cut on the muon requiring the muon to have a $p_{\mathrm{T}} > 25$ GeV/c.

The choice of the η range is determined by the trigger quality value. For $|\eta| > 2.1$, the CSC triggers have a reduced effieincy (algorithmic redundancy) resulting from the wiring of the CSC chambers. To minimize the effect of this wiring issue a requirement of $|\eta| < 2.1$ is imposed on the muon.

In this analysis, the cut is raised from the 15 GeV/c threshold to require muons with $p_{\mathrm{T}} > 25$ GeV/c so that both systematic uncertainties originating from theoretical acceptance uncertainties and background mis-modeling uncertainties are minimized (discussed further in chapters 8 and 10).

Muons from W boson decays comprise 10 percent of the total amount of muons passing the trigger and kinematic selection. Figure 5-1 shows the predicted compositions of all muons passing the HLT_Mu15 trigger with 20 GeV/c < p_{T} . The majority of muons coming in on the muon trigger originate from heavy quark decays. Other sources include light quark "decays in flight", punch through hadrons, and cosmic ray muons. With the exception of cosmic ray muons all of these events are classified as QCD background. In order to remove contamination of these backgrounds specific W boson identification cuts are required. The choice of the cuts is determined through an optimization metric.

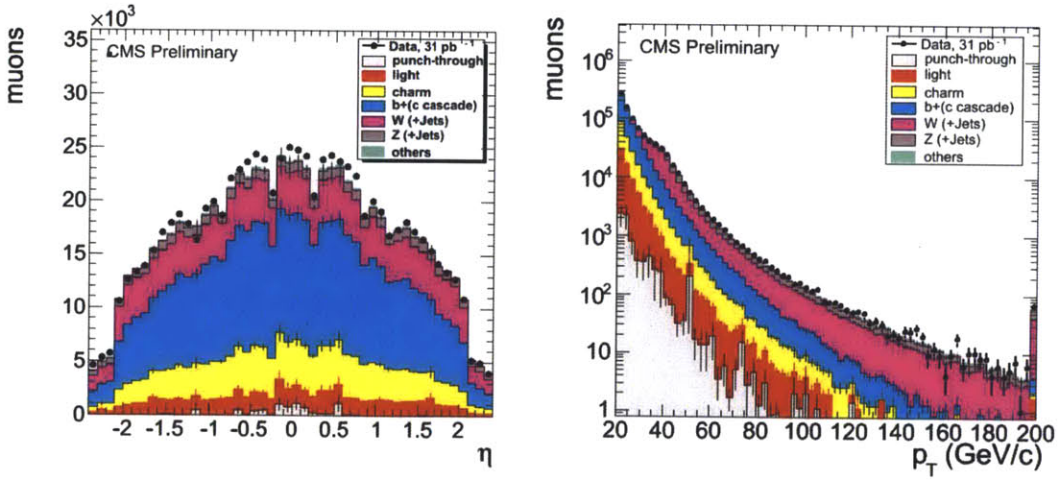

Figure 5-1: Comparison of data with expected composition of all reconstructed muons with $p_{\mathrm{T}} > 20$ GeV/c. The red, yellow, gray, and cyan colors result from muons decaying from QCD processes simulated with Pythia. The QCD processes are tagged by the quark responsible for the decay of the muon. The magenta and gray are from Powheg W/Z boson simulation. The discrepancy in the η distribution (left plot) at central η results from the uncertainty in the QCD production cross section, which is near ten percent.

Selection optimization technique

The core optimization metric, also known as figure of merit, used in this analysis is the significance of the selection defined as

$$\sigma_1 = \frac{S}{\sqrt{S+B}} \tag{5.1}$$

where S is the W boson signal events and B is number of events stemming from background processes. The denominator of the metric is obtained from an $S+B$ sample. This corresponds to the final selected signal sample (signal and background). Thus, for the optimization, the denominator sample is taken from the same single muon dataset used to select W bosons. The numerator samples are intended to consist of good "W-like" muons. Such a sample in data is obtained from muons resulting from Z boson decays to $\mu^+\mu^-$. Selection of Z bosons, outlined below, yields a background contamination less than three percent, thereby providing a clean source of isolated high p_{T} "W-like" muons.

Additional Metrics

In addition to the default metric, we consider optimization with two additional metrics defined to be

$$\sigma_2 = \frac{S}{\sqrt{S+B+\sigma_{\mathrm{b}}^2 B^{1.5}+\sigma_{\mathrm{s}}^2 S^{1.5}}} \tag{5.2}$$

$$\sigma_3 = \frac{S}{\sqrt{S+B+\sigma_{\mathrm{b}}^2 B^{2}+\sigma_{\mathrm{s}}^2 S^{2}}} \tag{5.3}$$

where σ_{b} is defined as the systematic uncertainty on the background measurement and σ_{s} to be the systematic uncertainty on the signal. For this study we take σ_{s} to be one percent and σ_{b} to be 10 percent. These are motivated by the expected final systematic uncertainties in the cross section analysis. Where, with 36 pb^{-1} of data, we expect $\approx 10^5$ W boson events. This implies a statistical uncertainty of $1/\sqrt{N} \approx 0.3\%$. Systematic uncertainties for this measurement are expected to be near 0.5 percent or even higher making a statistical based optimization ($\sqrt{S+B}$) not necessarily optimal.

In order to utilize these metrics, we mus separate S and B in denominator. To obtain S and B separation, we rescale Z boson events, roughly, to the expected W boson yield in data, this gives S. To determine B, we subtract the rescaled S distribution from the $S+B$ sample. These metrics and the original significance metric σ_1, shall be denoted by their name σ_{i} in the ensuing plots.

Z boson selection Well isolated muons similar to W boson decays are obtained by selection of muons from well identified Z boson events. This requires the Z boson event pass:

- the muon trigger (HLT_Mu15),

- isolation of one muon such that for all deposits within a cone $\sqrt{\Delta\eta^2 + \Delta\phi^2} < 0.3$,

$$\frac{\sum_{\text{tracks}} p_{\text{T}} + \sum_{\text{ECAL+HCAL deposits}} E_{\text{T}}}{p_{\text{T}}} < 0.15 \ , \tag{5.4}$$

- impact parameter (distance of closest approach to the vertex), d_0, of one muon $d_0 < 0.2$ cm,
- two muons with $p_{\text{T}} > 20$ GeV/c (muons may be either tracker or global muons), and
- combined mass of the two muons $m_{\ell\ell}$ such that 60 GeV/c^2 $< m_{\ell\ell} <$ 120 GeV/c^2.

In order to make the selection optimal for W bosons, the selected muons from Z boson events are reweighted by the kinematics of the W boson selection using the weight factors shown in figure 5-2. The weighting factor is determined by taking the two dimensional η and p_{T} distribution for simulated muons from W boson decays and dividing it by the simulated Z boson distribution of the non-isolated muon for the selection described above. These muon will further be referred to as the Reweightd $Z \to \mu\mu$ sample.

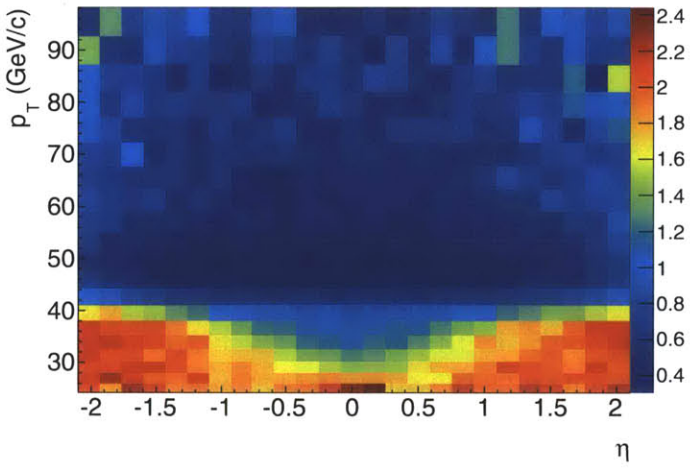

Figure 5-2: Kinematic weight factor in terms of η and p_{T} of an isolated muon for simulated W$\to \mu\nu$ compared to an isolated muon from Z$\to \mu^+\mu^-$ decays. The weight factor is obtained by dividing the two dimensional η, p_{T} distribution of the simulated muon from W boson decays by the non-isolated muon from the Z boson selection on simulated Z boons decays.

Optimization procedure

The optimization of each cut is performed with the most basic significance metric σ_1. To perform the optimization, each cut is separately optimized by applying the

previously determined optimal selection excluding the cut being optimized (so called N-1 selection). The optimization is applied iteratively, starting from no cut selection and continuing until modification of any cut reduces the value of σ_1. For muon reconstruction, where individual parameters are loosely correlated, convergence results within two iterations on each cut optimization.

5.3 Final selection

In the following sections, we present the optimized selection using the metric defined in equation 5.1. Optimization on the other two metrics are shown as a cross check of the optimal selection, these metrics are scaled to correpsond with the same value for the cut varaible at zero. Additionally, in each variable, we present the receiver operating characteristic (ROC) curve [73], which shows the efficiency of the background versus the signal efficiency.

5.3.1 Global Muon

In light of the similarity of the high level trigger with global muon reconstruction, all muons are required to pass global muon reconstruction. Loosening the cut to allow both tracker and global muons increases both the signal and background yield by one percent [70].

5.3.2 Number of pixel hits

A cut on the number of pixel hits removes backgrounds coming from light flavors (decays in flight) and cosmic ray muons. A light flavor decay occurs when a π or K meson decays into a muon. This occurs in the outer layers of the tracker causing a displaced track with no hits in the pixel detector. Cosmic ray muons are removed because the small size of the pixel detector decreases the incidence of cosmic rays impinging on the detector. In the pixel endcaps, the probability of a reconstructed muon from a cosmic ray is reduced even more because of a reduced cross section due to the vertical orientaiton of the endcap detectors.

Figure 5-3 shows the optimization of the number of pixel hits given the defined metrics. The optimum point varies for the three different metrics. In light of increasing signal efficiency, the optimal value of

- > 0 pixel hits

is chosen.

5.3.3 Number of tracker hits

As with the selection on the number of pixel hits, requiring hits in the inner silicon tracker is an excellent way of removing poorly reconstructed muons, typically resulting from decays in flight. A large number of hits further ensure muons are well

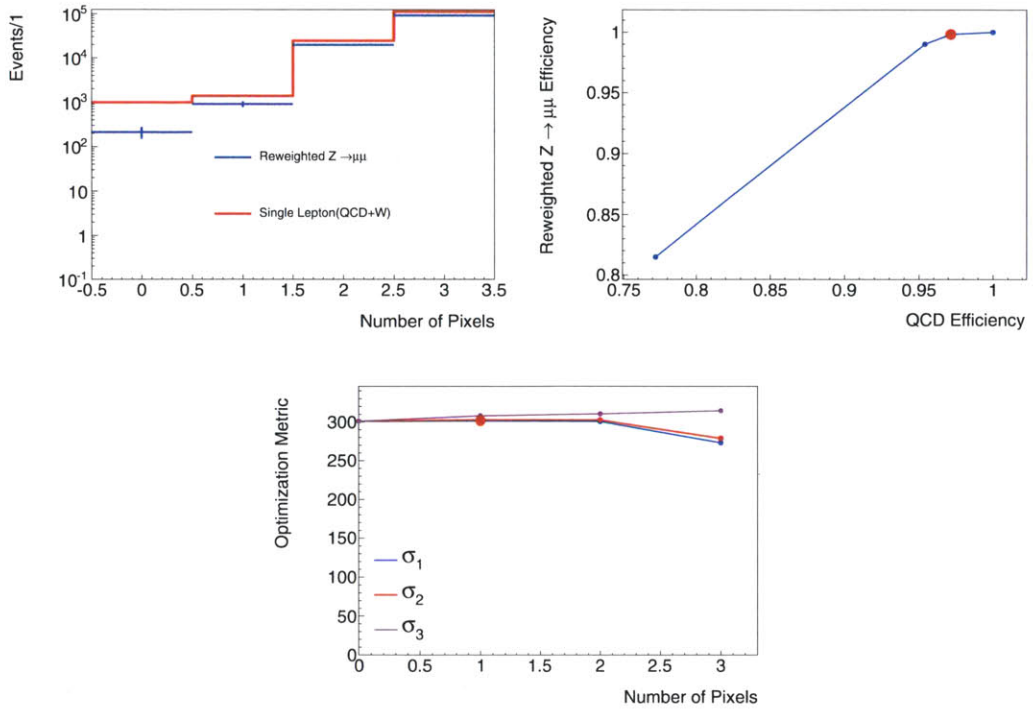

Figure 5-3: Comparison of number of pixel hits for muons from the single muon data set with all optimized cuts applied except for the specified variable. Signal and signal plus background contributions are plotted on the top left, efficiency of the signal is compared with that of the background (top right) and the optimization metric is shown on the bottom. The red dot shown in the middle and right plots indicates the optimal cut choice. Three optimization metrics σ_1, σ_2, and σ_3 are defined in equations 5.1,5.2, and 5.3 respectively.

reconstructed and prompt. Due mainly to the variation in the number of hits over muon η, the final optimum (figure 5-4) is found to be very loose at:

- >10 tracker hits

From figure 5-4, we find approximately 0.1 percent of signal events are recorded with a hit multiplicity below 10 hits.

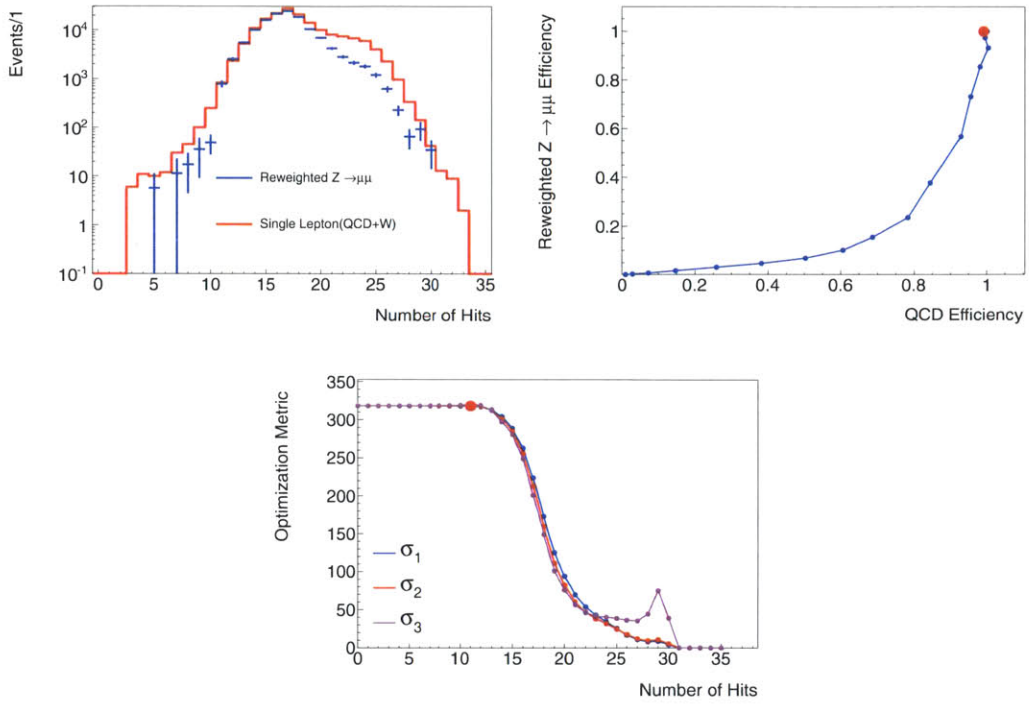

Figure 5-4: Comparison of number of tracker hits from the single muon data set with all optimized cuts applied except for the specified variable. Signal and signal plus background contributions are plotted on the top left, efficiency of the signal is compared with that of the background (top right) and the optimization metric is shown on the bottom. The excess of background events for number of hits near 25 is a result of the poor reconsturction of QCD events. The leftwards motion in the last point of the efficiency plot on the top right results from imperfect normalization of the signal sample, when performing the signal subtraction from the signal plus background sample. The red dot shown in the middle and right plots indicates the optimal cut choice. Three optimization metrics σ_1, σ_2, and σ_3 are defined in equations 5.1, 5.2, and 5.3 respectively.

5.3.4 Tracker fit quality

In order to select a muon track from a converged fit a requirement on the χ^2/NDF is imposed on the track fit. This cut has a significant inefficiency on muons with p_{T}

near 8 GeV/c; however, for leptons with $p_{\mathrm{T}} > 25$ GeV/c, this cut has little impact. Figure 5-5 shows comparison and optimization of the cut. The optimal cut value is found to be near $\chi^2/NDF < 2.5$; however, because of the small impact of this cut, we require

- $\chi^2/NDF < 10$

consistent with the selection of muons for other analyses performed in CMS [72].

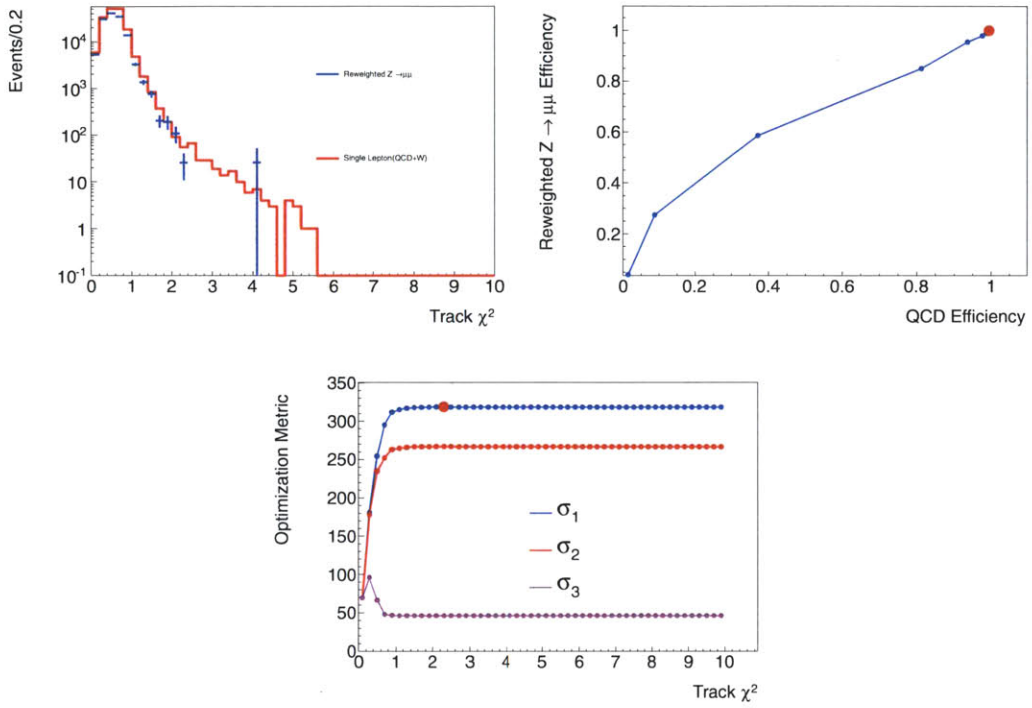

Figure 5-5: Comparison of number of tracker hits from the single muon data set with all optimized cuts applied except for the specified variable. Signal and signal plus background contributions are plotted on the top left, efficiency of the signal is compared with that of the background (top right) and the optimization metric (bottom). The red dot shown in the middle and right plots indicates the optimal cut choice. Three optimization metrics σ_1, σ_2, and σ_3 are defined in equations 5.1, 5.2, and 5.3 respectively.

5.3.5 Number of valid hits

A valid hit is a muon hit which, when fit with the global muon fitter, is included into the final fit for the momentum parameters. By virtue of having gone through global muon reconstruction, it is unlikely for a muon to not have a valid hit. The instance where this may occur is for a muon reconstruced near a gap in the muon chambers. The optimal cut value is found to be (figure 5-6)

- number of valid hits > 0 .

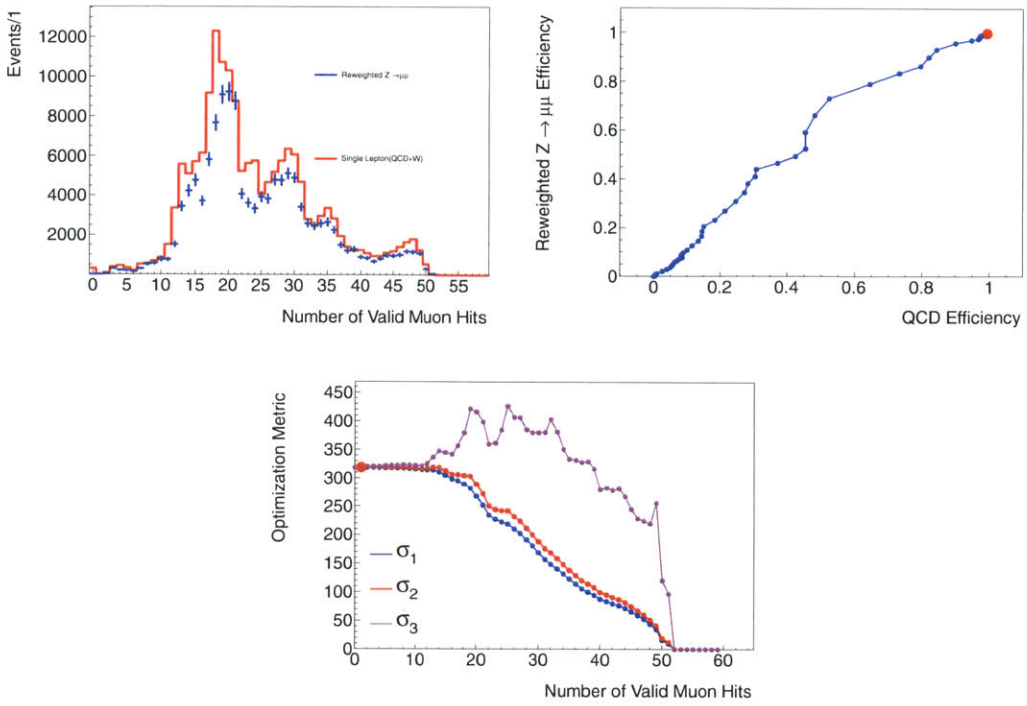

Figure 5-6: Comparison of number of valid hits in the global muon fit from the single muon data set with all optimized cuts applied except for the specified variable. Signal and signal plus background contributions are plotted on the top left, efficiency of the signal is compared with that of the background (top right) and the optimization metric is shown on the bottom. The red dot shown in the middle and right plots indicates the optimal cut choice. Three optimization metrics σ_1, σ_2, and σ_3 are defined in equations 5.1, 5.2, and 5.3 respectively.

5.3.6 Number of segments

Number of segments refers to the number of matched segments associated to a muon. Requiring the number of segments be > 1 has a small impact on the analysis, given that the level one trigger requires the muon to have two matched layers of muon chambers where a segment is reconstructed. Instances where there are less than two matched segments typically occur when pions "punch through" the calorimeters leaving a low energy track in the muon chambers [72]. This cut also removes kaons and pions decaying in the calorimeters, because the p_{T} of the muons from the kaon or pion decay will be different from the full K/π p_{T} measured in the tracker thereby reducing the matching quality. Figure 5-7 shows the optimization over the number of segments. The final result indicates an optimal point of:

- number of matched segments > 1,

consistent with the constraint of the level one trigger.

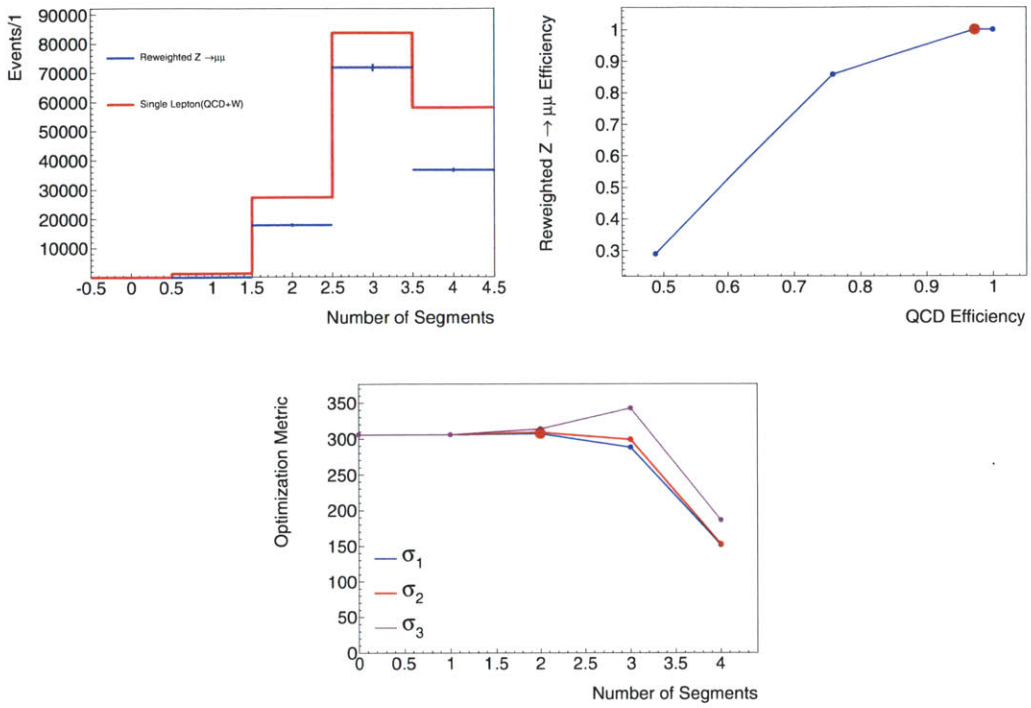

Figure 5-7: Comparison of the number of matched segments to a muon from the single muon data set with all optimized cuts applied except for the specified variable. Signal and signal plus background contributions are plotted on the top left, efficiency of the signal is compared with that of the background (top right) and the optimization metric is shown on the bottom. The red dot shown in the middle and right plots indicates the optimal cut choice. Three optimization metrics σ_1, σ_2, and σ_3 are defined in equations 5.1, 5.2, and 5.3 respectively.

5.3.7 Impact parameter

With the exception of isolation, the second most powerful discriminating variable to select W bosons is impact parameter (d_0). Impact parameter is defined as the distance of the closest point of approach of a track with respect to the primary interaction vertex. Muons with high impact parameter originate from two different processes: cosmic ray muons and heavy flavor decays.

The first background, cosmic ray muons, is completely removed by cutting on d_0. This is because the impact parameter position is known to $\approx$ 20 μm, thus a loose cut of 300 μm would give an allowable area of one mm^2 for which a cosmic ray muon must pass through to be selected. The likelihood of such an occurrence is about 5

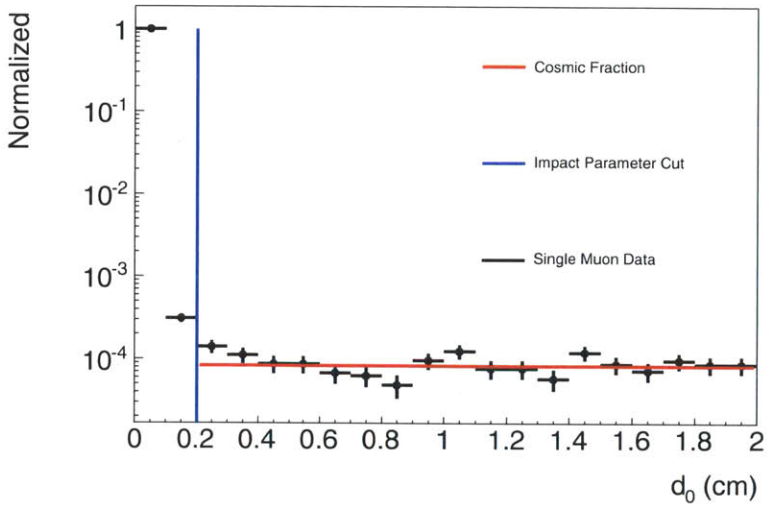

Figure 5-8: Plot of the impact parameter of muons from the single muon data set with all optimized cuts applied except for the specified variable. The red line indicates a fit to the data of a flat line. The blue indicates the impact parameter cut.

events per year . Figure 5-8 illustrates the cosmic ray muon contamination in terms of the muon d_0. For $d_0 > 0.2$ cm there is a flat trend in muon events coming from cosmic ray muons (indicated by the red line). This trend is extrapolated into the signal region to yield a predicted contamination of cosmic ray muons at 10^{-4}. To ensure that no cosmic ray muons with large impact parameter are in the sample a selection of $|d_0| < 0.2$ cm is applied.

Background muons with large impact parameters originate from heavy flavor, b and c quark decays. Due to Cabibbo suppression, b and c quarks have a long lifetime (10^{-12} s) and will decay away from the primary vertex. This produces muons displaced from the primary vertex. These displaced muons provide the largest single background contribution to W boson decays.. This variable is used later as a way of enhancing and reducing the heavy flavor contribution in control regions. Optimization of this cut is performed in a similar manner to other variables and is shown in figure 5-9. The optimization, however, is biased due to the difference in impact parameter between Z boson events and W bosons originating from the presence of a second lepton, which modifies the position of the primary vertex. Optimization yields a value near 0.007 cm. This value is treated as an upper bound for an optimal cut due to the existing bias. The ROC curve is not shown in figure 5-9 because of a necessity to rescale the Z boson yields to obtain coherent results.

5.3.8 Isolation

The most effective variable to separate out muons from QCD decays with those from W boson decays is isolation. The optimal isolation variable, determined through

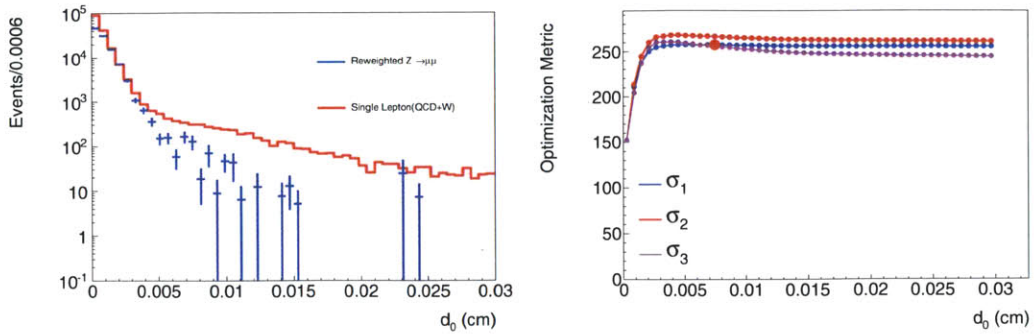

Figure 5-9: Comparison of the impact parameter d_0 of muons from the single muon data set with all optimized cuts applied except for the specified variable. Signal and signal plus background contributions are plotted on the left and the optimization metric is shown on the right. The red dot shown in the right plot indicates the optimal cut choice. Three optimization metrics σ_1, σ_2, and σ_3 are defined in equations 5.1, 5.2, and 5.3 respectively.

simulation, is found to be the sum of all of the track, HCAL, and ECAL deposits within a cone of $\Delta R = \sqrt{\Delta\eta^2 + \Delta\phi^2} < 0.3$ divided by the p_{T} of the reconstructed lepton. Dividing the isolation by p_{T} loosens the cut at high p_{T} where the majority of muons originate from W boson decays. The full isolation variable, χ_{iso} is written as

$$\chi_{\mathrm{iso}} = \frac{\sum_{\Delta \mathrm{R}<0.3} \left(p_{\mathrm{T}}^{Tracks} + E_{\mathrm{T}}^{ECAL} + E_{\mathrm{T}}^{HCAL}\right)}{p_{\mathrm{T}}} . \tag{5.5}$$

In order to remove effects from final state radiation emanating from the lepton, deposits are not included in the isolation calculation if they are within a veto cone of $\Delta R < 0.1$ for the HCAL, $\Delta R < 0.08$ for the ECAL, and $\Delta R < 0.01$ for the tracker. The veto cone size is determined from studies on final state radiation in simulation.

The isolation variable is effective at removing muons from decays of heavy flavored quarks. Muons originating from heavy flavor decays result from a cascaded set of decays down from heavy flavors to light flavors, leaving additional light flavored mesons along the same direction as the muon. This causes muons from heavy flavor decays to be typically less isolated. Other QCD backgrounds originating from decays in flight do not necessarily result from cascades down to lighter flavor and thus are typically more isolated than heavy flavor decays.

The optimization for the isolation variable is shown in figure 5-10. When considering the other optimization metrics σ_1, σ_2, the optimal cut choice appears to be close to zero. Such a strong cut would make the residual QCD background impossible to remove in the final extraction. The optimal choice with the default metric, σ_1 is found to be:

- $\chi_{\mathrm{iso}} < 0.1$

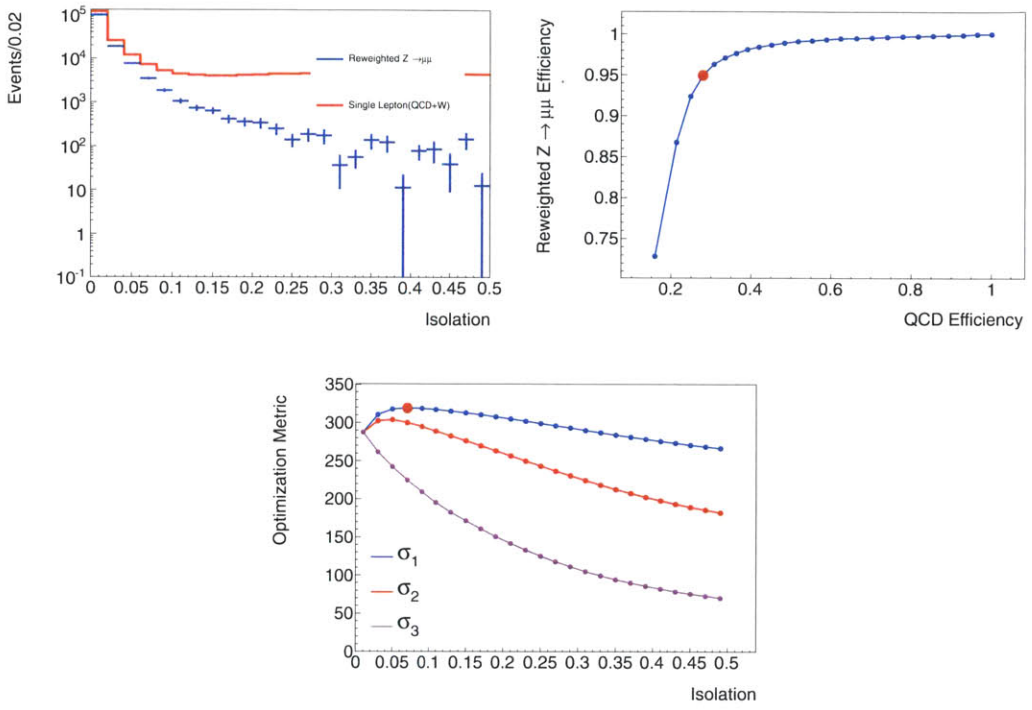

Figure 5-10: Comparison of the isolation of muons from the single muon data set with all optimized cuts applied except for the specified variable. Signal and signal plus background contributions are plotted on the top left, efficiency of data versus that of the background (top right) and the optimization metric is shown on the bottom. The red dot shown in the middle and right plots indicates the optimal cut choice. Three optimization metrics σ_1, σ_2, and σ_3 are defined in equations 5.1, 5.2, and 5.3 respectively.

5.3.9 Di-muon veto

In order to separate Z boson events from W boson events, events where a second muon with $p_{\mathrm{T}} > 10$ GeV/c is present are removed. In light of removing as many events as possible, the second muon is not required to be isolated or to pass any of the previous selection requirements. After this requirement, the remaining Z events in the W boson selection predominantly consist of events where the second lepton falls outside muon chamber diucial region, $|\eta| > 2.4$.

5.4 Selection summary

An optimization is performed to determine the baseline selection for muons from W and Z boson production. The baseline selection rejects poorly reconstructed muons originating from cosmic ray muons, QCD decays in flight, and heavy flavor decays. This baseline selection fo a sigle muon is outlined below:

- muon is a global muon,
- number per track of pixel hits > 0,
- track $\chi^2 < 10$,
- number of hits in the tracker > 10,
- number of valid hits in the muon chamber > 1,
- number of segments in the muon chamber > 1,
- impact parameter $d_0 < 0.2$ cm, and
- $\chi_{\mathrm{iso}} < 0.1$.

To further remove Z boson events from the W boson event selection, all events with a second muon with $p_{\mathrm{T}} > 10$ GeV/c are removed from the selection.

The final efficiency of this selection, excluding trigger, is near 95%. The QCD contamination is close to 10%.

Chapter 6

Muon Efficiency

Once a selection on the lepton is applied, the efficiency of the selection on W and Z boson events is required to perform the cross section measurement. As with the tuning of the selection variables in chapter 5, Z bosons are treated as a clean source of "W-like" muons used to determine the muon reconstruction and selection efficiency.

6.1 Z boson selection

Z boson candidates are selected by requiring the event to pass the lowest unprescaled single muon trigger (HLT_Mu15). Events are further selected by requiring a well identified isolated muon (chapter 5) with one exception; the p_{T} cut on the muons is lowered to include more events:

- $p_{\mathrm{T}} > 20$ GeV/c .

This muon selection is different than the Z boson selection presented in chapter 5 in that a well identified muon selection is established and used in this section whereas previously looser more general cuts were used. To identify the Z boson event, we additionally require a second track with $p_{\mathrm{T}} > 15$ GeV/c reconstructed in either the muon chambers or ther tracker, opposite charge with respect to the first lepton, and combined lepton plus track mass > 30 GeV/c^2. This second track requirement is the minimal pre-selection required to identify Z bosons. In the following sections, we determine the efficiencies by identifying the rate of Z boson reconstruction given tighter selections on the second lepton.

6.2 Efficiency calculation

The efficiency is measured through the "tag and probe" method. In this method, a Z boson event is "tagged" by requiring a well reconstructed, isolated lepton along with a component of the second lepton (*i.e.* track in the tracker). The well identified lepton and the second lepton component must have a combined mass compatible with the Z boson mass. The tagged event is then used to "probe" for an additional

component of the second lepton (*i.e.* track in the muon chambers). The efficiency measurement in data is compared with that of Monte-Carlo simulation to determine a set of correction factors to the simulated efficiency so that it corresponds with the measured data efficiency.

The reconstruction efficiency of a muon is factorized into five separate steps,

- track reconstruction efficiency ϵ_{track},
- Stand-Alone muon reconstruction efficiency ϵ_{SA},
- global muon reconstruction efficiency ϵ_{GB},
- isolation and identification efficiency ϵ_{ID}, and
- trigger efficiency $\epsilon_{\text{Trigger}}$.

The separation into different steps is performed to minimize the overall systematic uncertainty. The total efficiency of the five separate steps is determined through the multiplication of the separate efficiency measurements:

$$\epsilon_{\text{tot}} = \epsilon_{\text{track}}\epsilon_{\text{SA}}\epsilon_{\text{GB}}\epsilon_{\text{ID}}\epsilon_{\text{Trigger}} . \tag{6.1}$$

To perform the efficiency measurement the lepton which probes for the efficiency must be either uncorrelated with the efficiency being measured or factorizible with that efficiency. An example of an uncorrelated probe is a track for the Stand-Alone muon efficiency. Track reconstruction is performed with hits in the tracker. The measurment of the Stand-Alone muon efficiency is performed with hits in the muon chambers, because these objects do not overlap, they are completely uncorrelated, making their efficiencies uncorrelated. An example of a factorizable efficiency would be the use of a global muon as a probe to measure the identification and isolation efficiency given a global muon. In this case there is no bias, because the efficiency is defined by the probe (the global muon). In table 6.2, we list the separate tags and probes for the different efficiency measurements.

The separation of the tag and probe into different categories allows separate binning for each component of the efficiency measurement. Binning of the efficiencies accounts for the difference in kinematics (namely the muon p_{T} and η) between W and Z bosons. Large bin by bin variations in the efficiency will lead to a different efficiencies in each sample. In table 6.2 we list the number of bins used for each efficiency measurement. The individual binning choices are determined by minimizing the systematic uncertainty on each measurement. To minimize the systematic uncertainty on the W^+/W^- ratio, all efficiency measurements are carried out separately on positive and negative muon samples.

To perform each measurement a fit to the mass of the lepton plus probe system is performed simultaneously on the passing and failing sample. The fit returns an accurate estimate of the reconstruction efficiency in the presence of background. For instances where the expected background is negligible or the difference in the difference in the efficiency between signal and background is small, counting events is sufficient to determine the efficiency.

Measurement(Probe)	Tag	# η bins	# p_T bins
Track	Stand-Alone Muon	1	1
Stand-Alone	Track	6	1
Global muon	Track plus Stand-Alone Muon	1	1
Id and Isolation	Global Muon	6	3
Trigger	Global Muon passing Id and isolation cuts	6	3

Table 6.1: Tag and Probe efficiency measurement selection and binning overview

6.2.1 Efficiency calculation

The efficiency is performed by probing for the efficiency on an individual lepton. To see how the efficiency is obtained consider measuring the efficiency for the positive muon. Given that each Z boson event contains a positive muon, the efficiency of the positive muon is defined as

$$\frac{\text{total Passing}}{\text{total Events}} = \frac{N^{+}_{\text{pass}}}{N_{\text{tot}}} . \tag{6.2}$$

Likewise the negative muon efficiency is written as

$$\frac{\text{total Passing}}{\text{total Events}} = \frac{N^{-}_{\text{pass}}}{N_{\text{tot}}} . \tag{6.3}$$

The total efficiency, which is the average of the two efficiencies above is written as

$$\epsilon_{\text{avg}} = \frac{N^{-}_{\text{pass}} + N^{+}_{\text{pass}}}{2N_{\text{tot}}} , \tag{6.4}$$

$$= \frac{2N^{-+}_{\text{passpass}} + N^{+-}_{\text{passfails}} + N^{+-}_{\text{failpass}}}{2N_{\text{tot}}} , \tag{6.5}$$

where in the last step, we have separated out the events into their respective dilepton categories. For instances where both leptons pass N^{+-}_{passpass}, the event is used twice. In the instance where there are more than two probes, we calculate the efficiency on all objects, thus using the same event even more times. Calculating efficiency on each of the leptons separately has the additional advantage that binning is determined by the lepton for which the efficiency is being measured.

6.2.2 Fitting the efficiency

The fit for the efficiency is performed by simultaneously fitting the passing and failing tagged Z mass to a signal plus background model of the Z mass using an un-binned profile likelihood fit. Requiring a fit to the passing and failing samples allows for the efficiency to be floated in the fit, yielding an uncertainty that reflects the likelihood

profile variation in the parameters of the fit [74]. The fit range of the Z mass extends from 60 GeV/c^2 to 150 GeV/c^2 avoiding the low mass "turn-on" region where the yield is suppressed by low p_{T} cuts on the individual leptons (20 and 25 GeV/c). The upper mass cut, 150 GeV/c^2, is chosen to be the point where the background to signal ratio is about to one.

Signal efficiency

In order to fit the Z data two parametrized models for the signal are used. The different parametrizations reflect two approaches to modeling the Z mass. The first fit function is chosen as the default parametrization and the second parametrization is used to determine the systematic uncertainty on the efficiency measurement.

Parametrization one: Monte Carlo simulation convolved with a Gaussian The first fitted function is defined as the Monte Carlo simulated predicted shape $f_{\mathrm{mc}}(m_{\ell\ell})$ convolved with a Gaussian resolution (equation 6.6). The Monte Carlo generator used in this simulation is performed using Powheg [75] with Pythia [54] parton showering passed through the full CMS detector simulation (discussed in chapter 8). The simulated shape is obtained by reconstructing simulated detector deposits from a Monte Carlo dataset of 10^6 events. The resulting shape is obtained by interpolating the simulated dataset through a Gaussian kernel estimator, which treats each data point as a Gaussian about its value of $m_{\ell\ell}$ [76] and performs the interpolation by the density of the Gaussian points. Figure 6-1 shows a fit to a clean signal sample where both legs pass the default muon identification and isolation requirements. In this instance, we expect a background contamination fraction below one percent. The fit function form is written as

$$f\left(m_{\ell\ell}\right) = f_{\mathrm{mc}}\left(m_{\ell\ell}\right) \otimes \exp\left(-\frac{\left(x-x_0\right)^2}{\sigma^2}\right) \ , \tag{6.6}$$

where x_0 is a floated paramater that determines the offset of the Gaussian in the convolution and σ is the other floated parameter that determines the additional smearing of the mass beyond the simulated resolution. The performed fit is an unbinned profile likelihood fit, which determines directly the efficiency along with values for the signal parameters (x_0,σ) and background paramters (discussed later). The choice of using the simulated shape as a baseline incorporates all known simulation effects and the existing knowledge of the Z mass line shape in proton-proton collisions. The inclusion of the convolved Gaussian to the shape compensates for effects that are mis-modeled in the simulation. This includes shifts in muon energy scale, which change the mean x_0 of the Gaussian, and differences in the muon resolution, which change the width σ.

Parametrization two: Breit-Wigner convolved with a crystal ball The second function is written as a Breit-Wigner (BW) distribution convolved with a crystal

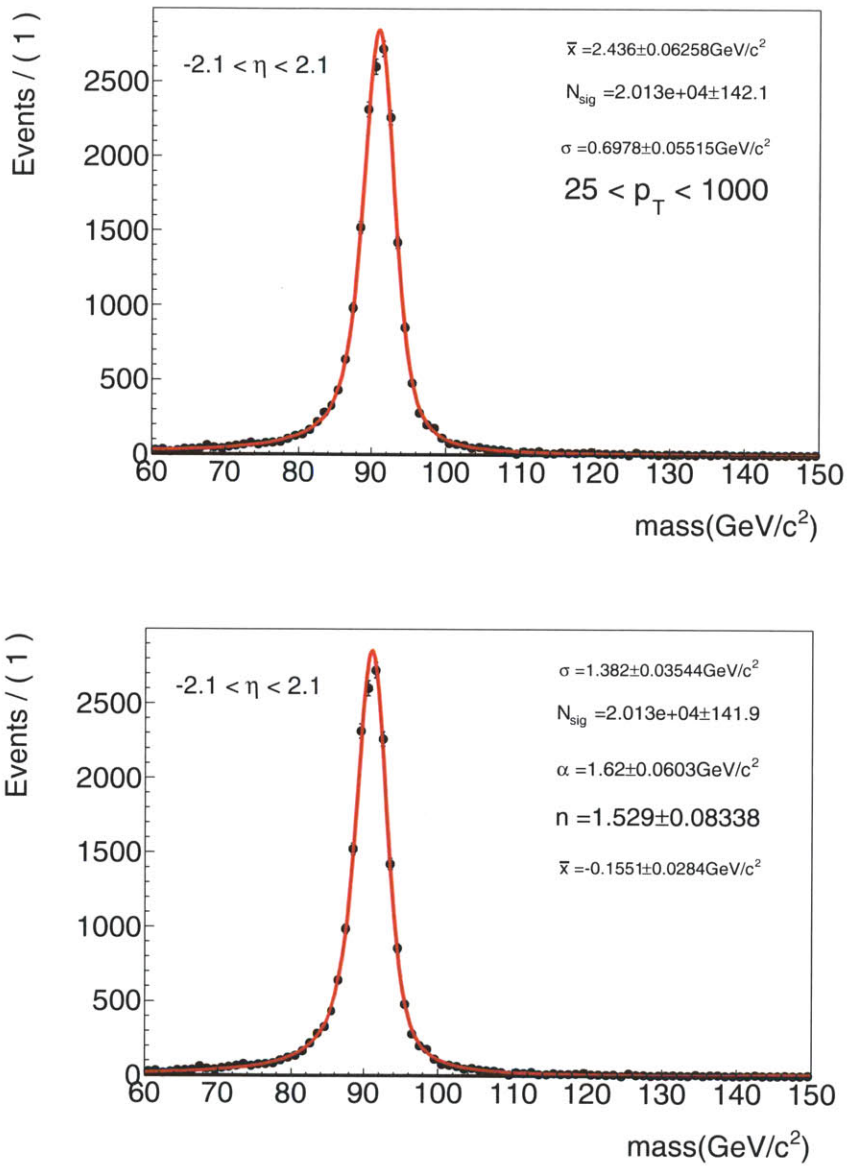

Figure 6-1: Fit to a Z boson signal sample. The signal sample is defined by requiring two muons passing the default identification and isolation cuts. The fit in the top plot is performed using a parameterization of the Monte Carlo simulation convolved with a Gaussian model. The bottom plot is performed with a Breit-Wiegner convolved with a crystal ball model.

ball function (CB):

$$f(m_{\ell\ell}) = BW(m_{\ell\ell}) \otimes CB(m_{\ell\ell}) \quad (6.7)$$

$$BW(x) = \frac{1}{\pi} \frac{\Gamma}{(x - m_z)^2 + \Gamma^2} \quad (6.8)$$

$$(6.9)$$

$$CB(x) = N \cdot \begin{cases} \exp\left(-\frac{(x-\bar{x})^2}{2\sigma^2}\right) & \text{for} \frac{x-\bar{x}}{\sigma} > -\alpha \\ A\left(B - \frac{x-\bar{x}}{\sigma}\right)^{-n} & \text{for} \frac{x-\bar{x}}{\sigma} \leq -\alpha \end{cases}, \tag{6.10}$$

$$A = \left(\frac{n}{|\alpha|}\right)^2 \cdot \exp\left(-\frac{|\alpha^2|}{2}\right), \tag{6.11}$$

$$B = \frac{n}{|\alpha|} - |\alpha| . \tag{6.12}$$

The Breit-Wigner models the Z pole distribution before effects that modify the shape, such as final state radiation or detector mis-modeling. For this reason, the mass, m_Z of the Breit-Wigner and the width of the Breit-Wigner, Γ, are fixed to their measured values [34]. The crystal ball function has been historically used to describe final state radiation emission for either electrons or muons [77]. The function consists of a Gaussian with a power law tail.

To determine the fit parameters of the combined convolved function, the full unbinned distribution was fit to the full dataset, floating all parameters in the crystal ball function. The resolution tail parameter n is then fixed and the fit is applied to individual p_T and η bins. Fixing the tail parameter n for individual bins leads to small biases, but also improved convergence on the limited data. The bias manifests as a small increase in the systematic uncertainty because this function is only used to determine a systematic uncertainty. In figure 6-1, a fit to the Z boson mass shape where both leptons are required to pass the default muon selection is performed. As with the previous model, the fit function models the data well.

Parametrization choice Parametrization one is chosen as the default method because the simulation is capable of describing effects that are not well modeled by the Breit-Wigner convolved with crystal ball model. This is most important when determining the isolation efficiency, where at high p_T, muons from Z boson decays with high energy photons radiating off the muon fail the isolation cut. These failing muons, shown in figure 6-2 induce an unphysical excess below the Z mass peak at 80 GeV/c^2. This excess cannot be fit well by the Breit-Wigner convolved with Gaussian model, but is fit using the Monte Carlo simulated model. To confirm this indeed is the effect the bottom plot in figure 6-2 shows a fit to the isolation variable where the ECAL deposit is not used in the isolation calculation, thereby removing the excess at 80 GeV/c^2.

Background model

Before an isolation cut is applied on the probe lepton, backgrounds originating from QCD and W plus jets comprise around five percent of the signal region. These backgrounds have considerable differences in efficiency to that of the signal and thus may bias the efficiency measurement. To remove the background from the efficiency calculation a background model consisting of an exponential (equation 6.13) is fitted

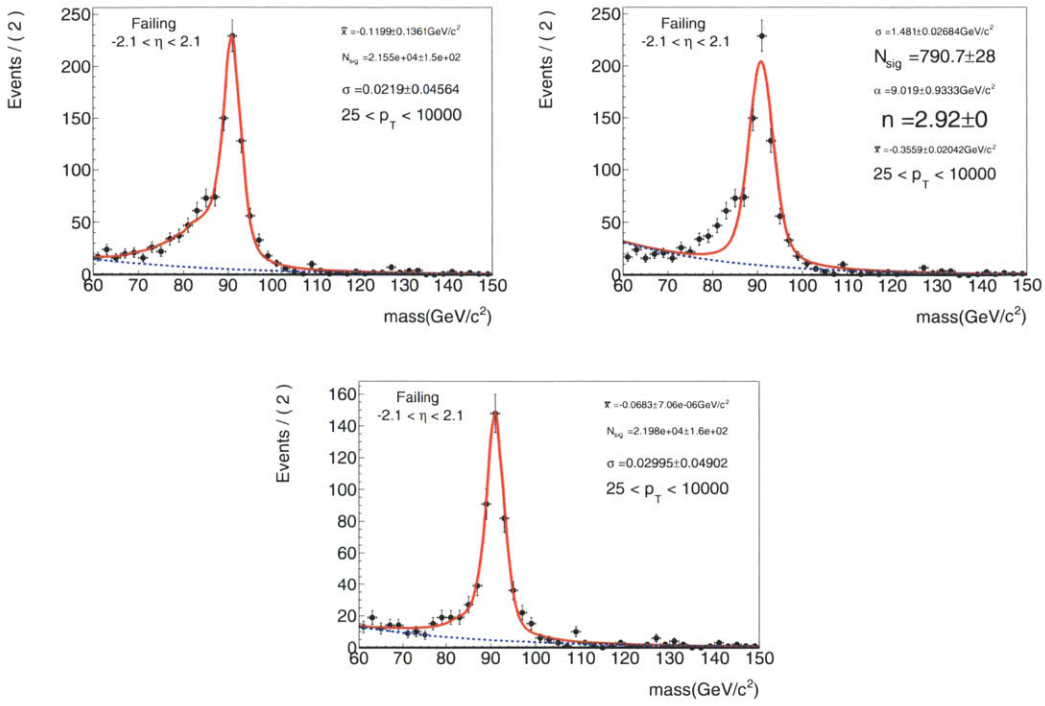

Figure 6-2: Fit to the full data set failing the default isolation cut. The top leftmost plot is fitted with the Monte-Carlo convolved with Gaussian model, the top rightmost plot is fitted with the Breit-Wigner convolved with crystal ball model. The bottom plot is fitted with the Monte-Carlo convolved with Gaussian model where ECAL isolation has been removed from the isolation cut. The dotted blue line denotes the background contribution to the fit.

along with the signal. The form of the exponential is written as:

$$f\left(m_{\ell\ell}\right) = A\exp\left(-\kappa m_{\ell\ell}\right) \ , \tag{6.13}$$

where the background fraction A and the decay constant κ are floated in the fit. The choice of an exponential model is determined by fitting to two different background samples:

- Monte Carlo simulation of a QCD and W plus jets sample with the same selection, and
- same-sign muon plus track distributions from data.

For a perfect simulation, the first model of the background would most closely describe the true shape. However, due to inaccuracies of the QCD and W plus jets production model and inconsistencies with data in the muon energy scale and resolution, the shape may be different between simulation and data. To check the behavior of the simulation, we fit the same-sign muon plus track distributions in data and simulation

along with the opposite-sign simulated distribution shown in figure 6-3. The same-sign simulated muon plus track distribution closely matches the opposite-sign simulated QCD background distribution (opposite muon plus track). This implies, the same-sign muon plus track distribution in data provides an excellent data driven cross check of the fit model performance. From the fit results, we find that comparison of the decay parameters between same-sign muon plus track data and simulation shows agreement. Repeating this on opposite-signed muon and track pairs in simulation, the same level of agrement between the model and data is preserved, with a deviation in simulation of the fitted decay parameter between same-signed and opposite-signed pairs of nearly five percent.

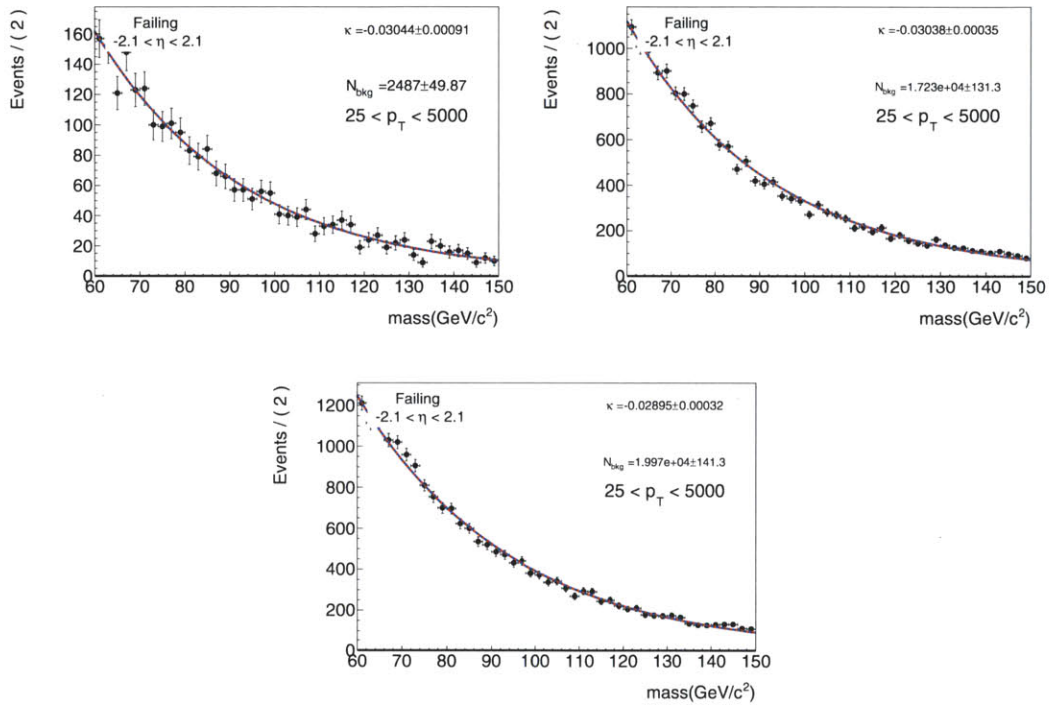

Figure 6-3: Fit with an exponential function (equation 6.13) of the mass distribution from same-sign muon plus track combinations in data (top left), Monte Carlo simulation of QCD, W plus jets (top right) and opposite-sign muon plus track in Monte Carlo simulation of QCD and W plus jets (bottom).

6.3 Efficiency scale factor

Each factorized efficiency measurement in *data* is fit or counted (where specified) separately in each bin. The efficiency in *simulation* for each bin is determined by counting events passing and failing the selection. These two measurements are then combined to produce a data to simulation scale factor κ defined as the ratio of the

data efficiency to the simulated efficiency.

$$\kappa = \frac{\epsilon_{\text{Data}}}{\epsilon_{\text{Simulation}}} \ . \tag{6.14}$$

The binning for the efficiency measurement was chosen to minimize the scale factor variation, separate out different sensitive regions of the detector, and allow the fit to have sufficient freedom to describe the data. The most important separation of the efficiencies was found to be between positively charged muons and negatively charged muons. This results from an asymmetry in the energy scale of the muons as a function of η (chapter 7), which induces positive muons in positive η to behave in a similar way to negative muons in the negative η coordinate. This further causes dips in the postivie muon efficiency in the transition region betwen the CSCs and the DTS η, that in turn, lead to excesses in the negative muon efficiency measurement.

When binning for the efficiency, we consistently use the same binning in η for all efficiency measurements where a binned efficiency is calculated. Thisη binning is separated into six different regions. The first two regions, $-0.8 < \eta < 0$, $0 < \eta < 0.8$, consist of muons reconstructed in the muon barrel DT chambers. These typically have a high efficiency and are well simulated. The second set of regions, $-1.2 < \eta < -0.8$, $0.8 < \eta < 1.2$, consist of the transition region where muons are partially reconstructed in the DT chambers and partially in the CSC chambers. This region is the most difficult to simulate accurately. The final two regions , $-2.1 < \eta < -1.2$, $1.2 < \eta < 2.1$ consist of muons completely in the CSC chambers. The p_{T} binning is determined by the variation of the scale factor in each efficiency measurement so as to minimize the bin per bin variation.

The fit quality is determined by the individual χ^2 of the fits and the fits are further checked by eye. All fits are found to describe the shape well, instances where worse agreement between data and the fit is present. The systematic uncertainty is checked to span all allowed efficiencies.

6.3.1 Track efficiency

The track reconstruction efficiency is defined as the efficiency of a track to be reconstructed given an expected track inferred from the existence of a Stand-Alone muon. The track efficiency has been measured through several other techniques [78] that do not use Stand-Alone muons. These other measurements result in efficiencies for well isolated high p_{T} tracks near 99.9 over the whole acceptance range.

To determine the efficiency, a well identified muon plus a Stand-Alone muon tag is used to probe for a track matched within a cone of $\Delta R < 0.3$, with a $p_{\text{T}} > 0.6 p_{\text{T}}^{\text{Stand-Alone}}$. Because of the lack of variation in the efficiency in p_{T} and η, the measurement is performed in one bin. The fit in one bin of the track efficiency measurement is shown in figure 6-4. The largest limitation compared with the other efficiency measurements is that the muon resolution from the Stand-Alone muon reconstruction is significantly worse than that of global muons. This results in a Z boson width more than twice that of the Z boson width reconstructed with global muons. The resulting efficiency is found to be $0.9998^{+0.000}_{-0.0007}$. It compares well with

the Monte-Carlo predicted value of $0.9996^{+0.0000}_{-0.0001}$, thus a scale factor of 1 ± 0.001 (incorporating a 0.1% systematic uncertainty) is quoted.

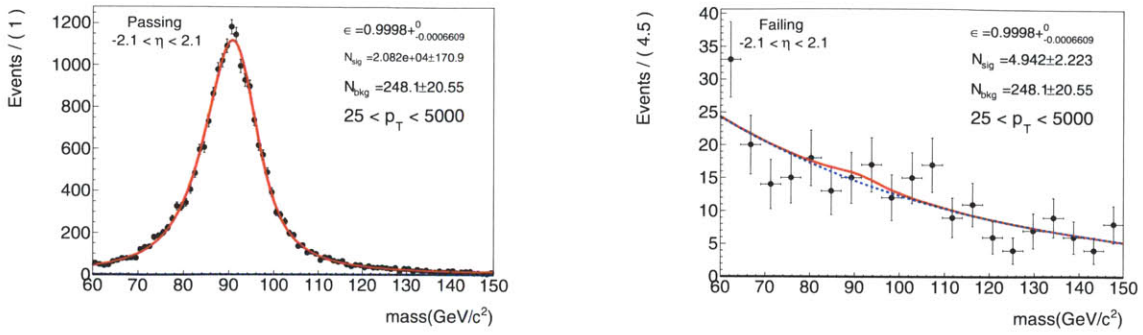

Figure 6-4: Track Efficiency measurement. Performed by using Stand-Alone muons as the probe with the Monte Carlo convolved with Gaussian model. The solid red line indicates the fit model of the combined signal and background. The dashed blue line indicates the background contribution to the fit.

6.3.2 Stand-Alone muon efficiency

The Stand-Alone muon efficiency is defined to be the efficiency of a Stand-Alone muon to be reconstructed given an expected Stand-Alone muon inferred from the presecence of a track . The efficiency is determined by probing for a Stand-Alone muon given a well identified muon plus track combination. This combination has the largest background contribution from QCD and W plus jets of any of the factorized efficiency measurements in this thesis. The large background contribution increases the efficiency uncertainty through the limitation of the fit to describe both an accurate signal and background model.

To minimize the effect, the efficiency measurement is performed in six η bins (previously defined in 6.3) and one p_{T} bin. The variation of the efficiency over the p_{T} of the lepton was checked and found to be 0.3 percent for the range of 25 GeV/c $< p_{\mathrm{T}}$ to $45 < p_{\mathrm{T}}$ GeV/c. This leads to a variation in the scale factor of 0.001 over the whole range in p_{T}. The η variation, on the other hand, is found to be near 2 percent, this necessitates binning in η. The η variation for the positive and negative muons is shown in figure 6-5 using both fit parametrizations. The differences between the fits result in an ambiguity in the background contribution leading to differences in the efficiency measurement. The differences from the two fit models are used to determine the systematic uncertainty (described later). The default (parametrization one) values are found in tables 6.2 and 6.3.

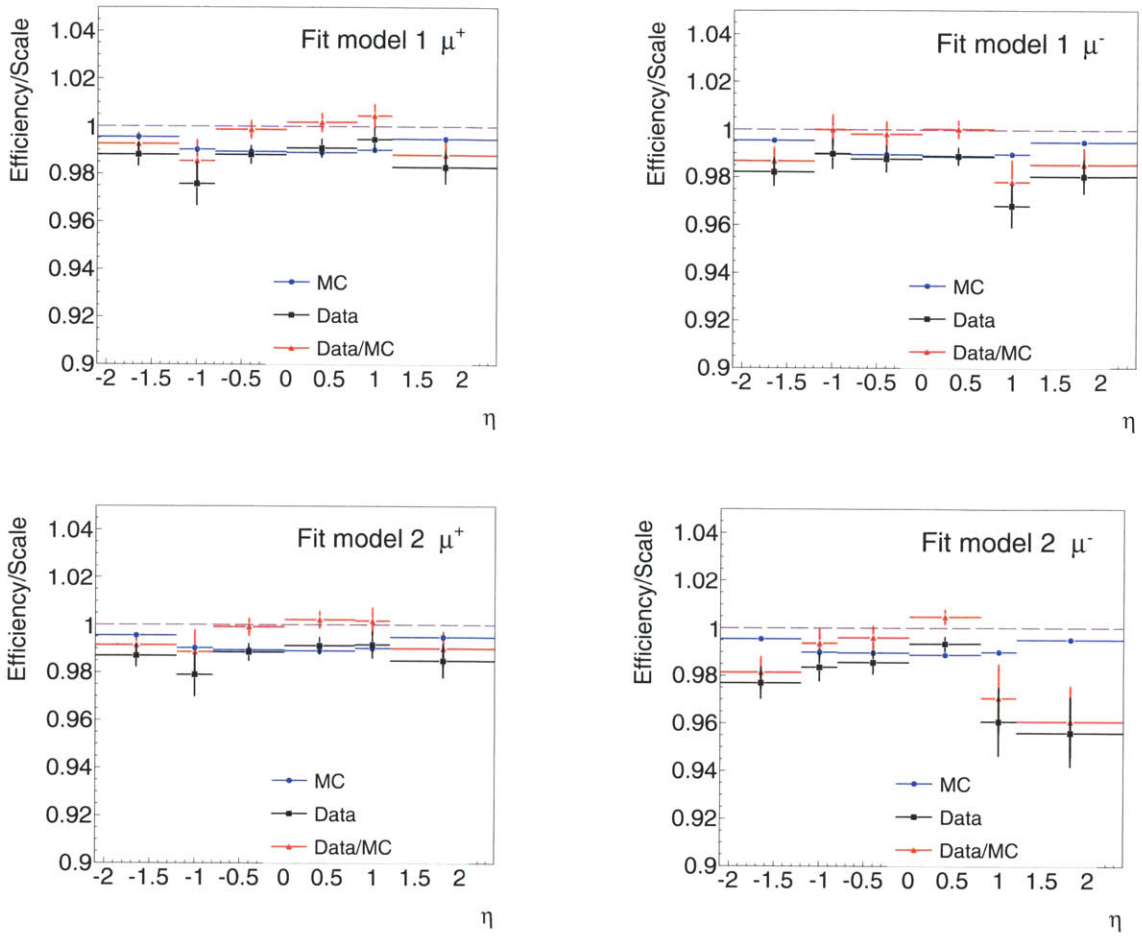

Figure 6-5: Stand-Alone efficiency and scale factors. The efficiency in data (black), Monte Carlo simulation (blue) and the scale factor (red) are performed by using a track as a probe for positive muons (left) and negative muons (right). The top plots result from a fit with the default parametrization (Simulation convolved with a Gaussian). The bottom plots result from fit using the second parametrization (Breit-Wigner convolved with a crystal ball).

6.3.3 Global muon efficiency

The global muon efficiency is defined to be the efficiency of a global muon given a track and a Stand-Alone muon are reconstructed. The measurement is performed by probing to see if a global muon is reconstructed given a tagged sample consisting of a well identified muon plus a track matched to a Stand-Alone muon by $\Delta R = \sqrt{\Delta\eta^2 + \Delta\phi^2} < 0.3$.

Due to the loose matching of the events and the more stringent cuts imposed during the course of Stand-Alone muon reconstruction, the efficiency in a sample of 5000 muons is found to be 100 percent. This compares well with the Monte Carlo

η	negative scale factor	positive scale factor
-2 - -1.2	0.9808±0.0070	0.9899±0.0052
-1.2 - -0.8	0.9918±0.0075	0.9874±0.0089
-0.8 - 0.0	0.9955±0.0051	0.9983±0.0040
0.0 - 0.8	1.0043±0.0037	0.9899±0.0071
0.8 - 1.2	0.9831±0.0079	1.0017±0.0055
1.2 - 2.1	0.9924±0.0057	0.9899±0.0071

Table 6.2: Scale factors for Stand-Alone muon reconstruction for negative muons (left) and positive muons (right) with 25GeV/c < p_{T} < 1000GeV/c.

η	negative ϵ(data)	positive ϵ(data)	negative ϵ(simulation)	positive ϵ(simulation)
-2 - -1.2	0.9763±0.0070	0.9854±0.0051	0.9954±0.0003	0.9955±0.0003
-1.2 - -0.8	0.9818±0.0074	0.9778±0.0088	0.9899±0.0006	0.9902±0.0006
-0.8 - 0.0	0.9852±0.0050	0.9877±0.0039	0.9896±0.0004	0.9894±0.0004
0.0 - 0.8	0.9930±0.0036	0.9902±0.0042	0.9887±0.0004	0.9891±0.0004
0.8 - 1.2	0.9731±0.0078	0.9918±0.0055	0.9898±0.0006	0.9901±0.0006
1.2 - 2.1	0.9875±0.0057	0.9848±0.0070	0.9951±0.0003	0.9948±0.0003

Table 6.3: Efficiencies for Stand-Alone muon reconstruction for negative muons (left) and positive muons (right) with 25GeV/c < p_{T} < 1000GeV/c.

simulated global muon efficiency of 99.99 percent. No additional scale factor is quoted for this efficiency measurement.

6.3.4 Identification and isolation efficiency

The identification and isolation efficiency is defined to be the efficiency of a muon to pass the identification and isolation cuts given that it is a global muon. This is determined by tagging a well identified muon plus a global muon and then probing to see if the global muon passes the identification and isolation cuts.

This efficiency measurement is particularly sensitive to the shape modeling uncertainty (leading to the 80 GeV/c^2 bump previously discussed). However, because the baseline for this efficiency is a well identified muon plus a global muon, the background contamination is small. Hence, it is possible to perform the efficiency measurement in 36 separate bins, six η bins, three p_{T} bins, and separately in positive and negative charge. This is furthermore required to minimize the systematic uncertainty because a variation in the efficiency scale factor is found to be several percent over both η and p_{T}. Additionally, it is found that the failing mass shape changes with p_{T}. Thus, biases may be induced in the fit for a coarse p_{T} binning. The optimal binning was determined to be three bins in p_{T}: 25 GeV/c < p_{T} < 33 GeV/c, 33 GeV/c < p_{T} < 40 GeV/c, and 40 GeV/c < p_{T}. This p_{T} binning has an overall variation in the scale factor between bins of less than one percent.

The results of the scale factor variation projected onto the p_T axis using the two different fit models is shown in figure 6-6. The increase in efficiency as a function of p_T originates mainly from the isolation definition, which becomes looser about the muon as the p_T is increased. The scale variation projected onto the η axis is shown in figure 6-7. Comparing the positive and negative scale factors we see that the positive scale factor is high for $\eta < 0$ and the negative scale factor is high for $\eta > 0$. This is consistent with the energy scale variations discussed in chapter 7. This results in a variation of the positive and negative charge ratio of about 0.5%. The efficiency and scale factors obtained from the first parametrization are found in tables 6.4 to 6.9.

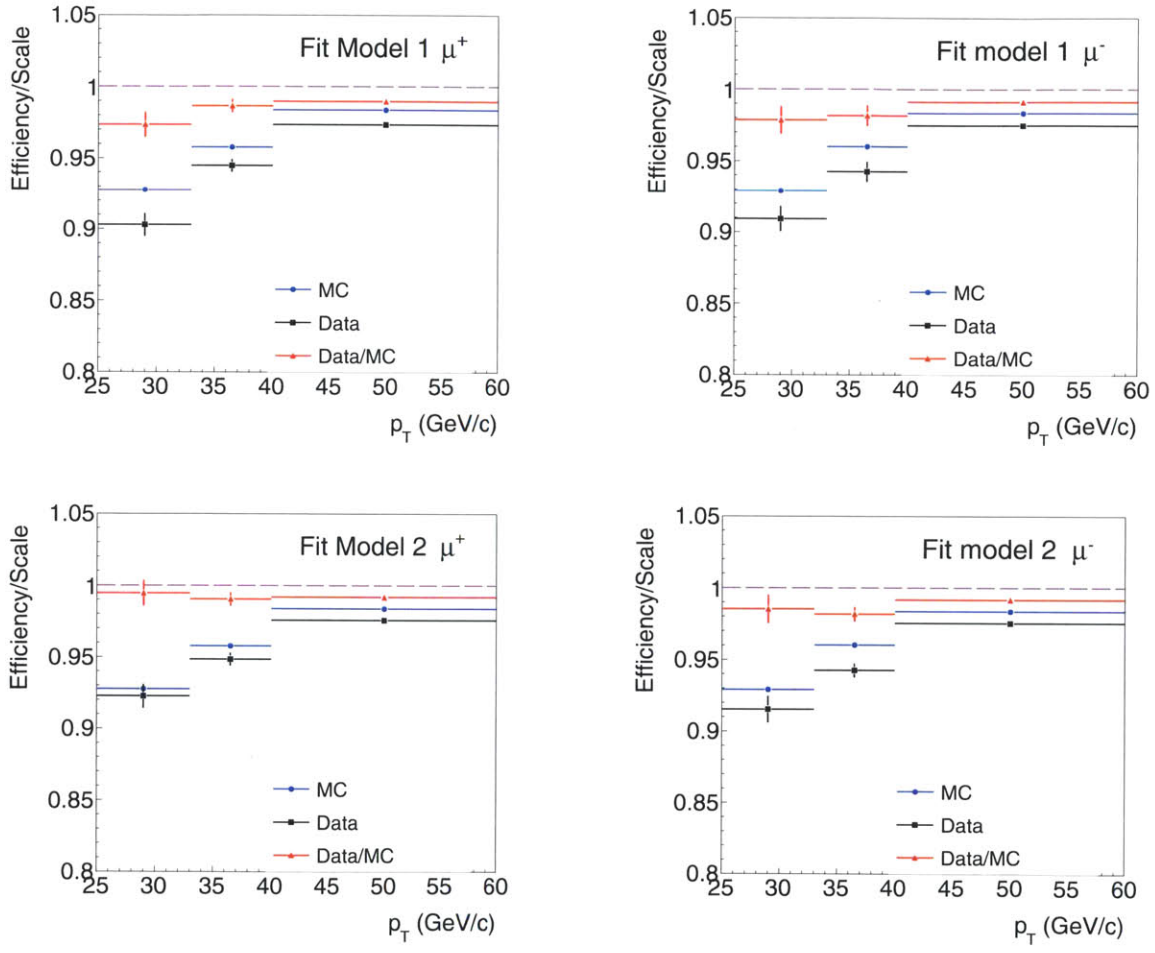

Figure 6-6: Projection of identification and isolation efficiency and scale factor in bins of p_T. The efficiency is ploted for data (black), Monte Carlo simulation (blue), and the scale factor (red) performed by using a global muon as a probe for positive muons (left) and negative muons (right). The top plots result from a fit with the default parametrization (Simulation convolved with a Gaussian). The bottom plots result from fit using the second parametrization (Breit-Wigner convolved with a crystal ball).

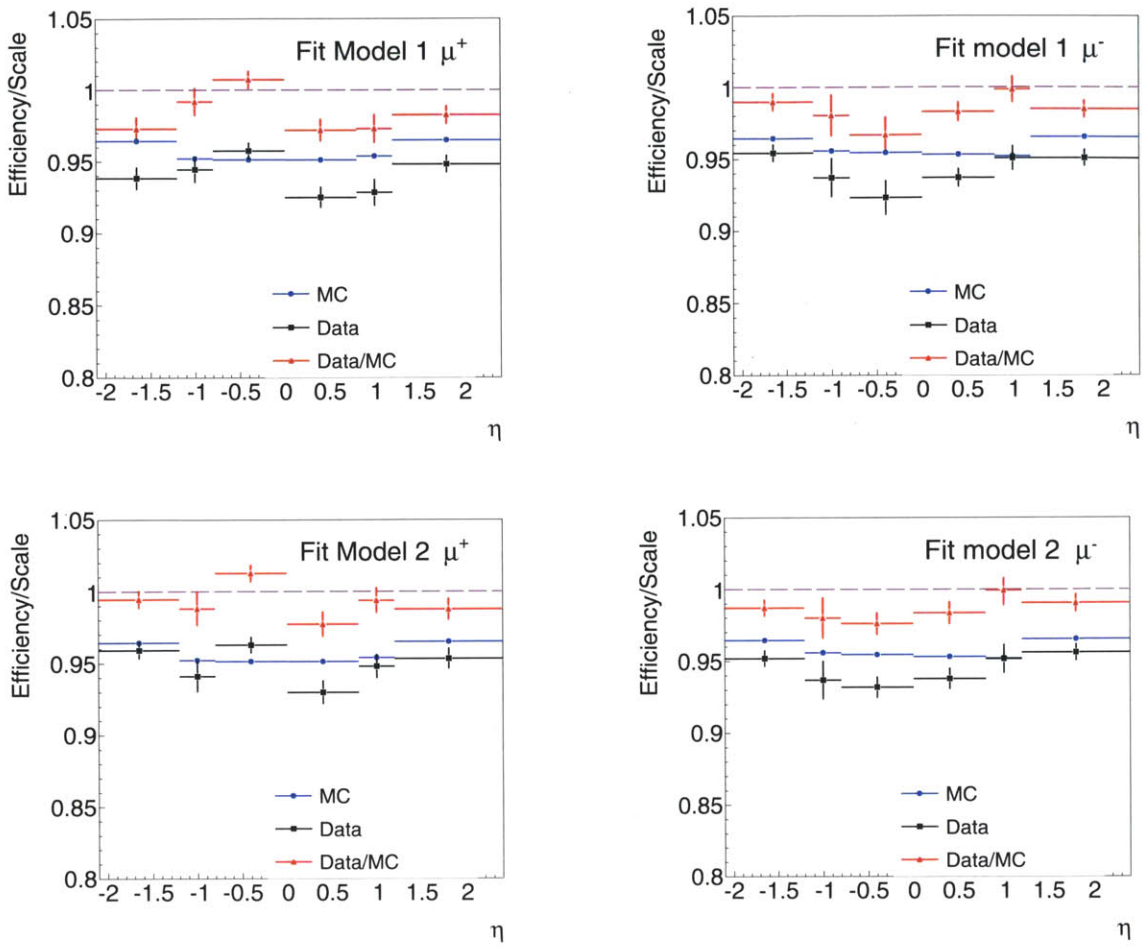

Figure 6-7: Projection of identification and isolation efficiency in bins of η for data (black), Monte Carlo simulation (blue), and the scale factor (red) performed by using a global muon as a probe. The top values result from a fit with the default parametrization (Simulation convolved with a Gaussian). The bottom values result from fit using the second parametrization (Breit-Wigner convolved with a crystal ball).

Trigger Efficiency

The final factorization of the efficiency measurement is the trigger efficiency. This is defined as the efficiency for a muon trigger to fire (both level one and HLT) within a cone of $\Delta R < 0.5$ of a well identified and isolated muon. The expected background, determined by both a fit and by the simulated prediction, is less than 1% and the difference in trigger efficiency between background and signal is determined from simulation to be $< 5\%$, thus we expect a variation < 0.1 % in the efficiency value between counting all events that are in the mass window as opposed to a fit of events that are in the mass window.

η	$p_T \in$ 25.0-33.0	$p_T \in$ 33.0-40.0	$p_T \in$ 40.0-1000.0
-2.1 - -1.2	1.0055±0.0152	0.9801±0.0107	0.9838±0.0052
-1.2 - -0.8	0.9748±0.0406	0.9780±0.0159	0.9885±0.0068
-0.8 - 0.0	0.9531±0.0182	0.9638±0.0334	0.9837±0.0049
0.0 - 0.8	0.9699±0.0177	0.9811±0.0106	0.9973±0.0045
0.8 - 1.2	0.9816±0.0241	1.0108±0.0143	1.0030±0.0024
1.2 - 2.1	0.9868±0.0158	0.9763±0.0111	0.9914±0.0007

Table 6.4: Scale factors for muon identification for negative muons.

η	$p_T \in$ 25.0-33.0	$p_T \in$ 33.0-40.0	$p_T \in$ 40.0-1000.0
-2.1 - -1.2	0.9460±0.0141	0.9451±0.0102	0.9721±0.0051
-1.2 - -0.8	0.9027±0.0375	0.9393±0.0152	0.9697±0.0066
-0.8 - 0.0	0.8780±0.0166	0.9249±0.0320	0.9669±0.0048
0.0 - 0.8	0.8947±0.0162	0.9379±0.0100	0.9785±0.0043
0.8 - 1.2	0.9060±0.0219	0.9633±0.0134	0.9827±0.0021
1.2 - 2.1	0.9282±0.0147	0.9449±0.0107	0.9794±0.0003

Table 6.5: Muon identification efficiency in data for negative muons.

η	$p_T \in$ 25.0-33.0	$p_T \in$ 33.0-40.0	$p_T \in$ 40.0-1000.0
-2.1 - -1.2	0.9408±0.0023	0.9643±0.0016	0.9881±0.0007
-1.2 - -0.8	0.9260±0.0036	0.9604±0.0023	0.9809±0.0011
-0.8 - 0.0	0.9212±0.0025	0.9596±0.0015	0.9829±0.0007
0.0 - 0.8	0.9224±0.0025	0.9559±0.0015	0.9812±0.0007
0.8 - 1.2	0.9230±0.0038	0.9531±0.0025	0.9798±0.0011
1.2 - 2.1	0.9406±0.0024	0.9678±0.0016	0.9878±0.0007

Table 6.6: Muon identification efficiency in simulation for negative muons.

η	$p_T \in$ 25.0-33.0	$p_T \in$ 33.0-40.0	$p_T \in$ 40.0-1000.0
-2.1 - -1.2	0.9459±0.0213	0.9813±0.0107	0.9939±0.0041
-1.2 - -0.8	0.9680±0.0263	1.0056±0.0133	0.9925±0.0066
-0.8 - 0.0	1.0407±0.0166	0.9913±0.0099	0.9960±0.0007
0.0 - 0.8	0.9469±0.0214	0.9936±0.0097	0.9888±0.0051
0.8 - 1.2	0.9497±0.0268	0.9910±0.0145	0.9833±0.0074
1.2 - 2.1	0.9797±0.0167	0.9821±0.0093	0.9870±0.0056

Table 6.7: Scale factors for muon identification for positive muons.

η	$p_T \in$ 25.0-33.0	$p_T \in$ 33.0-40.0	$p_T \in$ 40.0-1000.0
-2.1 - -1.2	0.8898±0.0199	0.9458±0.0101	0.9825±0.0040
-1.2 - -0.8	0.8921±0.0239	0.9579±0.0124	0.9750±0.0064
-0.8 - 0.0	0.9550±0.0150	0.9461±0.0093	0.9779±0.0001
0.0 - 0.8	0.8687±0.0195	0.9485±0.0092	0.9705±0.0050
0.8 - 1.2	0.8800±0.0246	0.9460±0.0136	0.9641±0.0072
1.2 - 2.1	0.9221±0.0156	0.9492±0.0088	0.9747±0.0054

Table 6.8: Muon identification efficiency in data for positive muons.

η	$p_T \in$ 25.0-33.0	$p_T \in$ 33.0-40.0	$p_T \in$ 40.0-1000.0
-2.1 - -1.2	0.9407±0.0024	0.9638±0.0017	0.9885±0.0007
-1.2 - -0.8	0.9216±0.0038	0.9526±0.0025	0.9823±0.0010
-0.8 - 0.0	0.9177±0.0025	0.9544±0.0015	0.9818±0.0007
0.0 - 0.8	0.9174±0.0025	0.9546±0.0015	0.9815±0.0007
0.8 - 1.2	0.9266±0.0037	0.9546±0.0025	0.9804±0.0011
1.2 - 2.1	0.9412±0.0023	0.9666±0.0016	0.9876±0.0007

Table 6.9: Muon identification efficiency in data for positive muons.

The efficiency is determined by counting events, an arbitrary binning is used to determine the efficiencies without any loss of statistical power. The maximal binning considered is 70 η bins for both positively and negatively charged leptons, which correspond roughly to all of the different sub divisions of the CSC and DT chambers. A comparison of the inclusive efficiency to that with the 36 efficiency bins used in the identification and isolation efficiency measurement yields a change in the W efficiency of 0.1 percent. Thus we utilize the same binning as that of the identification and isolation efficiency measurement.

The projected efficiency measurements found in figures 6-8 and 6-9 show an inefficiency comparing data and Monte Carlo simulation for events in the negative η transition region. This is a result of a timing misalignment between the level one trigger for the DT chambers and the level one trigger for the negative CSC chambers. This misalignment was resolved after the end of 2010 running.

Pre-Firing inefficiency

A phenomenon resulting from poor timing resolution in the muon chambers leads to an inefficiency caused by early firing of the muon chambers. A trigger which fires early enough will trigger the previous crossing. The actual crossing with the event, may have other triggers associated with it, but is not selected because consecutive events are not allowed to trigger CMS readout. The event, that passes the trigger, is then removed at the high level trigger because no track will be associated to the triggered track in the muon chambers. This inefficiency is not accounted for through

η	$p_T \in$ 25.0-33.0	$p_T \in$ 33.0-40.0	$p_T \in$ 40.0-1000.0
-2.1 - -1.2	0.8960±0.0165	0.9000±0.0137	0.9011±0.0097
-1.2 - -0.8	0.9050±0.0234	0.8273±0.0248	0.8408±0.0153
-0.8 - 0.0	0.9661±0.0097	0.9555±0.0086	0.9607±0.0055
0.0 - 0.8	0.9618±0.0105	0.9531±0.0085	0.9703±0.0048
0.8 - 1.2	0.8686±0.0269	0.8814±0.0221	0.8801±0.0135
1.2 - 2.1	0.8899±0.0176	0.9044±0.0140	0.8907±0.0100

Table 6.10: Trigger efficiency in data for negative muons.

η	$p_T \in$ 25.0-33.0	$p_T \in$ 33.0-40.0	$p_T \in$ 40.0-1000.0
-2.1 - -1.2	0.9344±0.0025	0.9372±0.0021	0.9345±0.0015
-1.2 - -0.8	0.9276±0.0037	0.9235±0.0032	0.9204±0.0021
-0.8 - 0.0	0.9800±0.0014	0.9792±0.0011	0.9796±0.0007
0.0 - 0.8	0.9773±0.0014	0.9792±0.0011	0.9787±0.0008
0.8 - 1.2	0.9108±0.0042	0.9180±0.0033	0.9145±0.0022
1.2 - 2.1	0.9365±0.0025	0.9338±0.0022	0.9347±0.0015

Table 6.11: Trigger efficiency in simulation for negative muons.

η	25.0-33.0	33.0-40.0	40.0-1000.0
-2.1 - -1.2	0.9589±0.0178	0.9603±0.0147	0.9643±0.0105
-1.2 - -0.8	0.9757±0.0255	0.8959±0.0270	0.9136±0.0167
-0.8 - 0.0	0.9858±0.0100	0.9758±0.0088	0.9807±0.0057
0.0 - 0.8	0.9842±0.0108	0.9734±0.0088	0.9914±0.0049
0.8 - 1.2	0.9536±0.0298	0.9601±0.0243	0.9623±0.0149
1.2 - 2.1	0.9502±0.0190	0.9685±0.0151	0.9529±0.0108

Table 6.12: Scale factors for trigger efficiency of negative muons.

η	$p_T \in$ 25.0-33.0	$p_T \in$ 33.0-40.0	$p_T \in$ 40.0-1000.0
-2.1 - -1.2	0.8947±0.0169	0.9108±0.0137	0.9190±0.0087
-1.2 - -0.8	0.8963±0.0254	0.8635±0.0227	0.8528±0.0145
-0.8 - 0.0	0.9544±0.0113	0.9599±0.0082	0.9660±0.0050
0.0 - 0.8	0.9616±0.0102	0.9658±0.0075	0.9547±0.0059
0.8 - 1.2	0.8649±0.0264	0.9087±0.0188	0.8864±0.0130
1.2 - 2.1	0.8615±0.0179	0.8904±0.0155	0.8969±0.0101

Table 6.13: Trigger reconstruction efficiency in data for positive muons.

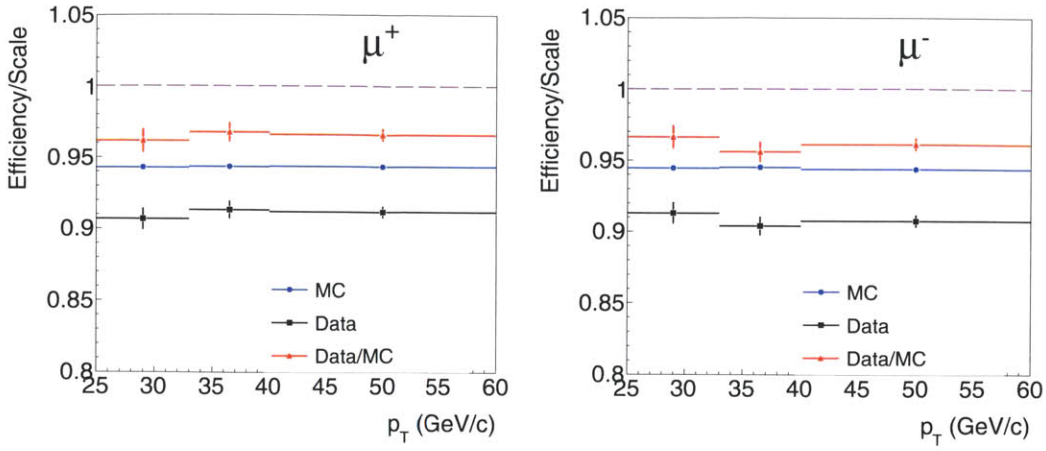

Figure 6-8: Projection of Trigger efficiency and the scale factor in bins of p_{T}. The efficiency for data (black), Monte Carlo simulation (blue), and the scale factor (red) for positive muons (left) and negative muons (right) performed by using a well identified and isolated global muon as a probe and counting events in the mass window.

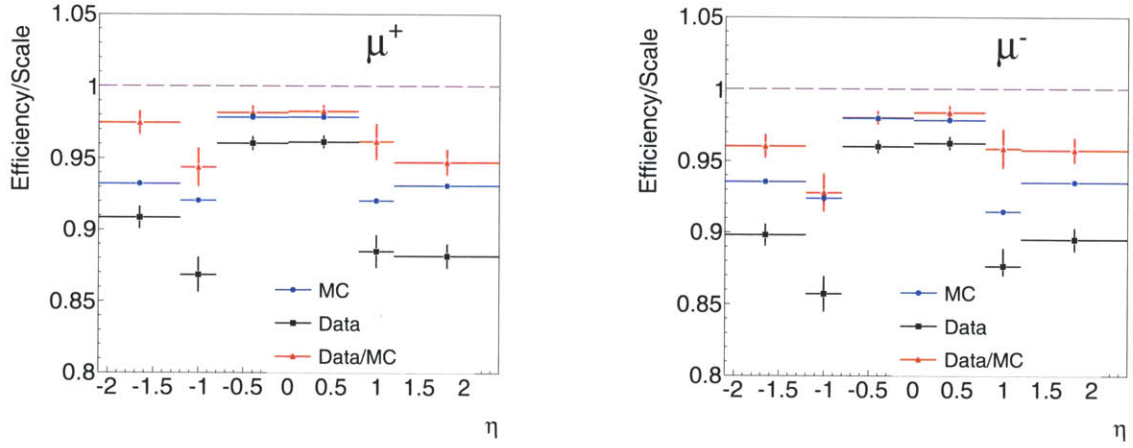

Figure 6-9: Projection of trigger efficiency and the scale factor in bins of η. The efficiency for data (black), Monte Carlo simulation (blue), and the scale factor (red) for positive muons (left) and negative muons (right) performed by using a well identified and isolated global muon as a probe and counting events in the mass window.

the tag and probe method.

To measure this effect we rely on 2011 data. In the 2011 data, prefired Z events are removed by gating the muon trigger with the proton bunch trigger. This permits a detailed calculation of the prefiring efficiency measurement by measuring the trigger efficiency before and after the gating. In figure 6-10, we plot the efficiency

η	$p_T \in$ 25.0-33.0	$p_T \in$ 33.0-40.0	$p_T \in$ 40.0-1000.0
-2.1 - -1.2	0.9309±0.0026	0.9341±0.0023	0.9318±0.0015
-1.2 - -0.8	0.9204±0.0040	0.9183±0.0033	0.9226±0.0021
-0.8 - 0.0	0.9788±0.0014	0.9780±0.0011	0.9782±0.0008
0.0 - 0.8	0.9783±0.0014	0.9792±0.0011	0.9779±0.0008
0.8 - 1.2	0.9163±0.0040	0.9231±0.0032	0.9213±0.0021
1.2 - 2.1	0.9328±0.0025	0.9281±0.0023	0.9315±0.0016

Table 6.14: Trigger efficiency in simulation for positive muons.

η	$p_T \in$ 25.0-33.0	$p_T \in$ 33.0-40.0	$p_T \in$ 40.0-1000.0
-2.1 - -1.2	0.9612±0.0183	0.9751±0.0149	0.9863±0.0095
-1.2 - -0.8	0.9738±0.0279	0.9403±0.0249	0.9243±0.0158
-0.8 - 0.0	0.9751±0.0116	0.9816±0.0085	0.9875±0.0052
0.0 - 0.8	0.9829±0.0105	0.9862±0.0077	0.9763±0.0061
0.8 - 1.2	0.9439±0.0291	0.9844±0.0206	0.9621±0.0143
1.2 - 2.1	0.9235±0.0194	0.9594±0.0169	0.9629±0.0110

Table 6.15: Scale factors for the trigger efficiency in positive muons.

as a function of η for a high level triggered muon with $p_T > 25$ GeV/c before and after the gating with the proton bunch trigger. A small increase in the efficiency measurement is present in the barrel consistent with the onset of pre-firing of muons in the barrel. The overall difference in the efficiency between gating and not gating with the beam coincidence, rescaled to W kinematics by applying the p_T-η weighting scheme performed in chapter 5, determines $\Delta\epsilon_W$ to be

$$\epsilon_{\text{pre-gate}} = 0.8817 \pm 0.0027 \ , \tag{6.15}$$

$$\epsilon_{\text{gate}} = 0.8873 \pm 0.0008 \ , \tag{6.16}$$

$$\Delta\epsilon = 0.0055 \pm 0.28 \rightarrow \Delta\epsilon_W = 0.0028 \pm 0.0014 \ . \tag{6.17}$$

Thus, a change in the trigger efficiency before and after pre-firing is found to 0.0028. In light of changes occurring from the timing of the muon chambers between 2011 data and 2010 an overall efficiency scale factor of 0.995 (consistent with the 2010 measurement of the prefiring [79]) is applied to the data with a systematic uncertainty of 0.005.

6.3.5 Secondary muon veto

The final selection requirement for the W boson is that no second muon with $p_T >$ 10 GeV/c is present in the event (di-muon veto). In simulation, this selection removes 0.2% of true W boson events. To confirm this value in data, muons from Z bosons are tagged and found to have an additional muon 0.1 ± 0.1 percent of the time, consistent

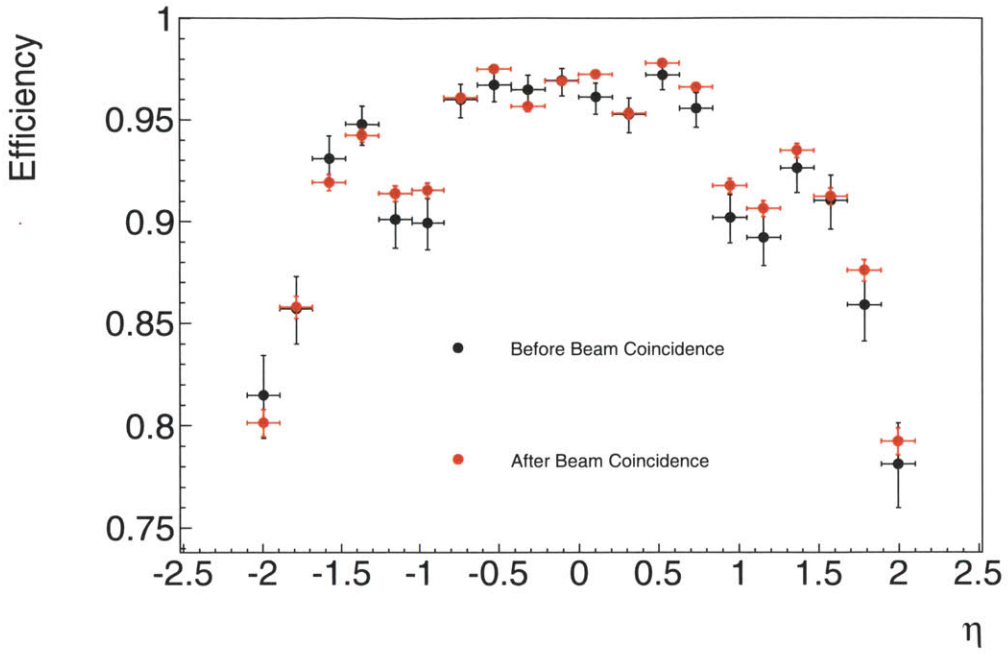

Figure 6-10: Efficiency of the 2011 Single Muon trigger with $p_{\mathrm{T}} > 24$ GeV/c (HLT_Mu24) as function of η for separate datasets before and after the gating with the beam coincidence trigger.

with the Monte Carlo prediction for Z bosons of 0.15 %. Thus, this effect introduces an additional systematic uncertainty of 0.1 percent due to the Di-muon veto.

6.4 Systematic uncertainties

Systematic uncertainties on the efficiency measurement originate predominantly from model assumptions in the efficiency fits. For efficiency measurements based on event counts, the trigger and global muon efficiencies, systematic uncertainties result from the per bin scale variation of events and from differences between background and signal efficiency. These effects have been determined to be less than 0.1%. Comparison of the track efficiency with several techniques leads to differences in the measured efficiency between the techniques below 0.1%. Hence, we quote a systematic uncertainty of 0.1% on all three of these efficiencies.

The other two efficiencies, the Stand-Alone muon efficiency and the identification and isolation efficiency are determined through fits. Systematic uncertainties on the efficiency measurement result from potential biases due to small data modeling inadequencies with the chosen functional form. Because both the mean and widths of the fit functions are floated, uncertainties resulting from mis-modeling of the resolution and energy scale are absorbed into the fit. However, effects resulting from the

inability of the functional forms to model the signal shape remain important. The systematic uncertainty for these two measurements are factorized into three separate effects, fitting bias, background modeling and signal shape modeling.

6.4.1 Fitting bias

In order to validate the fitting procedure, a series of toy data samples are generated by sampling a simulated "fake" data distribution. The "fake" data distribution is determined by sampling and generating toy data from a Monte Carlo simulated QCD shape combined with a Monte Carlo signal shape using the per-bin yields predicted from the fit.

The toy data samples are then fitted in each bin utilizing the same fitting technique used to determine the efficiency in data. The true efficiency of the fake signal sample, as determined by the per-bin yields from the fit, is then compared with the average fitted efficiency over all the toy samples. From the comparison, we deduce the behavior of the uncertainties on the fit and the resulting bias on the efficiency. This test, known as the closure test, validates the choice of the fitting technique.

From a series of 5000 toy samples, the mean of the fitted Stand-Alone efficiency is found to be

$$\epsilon^{Stand-Alone}_{\text{predicted}} - \epsilon^{Stand-Alone}_{\text{true}} = -0.14\% \pm 0.01\% \,, \tag{6.18}$$

$$\epsilon^{Id}_{\text{predicted}} - \epsilon^{Id}_{\text{true}} = -0.07\% \pm 0.01\% \,, \tag{6.19}$$

for the Stand-Alone, and identification and isolation efficiency respectively.

The pull distributions from toy experiments, defined by

$$\text{Pull}(x) = \frac{x - \bar{x}}{\sigma} \,, \tag{6.20}$$

where $\bar{x}$ is the true efficiency, x is efficiency determined by the fit, and σ is the uncertainty on the efficiency determined by the fit, results in a unit Gaussian with a mean given by the bias reported above. This indicates well behaved fits.

6.4.2 Background systematic uncertainty

The QCD and W plus jets background in both simulation and data is modeled well with an exponential. This is demonstrated by figure 6-3 which shows the fit of an exponential to same-sign and opposite-sign events in data and MC simulation. The same-sign models in both data and simulation have parameters consistent with each other.

To see this more clearly, figure 6-11 shows the decomposition of the simulated background into W plus jets events and QCD events. The red line is the simulated same-sign shape, which agrees well with same-sign data points. The difference between the same-sign and opposite-sign simulation is of similar order to the uncertainty bars of the data. This effect is shown in terms of relative fraction versus $m_{\ell\ell}$ in figure 6-12. From the figure, we determine the relative fractions of the two

backgrounds change by 10% between same-sign and opposite-sign events, yielding the small difference in shape.

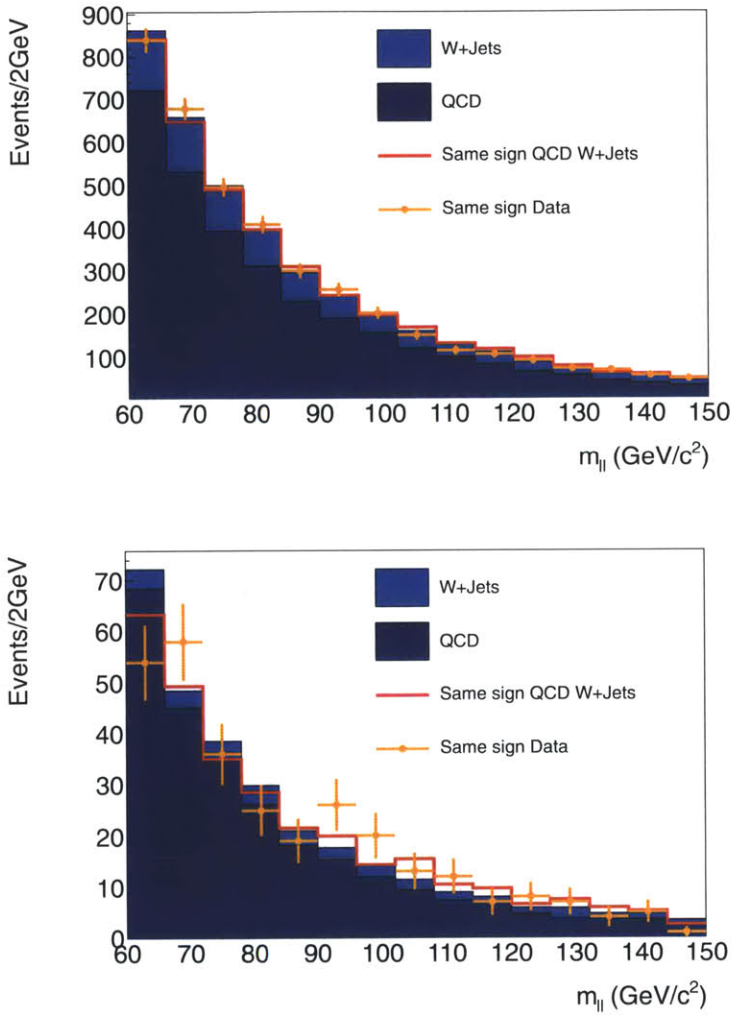

Figure 6-11: Simulated QCD and W plus jets background (blue shades) compared with same-sign data (yellow points) and simulation (red line) for the Stand-Alone muon efficiency (top) and the identification and isolation efficiency (bottom). The bump in the middle of the bottom plot corresponds to Z boson events failing the isolation requirement, where the charge is mis-reconstructed.

To calculate the systematic uncertainty we use the same-sign well identified muon plus track events from data as a template background shape from which we sample to make toy data. The advantage of using the data is that the overall trend in shape as a function of η is implicitly built in by selecting events with the desired kinematics. Additionally, using the data eliminates the potential for systematic biases due to mismatched between simulation and data and mis-modeling using analytic functions.

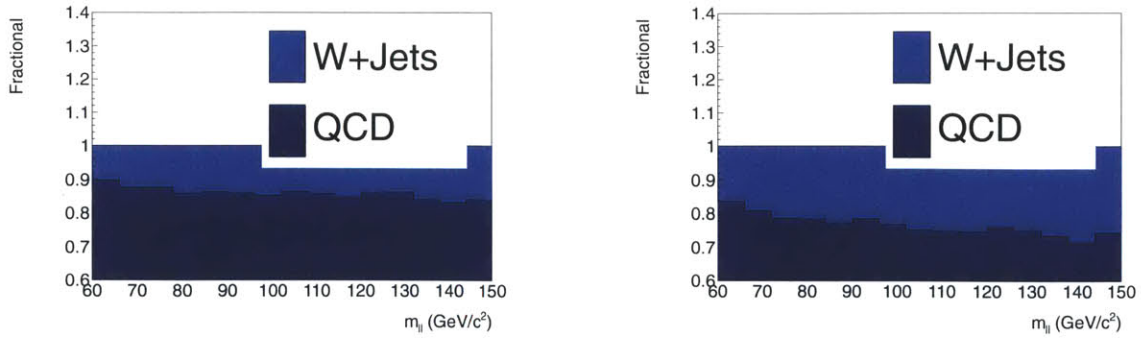

Figure 6-12: Relative bin by bin fraction of W plus jets to QCD for muon plus track events in Monte Carlo simulation. On the x axis is the combined mass of the muon plus track system. The left plot is for opposite-sign events, the right side is for same-sign events (note the change in the slope and fraction of W plus jets which yields a change in the overall shape)

η	Negative (%)	Positive (%)
-2.1 - -1.2	0.0841	0.1994
-1.2 - -0.8	0.2174	-0.6008
-0.8 - 0.0	-0.3854	-0.4158
0.0 - 0.8	-0.4362	-0.7455
0.8 - 1.2	-0.4431	-0.1147
1.2 - 2.1	-0.8250	-0.6018

Table 6.16: Background systematic uncertainty for Stand-Alone Muon efficiency measurements of negative muons (left) and positive muons (right).

When calculating the systematic uncertainty on the background estimate, a set of 5000 toy data samples are generated per bin using the same-sign data as a background model and the best fit signal shape as the signal model. The toy data samples are individually fitted determining a pull distribution for each bin. The systematic uncertainty is determined from the bias of the fit pulls. The results of the systematic uncertainties is found in tables 6.16 to 6.18. Typical bin by bin uncertainties are about 0.4% for the Stand-Alone muon efficiency and less for the identification and isolation efficiency.

As a final check of the exponential model figure 6-13 plots the fitted decay parameters for same-sign and opposite-sign events as a function of η of the lepton. The figure demonstrates agreement between the simulation and the same-sign events in data. The dis-agreement for opposite-signed events is larger between data and simulation. This results from a bias due to the presence of Z boson events in the fit. The bias is accounted for by the procedure outlined to determine the systematic uncertainty for the fitting bias (section 6.4.1).

η	$p_T \in$ 25.0-33.0 (%)	$p_T \in$ 33.0-40.0 (%)	$p_T \in$ 40.0-1000.0 (%)
-2.1 - -1.2	-0.2013	0.0377	0.0555
-1.2 - -0.8	-0.5199	-0.2114	-0.0963
-0.8 - 0.0	-0.6333	0.0787	0.0159
0.0 - 0.8	-0.5691	-0.1760	-0.2363
0.8 - 1.2	0.5452	-0.0730	0.1027
1.2 - 2.1	2.5840	-0.1266	-0.0508

Table 6.17: Background modeling systematic uncertainty in % for identification efficiency measurements of negative muons. As a comparison with the systematic uncertainty, the per-bin uncertainty on th efficiency is near 2% for the lowest p_T bin.

η	$p_T \in$ 25.0-33.0 (%)	$p_T \in$ 33.0-40.0 (%)	$p_T \in$ 40.0-1000.0 (%)
-2.1 - -1.2	-0.1105	-0.1038	-0.0293
-1.2 - -0.8	0.0410	0.3464	0.0500
-0.8 - 0.0	-0.3690	-0.0732	-0.0059
0.0 - 0.8	-0.8468	-0.2450	-0.1763
0.8 - 1.2	-1.2401	0.1795	0.0625
1.2 - 2.1	-0.5070	0.0739	-0.0697

Table 6.18: Background modeling systematic uncertainty in % for identification efficiency measurements of positive muons.

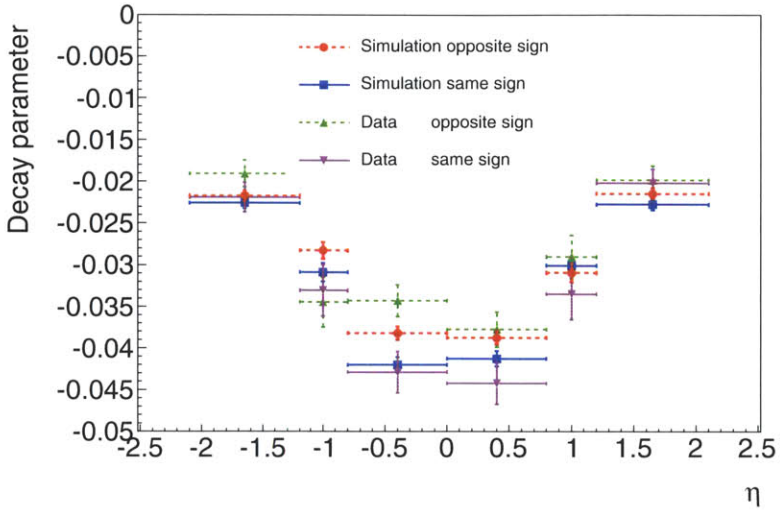

Figure 6-13: Trend in decay parameter as a function of probe η for simulation and data using both same-sign (solid line) and opposite-sign (dashed line) events.

6.4.3 Muon signal systematic uncertainty

The muon signal shape systematic uncertainty is determined by using the Breit-Wigner convolved with crystal ball model (parametrization two of the signal). The choice of the Breit-Wigner model accounts for two effects. First, in some regions of muon η the resolution in Monte-Carlo simulation is larger than the resolution in data. To account for differences in resolution the default fit model uses a convolution of a Gaussian with varying width. Unfortunately, a convolution only leads to a larger resolution, thus it cannot model effects where the resolution is better in data. With the Breit-Wigner based model, all possible resolutions are possible, thus allowing for instances where the simulated resolution is worse than in data. The effect of smaller resolution in data than in Monte-Carlo simulation will bias the default efficiency measurement low, and leave the Breit-Wigner based parametrization unbiased.

The second effect originates from the mis-modeling of the radiation of photons off of the muon (known as FSR) in simulation, which is known to be imperfect for particular regions of lepton p_{T}. In these instances, the FSR from the muon leaks out of the ECAL isolation veto cone causing a secondary bump in the failing sample of the signal. With the Breit-Wigner basedmodel, the FSR will be fitted by a tail that goes through the mean of the failed sample. This results in an upward bias in the efficiency measurement. The effect of this FSR mismodelling motivates the factorization of the Stand-Alone muon efficiency from the identification and isolation efficiency.

Both of these effects force the predicted efficiency from the Breit-Wigner based parametrization to be biased high compared to that of the default parametrization, thus it is sufficient to use this second model to account for both effects. A confirmation of this was verified with fits of toy data.

η	Negative (%)	Positive (%)
-2.1 - -1.2	-0.3343	-0.3352
-1.2 - -0.8	-0.4282	-0.4505
-0.8 - 0.0	-0.1632	-0.1651
0.0 - 0.8	-0.2904	-0.2864
0.8 - 1.2	0.3735	0.3860
1.2 - 2.1	0.0348	0.0393

Table 6.19: Systematic uncertainty on the signal model Stand-Alone muon efficiency measurements of negative muons (left) and positive muons (right)

η	$p_{\mathrm{T}} \in$ 25.0-33.0 (%)	$p_{\mathrm{T}} \in$ 33.0-40.0 (%)	$p_{\mathrm{T}} \in$ 40.0-1000.0 (%)
-2.1 - -1.2	-0.3865	0.5456	-0.0056
-1.2 - -0.8	2.6734	0.2047	0.6537
-0.8 - 0.0	0.0506	0.2477	0.1203
0.0 - 0.8	0.9843	0.1831	-0.0888
0.8 - 1.2	2.1322	-0.0398	0.2201
1.2 - 2.1	-0.2168	0.3213	0.0559

Table 6.20: Signal model systematic uncertainty in % for identification efficiency measurements of negative muons. The large systematic uncertainty in the control region results from difficulty in the describing the true Z boson shape in data in this region.

To calculate this systematic uncertainty, we fit the Breit-Wigner convolved with a crystal ball model to data and generate toy data off the shape fitted to data. The toy data is then fit with the default parametrization. The resulting bias on the efficiency is quoted as a systematic uncertainty. The values are found in tables 6.19 to 6.21. Systematic uncertainties on the signal shape modeling are smaller for the Stand-Alone efficiency than for the identification efficiency because the failing signal shape for the Stand-Alone efficiency is very similar to the passing signal shape and well fit by both models. The overall systematic uncertainty is roughly 0.5%.

6.4.4 Systematic uncertainties propagation

The systematic uncertainties are propagated into the efficiency measurement assuming full positive bin by bin correlation (*ie* we re-calculate the efficiency by adding $+|\sigma_{\mathrm{sys}}|$ to each of the bins). This maximizes the result of systematic uncertainty on the final result, ensuring coverage over final efficiency measurement. For an efficiency measurement ϵ_{ij} where each index denotes a bin $i \in \eta$, $j \in p_{\mathrm{T}}$, and per bin systematic

η	$p_T \in$ 25.0-33.0 (%)	$p_T \in$ 33.0-40.0 (%)	$p_T \in$ 40.0-1000.0 (%)
-2.1 - -1.2	-0.5845	0.6560	-0.1177
-1.2 - -0.8	0.4175	0.8423	0.0473
-0.8 - 0.0	-1.4898	0.4660	-0.0458
0.0 - 0.8	1.5943	0.1792	-0.0017
0.8 - 1.2	0.6179	0.7178	0.1162
1.2 - 2.1	-0.7247	0.1313	-0.0714

Table 6.21: Signal model systematic uncertainty in % for identification efficiency measurements of positive muons.

Efficiency Type	Scale Factor	Signal uncertainty (%)	Background uncertainty (%)
Track	1.0±0.001	0.1	0.00
Stand-Alone	0.9945±0.0024	0.34	0.17
Global	1.0±0.001	0.1	0.00
Identification	0.9842±0.0052	0.24	0.45
Trigger	0.9677±0.0060	0.00	0.00
Combined	0.9426±0.0080	0.40	0.46

Table 6.22: Summary of scale factors and systematic uncertainties for Positive Muons

uncertainty σ_{ij}, the total systematic uncertainty, σ_{tot}, is written as

$$\sigma_{tot} = \sum_{ij} f_{ij}\sigma_{ij} , \tag{6.21}$$

where f_{ij} is the relative fraction of W boson events per each bin. In the case where multiple un-correlated uncertainties exist for a given bin (σ_{1ij} and σ_{2ij}) the uncertainty in each bin is given by adding in quadrature all of the uncertainties in each bin, and then summing over the uncertainty assuming full correlations.

$$\sigma_{tot} = \sum_{ij} f_{ij}\sigma_{1ij} \oplus \sigma_{2ij} . \tag{6.22}$$

This contrasts with statistical uncertainties, which are uncorrelated between bins, thus requiring one add them in quadrature.

The final results of the systematic uncertainty weighted to W boson kinematics (f_{ij} for W bosons) are shown in tables 6.22 and 6.23. The overall systematic uncertainties are slightly less than one percent, which is comparable with the theory and signal extraction uncertainties.

Efficiency Type	Scale Factor	Signal uncertainty (%)	Background uncertainty (%)
Track	1.0±0.001	0.1	0.00
Stand-Alone	0.9923±0.0024	0.23	0.27
Global	1.0±0.001	0.1	0.00
Identification	0.9823±0.0059	0.24	0.41
Trigger	0.9654±0.0056	0.00	0.00
Combined	0.9364±0.0083	0.32	0.46

Table 6.23: Summary of scale factors and systematic uncertainties for Negative Muons

6.5 Summary

The efficiency for the muon selection defined in chapter 5 is measured here. We divide the efficiency into five separate components and perform the "tag and probe" method on all five efficiencies using Z boson events. Two efficiency measurements drive the systematic uncertainty: the Stand-Alone muon and the identification and isolation efficiency. The Stand-Alone muon efficiency has a large background contamination, which leads to a large systematic uncertainty on the background contribution. The identification and isolation efficiency is sensitive to poorly simulated events, which fail the identification and isolation cuts. This leads to a large systematic uncertainty on the signal modeling. The final efficiency is quoted as a scale factor to the Monte Carlo simulated efficiency κ for positive and negative muons:

$$\kappa_+ = 0.9426 \pm 0.0080(\text{stat}) \pm 0.0064(\text{sys}) \ , \tag{6.23}$$

$$\kappa_- = 0.9364 \pm 0.0083(\text{stat}) \pm 0.0066(\text{sys}) \ . \tag{6.24}$$

Chapter 7

Muon Energy Scale and Resolution

The W and Z boson selections require the lepton p_{T} to be above a specified threshold, thus knowledge of the true scale of the reconstructed p_{T} and its resolution directly impact the final cross section measurement.

The muon p_{T} and resolution is determined from hits in the tracker. Any deviation in the recorded position versus the true position of the tracker hit on the silicon module leads to a degraded resolution of the p_{T} measurement. In order to minimize the effect of a misplaced silicon module, a technique to align tracker modules is performed. The technique relies on minimizing the χ^2 for a given track by modifying the momentum and the silicon positions within a tolerance level [80]. The combination of many track measurements determine a minimization that is either fit globally for all tracker modules and track parameters (Millipede II algorithm [81]) or iteratively through updates on the global positions with a Kalman filter (HIP algorithm [82]). Both methods have been found to be very effective at eliminating large deviations between the expected and true position of the silicon modules. However, pathological modes can form whereby systematic shifts in the modules yield zero change in χ^2 of the fitted track. Such variations (where $\Delta\chi^2 = 0$) are called weak modes.

Weak modes consist of shifts of a large group of silicon modules, such as a rotation in ϕ of all modules in positive η (twist mode). Weak modes in the tracker are very difficult to eliminate with the current alignment algorithms. The only known way is to adjust modules by informed guessing. To understand the energy scale and resolution of the existing tracker alignment, a strategy was developed to measure and correct the weak mode effects on the final muon kinematics. As with tag and probe, the strategy relies strongly on the fitting the Z boson mass line shape over specified muon η and ϕ regions to deduce the variations in the energy scale and resolution.

In this chapter, two muons are selected which match the criteria of a well identified, isolated muon as used in the W$\rightarrow \mu\nu$ signal selection. The mass of the two leptons is required to be 60 GeV/c^2 $< m_{\ell\ell} <$ 120 GeV/c^2 ensuring good selection of Z bosons. This selection is chosen to enable a reliable determination of the muon energy scale and resolution for W boson events.

7.1 Fitting Z boson mass

In chapter 6, we presented two fit models, which describe the Z mass line shape well. In this section, two models similar to the previous fit models are used to determine the energy scale and resolution. The functions are slightly different so that two necessary parameters, the energy scale and the resolution can be extracted dexterously and applied to Monte Carlo simulation to assess systematic uncertainties from the scale and resolution. Each fit assumes that both the energy scale is roughly independent of p_{T} and the muon resolution is modeled by a Gaussian. Both these assumption are well motivated by studies with Monte Carlo simulation and fits to the data [53].

7.1.1 Parametrization one: Voigtian with a crystal ball tail

The default fit function is similar to the Breit-Wigner convolved with crystal ball parameterization used previously in chapter 6. The Breit-Wigner convolved with crystal ball parametrization models the data well; however, the convolution, which is performed through a numerical Fourier transform, is too computationally intensive to be used in a fit of the energy scale. In place of using a crystal ball convolved with a Breit-Wigner, we subdivide the crystal ball into its two separate components: a Gaussian, and a polynomial. This gives two functions a Gaussian convolved with a Breit-Wigner and a polynomial convolved with Breit-Wigner. The Gaussian convolved with a Breit-Wigner is replaced by an analytic Gaussian convolved with Breit-Wigner known as a Voigtian distribution. This is written as

$$V\left(m_{\ell\ell};\sigma,\Gamma\right) = \frac{Re\left[e^{-z^2}1-erf\left(z\right)\right]}{\sigma\sqrt{2\pi}}\text{, where } z=\frac{m_{\ell\ell}+i\Gamma}{\sigma\sqrt{2}}\,. \tag{7.1}$$

The second component, a decaying polynomial convolved with a Breit-Wigner is approximated as a polynomial. This follows by considering the convolution, $C\left(m_{\ell\ell}\right)$ of the crystal ball polynomial with a Breit-Wigner,

$$C\left(m_{\ell\ell}\right) = \int_{-\infty}^{+\infty} dx' \frac{\Gamma}{\pi\left(\left(x-x'\right)^2+\Gamma^2\right)\left(K-\frac{x'-m_{\ell\ell}}{\sigma}\right)^n}\,. \tag{7.2}$$

The convolution of the two components is dominated by the instances where one of the denominator components is near zero. This is well approximated by a polynomial (when n in the crystal ball is > 1).

$$C\left(m_{\ell\ell}\right) \approx \frac{A}{\left(B+m_{\ell\ell}\right)^n}\,. \tag{7.3}$$

Taking this approximation, we stitch the Voigtian together with $C\left(m_{\ell\ell}\right)$ to make a simplified model of Z boson mass line shape consisting of Voigtian with a crystal ball

like tail,

$$f(m_{\ell\ell}) = N \cdot \begin{cases} V(m_{\ell\ell};\sigma,\Gamma) & \text{for } \frac{x-\bar{x}}{\sigma} > -\alpha \\ A\left(B - \frac{x-\bar{x}}{\sigma}\right)^{-n} & \text{for } \frac{x-\bar{x}}{\sigma} \leq -\alpha \end{cases}, \tag{7.4}$$

$$A = \left(\frac{n}{|\alpha|}\right)^2 \cdot \exp\left(-\frac{|\alpha^2|}{2}\right), \tag{7.5}$$

$$B = \frac{n}{|\alpha|} - |\alpha|, \tag{7.6}$$

where α is a floated parameter that describes the introduction of the polynomial in units of the width, σ, from the peak of the voigtian distribution.

The choice of this fit function allows for fast convergence over likelihood fits of many variables. Figure 7-1 shows a fit to the inclusive Z mass line shape in data using the Voigtian with a crystal ball function. The fit describes the data well over the whole mass range.

In order to perform the fit in smaller bins of η the two tail parameters α and n are fixed to the inclusive measurement. Fixing the tail parameters describes the Z line shape well for $|\eta| < 1.5$. Further out in η a small disagreement in the tail is present. This disagreement is a consequence of both fixing the tail parameters and non-Gaussian tails in the p_{T} resolution. To determine the scale of this effect 2500 toy data samples using the simulated Z mass line shape at different energy scales and resolutions were generated and fit. The resulting bias for energy scale variations of both one and two percent was found to be within 0.04 percent the true energy scale and 0.2 GeV/c^2 in the resolution for additional smearing of up to 5 GeV/c.

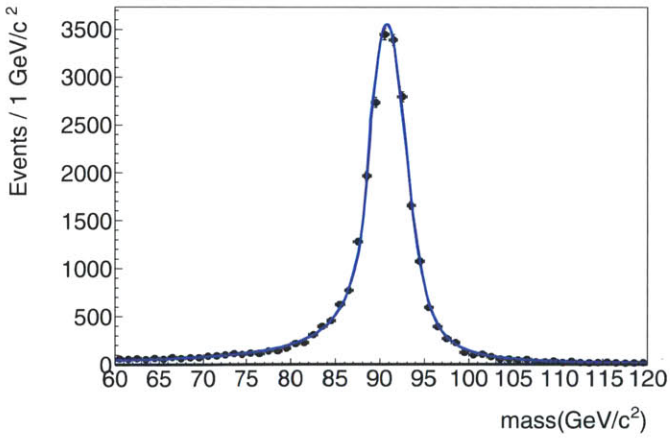

Figure 7-1: Fit of Voigtian with crystal ball tail to Z boson data

7.1.2 Parametrization two: Monte Carlo simulation convolved with a Gaussian

As a cross check to the previous fit function (parametrization one) we consider a Gaussian convolved with Monte Carlo simulation :

$$f(m_{\ell\ell}) = f_{\mathrm{mc}}(\lambda m_{\ell\ell}) \otimes G(0,\sigma), \tag{7.7}$$

where in this case f_{mc} is the predicted Monte Carlo simulated shape of the mass, λ is the energy scale of the reconstructed leptons, and σ is the additional smearing to the Monte Carlo simulated mass shpe. This function differs from the Monte Carlo simulated mass shape convolved with Gaussian function used in section 6 in that a re-scaling, λ, is applied to the mass function as opposed to a linear shift in the mean of the Gaussian, G. Use of λ in the fit is more physical than a shift in the Gaussian mean because a mismeasurement causes the p_{T} to scale incorrectly. A fit to the inclusive data using this function is shown in figure 7-2. The fit over all data yields an additional smearing on the p_{T} of 0.1 GeV/c^2 and a scale of 1.001, indicating good agreement between the inclusive data line shape and the simulated line shape.

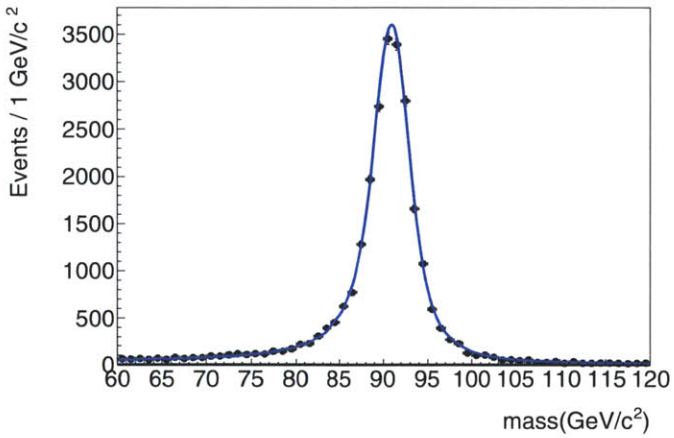

Figure 7-2: Fit of the Monte Carlo simulatied mass shape convolved with a Gaussian to Z boson data

7.2 Weak modes in the tracker

Figures 7-1 and 7-2 both indicate that the fitted Z mass is within 0.1 percent of the world averaged value. This is not surprising because the alignment of the tracker yields excellent overall energy scale resolution. However, summing over the ϕ and η coordinates of the leptons minimizes the effect of weak modes. To separate out these effects, we consider the energy scale variation over η, ϕ, and charge. This is performed

by fitting for the combined mass of the two muons for all events where the negative or positive muon within a designated η or ϕ range (*ie* $0.8 < \eta < 1.2$) is binned and fitted.

Figure 7-3 shows the results for the mass variation as a function of ϕ of the positive and negative lepton. Both fit methods show a clear sinusoidal variation in ϕ. This variation has been determined to be a result of a global twist of modules about the z axis of the detector [72].

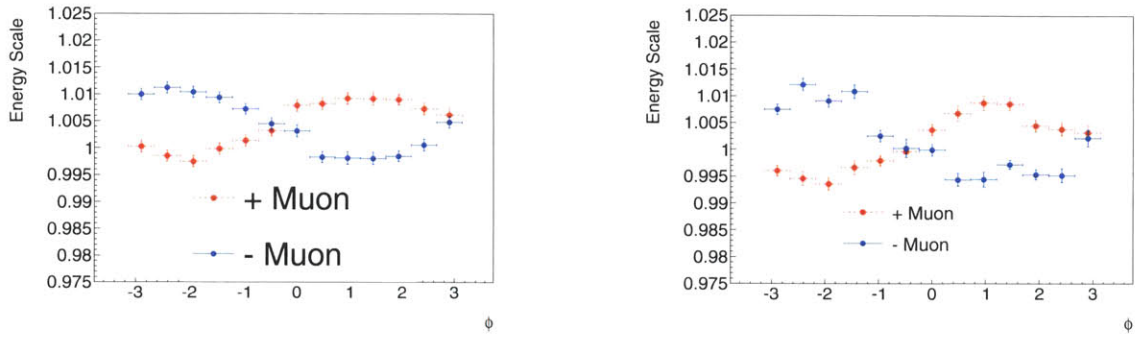

Figure 7-3: Energy scale variation as a function of ϕ obtained from fits using a Voigtian with a crystal ball tail (left) and Monte Carlo convolved with a Gaussian (right).

The η variation of the leptons is found in figure 7-4. The energy scale varies one percent over the whole range of η. This variation roughly follows a third order polynomial, where the scale deviates either high or low depending on the sign of the muon and the sign of η. The cause of the η variations in the data is at present unknown.

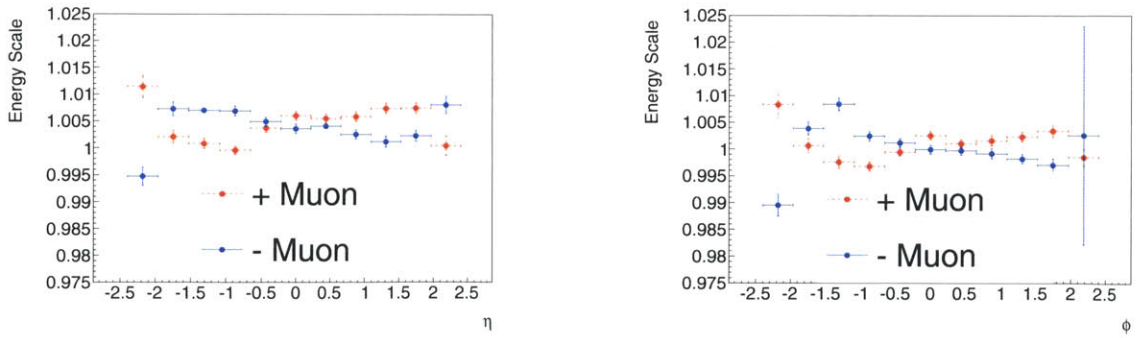

Figure 7-4: Energy scale variation as a function of η obtained from fits using a Voigtian with a crystal ball tail (left) and Monte Carlo convolved with a Gaussian (right).

In addition to the energy scales, the resolutions, and additional smearing for the two fit models are shown in figure 7-5. The resolutions are found to be near 1.5 GeV/c^2.

This poses a problem for the Monte Carlo simulation convolved with Gaussian fit, because the resolution in Monte Carlo simulation is found to be about 0.1 GeV/c^2 higher at 1.6 GeV/c^2. The convergence of the resolution parameter in the Monte Carlo simulation convolved with Gaussian fit model is thus ill defined. From figure 7-5, we find the muon resolution variation in η gets worse with η due to the increased scattering caused by additional material in the tracker at high η. The variation is roughly flat until $\eta \approx 1.5$ and then increases to near 2.5 GeV/c^2 in the endcaps. The resolution between positive and negative muons is within one standard deviation over the whole range. Hence, for the rest of this thesis we assume the resolution to be the same in both charges.

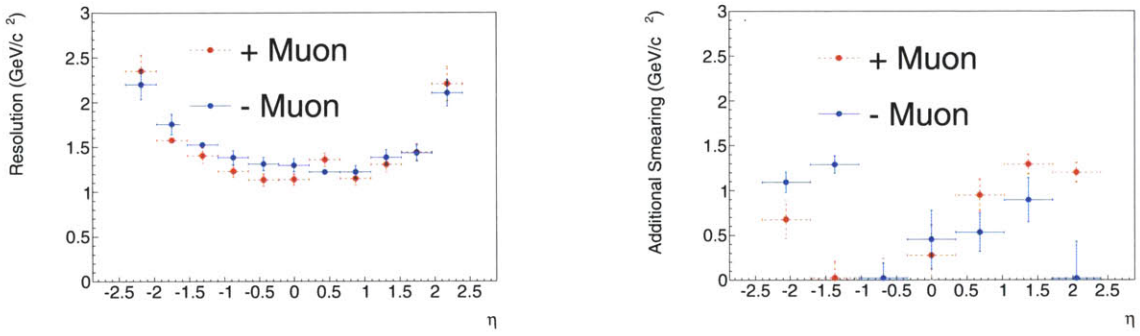

Figure 7-5: Resolution as a function of η obtained from fits using a Voigtian with a crystal ball tail (left) and Monte Carlo convolved with a Gaussian (right).

7.3 Fit to energy scale corrections

To determine the energy scale, we simultaneously fit the mass distribution over the coordinates of both the positive and negative muon. The fit is performed simultaneously on the scale of both leptons so as to eliminate biases in the mass distribution that are caused by correlations in the kinematics. To understand this effect consider the binned plots in figure 7-3. The energy scale for a specific bin ϕ_i is a combination of negative muons with a specified $\phi \in \phi_i$ and some distribution of positive muons with $\phi \in -\pi, \pi$. The distribution in the second lepton shifts the mass of the Z boson up or down depending on which values of ϕ the positive muons have.

Although integration over the second lepton's coordinates lead to biases, we assume no bias between ϕ and η scale variations. Thus, we fit separately for the ϕ, η scale, and resolution variations. The fit of the two functions are thus performed over three dimensions: the *mass distribution*, and either η or ϕ of the *positive* and *negative*

muon. This is written as:

$$F\left(m_{\ell\ell}|\phi_+,\phi_-,\sigma\right) = V\left(m_{\ell\ell}\sqrt{f_+\left(\phi_+\right)f_-\left(\phi_-\right)},\sigma\right) , \quad (7.8)$$

$$F\left(m_{\ell\ell}|\eta_+,\eta_-,\sigma\right) = V\left(m_{\ell\ell}\sqrt{f_+\left(\eta_+\right)f_-\left(\eta_-\right)},\sigma\left(\eta_+,\eta_-\right)\right) , \quad (7.9)$$

where f_{i} are the energy scale functions of the lepton with charge i and V is the modified Voigtian fit parametrization. The two functions $F\left(m_{\ell\ell}|a_+,a_-,\sigma\right)$ describe the the Z mass line shape conditional on the value of the parameters ϕ_{i} or η_{i}, and the resolution σ. The choice of using a conditional parametrization as oppose to a full 3-dimensional parametrization in the fit removes the necessity for a probability distribution over the conditional parameters. The final likelihood minimization in the fit is performed using an unbinned maximum likelihood estimator.

In addition to the energy scale f, the resolution σ is also floated when fitting over η. The form of the function is given by

$$\sigma\left(\eta_+,\eta_-\right) = \sqrt{\sigma_+^2\left(\eta_+\right)+\sigma_-^2\left(\eta_-\right)} \quad (7.10)$$

Floating the resolution simultaneously with the energy scale removes any systematic biases, which are present if they are fit independently.

In light of making the simulation as realistic as possible weak modes are inserted in both the η and ϕ scale variation of the simulation. Corrections for the energy scale mis-alignments in simulated events is performed with the same fit used on data. In the following sections, we discuss the choice of parametrization and the ensuing results. The results are shown for both the data and Monte Carlo simulated corrections.

Following the determination of the energy scale, the resulting fit parameters are then be used to determine the corrected lepton p_{T} by rescaling the corresponding energy,

$$p_{\mathrm{T}}^{corrected} = p_{\mathrm{T}}/f_{\mathrm{i}}\left(\eta_{\mathrm{i}},\phi_{\mathrm{i}}\right) . \quad (7.11)$$

7.3.1 Scale variation in ϕ

The ϕ scale variation fit is performed for the Z boson mass distribution over the two coordinates ϕ_+ and ϕ_- of the charged muons resulting from the Z boson decay. To fit for the ϕ variations, the resolutions are held fixed to a value σ determined by a fit to the inclusive data sample. The fit is then performed over the data for the function in 7.8 using a mass function given by

$$m_{\ell\ell}\left(\phi_+,\phi_-\right) = m_{\mathrm{Z}}\sqrt{f_+\left(\phi_+\right)f_-\left(\phi_-\right)}+c \quad (7.12)$$

$$m_{\ell\ell}\left(\phi_+,\phi_-\right) = m_{\mathrm{Z}}\sqrt{\left(1+a_+\sin\left(\phi_++b_+\right)\right)\left(1+a_-\sin\left(\phi_-+b_-\right)\right)}+c \quad (7.13)$$

where m_{Z} is the world averaged Z boson mass, a,b,c are floated parameters, and the underscores correspond with the respective charge of each lepton performed in the fit. The choice of a sinusoidal form for the energy scale functions f is motivated by

the large weak mode observed in ϕ (figure 7-3)

Figure 7-6 shows the energy scale functions f_+ and f_- in ϕ_+, ϕ_- (lines) from the simultaneous fit over the two variables compared to fits binned over a single lepton ϕ (data points discussed section 7.2). The binned fits are expected to be different from the simultaneous fits because binning and fitting induces a bias resulting from kinematic correlations from the binned muon with the second muon in the Z boson decay.

Binned fits to the Z boson mass with energy scale corrections from the fit applied, are shown in the bottom of figure 7-6. Once the corrections are applied, the energy scale variation is found to be flat over the whole ϕ range in both data and Monte Carlo simulation. In order to span the residual variations after corrections are applied an overall energy scale systematic uncertainty is taken to be 0.004 (green band).

The fitted parameters are shown in table 7.1. The parameters, determined from fits to simulation, are nearly symmetric between positive and negative leptons. This is most clear in the angular shift parameter b, which is $\approx$ 1.3 for both charges. The parameters determined from fits to data, on the other hand, are found to be asymmetric, with a scale variation much larger for the positive muon.

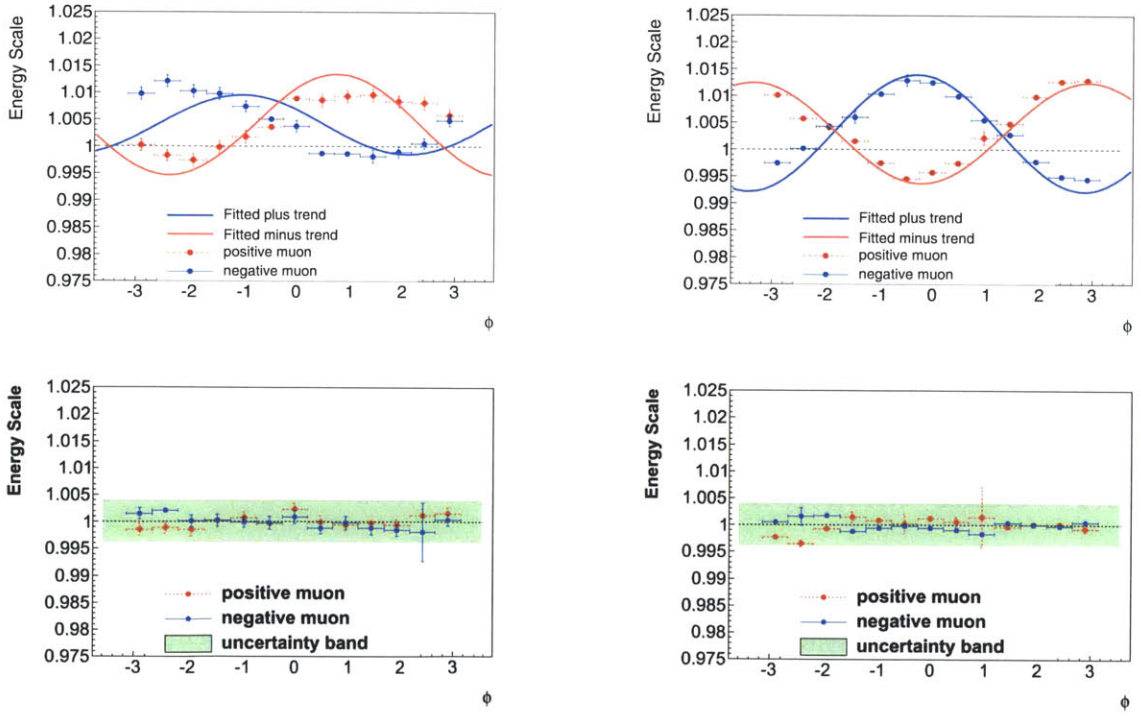

Figure 7-6: Energy scale shift as a function of ϕ obtained from the fit of the two charged leptons (line) compared with the fits binned in a single lepton ϕ. The fits are plotted for the data (top left) simulation (top right). The bottom plots show the binned fit results after the application of the energy scale corrections.

name	Simulation	Data
a_+	-0.0109±0.002	-0.0055±0.0015
a_-	0.0094±0.0018	0.0094±0.0015
b_+	-1.279±0.27	-0.540±0.28
b_-	-1.362±0.25	0.806±0.17
c (GeV/c^2)	0.28±0.02	0.37±0.02

Table 7.1: Best fit parameters to data and simulation following the parameter naming scheme used in equation 7.12.

7.3.2 Scale variation in η

The variation in the energy scale as function of η is determined by fitting simultaneously the energy scale and the resolution of each lepton. To model the energy scale, a third order polynomial in η is chosen. This is motivated by the shape of the variation in figure 7-4. The form of the energy scale variation of the Z mass in equation 7.9 is thus written as

$$m_{\ell\ell}(\eta_+,\eta_-) = m'_{\mathrm{Z}}\sqrt{f_+(\eta_+)\,f_-(\eta_-)} + c \tag{7.14}$$

$$m_{\ell\ell}(\eta_+,\eta_-) = m'_{\mathrm{Z}}\sqrt{(1+a_+\eta+b_+\eta^2+c_+\eta^3)\,(1+a_-\eta+b_-\eta^2+c_-\eta^3)} + c \tag{7.15}$$

where a, b, c are the parameters floated in the fit. The η fit is performed after the fit to the ϕ scale and the corrections to the mass based on the ϕ scale are applied; this is designated by m'_{z} in place of m_{Z}. Applying the ϕ corrections minimizes the correlation between η and ϕ by ensuring the scale variation in ϕ is nearly constant. In the fit, the resolution of the two leptons is floated along with the energy scale over η, utilizing the form given in equation 7.17. The results of the resolution are discussed in section 7.3.3. Also in the fit, the tail parameters α and σ_2 are fixed to a fit over the whole dataset. Fixing of parameters in the fit induces biases in the resulting energy scale measurement. Biases on the energy scale from fixing these tail parameters was determined from fits to toy data samples to be less than 0.1%.

Figure 7-7 shows the comparison of the binned fits (points) with the fits performed simultaneously in η_+, η_- (line). The binned fit deviates more from the full two variable fit than in the ϕ case because the Z kinematics in the detector acceptance window force an asymmetry in the correlated η_+, η_- distribution by requiring one lepton to be at lower η. The corrections, shown on the bottom of figure 7-7, show that for $|\eta| > 2.1$, the third order polynomial description of the energy scale variation breaks down. This region in η is outside the kinematic acceptance used for the W boson selection, thus it is safely ignored. After corrections, the final scale variation in the selected region of $|\eta| < 2.1$ is found to be well within the ±0.004 scale uncertainty band.

The fit parameters are shown in table 7.2. The final results have a strong dependence on the odd order polynomials, making the scale variation for positive muons high at positive η and low at negative η.

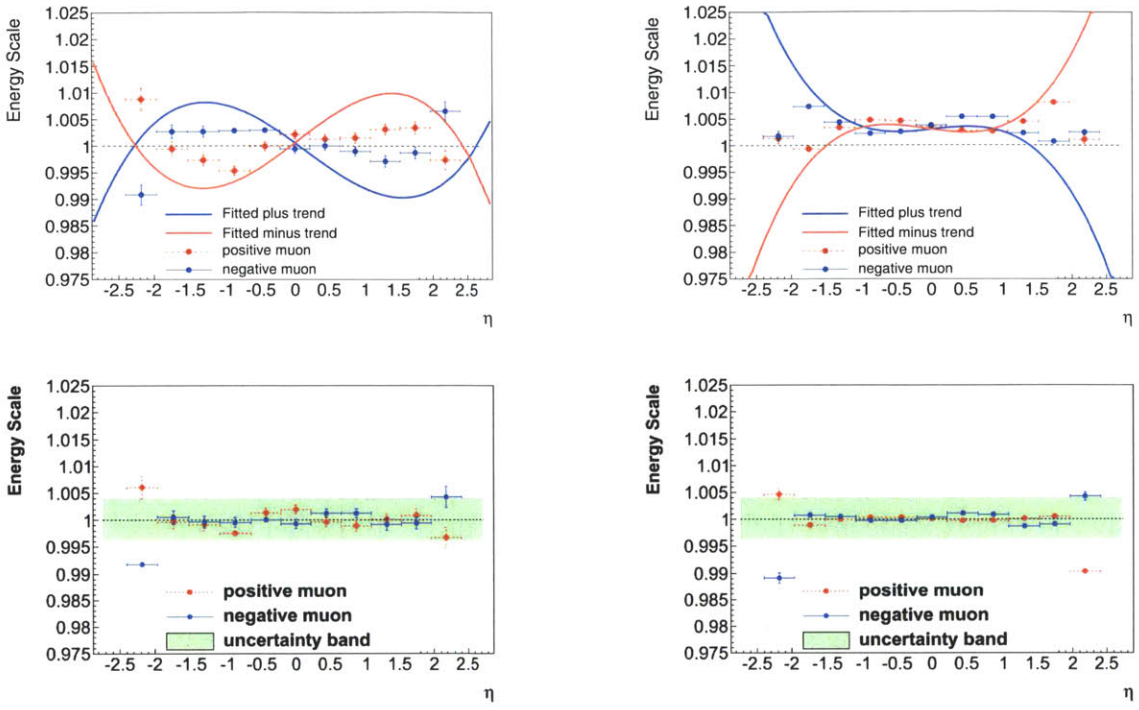

Figure 7-7: Energy scale variation as a function of η obtained from the fit simultaneous on the postive and negative leptons (line) compared with the fits binned in one of the lepton coordinates (point). The lines do not follow the points (binned) exactly due to a kinematic bias in the binned fits. This is performed for data (top left) simulation (top right).

7.3.3 Fit to resolutions

The resolution is determined simultaneously with the η energy scale variation. To model the resolution a fourth order polynomial is used while fixing the resolution functions of both the positive and negative leptons to be the same. The form of the fitted resolution function used in the fit function 7.9 is given by:

$$\sigma(\eta) = \sigma_0 + a\eta + b\eta^2 + c\eta^3 + d\eta^4 , \tag{7.16}$$

$$\sigma(\eta_+, \eta_-) = \sqrt{\sigma(\eta_+)^2 + \sigma(\eta_-)^2} , \tag{7.17}$$

where the parameters a, b, c, d are floated.

In figure 7-8, the fitted resolutions to Monte Carlo simulation and data are compared (along with the binned fits). The fitted resolutions are both very close in shape and follow the trend of the binned fits well. To gauge the level of agreement a band corresponding to adding or removing 0.5 GeV/c^2 of smearing around the simulated resolution is plotted. This band covers both the fitted points and the data function for $|\eta| < 2.0$. This band is used as the systematic uncertainty on the resolution

name	Simulation	Data
a_+	0.0014±0.0005	-0.0093±0.0018
a_-	-0.0019±0.0000	0.0098±0.0019
b_+	0.00012±0.00034	-0.00064±0.00012
b_-	0.00042±0.00036	0.00022±0.00005
c_+	-0.0019±0.0004	0.0016±0.0003
c_-	0.0020±0.0004	-0.0018±0.0003
c (GeV/c^2	0.27±0.06	0.05±0.02

Table 7.2: Best fit parameters to and simulation following the parameter naming scheme used in 7.14.

name	Simulation	Data
σ_0 (GeV/c^2)	1.40±0.02	1.30±0.02
a	0.0854±0.0171	0.0035±0.0163
b	-0.091±0.018	-0.012±0.011
c	-0.047±0.009	-0.014±0.006
d	0.057±0.0011	0.037±0.007

Table 7.3: Best fit parameters to data and simulation following the parameter naming scheme used in 7.17.

measurement.

Results of the fit parameters are presented in table 7.3; because the resolution appears to be sign independent, the odd polynomial terms, a and c are small. The resolution at $\eta = 0$, σ_0, is 1.40 GeV/c^2 in simulation and 1.30 GeV/c^2 in data. Thus, to obtain the same resolution in data and simulation, one must smear the generator level lepton p_{T}. Smearing the generator lepton p_{T} with a Gaussian poses a difficulty because non-Gaussian tails of the resolution function, which are well simulated, will not be modeled by smearing with a Gaussian. We do not apply any additional smearing because the difference in the resolution between simulation and data is within 0.5 GeV/c^2.

7.4 Systematic uncertainties

The systematic uncertainties on the energy scale fits result from assumptions on the fit model to describe the mass distribution, the η and ϕ variation, and the resolution variation. The effectiveness of the mass distribution parametrization to measure the proper energy scale and resolution is discussed in the fit validation section (7.4.1). The systematic uncertainties of the parametrizations of the energy scale and the resolution over ϕ and η is discussed in section 7.4.2 and section 7.4.3 respectively.

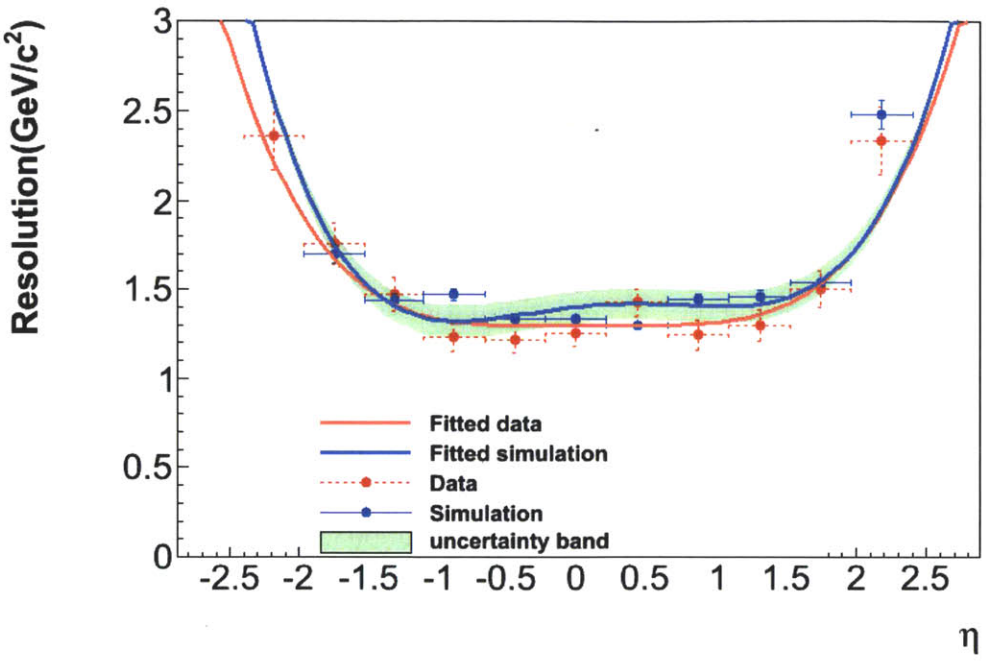

Figure 7-8: Comparison of the fitted resolutions between data (blue) and simulation (red) using both the simultaneous fit in both lepton parameters (line) and the fit binned in η of the specified lepton (points). The green band corresponds to adding or removing a smearing of 0.5 GeV/c^2.

7.4.1 Fit validation

Before one considers the systematic uncertainty on the energy scale and the resolution, the measured energy scale and resolution using the Voigtian crystal ball model needs to be consistent with the true energy scale and resolution. This is particularly important for the resolution where biases in the resolution are induced due to fixing the tail parameters in the fit.

To validate the energy scale variation a series of 5000 toy data samples were generated from the simulated Z boson mass distribution where the energy was scaled up and down by either 1 or 2 percent. Each toy data set is then fit with the Voigtian crystal ball tail model and the energy scale and resolutions are extracted from the fit. The resulting central value of the fit parameters averaged over all the fits to the toy data samples shows a bias of ≤ 0.05 percent on the energy scale returned from the fit.

The resolution was tested by generating and fitting 5000 toy data samples of the simulated Z boson mass with additional Gaussian smearing applied. The mean of the resulting resolution parameter is compared with the true smearing in figure 7-9. The predicted smearing follows the simulated smearing to within a few percent.

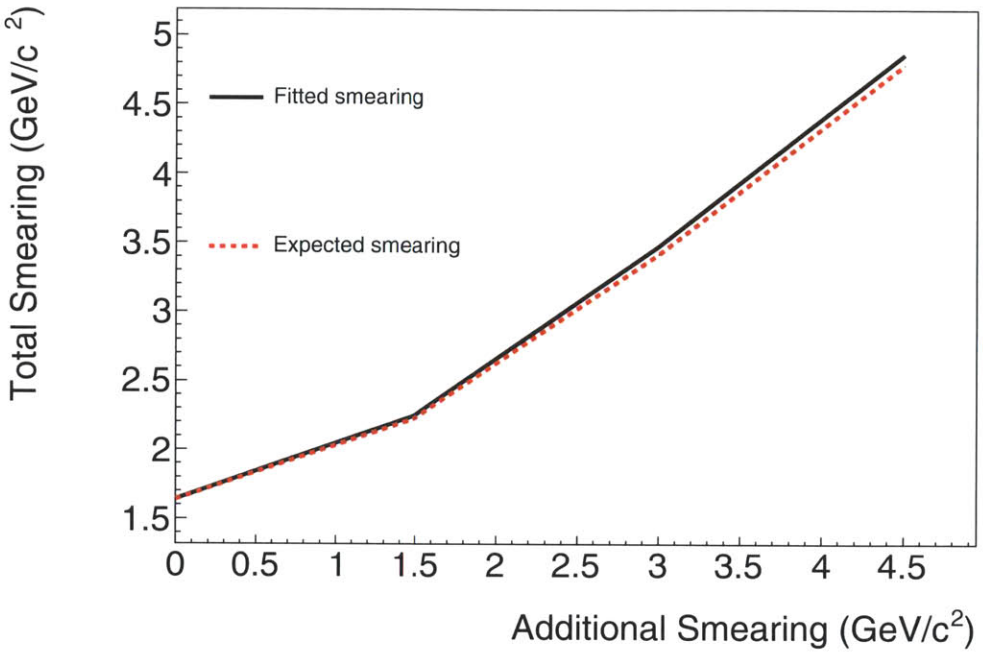

Figure 7-9: Comparison of the true smearing of toy data samples with the mean over 5000 toy data samples of additional smearing determined from the fit.

7.4.2 Scale uncertainty

The systematic uncertainty on the muon energy scale arises from two places: the fit uncertainty, effectiveness of the model to describe the data. The fit uncertainty for the the η and ϕ scale is determined from the uncertainties on the parameters of the fit model. It contributes to scale variations less than 0.001. The effectiveness of energy scale models (a sinusoid in ϕ and a cubic in η) to describe the true variation is difficult to assess. Typically, this is addressed by adding additional terms to the fitted model or trying alternative fit models. In this case, the uncertainty is assessed by looking at the binned fit variation over the range of η and ϕ of the two charged leptons after corrections are applied. The mass variations after corrections are shown in figures 7-6 and 7-7. After corrections the bin per bin variations are less than 0.002 in scale variation. Hence, we determine the systematic uncertainty by placing a band which covers all variations, we conservatively use an overall scale variation of 0.004.

7.4.3 Resolution uncertainty

The affect of the resolution on the acceptance and data is determined with the resolution in Monte-Carlo simulation. Thus, the resolution uncertainty is determined by considering a band around the Monte-Carlo simulation, which spans the fitted resolution in data. This is found to correspond with an additional 0.5 GeV/c^2 of smearing.

The uncertainty band for the resolution if shown in 7-8.

7.5 Extrapolation of corrections

The final fit to the energy scale and resolutions are propagated to the W boson by applying the energy scale corrections lepton per lepton (equation 7.11). The systematic uncertainties are taken by rescaling the corrected lepton energy by ± 0.004. The resolution uncertainty is done in the same manner by additionally smearing the simulation, or when the resolution in data is better than simulation, by smearing the generator level boson p_{T}.

As a final cross check of the energy scale, in figure 7-10 we plot the Z mass shape before and after corrections on data and simulation. The final corrections are noticeably better when both leptons have $|\eta| < 1$. This plot is not the most effective because the effects of the scale variation is small on Z bosons due to a cancellation of the energy scale when positive and negative muons are combined.

7.6 Summary

In conclusion, we have developed a fully analytic parametrization of the Z mass line shape, which enables a three dimensional fit of the line shape as a function of either the η or ϕ coordinate of each charged lepton. The resulting fit parameters yield a correction to the energy scale and resolution, which eliminate energy scale variations beyond 0.004. The final systematic uncertainty on energy scale and resolution after corrections is found to be:

$$\sigma_{\mathrm{scale}} = 0.004 \,, \tag{7.18}$$

$$\sigma_{\mathrm{res}} = 0.5 \text{ GeV}/c. \tag{7.19}$$

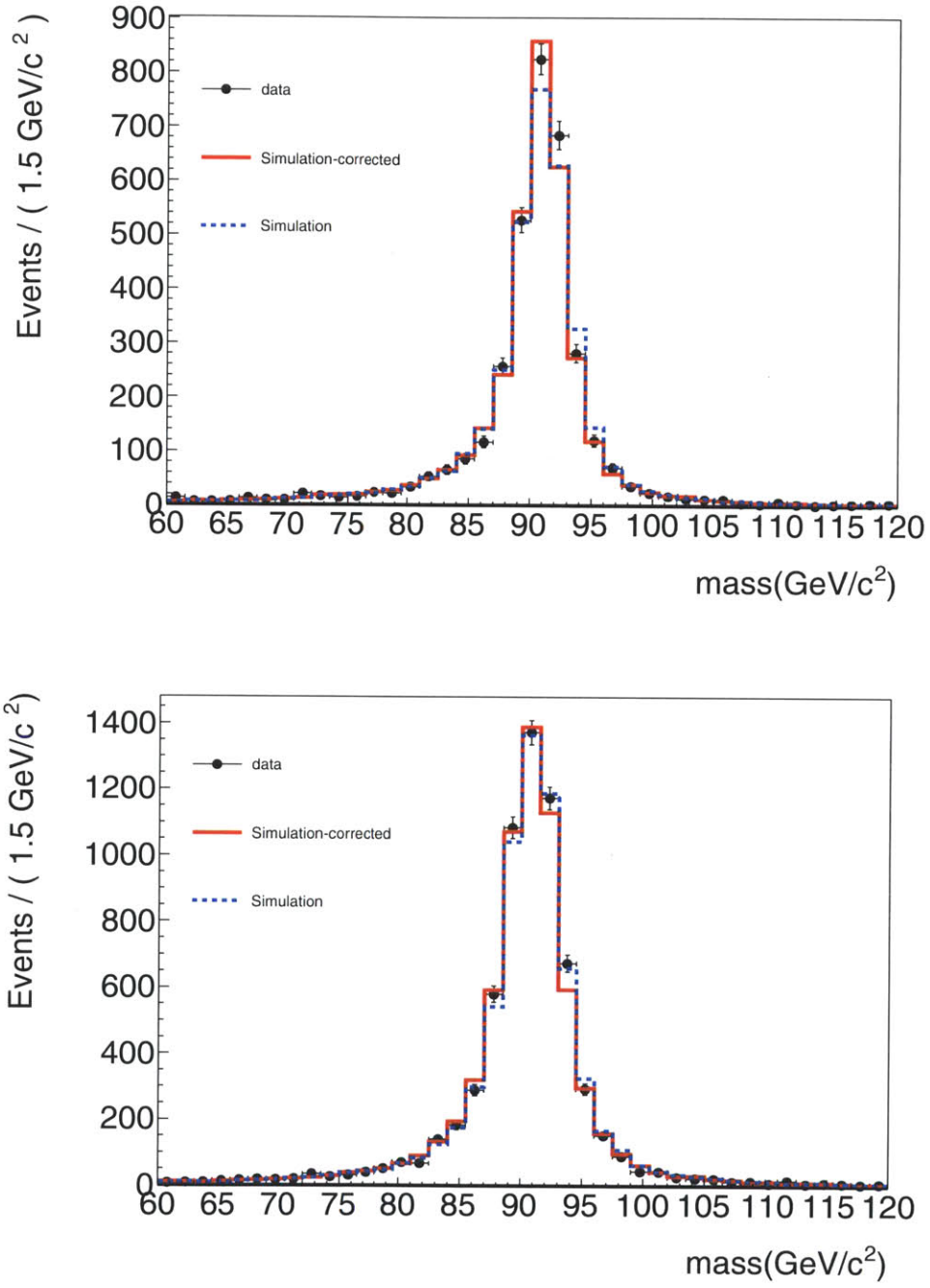

Figure 7-10: Comparison of the dilepton data mass shape with Z boson simulation before (blue dashed line), after (red solid line) data and simulation energy scale corrections are applied. The top plot requires both leptons to have $|\eta| < 1$ the bottom consists of the inverse sample where $|\eta| > 1$ for at least one of the leptons.

Chapter 8

Theoretical Modeling

The theoretical modeling of the W and Z bosons plays an important role in the cross section calculation. First of all, the limited coverage of the detector implies certain regions of phase space are inaccessible to muon reconstruction. Thus, an extrapolation from the reconstructed region to the full region is necessary. This extrapolation is performed with the acceptance measurement. Secondly, the cross section measurement relies on a shape, determined from theoretical modeling of an event simulated in the CMS detector. Uncertainties in the theoretical modeling of the shape increase the uncertainties in the final measurement. In this chapter we address the impact of the uncertainty of the theoretical calculations on the impact of these measurements on the final cross section result.

8.1 Acceptance

The acceptance is used to extrapolate the cross section in the fiducial detector region to the fully inclusive value. It is defined as the fraction of kinematic phase space of the final observables over the total allowable region. This is written as:

$$a = \frac{1}{\sigma_0} \int_{\text{allowed region}} dp_{\mathrm{T}}^{\ell} d\eta_{\ell} \frac{d\sigma}{dp_{\mathrm{T}}^{\ell} d\eta_{\ell}} \tag{8.1}$$

For the W analysis, a cut on final kinematic observables is typically performed on either $\not\!\!E_{\mathrm{T}}$, the lepton kinematics $p_{\mathrm{T}}^{\ell}, \eta^{\ell}$ or a combination of these parameters. For this analysis, the kinematic cuts on the leptons is determined by minimizing the theoretical uncertainty on the acceptance. The uncertainty on the differential cross section originates from three sets of effects.

- QCD effects
- Electroweak effects
- Parton distribution effects

The optimal acceptance cut is determined, in part, by minimizing our theory uncertainty modelling, is found to be:

$$p_{\mathrm{T}} > 25 \text{ GeV}/c \text{ and } |\eta| < 2.1 \tag{8.2}$$

A cut on the $\not\!\!E_{\mathrm{T}}$ increases the acceptance uncertainty by an additional percent because of the inclusion of the uncertainty on the $\not\!\!E_{\mathrm{T}}$ modeling and the additional theoretical uncertainty from a second lepton cut, thus it is not used in this thesis. The value for the acceptance is determined with the W boson Monte Carlo generator known as Powheg [75]. Applying equation 8.1, we find for $\mathrm{W}^{\pm}$:

$$a_{\mathrm{W}^+} = 0.4109 \pm 0.0004 \tag{8.3}$$

$$a_{\mathrm{W}^-} = 0.4004 \pm 0.0004 \tag{8.4}$$

where the uncertainty is the statistical uncertainty from the Monte Carlo simulation.

In the past decade, due to the inclusion of higher order calculations, the theoretical understanding of W and Z boson production has improved considerably. In the following sections, we outline the impact of the higher order corrections by first presenting the leading order cross section formula and then progressively adding in corrections coming from the higher order perturbative calculations. By progressively adding in the different contributions to the final cross section, we mean to build up the intuition in use of the theoretical framework. This intuition leads to an assessment of the uncertainties on of the acceptance calculation and the differential distributions of the boson decay.

8.1.1 Leading order W cross section

W boson production is a Drell-Yan process. Drell-Yan production is an s-channel process, whose interaction proabaility is that of a Breit-Wigner form mass resonance about the mass of the boson. This is then convolved with the parton density functions in the proton over the varibles x_1 and x_2 , which describe momentum fraction x_{i} of a proton. To give the differential cross section in terms of the energy of production, $\frac{d\sigma_{\mathrm{tot}}}{dQ}$, as

$$\sigma_{\mathrm{i}}\left(x_1, x_2, Q^2\right) = \frac{\pi g_{\mathrm{w}}}{12\hat{s}x_1x_2}|V'_{\mathrm{qq}}|^2 \frac{Q^2}{\left(Q^2 - M_{\mathrm{W}}^2\right)^2 + Q\Gamma_{\mathrm{W}}^2/M_{\mathrm{W}}^2} \tag{8.5}$$

$$\frac{d\sigma_{\mathrm{tot}}}{dQ^2} = \int dx_1 dx_2 f_{\mathrm{q}}\left(x_1, Q^2\right) f'_{\mathrm{q}}\left(x_2, Q^2\right) \sigma_{\mathrm{i}}\left(x_1, x_2, Q^2\right) \tag{8.6}$$

where g_{w} is the weak coupling constant, $V_{\mathrm{qq}'}$ is the CKM matrix term of the two quarks q and q', M_{W} is the mass of the W, Γ_{W} is the width of the W boson decay, f_{i} are the parton distribution functions with proton momentum fractions x, Q^2 the energy scale of the interaction, and s is the center of mass energy defined as $\hat{s} = s_{\mathrm{beam}}\left(x_1x_2\right)$ ($s_{\mathrm{beam}} = 7$ TeV). A diagram of the leading order production is shown in figure 8-1.

The leading order formula has a linear dependence on the parton distribution

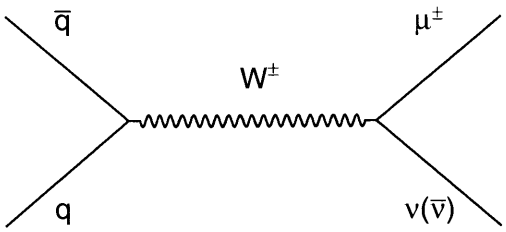

Figure 8-1: Leading order Feynman diagram for W boson production

functions, this dependence translates directly to prediction of the boson rapidity. To obtain the rapidity distribution we have for x_1 and x_2 the two momentum fractions of the proton:

$$p_z = \sqrt{\hat{s}}\,(x_1 - x_2)\ , \tag{8.7}$$

$$E = \sqrt{\hat{s}}\,(x_1 + x_2)\ , \tag{8.8}$$

$$y = -\log\left(\frac{E + p_z}{E - p_z}\right)\ , \tag{8.9}$$

$$= -\log\left(\frac{x_1}{x_2}\right)\ . \tag{8.10}$$

Thus, the rapidity is defined by the distributions of the PDFs $f_{q'}(x_2)f_q(x_1)$. Reinterpreting this in the context of the cross section, yields the differential cross section as a function of the rapidity:

$$\frac{d\sigma}{dy} = \int dx_1 dx_2 \delta\left(y - y\left(x_1, x_2\right)\right) f_q(x_1) f_{q'}(x_2) \sigma_i\ , \tag{8.11}$$

$$\frac{d\sigma}{dy} = \int dx_2 f_{q'}(x_2) f_q\left(x_2 \exp\left(-y\right)\right) \sigma_i\ . \tag{8.12}$$

In terms of the W boson, the dominant production in a proton proton collider is determined by collision of one of the valence quarks with a sea quark. For W^+, the dominant parton distribution function combinations are $f_u\left(x_1\right) f_{\bar{d}}\left(x_2\right)$, while for W^- the dominant combination comes from $f_d\left(x_1\right) f_{\bar{u}}\left(x_2\right)$. Rewriting the previous cross

section equation for W^+ we have, writing $M_W(Q^2)$, to be a Breit-Wigner about M_W,

$$
\begin{aligned}
s &= M_w^2(Q^2) \approx M_W \ , && (8.13)\\
&= s_{\text{beam}} x_1 x_2 \ , && (8.14)\\
&= s_{\text{beam}} x_1^2 \exp(-y) \rightarrow x_1 = \frac{M_W}{s_{\text{beam}}}(s)\exp(y/2) \ , && (8.15)\\
\frac{d\sigma^+}{dy} &= \int dx_2 f_u(x_2) f_{\bar{d}}(x_2 \exp(-|y|))\,\sigma_i \ , && (8.16)\\
\frac{d\sigma^+}{dy} &= \int dx_2 f_u\left(\frac{M_W}{s_{\text{beam}}}\exp(|y|/2)\right) f_{\bar{d}}\left(\frac{M_W}{s_{\text{beam}}}\exp(-|y|/2)\right)\sigma_i \ . && (8.17)
\end{aligned}
$$

Now knowing the that the forms of f_i are all similar for small x with a dominant term given by $f_i \sim x^a$, we expect the the production of W bosons to be flat in the central region.

This derivation implies that with the leading order cross section formula, one can already calculate a rapidity distribution from the parton distribution functions. Other aspects that contribute to boson production are missing at leading order, most notably the boson p_T, which at leading order is zero. From data, it is known that the boson p_T extends out to several 100 GeV/c. Contributions to the cross section calculation which give a non-zero W boson p_T distribution are introduced at NLO. Thus, we must consider higher order corrections to predict the boson p_T distribution.

8.2 Higher order QCD corrections

Higher order QCD corrections contribute to the cross section measurement in several different ways. One way is through the production of an additional quark or gluon (figure 8-2). Contributions of this form come in at the next to leading order QCD calculation and contribute to W boson production at high p_T.

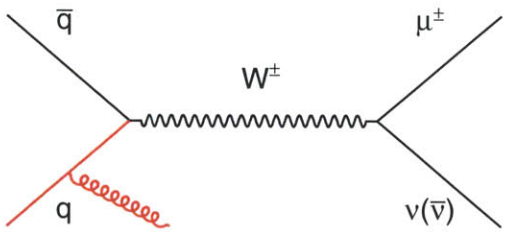

Figure 8-2: W boson production with a gluon jet at next-to-leading order, the red indicates the NLO correction to the LO diagram

The second contribution comes from loop corrections to the cross section (figure 8-3). These modify the production by regulatingthe total cross section at low p_T

where quark and gluon production, such as the process in figure 8-2, have a divergent contribution to the total cross section.

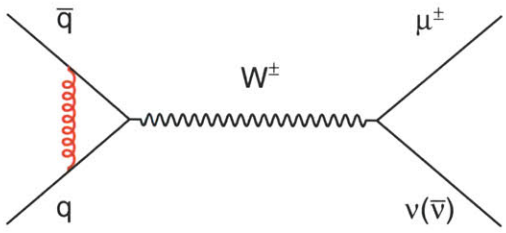

Figure 8-3: Next to leading order loop diagram for W boson production.

The third contribution originates when soft gluons produced during W boson production are radiated collinearly off the quarks involved in the production. This occurs in this regime near a gluon $p_{\mathrm{T}} \approx 1$ GeV/c(the red component in 8-2). The effect is the QCD analog to QED infrared divergence [83, 84]. The effect is described through the theoretical formalism known as resummation. An example of such a process is shown in figure 8-4.

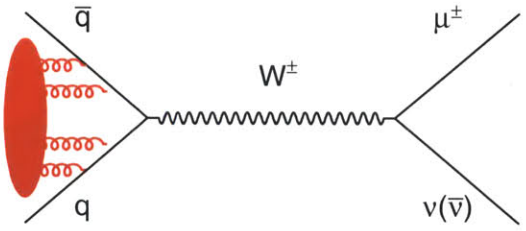

Figure 8-4: Resummed quark diagram for W boson production. The resummation integrated over an infinite amount of collinear quarks and gluons (given by the red blob).

The three QCD contributions desribed above constitute higher order QCD effects, the first two give corrections involving a finite amount of additional quarks or gluons; the third component yield corrections involving an infinite set of radiative quarks and gluons at low energy.

8.2.1 Extending to higher orders

The cross section at higher orders follows from an extension of the leading order form to incorporate infrared radiation. This starts with the matrix element for a general

next to leading order process consisting of a boson plus quark or gluon production $pp \to Vq$ or $pp \to Vg$. The cross section we write as [85, 86]

$$\frac{d\sigma}{dQ^2 dy dQ_{\mathrm{T}}^2} = \frac{\alpha_{\mathrm{s}}}{2\pi} C_{\mathrm{F}} \left(\sum_{\mathrm{qq'}} \left(\int_{\mathrm{x_1}}^1 \frac{dx_1}{x_1} \int_{\mathrm{x_2}}^1 \frac{dx_2}{x_2} f_{\mathrm{q}} f_{\mathrm{q'}} M_{\mathrm{qq'}}^2 \right) \right) , \tag{8.18}$$

where here, we have summed over the possible quark and gluon contributions q or q' with $M_{\mathrm{qq'}}^2$ the square of the respective matrix element describing $qq' \to Vq$. The simplest of such matrix elements, $pp \to Vg$ (figure 8-2) is written as

$$M_{\mathrm{q\bar{q}}} = \left(\frac{\left(1 - Q^2/(x_1 x_2 s)\right)^2}{q_{\mathrm{T}}^2} + \frac{2Q^2}{x_1 x_2 s q_{\mathrm{T}}^2} - \frac{2}{x_1 x_2 s} \right) . \tag{8.19}$$

Integrating over the appropriate kinematic regime (namely the allowed region for which the gluon to radiate) 8.18 becomes

$$\begin{aligned} \frac{d\sigma}{dQ^2 dQ_{\mathrm{T}} dy} = & \frac{\alpha_{\mathrm{s}}}{2\pi} \frac{C_{\mathrm{F}}}{Q_{\mathrm{T}}^2} \left(\log\left(Q^2/Q_{\mathrm{T}}^2\right) - \frac{3}{2Q_{\mathrm{T}}^2} + \mathcal{O}\left(Q_{\mathrm{T}}\right) \right) f(x_1) f(x_2) + \frac{1}{Q_{\mathrm{T}}^2} f_1(x_1) \left(P_{\mathrm{ab}} \otimes f_{\mathrm{a}}\left(x_2\right)\right) \\ & + \frac{1}{Q_{\mathrm{T}}^2} f_2(x_2) \left(P_{\mathrm{ab}} \otimes f_{\mathrm{a}}\left(x_1\right)\right) , \end{aligned} \tag{8.20}$$

where the convolution terms, $P \otimes f$ are defined by the probability of the quark or gluon, a, to radiate becoming a new quark b. Additionaly, in the equation above we have implicitly imposed a standardized Q^2 for the PDFs:

$$P_{\mathrm{ab}} \otimes f_{\mathrm{a}}\left(x\right) = \int_{\mathrm{x}}^1 \frac{dy}{y} P_{\mathrm{a\to b}}\left(\frac{x}{y}\right) f_{\mathrm{a}}(x) , \tag{8.21}$$

$$f_{\mathrm{i}}(x) = f_{\mathrm{i}}(x, Q^2) . \tag{8.22}$$

Intuitively, equation 8.20 is envisaged as the probability of the original quarks in the PDF to fragment into quarks and gluons (the last two terms) combined with the cross section of soft gluon fragmentation in the hard event (the log and 3/2 terms on the left hand of 8.20). The log and 3/2 terms are divergent as $Q_{\mathrm{T}} \to 0$, thus giving the largest contribution to the differential cross section calculation. The cross section itself does not diverge due to regulation of the divergent terms [87]. In this instance for small values of Q_{T}, it is possible for a large number of soft gluon emissions, thus the form of the cross section follows by considering an expansion in the dominant log terms

$$Q_{\mathrm{T}}^2 \frac{d\sigma}{dQ_{\mathrm{T}}} = 1 + \alpha_{\mathrm{s}} \sigma_{\mathrm{hard}} + \alpha_{\mathrm{s}}^2 \sigma_{\mathrm{hard}}^2 + \ldots , \tag{8.23}$$

$$= 1 + \alpha_{\mathrm{s}} C_{\mathrm{F}} \left(\log\left(Q^2/Q_{\mathrm{T}}^2\right) - 3/2Q_{\mathrm{T}}^2 \right) + \ldots , \tag{8.24}$$

$$= \exp\left(\alpha_{\mathrm{s}} C_{\mathrm{F}} \left(\log(Q^2/Q_{\mathrm{T}}^2) - 3/2Q_{\mathrm{T}}^2 \right) \right) . \tag{8.25}$$

The exponent term is known as the Sudakov form factor. The method of absorbing the expansion of the all terms into a Sudakov form factor is known as QCD resummation. In order to incorporate p_{T} conservation, the cross section is performed in the two dimensional Fourier transform of p_{T}, known as the impact parameter, b. Transverse momentum conservation is ensured by inserting a delta function:

$$\delta^2\left(\sum_{\mathrm{i}=1}^{n}\vec{k}_{\mathrm{Ti}}-\vec{p}_{\mathrm{T}}\right)=\frac{1}{4\pi^2}\int d^2be^{-i\vec{b}\cdot\vec{p}_{\mathrm{T}}}\prod_{\mathrm{i}=1}^{n}e^{i\vec{b}\cdot\vec{k}_{\mathrm{Ti}}} \tag{8.26}$$

This yields the final cross section formula, given by

$$\frac{d\sigma}{dQ_{\mathrm{T}}^2dQ^2}=\sigma_0\frac{1}{2}\int_0^\infty dbbJ_0\left(bQ_{\mathrm{T}}\right)\exp\left(-S(b,Q^2)\right)\left(q_1q_2\right)\ , \tag{8.27}$$

where J_0 is the Bessel function of zeroth order, q_1q_2 is the integral over the PDFs, and the modified Sudakov is written as

$$S(b,Q,C_1,C_2)=\int_{\mathrm{C_1^2/b^2}}^{C_2Q^2}\frac{d\mu}{\mu^2}\left(A\left(\alpha_{\mathrm{s}}(\mu),C_1\right)\log\left(\frac{C_2^2Q^2}{\mu^2}\right)+B\left(\alpha_{\mathrm{s}}(\mu),C_1,C_2\right)\right) \tag{8.28}$$

$$A\left(\alpha_{\mathrm{s}}(\mu),C_1\right)=\sum_{\mathrm{n}=0}^{\infty}\left(\frac{\alpha_{\mathrm{s}}}{\pi}\right)A^{(n)}\left(C_1\right)\ , \tag{8.29}$$

$$B\left(\alpha_{\mathrm{s}}(\mu),C_1\right)=\sum_{\mathrm{n}=0}^{\infty}\left(\frac{\alpha_{\mathrm{s}}}{\pi}\right)B^{(n)}\left(C_1\right)\ , \tag{8.30}$$

where we have now generalized the coefficients A and B to be expressed in orders of α_{s}. This form extends the cross section to incorporate terms from higher order calculations. This is known as the CSS formalism [88].

8.2.2 Generalized cross section to all orders

The generalized form of the cross section out to all orders is written in terms of three different components, a non-perturbative component, a perturbative component, and a resummed component. The combination of the terms is written as

$$\begin{aligned}\frac{d\sigma}{dQ^2dydQ_{\mathrm{T}}^2}&=\frac{1}{96\pi^2S}\frac{Q^2}{\left(Q^2-M_{\mathrm{V}}^2\right)^2+Q^4\Gamma_{\mathrm{V}}^2/M_{\mathrm{V}}^2}\\&\times\left(\frac{1}{2\pi^2}\int d^2be^{i\vec{Q}_{\mathrm{T}}\cdot\vec{b}}\sum_{\mathrm{j,k}}W_{\mathrm{jk}}^P(...)\tilde{W}_{\mathrm{jk}}^{NP}(...)+Y(...)\right)\end{aligned} \tag{8.31}$$

where the resummed component is written as W^P, the non-perturbative component is written as $\tilde{W}_{\mathrm{jk}}^{NP}$ and the perturbative component is written as Y. The overall Q^2 distribution is a standard Breit-Wigner with a vector boson (either W or Z) mass of

M_V and a vector boson width of Γ_V. The perturbative Y component is determined from the expansion of $\mathcal{O}(Q_T)$ terms, which were ignored earlier in equation 8.20 when considering only the divergent terms.

Each of these components contribute to a different region of the calculation. This is interpreted in figure 8-5 within the context of the theoretical impact parameter b and in more practical terms of the p_T of the vector boson.

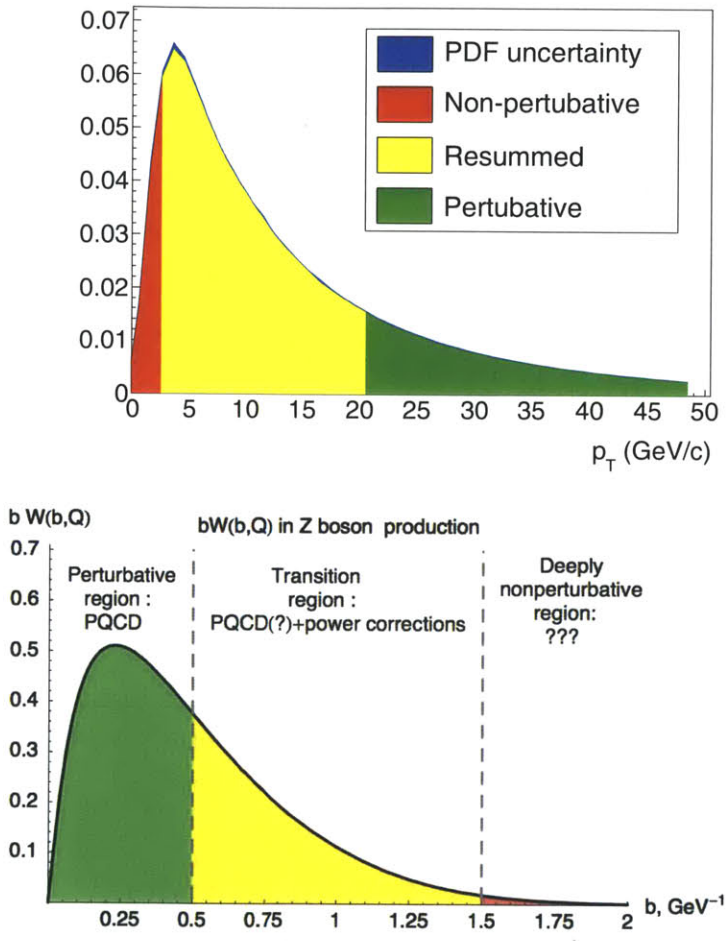

Figure 8-5: Plot of the W boson p_T (top) and the W boson theoretical impact parameter (bottom). The red, yellow, and green define qualitatively the different perturbative regimes of the W boson. The PDF uncetainty band is shown here to show the importantce on the PDF parameterization in terms of the three pretrubative QCD regions. [89]

Resummed component The form of the resummed component is determined from the previous derivation of the Sudakov exponent. It is written as

$$W_{jk}^{P} = \exp(S) |V_{jk}|^2 \left((C_{ja} \otimes f_a)(x_1) (C_{kb} \otimes f_b)(x_2) + (j \leftrightarrow k) \right) . \quad (8.32)$$

In this notation, we have the Sudakov $\exp(S)$ is written as in 8.28 and the C terms are the generalized expansions of $P \otimes f$ described in equation 8.20.

In the framework of Collins Soper Sterman formalism (CSS formalism), it has been shown that the values of A and B are derived by the renormalization group equations [88]. This enables the extensions of the resummed formulae out to the higher order by just expanding the QCD renormalization group equations.

At first order, the value for A is C_{F} and for B is $3/2$. This values are obtained from the W gluon production cross section (equation 8.20). The extension of these terms is presently known to third order in A and to second order in B. In terms of the resummation, expansion out to three orders in the logorithmic terms is written as Next to Next to Next to Leading Log or NNNLL.

In addition to the parameters A and B, the terms that modify the parton distribution function q_1 and q_2 must also be expanded in terms of the strong coupling. The full calculation yields C_{kb} (the Wilson coefficients), which follows from a generalization of the DGLAP evolved $q(x)$. This term is additionally dependent on the order of the α_{s} expansion and presently is calculated out to first order.

Non-perturbative component The non-perturbative component of the cross section formula is needed for regions of small p_{T} where the strong coupling $\alpha_{\mathrm{s}} > 1$. It is inserted into the resummed calculation by imposing a transition as one goes dowon to low p_{T} form the resummed calculation into the non-pertrubative regime through an effective impact parameter cutoff, give by b^*. The transition is induced by the parametrization given by

$$W_{\mathrm{tot}} = W_{\mathrm{jk}}^{NP}(b) W_{\mathrm{jk}}^{P}(b^*) , \tag{8.33}$$

$$b^* = \frac{b}{\sqrt{1 + (b/b_{\mathrm{max}})^2}} , \tag{8.34}$$

whereby the perturbative component is a function of b^*, which cuts off at b_{max}. The CTEQ best fit value for this parameter, using Tevatron data is $b^* = 1.5$ GeV.

A number of different parametrizations exist for the non-perturbative component. All of them are similar to a Gaussian distribution centered around zero. This imposes a so-called "intrinsic k_{T}" smearing of events at low p_{T}. The model used is this analysis is the BLNY [90], which has been tuned to Tevatron data [91, 92]. The general form of the BLNY distribution is given by

$$W_{\mathrm{jk}}^{NP} = \exp\left(-g_1 b^2 - g_2 b^2 \log\left(\frac{Q}{2Q_0}\right) - g_1 g_3 \log(100 x_1 x_2)\right) \tag{8.35}$$

Perturbative component The final component in the cross section is the completely perturbative non-divergent term, known as the Y component. The Y component consists of the nearly complete NNLO differential calculation matched to the resummed component. It modifies the final shape by correcting the production at high p_{T}. The Y correction is written as the matrix element component, where the

divergent asymptotic cross section component at low p_{T} is removed.

$$Y = \frac{d\sigma}{dQ^2 dy dQ_{\mathrm{T}}^2}|_{\mathrm{NNLO}} - \frac{d\sigma}{dQ^2 dy dQ_{\mathrm{T}}^2}|_{\mathrm{asymptotic}} \tag{8.36}$$

The matching of this cross section with the resummed component is unclear. The fixed order and the resummed cross section have components that are calculated at different orders in α_{s}, thus a direct matching would not be consistent [93]. In order to overcome this difference in matching, the cross sections are matched by their values for $\frac{d\sigma}{dQ_{\mathrm{t}}}$ in the region 20 GeV$< Q_{\mathrm{T}} <$ 50 GeV where both calculations are accurate [94].

Cross section implementation: Resbos

The combination of the full differential and matched resummed cross section is implemented in the software program Resbos [95, 96]. The calculation is performed in two steps. The first part of the calculation produces the differential cross section, $\frac{d\sigma}{dQ^2 dy dQ_{\mathrm{T}}^2}$. The second step samples from the differential cross section, producing a Monte Carlo dataset consisting of a W boson, a lepton, and a neutrino. An infinite sum over the quarks ans gluons is are implicitly integrated over in the calculation, thus none of the quarks and gluons are produced, making simulation of events impossible. The Y components are determined by an additional grid, which is added to the existing resummed calculation and samples after the original grid.

To examine the effects of the resummation on the boson distributions, a comparison of the W boson NLO y and p_{T} distributions with and without resummation is presented in figure 8-6. The inclusion of the resummation increases the p_{T} of the boson and flattens out of the rapidity distribution.

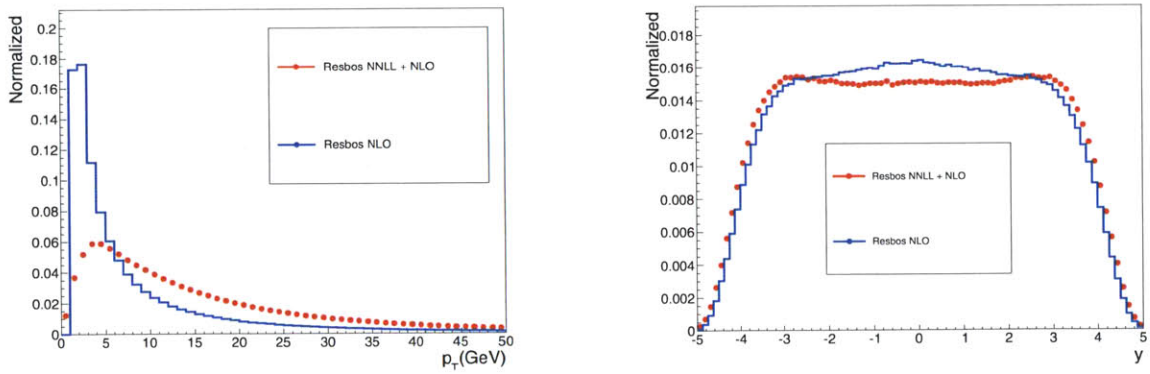

Figure 8-6: Comparison of p_{T} and rapidity (y) distribution using Resbos with (red, Resbos NNLL plus NLO) and without (blue, NLO) resummation terms using CTEQ 6.1. A p_{T} cutoff on quark and gluon effects for $p_{\mathrm{T}} > 1.4\mathrm{GeV}/c$, applied to both samples

The uncertainty on the resummed distribution is comparable to the addition of the highest order correction to the resummed calculation. To assess the scale of

the effect going from second to third order in the expansion of A, we plot the p_{T} distributions of the second and thirder ordersin figure 8-7. The effect shown yields a small increase in boson production at low p_{T}. This effect translates to a difference in sample acceptance of 0.05%.

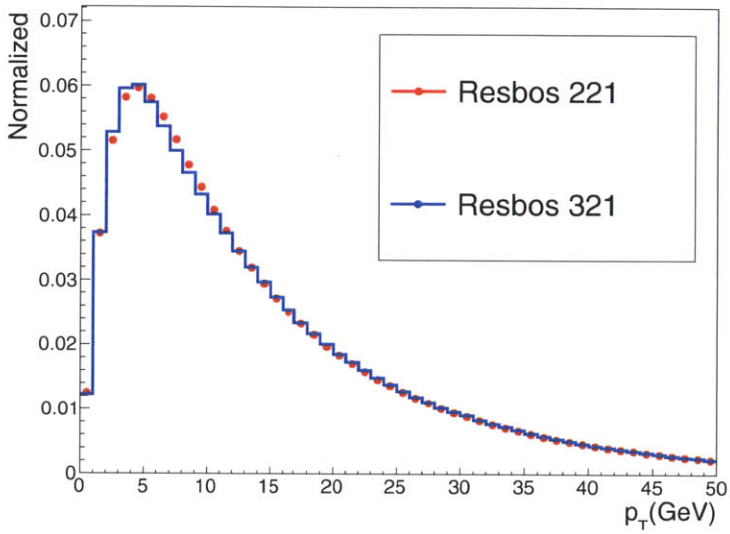

Figure 8-7: Comparison of Resbos NLO p_{T} distribution having NNNLL order expansion in the A coefficient (321) and PDF set with Resbos NNLL NLO

The shift from leading order to higher orders in the the perturbative calculation mainly affects the high p_{T} region of the boson. The scale of this effect is demonstrated in figure 8-8. As one transitions from LO to NLO the p_{T} tail beyond 50 GeV/c increases significantly. Transitioning to the NNLO corrections, the effect on the p_{T} distribution leads to a ten percent change in the tail near 100 GeV/c.

8.2.3 Parton shower Monte Carlo simulation

Resbos contains all of the elements of the full cross section calculation. However, it is not capable of simulating the individual quarks and gluons. For an accurate simulation of all of the physics processes, these components are a necessity in simulation.

To simulate the quark and gluon production in the event, we instead create a parton shower. This is performed by simulating the splitting of partons into multiple partons, using the branchings $q \to qg$, $g \to gg$, and $g \to qq$ (known as the splitting functions). The evolution of these splitting functions at a virtuality scale Q^2 is performed with the DGLAP (Dokshitzer-Gribov-Lipatov-Altarelli-Parisi) equation [6, 7, 8]. The final shower of quarks and gluons results through the repeated iterative splitting of partons. The resulting quarks and gluons produced are passed into simulation, where they are hadronized producing mesons and baryons, which are reconstructed into jets. When W and Z bosons are produced, these showers recoil of the W and Z bosons giving the bosons a p_{T} distribution.

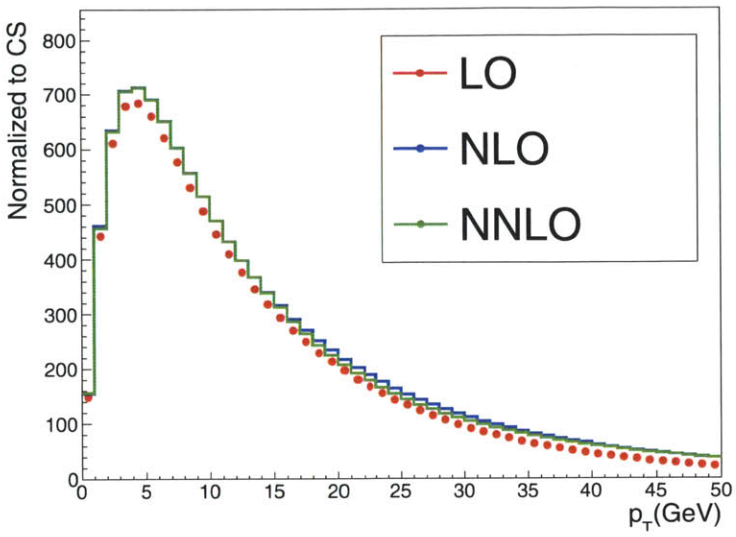

Figure 8-8: Comparison of the Resbos p_T distribution with different orders of perturbative corrections using CTEQ 6.6. The distributions are normalized to their absolute cross sections.

The main disadvantage of the parton shower is its limited accuracy in the description the quark and gluon showering. The showering terms are determined from the leading order quark and gluon splittings, resulting in leading-log (LL) accuracy [97]. To go beyond the LL shower approximation, branchings going from one hadron to three or more additional particles are necessary. In an attempt to improve the generation of parton showers, some effects beyond LL are incorporated through momentum conservation, showering by angular or p_T ordering, and optimally choosing a scale for α_s.

Two parton shower Monte Carlo simulations are in common use, Pythia [54] and Herwig [55]. The ordering of the shower simulation in Pythia is done in p_T. This is performed by showering the highest p_T splitted quark first and then proceeding to the lower p_T components. The ordering in Herwig is performed by the angle of the partons which have branched off the shower. Herwig starts from largest angle with respect to the original parton and works inwards. This performed because the highest p_T(angle) particles are not modified by decays originating from lower p_T(angle) particles.

In addition to the parton shower, Pythia models the non-pertrubative component by introducing a proton intrinsic k_T for quarks and gluons in the proton. It also models the hadronization of the quarks and the gluons, the leading order matrix element of many processes, and a number of other effects. In many instances, these effects are not completely modeled, but parametrized so that they are tuned to the data. The tuning of the parton shower in Pythia is performed on low energy QCD collisions. Tuning was performed in CMS on collisions at 7 TeV yielding a tune known as the Z2 tune [98]. This tune is used in all Pythia related studies in this document.

Powheg

Next to leading order cross section calculations have negative valued contributions originating from loop diagrams (figure 8-3). Inclusion of these negative valued calculations would require negative weighted Monte Carlo events. The Monte Carlo W boson generator Powheg (Positive Weight Hardest Emission Generator) tries to address the issue of the negative weighted events by constraining the kinemati region requiring negative weighted events to a small area of phase space and then relying on the LO calculation to generate the kinematic distribution in that region.

In Powheg, a vector boson event is generated first by sampling differential cross section generating a parton, boson, and lepton. The boson, the leptons and the parton are then passed to Pythia to perform the parton showering. In Pythia, the hard parton produced by Powheg is treated as the hardest parton emission when parton showering is performed. To avoid complications in the resummed regime, the parton produced by Powheg is only passed onto Pythia if it is a above tunable threshold, which by default is set to one GeV. Additionally, to improve the accuracy of the showering step Powheg uses the NLO strong coupling value in the Sudakov coefficient. This causes the parton shower to act more like an NLL resummed calculator.

Through this prescription, Powheg coincides at large p_{T} with the correct NLO calculation and at low p_{T} with the standard shower Monte Carlo Pythia (or LL resummed distribution). Figure 8-9 compares the Powheg distribution with the predicted resummed distribution from Resbos. The p_{T} distribution of Powheg is close to Resbos making corrections to Powheg small (on the order of a few percent). The major difference originates in a larger fraction of events in the tail and a shift peak of the p_{T} distribution at ≈ 5 GeV/c.

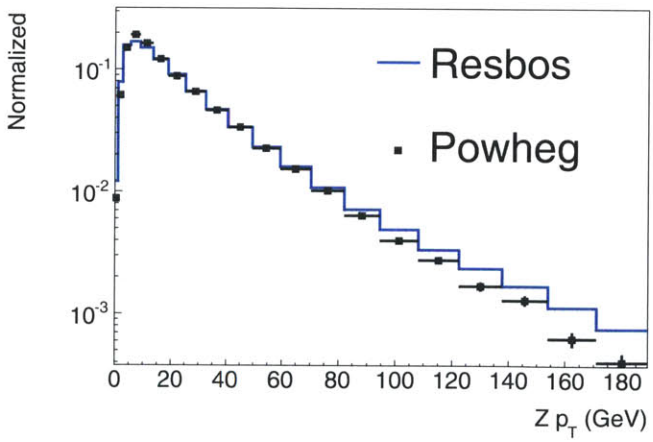

Figure 8-9: Comparison of Powheg Monte Carlo Simulation with Resbos.

8.2.4 Differential NNLO calculation

The resummed calculation used in Resbos included a Y component, with contributions from the NNLO calculation for the perturbative high p_T region. The fully differential NNLO cross section $d\sigma/dp_T dy dQ^2$ was only completed in 2006 [26]. It is implemented through a program called FEWZ (Fully Exclusive W,Z production through NNLO in pQCD) [26]. At each order of perturbation, the differential cross section incorporates more initial states summarized by

- $q\bar{q}$ production at LO,
- qg production at NLO, and
- gg and qq production at NNLO.

The core idea of this calculation relies on an automated extraction of the infrared singularities from real radiation matrix elements and a numerical cancellation of these singularities with virtual corrections. The final calculation includes the spin correlations of boson with all of the initial state products as well as the finite width effects coming from the boson width.

Although FEWZ has the full NNLO differential cross section, it does not contain any resummed or parton shower based calculation. This makes it valid for only the yellow region in figure 8-5. A comparison of FEWZ with Resbos is found in figure 8-10. The result shows excellent agreement between the two calculations for $p_T > 20$ GeV/c. This validates the hard matrix element component of Resbos (the Y component) and determines the region where full NNLO calculation is important.

The advantage of the fully differential cross section is the computation of the differential distribution with a modified strong coupling constant α_s. Modifying the α_s effectively probes higher order (beyond NNLO) calculations [99]. Thus, FEWZ is used to check the effects of beyond NNLO corrections to the boson, by comparing the behavior of the NNLO differential cross section for modified α_s.

8.2.5 Comparison with data

To test the performance of the various differential calculations, we rely on Z boson differential distributions in data. The two leptons in the Z boson allow for complete determination of the Z boson four vector, providing a check of both the Z p_T differential distribution and the Z rapidity distribution. To perform the comparison we require a parton shower Monte Carlo simulation so that cuts may be performed on simulated detector effects, such as trigger and isolation. Corrections to this Monte Carlo simulation are then performed through one of two means: the Monte Carlo parameters are either tuned to data, or the Monte Carlo is reweighted with Resbos.

The Z boson selection is obtained by requiring two muons with the identification selection presented in chapter 5. To capture the most inclusive distribution, we require a low mass cut on the combined di lepton system of $m_{\ell\ell} > 40$ GeV/c^2.

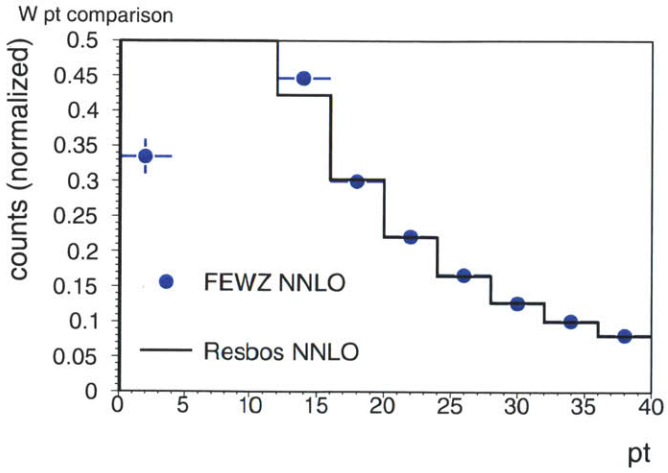

Figure 8-10: Comparison of generated Resbos p_{T} distribution with FEWZ. Normalization is to the $p_{\mathrm{T}} = 20$ GeV/c bin

Powheg Performance with data The comparison of the boson p_{T} distribution between data and Powheg is presented in figure 8-11. At low p_{T}, a small disagreement is visible between Powheg and data. The disagreement is comparable to the additional resummed terms shown in figure 8-7. Additionally, the low p_{T} component missing contributions from the non-perturbative region may further broaden the p_{T} distribution [100]. At high p_{T} a large deficit between Powheg and the data is visible. In this region, it is expected that the hard matrix element coming from higher order corrections leaves a large contribution. This contribution increases the yield at high p_{T} by 15 to 20 percent.

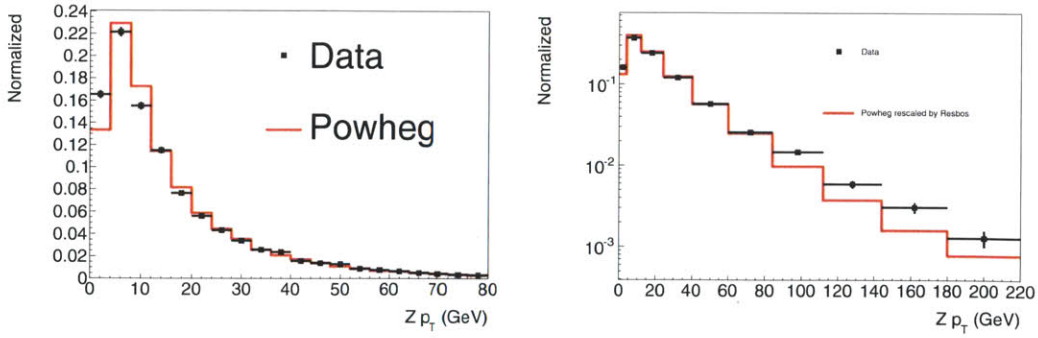

Figure 8-11: Comparison of the Z boson p_{T} distribution of Powheg with data. Both data and Monte Carlo simulation are normalized to area. The result is shown for low p_{T} (left) and for a high p_{T} binning (right).

The agreement of Powheg between data and simulation at low p_{T} is improved by tuning the minimum threshold for hard parton inclusion. Increasing the threshold

increases the contribution at low p_T coming from the tuned Pythia showering and reduces the influence of the hard matrix element contribution from Powheg. This tuning is the equivalent of moving the threshold between yellow (resummed) and green (perturbative) in figure 8-5. We consider moving the threshold up through that region and comparing the resulting p_T distribution because the resummed contribution has a significant effect for a p_T up to a region of around 20 GeV/c,

To perform the comparison, we utilize the newest version of Powheg, known as the Powheg Box (the default presented above is with the previous version of Powheg, Powheg 1.1). The χ^2 per number of degrees of freedom of the p_T distribution between data and Monte Carlo simulation is minimized with respect to the variation of the minimum hard scatter parameter. Figure 8-12 shows the result of χ^2 minimization and the resulting p_T distributions of the Z boson. The red histogram, which is the p_T distribution with the minimum χ^2 shows a considerable improvement with respect to the default Powheg (the blue line). The optimal value of the minimum hard scatter is found to be $p_T = 30$ GeV/c. This indicates, from the left plot showing the variations in tune, that the resummed contribution originating from the Pythia parton shower improves the p_T description for $p_T < 15$ GeV/c

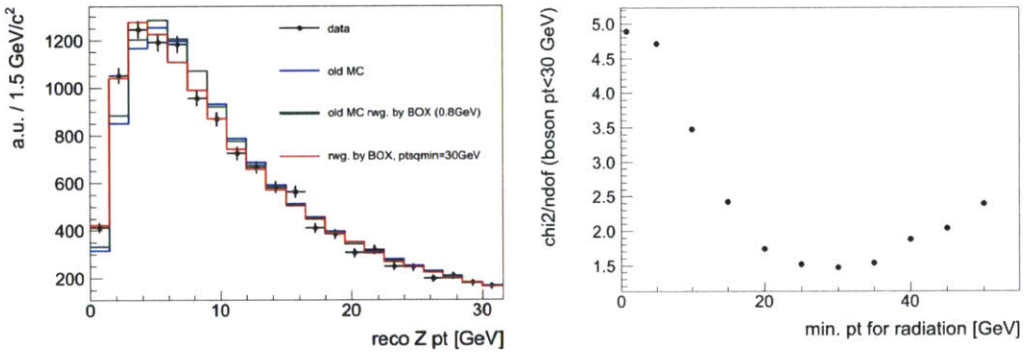

Figure 8-12: Comparison of different predicted p_T distributions with the data (left). The blue line represents the default Powheg Monte Carlo simulation used to determine the acceptance. The green line is the default Powheg Box simulation, used to tune the p_T distribution. The red line is tuned the Powheg box p_T distribution corresponding to the minimal χ^2 as determined by the right plot. The right plot shows the χ^2/NDF variation between data and tuned Powheg as a function of the minimal p_T for the inclusion of the hard parton (here called min p_T for radiation).

Resbos performance with data The comparison of Resbos with data is performed by re-weighting the Z boson differential distributions produced with Powheg Monte Carlo simulation to correspond with the Z boson differential distributions produced by Resbos. To perform the reweighting each event in the Powheg simulation

is assigned a weight determined by

$$w_{\mathrm{i}} = \frac{P_{\mathrm{Resbos}}\left(p_{\mathrm{T}}^{Z}, y_{\mathrm{Z}}\right)}{P_{\mathrm{Powheg}}\left(p_{\mathrm{T}}^{Z}, y_{\mathrm{Z}}\right)}, \tag{8.37}$$

where P is the probability of a Z boson event to be within a specified region of p_{T} and rapidity, y. The reweighting is done in terms of the generated p_{T} and rapidity in both Powheg and Resbos, because no simulation effects are present in Resbos. For the distributions going beyond $p_{\mathrm{T}} > 100$ GeV/c one bin in rapidity is used so as to minimize the effect of statistical fluctuations.

In figure 8-13, we present the low and high p_{T} distributions of the Powheg Monte Carlo simulation reweighted by Resbos. Comparison with figure 8-11 shows considerable improvement in the overall agreement between the data and the Monte Carlo simulated p_{T} distribution. At low p_{T}, the width of the distribution is increased improving the overall agreement in shape. At high p_{T}, the additional matrix element corrections push p_{T} distribution up with respect to Powheg, yielding a much improved data simulation agreement.

Following the reweighting, some residual disagreement between data and Resbos still exist. The disagreement at low p_{T} occurs in two regions. The first region, near p_{T}=5 GeV/c, is influenced from uncertainties in the non-perturbative component of the differential distribution. The second region, near p_{T}=20 GeV/c, occurs at the transition region between the matrix element (Y component) and the resummed calculation. This region is particularly difficult to model because it involves matching the resummed calculation, performed out to all orders in the strong coupling, with the hard matrix element, which is calculated out to finite order. Similar discrepancies has previously been observed at the Tevatron [92].

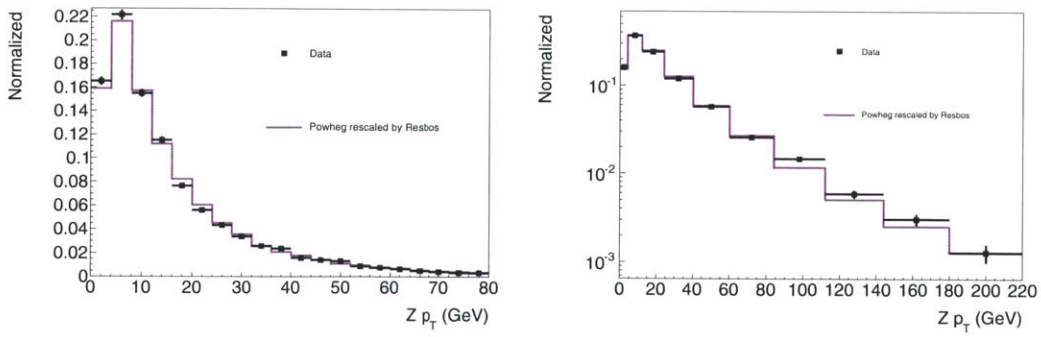

Figure 8-13: Comparison of the Z boson p_{T} of Powheg rescaled by Resbos p_{T} distribution with data. Both data and Monte Carlo simulation are normalized to area. The result is shown for low p_{T} (left) and for a high p_{T} binning (right).

QCD systematic uncertainty

The knowledge of the highest order QCD corrections are utilized to determine an uncertainty on the acceptance measurement. The acceptance measurement is performed with Powheg (version 1.1), which is a partial NLL, and NLO cross section measurement. The logical extension in resummed order is to go from NLL to NNLL or higher. The difference between the two determines the scale for the additional higher order resummed corrections. The extension of the pertrubative order of Powheg would be to utilize the NNLO matrix element. Again, the difference between the NLO and the NNLO bound the scale of corrections at NNLO and beyond.

We determine the uncertainty from the higher order resummed terms and the higher order matrix element corrections, simultaneosly with Resbos NNLO. The use of both sets of corrections minimizes the acceptance uncertainty because it incorporates the correlated effects of going to higher orders in both resummed and perturbative QCD. The effects do not cancel with each other because they both push the acceptance in the same direction (the signs on α_s are the same for both calculations). The expected p_T distribution is additionally predicted to be very close to the Resbos p_T distribution, which was further confirmed by figure 8-13. The two effects not incorporated into Resbos are the matching between the resummed, Y component, and the low p_T non perturbative uncertainty. To assess the order of these effects, the Z boson data/simulation weight w_i defined by

$$w_i\left(p_T\right) = \frac{P^Z_{\text{Data}}\left(p^Z_T\right)}{P_{\text{Resbos}}\left(p^Z_T\right)}, \tag{8.38}$$

is used to reweight the acceptance measurement by fitting a fifth order polynomial to $w_i(p_T)$ and correcting the acceptance to get a_{corr}:

$$a_{\text{corr}} = \frac{1}{\sigma_0}\int dp^\ell_T d\eta_\ell w_i\left(p^Z_T\left(\ell\right)\right)\frac{d\sigma}{dp^\ell_T d\eta_\ell}. \tag{8.39}$$

This correction to the acceptance is performed by either integrating over the kinematics of the Powheg or Resbos generated kinematics. For comparison purposes, we consider both possibilities. These data corrected acceptance values are used as cross checks to systematic uncertainty on the acceptance.

The systematic uncertainty is determined by taking the difference in acceptance between Resbos and Powheg at the generator level. To make the generator kinematic distributions from Powheg and Resbos match the data, the lepton, and the neutrino are smeared with their respective p_T and $\not\!\!E_T$ resolutions and uncertainty fluctuated resolutions. Figure 8-14 demonstrates the difference in acceptance as a function of p_T of the lepton. As a cross check, the data weighted acceptance is found to be within 0.3% of the Resbos Powheg difference.

This systematic uncertainty recipe is repeated on the Z boson for a sample consisting of two muons passing the W selection whose combined mass is within 60 GeV/c^2 < $m_{\ell\ell}$ < 120 GeV/c^2. The individual W and Z boson systematic uncertainties for the default acceptance cuts are reported in table 8.1.

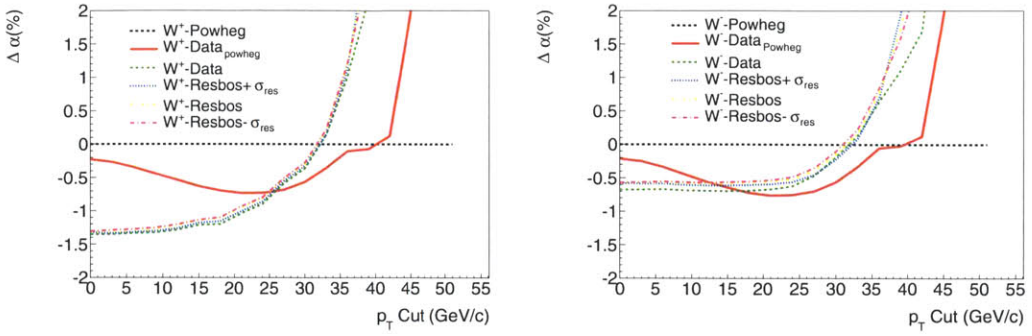

Figure 8-14: Change in the acceptance between Resbos, Powheg, data reweighted (equation 8.39) Powheg(red), data reweighted Resbos (green) as a function of p_{T} for W^+ bosons (left) and W^- bosons(right). The various $\pm\sigma_{\mathrm{res}}$ correspond to the change in the acceptance if Powheg and Resbos are both smeared by the up and low bands of the detector resolution.

Quantity	$\Delta A/A$
W^+ acceptance (μ)	$(-0.72 \pm 0.11)\%$
W^- acceptance (μ)	$(-0.50 \pm 0.09)\%$
W acceptance (μ)	$(-0.65 \pm 0.07)\%$
Z acceptance (μ)	$(-1.19 \pm 0.18)\%$
$\mathrm{W}^+/\mathrm{W}^-$ ratio (μ)	$(-0.23 \pm 0.14)\%$
W/Z ratio (μ)	$(+0.53 \pm 0.20)\%$

Table 8.1: Changes in acceptance from resummation and NNLO QCD effects.

Higher order QCD correction systematic uncertainty

The higher order QCD uncertainties are determined with the complete NNLO differential cross section calculator FEWZ. Fixed order QCD calculations bound the higher order perturbative calculations (beyond NNLO) by varying the scale μ for $\alpha_{\mathrm{s}}(\mu)$ and recalculating the acceptance. The choice of scale variation is conventionally chosen to be either $\mu = 2M_{\mathrm{W}}$, M_{W}(default value), or $M_{\mathrm{W}}/2$, a choice of scales, which is known to span more than 90 percent of all hard interactions [99]. The systematic uncertainty is determined from the conventional scale choice by taking the half maximum difference of the acceptance calculation over the three different energy scales.

$$\delta_{\mathrm{scale}} = \frac{1}{2} \cdot \max\left\{|A_{\mathrm{M}} - A_{\mathrm{M}/2}|,\ |A_{\mathrm{M}} - A_{2\mathrm{M}}|,\ |A_{2\mathrm{M}} - A_{\mathrm{M}/2}|\right\}. \tag{8.40}$$

Due to the difficulty in calculating the differential W boson cross section, the calculation was performed over several hundred computer processors for a period of one day. The resulting systematic uncertainties are summarized in table 8.2.

Quantity	δ_{scale}
W^+ acceptance (μ)	$(0.49 \pm 0.35)\%$
W^- acceptance (μ)	$(0.37 \pm 0.37)\%$
W acceptance (μ)	$(0.44 \pm 0.21)\%$
Z acceptance (μ)	$(0.09 \pm 0.20)\%$
W^+/W^- ratio (μ)	$(0.36 \pm 0.61)\%$
W/Z ratio (μ)	$(0.38 \pm 0.29)\%$

Table 8.2: Systematic uncertainty on the acceptance from missing higher order corrections.

8.3 Electroweak corrections

The Electroweak corrections include all QED radiative effects beyond leading order in α. These effects lead to the production of one or more photons. The corrections modify the differential cross section in a similar manner as the QCD corrections; however, the coupling α is more than ten times smaller than α_s making the contribution of these effects significantly smaller. As with the QCD corrections, the photon radiative corrections come in two flavors. The first flavor, final state radiation (FSR), consists of a radiative photon originating from the final state muon as depicted in the right of figure 8-15. The second flavor of radiative corrections come from the order α Electroweak corrections. These corrections consist of a set of radiative loop corrections and order α radiative photons originating from radiative W bosons. An example of such an effect is shown in the left of figure 8-15, which shows a photon radiated from a W boson.

Generator level simulation is not sufficient to determine the affect on the acceptance becausethe Electroweak corrections introduce photons, which are not accounted for at generator level. To incorporate photon effects into the acceptance calculation simulation of the photon's path in the CMS detector is necessary, so that the isolation about the muon is recalculated.

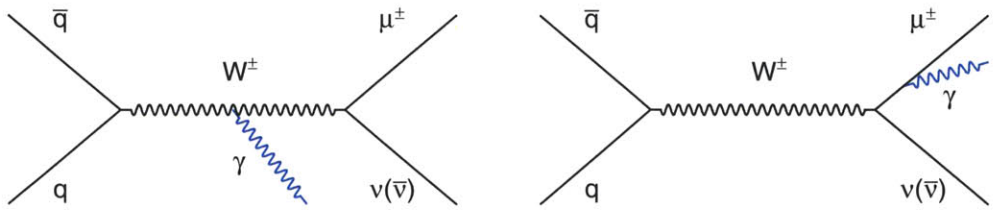

Figure 8-15: Diagrams showing the corrections from final state radiation (right) and from a radiative photon originating from the W boson(left).

8.3.1 Final state radiation(FSR)

Final state radiation consists photon radiation from the muon during production for the W boson event. Muons radiate photons with energies down to several tens of MeV, which summed over all photons leads to an average drop in the p_{T} distribution by four percent. As with gluons at low energy, calculation of the radiation leads a divergenc the collinear limit of radiative photons. This divergence is expanded yielding a QED Sudakov form factor of the form [4].

$$\exp\left(-\alpha \log\left(Q^2/\mu^2\right)\right) \tag{8.41}$$

The simulated effect out to leading log is thus performed through a parton shower equivalent technique on the photon radiation. This is performed by iterative sampling of the probability distribution for lepton radiation $P(\ell \rightarrow \ell\gamma)$, for each radiated photon and lepton down to a infrared cutoff energy.

To incorporate the final state radiation three separate implementations are considered: Pythia [54], Horace [101], and Photos [102]. Each implementation utilizes a different photon energy cut off and a different approximation of the probability distribution of photon radiation. Pythia is the baseline FSR implementation, because it is interfaced with the rest of Pythia and is called by default following the parton shower. The Horace generator is capable of simulating both final state radiation and additional $\mathcal{O}(\alpha)$ Electroweak corrections [101]. Unlike Pythia, The FSR generator for Horace has the full leading log matrix element.The final FSR generator, Photos, like Horace utilizes a different parameterization of the full matrix element to determine final state radiation. Due to a limitation in previous versions of the simulation, Photos could not be extended down to radiative photon energyies below roughly one GeV. Thus it is only used as a cross check.

A comparison of the highest energy photon p_{T} and distance ΔR with respect to the lepton is shown in figure 8-16. The comparison is performed by applying the three different FSR models on the exact same kinematic events produced by a leading order matrix element generator implemented in Horace and interfaced with Pythia QCD showering. Excluding the low p_{T} region of Photos, which is not simulated, the highest energy photon p_{T}, distributions, shown in figure 8-16, are all similar. However, the ΔR between the photon and the lepton vary with each generator. The overall effect of this on the final acceptance is small.

8.3.2 Electroweak corrections of $\mathcal{O}(\alpha)$

$\mathcal{O}(\alpha)$ corrections to W and Z boson production contribute additional photons in the event. The Monte Carlo generator, Horace, incorporates the complete set of Electroweak corrections. The corrections is turned on and off to separately compare the effects of final state radiation and the $\mathcal{O}(\alpha)$ Electroweak corrections. Figure 8-16 shows the photon p_{T} spectrum originating from the combined Electroweak and final state radiation corrections (red) with the FSR corrections alone (blue). The Electroweak corrections result in an additional contribution of photons at large ΔR

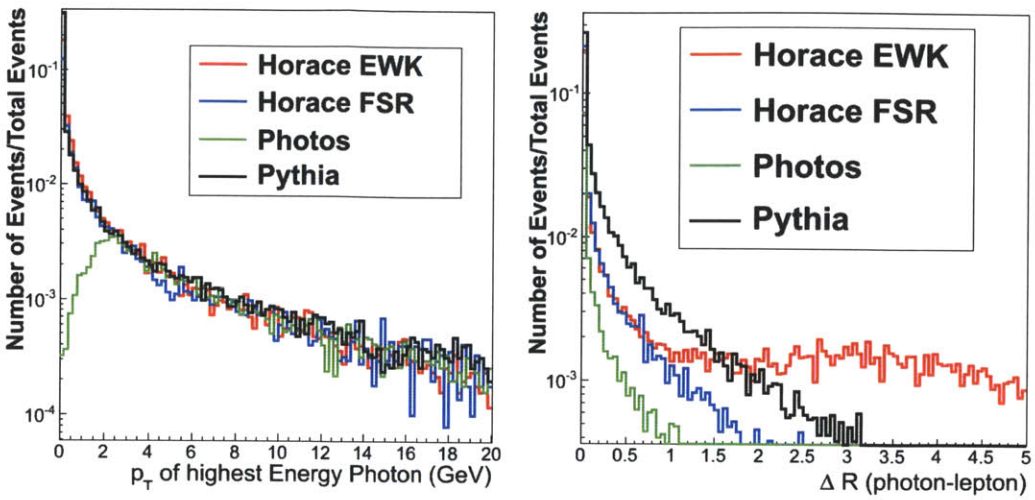

Figure 8-16: Comparison of different FSR models on the maximum photon p_{T} (left) and the distance $\Delta R = \sqrt{\Delta\eta^2 + \Delta\phi^2}$ of all photons from the lepton. The Horace generator is shown twice: only the FSR model applied (blue line) and also with the FSR and EWK corrections applied (red line).

originating mainly from the W radiative photons.

8.3.3 Systematic uncertainty

The final state radiation and the Electroweak corrections both contribute a systematic uncertainty on the final W boson acceptance. The final state radiation uncertainty is determined by difference in the acceptance between the Horace FSR model and the Pythia FSR model because Horace has a more complete FSR model compared to Pythia,. The $\mathcal{O}(\alpha)$ Electroweak corrections are missing from the baseline Pythia simulation. To determine the effect of these missing corrections the systematic uncertainty is taken from the difference in the acceptance between Horace where the Electroweak corrections are turned on and off.

In determining the systematic uncertainty, the same generator level lepton and boson kinematics from the leading order Horace matrix element are passed to the different FSR programs, thereby isolating the effect of the FSR. The difference in the acceptance with respect to the baseline Pythia simulation is shown in figure 8-17. For both W^+ and W^- the effect of the final state radiation is below 0.5% for lepton $p_{\mathrm{T}} > 25$ GeV/c. The electroweak corrections increase the acceptance for W^- boson decays and decrease the acceptance slightly by W^+ boson decays. The cross check FSR model (Photos) additionally differs from the default FSR model by < 0.5 percent, further justifying the choice of the systematic uncertainty. The full results are given in table 8.3.

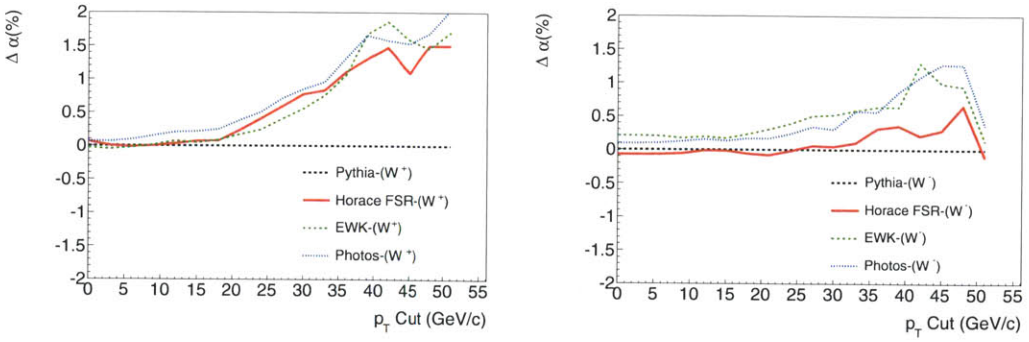

Figure 8-17: Change in the acceptance with a p_{T} cut defined by the x-axis for several different FSR models in W^+ bosons (left) and W^- bosons (right).

Quantity	FSR	EWK
W^+ acceptance (μ)	$(+0.34 \pm 0.14)\%$	$(-0.04 \pm 0.14)\%$
W^- acceptance (μ)	$(+0.02 \pm 0.16)\%$	$(+0.39 \pm 0.17)\%$
W acceptance (μ)	$(+0.21 \pm 0.10)\%$	$(+0.13 \pm 0.11)\%$
Z acceptance (μ)	$(+0.36 \pm 0.25)\%$	$(-0.45 \pm 0.23)\%$
$\mathrm{W}^+/\mathrm{W}^-$ ratio (μ)	$(+0.31 \pm 0.21)\%$	$(-0.43 \pm 0.22)\%$
W/Z ratio (μ)	$(-0.01 \pm 0.27)\%$	$(-0.58 \pm 0.26)\%$

Table 8.3: Acceptance differences from FSR modeling and missing Electroweak corrections

8.4 Parton distribution function uncertainties

The last input into cross section is determined by the parton distribution functions. This has a large effect on the boson rapidity distribution (as shown for leading order in section 8.1.1), but not on the boson p_{T} distribution, where PDFs contribute at $\mathcal{O}(\alpha)$ to the Wilson coefficient terms in equation 8.32.

The parton distribution functions are parametrized in terms of a general polynomial form (for CTEQ the parametrization in equation 1.6 is used). The resulting parametrization is then fit to a large amount of different datasets, this yields a set of uncertainties on each fitted parameter for each specified quark parton distribution function. The uncertainties on each parameter is propagated through, by decomposing the uncertainties in terms of the independent eigenvectors of the Hessian matrix and propagating the diagonalized uncertainties into parton distribution function [103]. This yields a set of 2N modified PDF sets, corresponding to the propagation of the $+\sigma$ and $-\sigma$ uncertainties for all N independent eigenvectors of the parton distribution function parametrization.

The propagation of the uncertainties is then performed by iterating over all parton distribution functions and calculating the desired observable. The spread in the observables yields an uncertainty band on the predicted W and Z boson, muon, and

neutrino distributions. Figure 8-18 shows the maximum spread in the boson rapidity and p_{T} distributions obtained by running over all of the 2N PDFs (using CTEQ 6.6) and calculating the fully resummed NNLO plus NNNLL distribution each each set. The uncertainty uncertainty band is near two percent over the whole range of the rapidity distribution and below one percent over the p_{T} distribution. The effect of this variation translates to $\mathcal{O}(1)$ percent uncertainty on the muon rapidity distribution and $\mathcal{O}(0.1)$ percent uncertainty on the muon p_{T} distribution.

To determine the systematic uncertainty on the acceptance from PDFs, we recalculate the acceptance for events reweighted event by event to match the kinematic distribution of a specific PDF [103]. The change in the acceptance, summed up over all of the PDFs in the uncertainty set following the desired recipe of each set, determines the systematic uncertainty. For each event, the event weight w_{i} is determined by the ratio of the desired PDF with respect to the default PDF. The form of the weight is written as

$$w_{\mathrm{i}} = \frac{f_{\mathrm{a}+\sigma}(x_1) f_{\mathrm{b}+\sigma}(x_2)}{f_{\mathrm{a}}(x_1) f_{\mathrm{b}}(x_2)} , \tag{8.42}$$

where $f_{\mathrm{a}}(x_1) f_{\mathrm{b}}(x_2)$ are the default parton distribution functions used in the cross section calculation and $f_{\mathrm{a}+\sigma}(x_1) f_{\mathrm{b}+\sigma}(x_2)$ are the PDFs fluctuated by the chosen uncertainty eigenvector.

For the event weighting to match the true kinematic distributions obtained by performing the full cross section calculation with the desired PDF set, the cross section must scale linearly in the parton distribution functions $f_{\mathrm{a}}(x_1) f_{\mathrm{b}}(x_2)$. A linear dependence is not completely evident from the cross section calculation because the cross section calculation, equation 8.32, has non linear contributions coming from the parton distribution functions. To check the linearity, samples were generated with Resbos performing the full cross section calculation on each PDF uncertainty set. The acceptance calculation using each of these samples are compared with a generated Resbos sample using the default reweighting method. The resulting difference in the acceptance between the two was found to be within 0.2 percent on each uncertainty fluctuated set. Propagating the uncertainty through to the systematic uncertainty calculation, the missing terms lead to an additional systematic uncertainty contribution below 0.1 percent.

8.4.1 Systematic uncertainty

To determine the systematic uncertainty on the acceptance originating from the parton distribution functions, we follow the PDF4LHC recommendation [104]. The recommendation stipulates that we take the maximum uncertainty band on the acceptance from the uncertainty predictions using the three PDF sets CT10, MSTW2008, and NNPDF2.0. The uncertainty on each prediction must incorporate both the PDF uncertainties and the α_{S} uncertainties following the specified recipe as defined by each PDF set group.

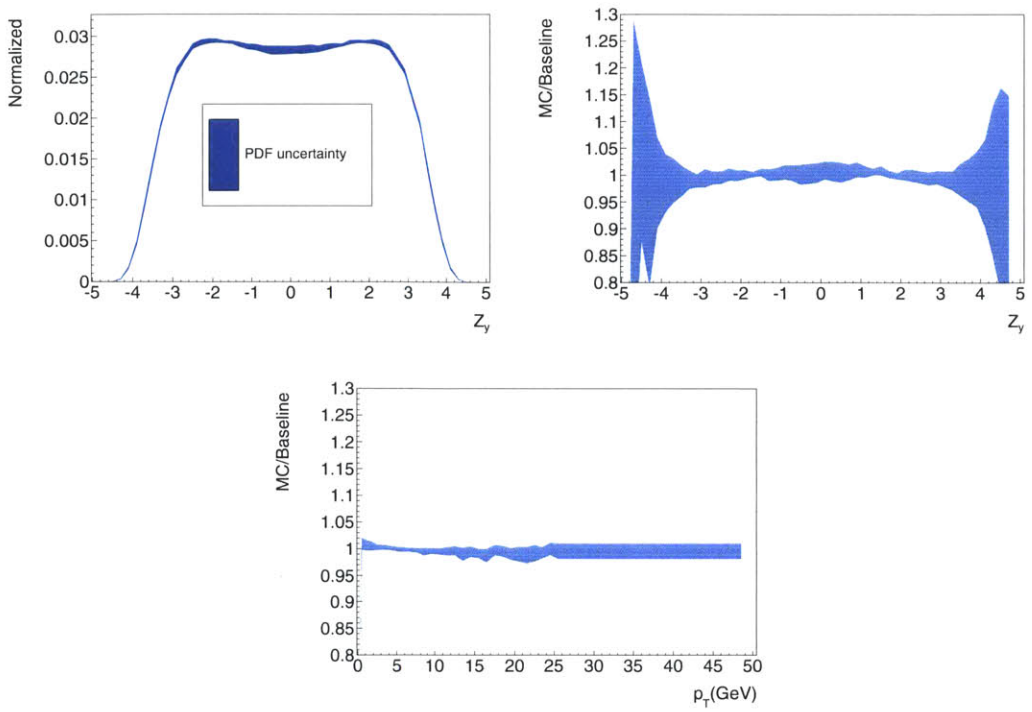

Figure 8-18: Uncertainty band spanning the PDF variations for rapidity (top left) rapidity normalized by the central value (top right) and p_{T} normalized by the central value (bottom).

8.4.2 Uncertainty with CT10

The PDF uncertainty calculation recommended by the CTEQ group given below as [105],

$$\Delta a^{+} = \sqrt{\sum_{\mathrm{i}=1}^{N} \left[\max\left(a_{\mathrm{i}}^{+} - a_0,\, a_{\mathrm{i}}^{-} - a_0,\, 0\right)\right]^2}, \tag{8.43}$$

$$\Delta a^{-} = \sqrt{\sum_{\mathrm{i}=1}^{N} \left[\max\left(a_0 - a_{\mathrm{i}}^{+},\, a_0 - a_{\mathrm{i}}^{-},\, 0\right)\right]^2}, \tag{8.44}$$

where a_0 is the acceptance for the default (central value) PDF set, i runs over the uncertainty eigenvectors, and also a_{i}^{+} and a_{i}^{-} denote respectively the acceptances for the ith positive and negative PDF uncertainty, the total number of uncertainty eigenvectors for CT10 is 26 (52 error PDFs).

The α_{s} uncertainty is obtained by calculation the $\Delta a^{\pm}$ (equation 8.43) for an uncertainty set given a central value PDF sets where α_{s} is varied from 0.116-0.120, a range which spans the 68% confidence level(CL) around the central value of 0.118. These sets are provided in the complementary CT10as PDF set [5].

The PDF and α_s uncertainties are added in quadrature yielding the final uncertainty values $\Delta a^{\pm}_{\mathrm{CT10}}$. The uncertainty PDFs for CT10 consider 90% CL variations, hence the uncertainty computed from equation 8.43 is scaled down by 1.645 to obtain the 68% CL uncertainty.

8.4.3 Uncertainty with MSTW2008

For MSTW, the full PDF and α_S combined uncertainty is obtained by calculating $\Delta a^{\pm}$(Equation 8.43) over the five PDF sets (40 error PDFs each) corresponding to $\alpha_s = \alpha_s^0$, $\alpha_s^0 \pm 0.5\sigma$, $\alpha_s^0 \pm \sigma$, where σ is the 68% CL uncertainty on α_s^0, the nominal value in MSTW. The combined uncertainty is given by comparing the max and min acceptance over all α_s (equations (9) and (10) from [9]),

$$\Delta a^{+} = \max_{\alpha_s} \{a_{\alpha_s} + \Delta a_{\alpha_s}\} - a_0, \tag{8.45}$$

$$\Delta a^{-} = a_0 - \max_{\alpha_s} \{a_{\alpha_s} - \Delta a_{\alpha_s}\}, \tag{8.46}$$

where a_0 is computed with the central value PDF with nominal α_s^0 .

8.4.4 Uncertainty with NNPDF2.0

For NNPDF [106], uncertainty sets corresponding the eigenvectors of the Hessian matrix are not provided for the PDFs. Instead a set of PDFs that sample over the uncertainties of the covariance matrix at a number of different α_s points are provided. The PDF plus α_s uncertainty is obtained by running over all PDF sets Gaussian distributed around the central value $\alpha_s = 0.119 \pm 0.001$. The breakdown of the sampling is shown in Table 8.4.4.

α_s	0.116	0.117	0.118	0.119	0.120	0.121	0.122
N_{rep}	5	27	72	100	72	27	5

Table 8.4: Number of replicas used for each α_s value to compute PDF plus α uncertainty with NNPDF.

The uncertainty from the PDF sets is computed by calculating the standard deviation over all events with $\Delta a > 0$ or $\Delta a < 0$. The resulting uncertainty follows:

$$\Delta a^{+} = \sqrt{\frac{1}{N^{+}} \sum_{\mathrm{i}=1}^{N^{+}} (a_{\mathrm{i}} - a_0)^2}, \tag{8.47}$$

$$\Delta a^{-} = \sqrt{\frac{1}{N^{-}} \sum_{\mathrm{j}=1}^{N^{-}} (a_0 - a_{\mathrm{j}})^2}, \tag{8.48}$$

where a_0 is computed with the central value PDF at $\alpha_s = 0.119$, i runs over the N^+ PDF sets where $a_i > a_0$, and j runs over the N^- PDF sets where $a_j < a_0$.

8.4.5 Results

To combine the three separate PDF sets and quote an uncertainty, the envelope spanning all allowable acceptances $a \pm \Delta a$ is first computed, the resulting uncertainty is the size of the envelope divided by two. This is written as

$$\Delta_{\max} = \max_i \left(a_i + \Delta a_i^+\right), \tag{8.49}$$

$$\Delta_{\min} = \min_i \left(a_i - \Delta a_i^-\right),$$

$$\text{PDF}+\alpha_s \text{ uncertainty} = \frac{1}{2}\left(\Delta_{\max} - \Delta_{\min}\right), \tag{8.50}$$

where i runs over the three different PDF sets CT10, MSTW2008, and NNPDF2.0. This method encompasses the central value and 68% CL uncertainty for all three PDF sets. Table 8.5 lists the acceptances with PDF and α_s uncertainties for each PDF set considered, as well as the final systematic uncertainties in each channel.

Quantity	A_{CT10}	A_{MSTW}	A_{NNPDF}	Syst
W^+ acceptance (μ)	$0.4109^{+0.0025}_{-0.0030}$	$0.4103^{+0.0023}_{-0.0019}$	$0.4141^{+0.0020}_{-0.0022}$	1.00%
W^- acceptance (μ)	$0.4004^{+0.0041}_{-0.0041}$	$0.4047^{+0.0027}_{-0.0024}$	$0.3983^{+0.0036}_{-0.0034}$	1.56%
W acceptance (μ)	$0.4055^{+0.0030}_{-0.0024}$	$0.4068^{+0.0018}_{-0.0019}$	$0.4065^{+0.0022}_{-0.0023}$	0.69%
Z acceptance (μ)	$0.3191^{+0.0045}_{-0.0043}$	$0.3195^{+0.0019}_{-0.0020}$	$0.3183^{+0.0023}_{-0.0024}$	1.37%
W^+/W^- ratio (μ)	$1.0262^{+0.0122}_{-0.0112}$	$1.0137^{+0.0052}_{-0.0067}$	$1.0395^{+0.0091}_{-0.0081}$	2.02%
W/Z ratio (μ)	$1.2709^{+0.0135}_{-0.0119}$	$1.2735^{+0.0087}_{-0.0096}$	$1.2772^{+0.0025}_{-0.0041}$	1.0%

Table 8.5: Acceptances with PDF plus α_s uncertainties and the resulting systematic uncertainties.

8.5 Summary

In this section, a detailed outline of the most accurate theoretical Drell Yan calculations are presented. The theoretical calculations and their uncertainty directly affect the W and Z boson cross sections through the acceptance and indirectly by their shape uncertainties.

The most accurate QCD corrected simulation is determined with Resbos. Comparison of the Z boson p_T distribution between data and Resbos reveal agreement in the prediction with data along most of the p_T range, motivating the choice of using it

as a baseline to determine the QCD modeling uncertainties. In view of reducing the acceptance uncertainty in future analyses, we determined an optimal tune of Powheg simulation which describes the Z boson p_{T} well for $p_{\mathrm{T}} < 50$ GeV/c.

The largest contribution to the acceptance uncertainty comes from the parton distribution function. This is determined using the official pdf4LHC recommendation [104]. Other contributions to the systematic uncertainty originating from FSR and higher order corrections have a small effect on the acceptance uncertainty.

Chapter 9

Model of $\not\!\!E_{\rm T}$

The W boson cross section is extracted by fitting the $\not\!\!E_{\rm T}$ distribution of the single lepton selection. To extract the W boson yield, we utilize a template for the W boson $\not\!\!E_{\rm T}$ shape derived from simulation with resolutions corrected to match the resolutions in data. In this section, a method to derive both the corrections and the uncertainties on the $\not\!\!E_{\rm T}$ is presented.

The W boson event has three decay constituents: the lepton, the neutrino, and the hadronic recoil. The two visible components, the lepton, and the hadronic recoil, are summed vectorial to yield the $\not\!\!E_{\rm T}$. The term "recoil" evokes the hadronic activity that balances the $p_{\rm T}$ of the bosons; however because $\not\!\!E_{\rm T}$ is defined as the negative vector sum of *all* detector deposits, the recoil includes deposits from the underlying event and pile-up.

9.1 Definitions

The recoil $\vec{U}$ is defined as the vector sum of all components excluding the leptons. This is written in terms of the $\not\!\!E_{\rm T}$:

$$\vec{U} \;=\; -\vec{\not\!\!E}_{\rm T} - \Sigma_{\rm i}\vec{p_{\rm T}}\left(\ell_{\rm i}\right) \;. \tag{9.1}$$

The recoil is a two dimensional vector which we define by the axes oriented parallel (U_1) and perpendicular (U_2) to the true boson $p_{\rm T}$ direction. This convention provides maximal separation between contributions to $\vec{U}$ from the hadronic radiation accompanying boson production (along U_1) with addition hadronic effects in the event. Figure 9-1 illustrates the decomposition of $\vec{U}$ for W boson events.

Z bosons are selected without significant background and $\vec{p}_{\rm T}^{\,Z}$ is accurately reconstructed in data from the two final state leptons. This permits the decomposition of $\vec{U}$ into U_1 and U_2 components in terms of their projection on $\vec{p}_{\rm T}^{\,Z}$. Both the mean values of U_1 and U_2, and resolutions vary with $p_{\rm T}^{\rm Z}$. The variation is parametrized into a function with parameters determined by a fit to Z boson events in data and Monte Carlo simulation. Comparison of the behavior of the parametrized recoil functions of U with respect to $p_{\rm T}$ between data and Monte Carlo simulation defines a scale factor,

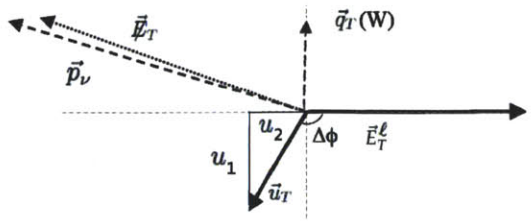

Figure 9-1: The transverse recoil vector $\vec{U}$ is split into components U_1 and U_2 that respectively lie parallel and perpendicular to the direction of boson p_{T}.

κ_{i} which is used to correct simulation to match the data.

$$\kappa_{\mathrm{i}}\left(p_{\mathrm{T}}\right) \;=\; \frac{U_{\mathrm{i}}^{Z}\left(p_{\mathrm{T}}|data\right)}{U_{\mathrm{i}}^{Z}\left(p_{\mathrm{T}}|simulation\right)}\;, \tag{9.2}$$

where U^Z is taken from the parametrization for a defined $p_{\mathrm{T}}^{\mathrm{Z}}$

The scale factor is used to correct the simulated W boson recoil to match the expected W boson recoil in data. This is performed by first fitting for the parametrized functions which describe U_1 and U_2 in W Monte Carlo simulation and then correcting the fitted parameters by multiplying with the appropriate Z boson scale factors κ_{i}. Application of a scale factor incorporates the kinematic differences between W and Z boson which lead to different values of U_1 and U_2. To minimize the effect of kinematic biases between W^+ and W^- bosons. The scale factors are applied to separate fitted parameterizations of the W^+ and W^- bosons. In light of being succinct, we describe the application generally to the W boson, with the implicit assumption that this is done separately on both positive and negative bosons.

9.2 Samples and selections

The same event selections described previously for the Z boson in chapter 7 and for W bosons in chapter 5 are used. The W and Z simulation samples must be produced using the same generator, underlying event model, and reconstruction conditions to ensure consistency in the determination and application of the recoil scale factors. For this thesis Powheg with the Z2 tune is utilized for both the W and Z boson simulations.

9.3 Recoil parametrization

To determine the hadronic recoil, the mean and shape of U_1 and U_2 are fitted as a function of boson p_{T}. Several techniques have been developed to fit U_1 and U_2. The simplest technique relies on the assumption that the resolution of the recoil has a Gaussian shape. The more complicated models rely on the assumption that the

resoluion is described by a double Gaussian. In this section, we first present the simplest model followed by progressively more complicated models leading to the final model used to determine the W boson cross section.

9.3.1 Gaussian recoil parametrization

The parametrization of U_1 and U_2 as functions of $p_{\mathrm{T}}^{\mathrm{Z}}$ follow a multi-step procedure:

1. Bin U_{i} in units of $p_{\mathrm{T}}^{\mathrm{Z}}$
2. Fit the distribution of U_{i} in each bin with a Gaussian
3. Fit a polynomial $f_{\mathrm{i}}(p_{\mathrm{T}}^{\mathrm{Z}})$ to the distribution of Gaussian means. This produces a *response curve.*
4. Fit a polynomial $\sigma_{\mathrm{i}}(p_{\mathrm{T}}^{\mathrm{Z}})$ to the distribution of Gaussian widths. This produces a *resolution curve.*

Binning and fitting

The fits performed per bin to U_1 and U_2 are binned maximum likelihood fits of Gaussian probability distribution functions. The Gaussian model was used in previous Tevatron studies[107, 108]. The Gaussian fits are not particularly sensitive to the U_1 and U_2 bin widths. A width of 2 GeV/c per $p_{\mathrm{T}}^{\mathrm{Z}}$ bin ensures there are at least 50 events in each bin, yet it is not too coarse to resolve the resolution and response curves. The fit is performed in a region of $p_{\mathrm{T}} < 60$ GeV/c. Figure 9-2 is an example of a Gaussian fit in data and Monte Carlo simulation for a single $p_{\mathrm{T}}^{\mathrm{Z}}$ bin.

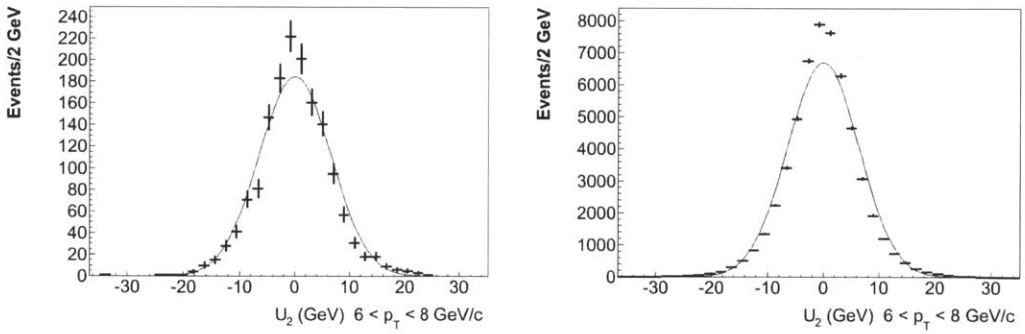

Figure 9-2: Example Gaussian fits to U_1 in data (left) and MC (right) for the 8 GeV/c $< p_{\mathrm{T}}^{\mathrm{Z}} <$ 10 GeV/c bin.

In the following sections, the response and resolution curves are shown. In each curve, two different uncertainty bands are plotted. In the first uncertainty band, we assume maximal (anti-)correlation between recoil model parameters, in this scenario the errors are propagated by adding the individual uncertainties linearly (as

oppose to in quadrature, if they were not correlated). This "worst-case" assumption gives the conservative uncertainty bands shown in red. Model uncertainties are more appropriately propagated using the full covariance matrix (yellow band).

Response parametrization

In the case of U_1, the evolution of the Gaussian mean should closely track the boson p_{T}. By design, U_2 should be largely independent of boson p_{T} ($p_{\mathrm{T}}^{\mathrm{V}}$). The results below confirm this expected behavior.

U_1 response parametrization The U_1 response shown in figure 9-3 is linear and modeled by linear function: $a + b\, p_{\mathrm{T}}^{\mathrm{V}}$. For low $p_{\mathrm{T}}^{\mathrm{V}}$, recoil is dominated by low energy particles that are not well reconstructed. This leads to a slight, non-linear turn-on in the response curve before the curve assumes a constant slope. The constant term in the linear model (a) takes on a small, positive value to accommodate this effect. Figure 9-3 shows the result of the linear fit to U_1. The fit to data gives a χ^2/NDF of 0.74 while the fit to Monte Carlo simulation yields $\chi^2/NDF = 0.51$.

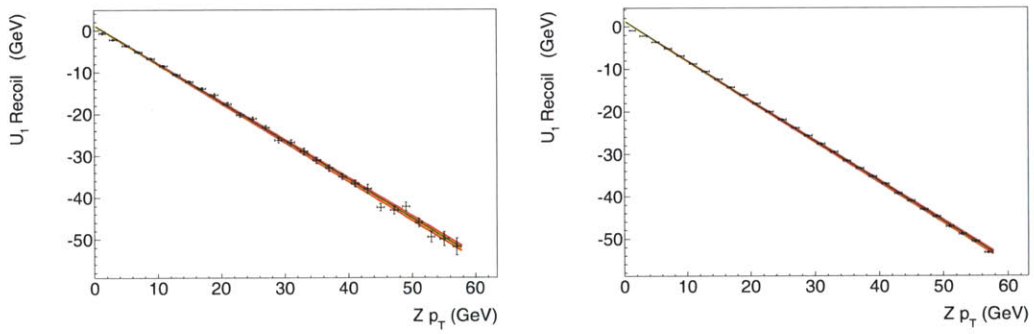

Figure 9-3: Fit of the U_1 response to Z boson data (left) and Z boson simulation (right). The yellow band represents one σ uncertainty from propagation of the full covariance matrix. The red band is the one σ uncertainty adding the uncertainties linearly (maximal correlation)

U_2 response parametrization The mean of U_2 is expected to be zero, independent of $p_{\mathrm{T}}^{\mathrm{Z}}$. Figure 9-4 shows the result of the linear fit to U_2. We find U_2 is consistent with zero in both data and Monte Carlo simulation.

Resolution parametrization

The resolution of U_1 and U_2 behave as different functions of p_{T}^{V}. The U_1 resolution increases with the p_{T} of the boson, consistent with the increase in hadronic activity produced in the U_1 direction. By contrast, the U_2 resolution does not vary as much with boson p_{T}.

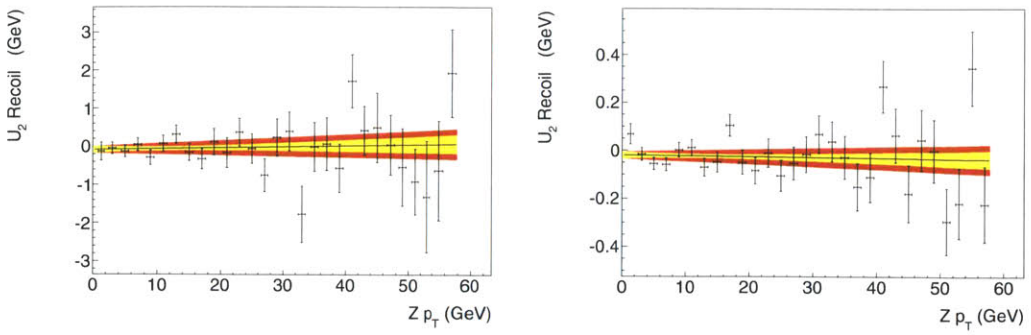

Figure 9-4: Fit of the U_2 response to Z boson data (left) and Z boson simulation (right). The yellow band represents the one σ uncertainty from propagation of the full covariance matrix. The red band is the one σ uncertainty assuming maximal correlation.

U_1 resolution parametrization U_1 resolution receives contributions from two components. The first contribution comes from the underlying event and is independent of boson p_{T}. The second contribution is due to hadronic recoil. This component does not contribute when the boson p_{T} is zero, but increases as the boson p_{T} grows.

A quadratic model for U_1 resolution is utilized based on empirical evidence and guidance from[107]. Figure 9-5 presents the results of a quadratic fit to data and simulation. The quadratic function describes both data and simulation well. Adding an additional cubic term to the resolution function, the cubic term is found to be consistent with zero and the χ^2/NDF for the fit increases. Thus, a quadratic is determined to be a sufficient description of U_1 resolution in both data and simulation.

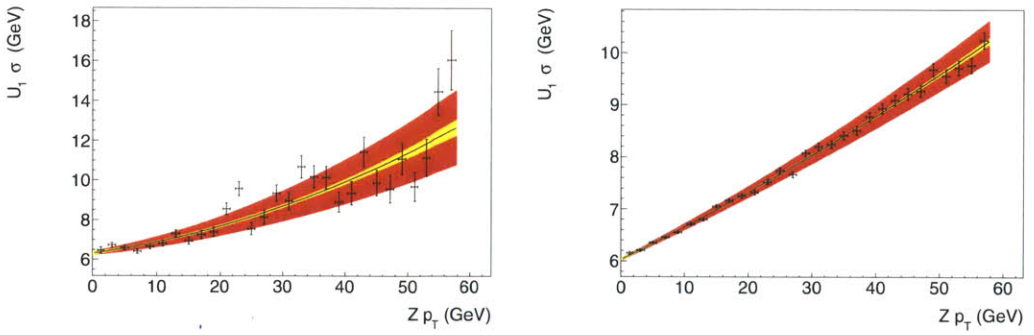

Figure 9-5: Fit of U_1 resolution to Z boson data (left) and Z boson simulation (right). The yellow band represents the one σ uncertainty from propagation of the full covariance matrix. The red band is the one σ uncertainty assuming maximal correlation.

U_2 resolution parametrization The U_2 resolution depends mainly on the underlying event and pile-up. Soft transverse radiation from the hadronic products recoiling against the Z boson will also leave a small contribution to the resolution. Therefore, as with U_1, a quadratic model is used to describe the U_2 resolution. In simulation, the p_{T}^{Z} variation for U_2 over a range of 0 GeV/c< p_{T} < 50 GeV/$c$is 75 percent less that of the variation over U_1, however in data, the variation of U_2 is 30 percent less the variation of U_1. The difference between data and Monte Carlo simulation results from the different parton shower composition in data and Monte Carlo simulation.

Figure 9-6 plots the results of the U_2 resolution fits in data and MC simulation. Both show a linear rise in resolution as a function of p_{T}^{Z}, which can be fitted with the quadratic model. For $p_{\mathrm{T}} \approx 0$, the fitted values for U_1 and U_2 are within one standard deviation of each other, as expected, because there is no hadronic recoil originating from the boson.

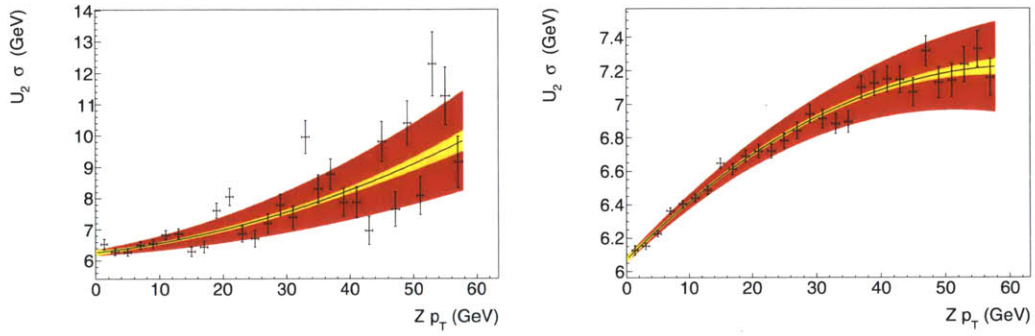

Figure 9-6: Fit of U_2 resolution to Z data (left) and Z simulation (right). The yellow band represents the one σ uncertainty from propagation of the full covariance matrix. The red band is the one σ uncertainty assuming maximal correlation.

9.3.2 Unbinned method

In lieu of binning in p_{T} and fitting a Gaussian for the response mean and resolution, the unbinned method employs a linear fit of the U_1 and U_2 distributions versus p_{T}. This results in a fit with a similar mean to the binned fit with reduced uncertainties and without bias from the choice of binning. This procedure also has the advantage that a linear fit of points has an analytic solution, thus fit convergence is guaranteed. On the other hand, skipping the individual Gaussian fits produces a result that is less intuitive. To describe the behavior of the resolutions in the unbinned method, we utilize the polynomial models developed from parametrized fits of the binned method.

Unbinned response

Figure 9-7 shows the unbinned fit to the response data. Each point signifieds a Z boson event in data. The uncertainties compared to those resulting from the binned

fit are smaller.

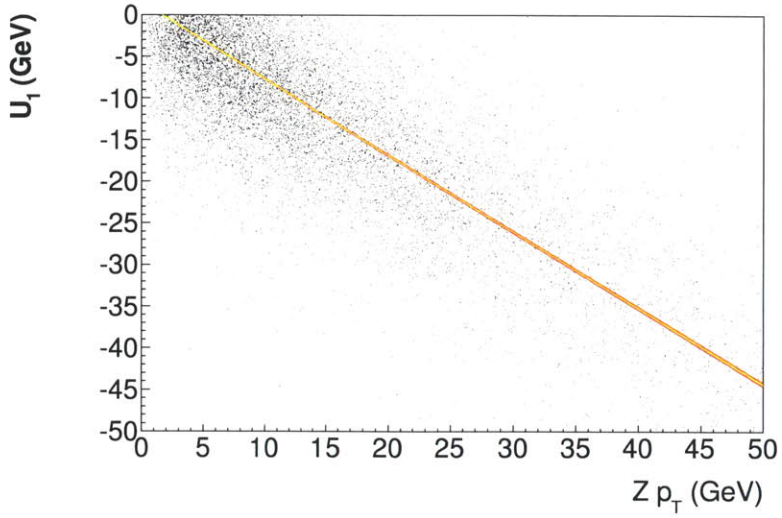

Figure 9-7: Unbinned fit of the U_1 response to both Z Data. The yellow represents the error set resulting from the fully propagated covariance matrix. The red set represents the maximally correlated error set.

Unbinned Resolution

To perform an unbinned measurement of the resolution, in place of fitting for a Gaussian in a specified p_{T} bin, we assume that for any infinitesimal region of boson p_{T}, $dp_{\mathrm{T}}^{\mathrm{Z}}$, the resolution is distributed as a Gaussian. Under this assumption, we consider the absolute value of the difference of all points x' with respect to the mean x, this we write as $|x - x'|$. For Gaussian distributed points x' about a mean x with resolution σ, the expectation of the value $|x - x'|$ is written as (equation 9.3).

$$\langle |x - x'| \rangle = \int_{-\infty}^{\infty} dx' |x' - x| \left(\frac{\exp\left(-\frac{(x'-x)^2}{2\sigma^2} \right)}{\sqrt{2\pi\sigma^2}} \right) = \frac{2\sigma}{\sqrt{2\pi}} \,. \tag{9.3}$$

Consequently, consider the distribution $|U_{\mathrm{i}} - U_{\mathrm{i}}^{mean}\left(p_{\mathrm{T}}^{\mathrm{Z}}\right)|$ versus boson p_{T}, where $U_{\mathrm{i}}^{mean}\left(p_{\mathrm{T}}^{\mathrm{Z}}\right)$ is the fitted response. The mean of this value $\langle |U_{\mathrm{i}} - U_{\mathrm{i}}'| \rangle$ is the resolution σ multiplied by $2/\sqrt{2\pi}$. Thus, by fitting a polynomial to the $|U - U_{\mathrm{i}}(p_{\mathrm{T}})|$ distribution versus p_{T} we can extract the resolution as a function of boson $\sigma(p_{\mathrm{T}})$ by scaling the polynomial fit result by $2/\sqrt{2\pi}$. The detailed procedure to perform this follows as:

1. For each event plot a point where U_{i} is the y-axis and $p_{\mathrm{T}}^{\mathrm{Z}}$ is on the x-axis

2. Fit this plot to a linear polynomial. This is the response $U_{\mathrm{i}}^{mean}(p_{\mathrm{T}}^{\mathrm{Z}})$

3. For each event plot a point where the y-axis is $|U_{\rm i} - U_{\rm i}^{mean}(p_{\rm T}^{\rm Z})|$ and the x-axis is $p_{\rm T}^{\rm Z}$

4. Fit this plot to a quadratic polynomial. This fit function is the resolution scaled by a constant: $2\sigma(p_{\rm T}^{\rm Z})/\sqrt{2\pi}$.

5. Multiply this modified resolution by the constant $\sqrt{2\pi}/2$ and extract the resolution $\sigma(p_{\rm T}^{\rm Z})$

As before, the procedure involves fitting a polynomial to a set of point. Thus, this fit has an analytic solution and thus is guaranteed to converge.

Figure 9-8 shows the fitted polynomial and the extracted resolution function in Z boson data. Comparing the value at zero $p_{\rm T}$ of the resolution function in data between U_1 and U_2, the values are found to be within one half standard deviation of each other. When comparing the unbinned method with the binned method, the variation in the resolutions of the binned method are found to be systematically larger to the unbinned method by 10%. This systematic bias is a result of the binning (the fitted width of U_1 will be larger than the true width because of the shifting mean).

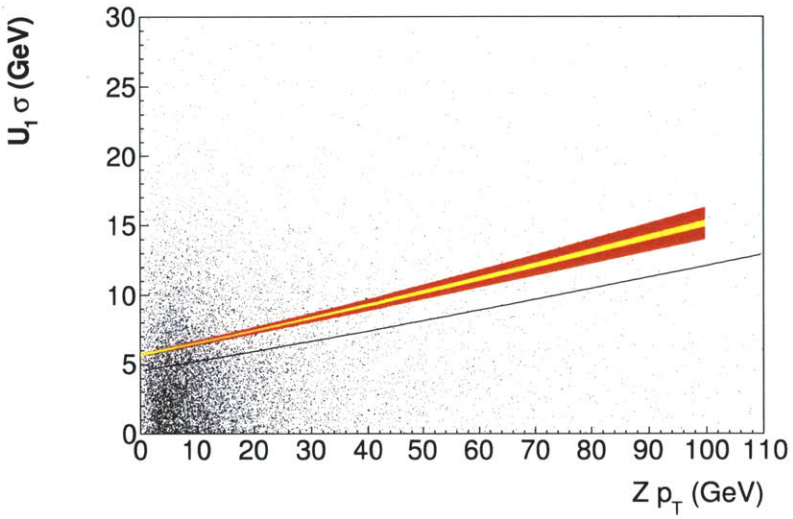

Figure 9-8: Unbinned fit for the U_1 resolution to Z boson data. The yellow represents the uncertainty band resulting from the fully propagated covariance matrix. The red band represents the maximally correlated uncertainty band. The black line is the result of the unbinned fit to $|U_{\rm i} - U_{\rm i}(p_{\rm T})|$. The shift of the resolution parameter up with respect to the black line results from the $\sqrt{2\pi}/2$ scaling.

9.3.3 Non-Gaussian resolution

The previous fits make the assumption that the resolution for U_1 and U_2 is described well by a Gaussian. This assumption is not a valid description of the resolution over

the whole range. In figure 9-9, we plot fits to the pull variable, which defined from the fits for the response $U_{\rm i}\left(p_{\rm T}^{\rm V}\right)$ and Gaussian resolution $\sigma\left(p_{\rm T}^{V}\right)$ is written as

$$a_{\rm i} \;=\; \frac{U_{\rm i} - U_{\rm i}^{mean}(p_{\rm T}^{\rm V})}{\sigma_{\rm mean}(p_{\rm T}^{\rm V})} \;. \tag{9.4}$$

The red line in the fit is the result of a Gaussian fit to the pull distribution. It demonstrates that a Gaussian fit is capable of describing a similar resolution shape, but it does not describe the tails and the peak well.

The actual shape of the resolution stems from the fact that the resolution is Gaussian for specific value of the total transverse energy deposit in the detector, $\sum E_{\rm T}$; however, it varies over the whole range of $\sum E_{\rm T}$. This variation is quite large making the option of constructing a Gaussian description of the recoil in bins of $\sum E_{\rm T}$ difficult .

In order to describe the non-Gaussian resolution, we model the resolution with a sum of two Gaussians having the same mean (a double Gaussian). A fit to the pull variable using a double Gaussian is the blue line shown in figure 9-9. This model describes the shape of $a_{\rm i}$ well.

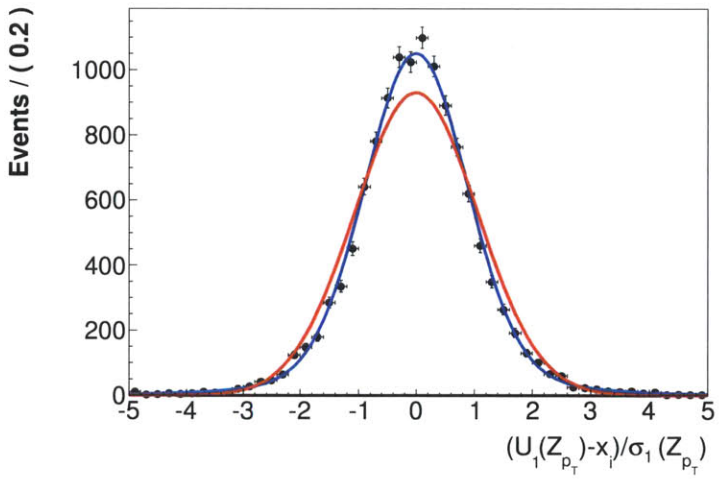

Figure 9-9: Fit to the pull variable $a_{\rm i}$ of the recoil U_1 the red is the best fit of a Gaussian model the blue is the best fit of a double Gaussian model.

9.3.4 Double Gaussian method

The double Gaussian method is a direct extension of the unbinned method, where the assumption is now taken that the unbinned fit previously used to determine the resolution σ, instead determines the mean of a double Gaussian.The fitted mean is

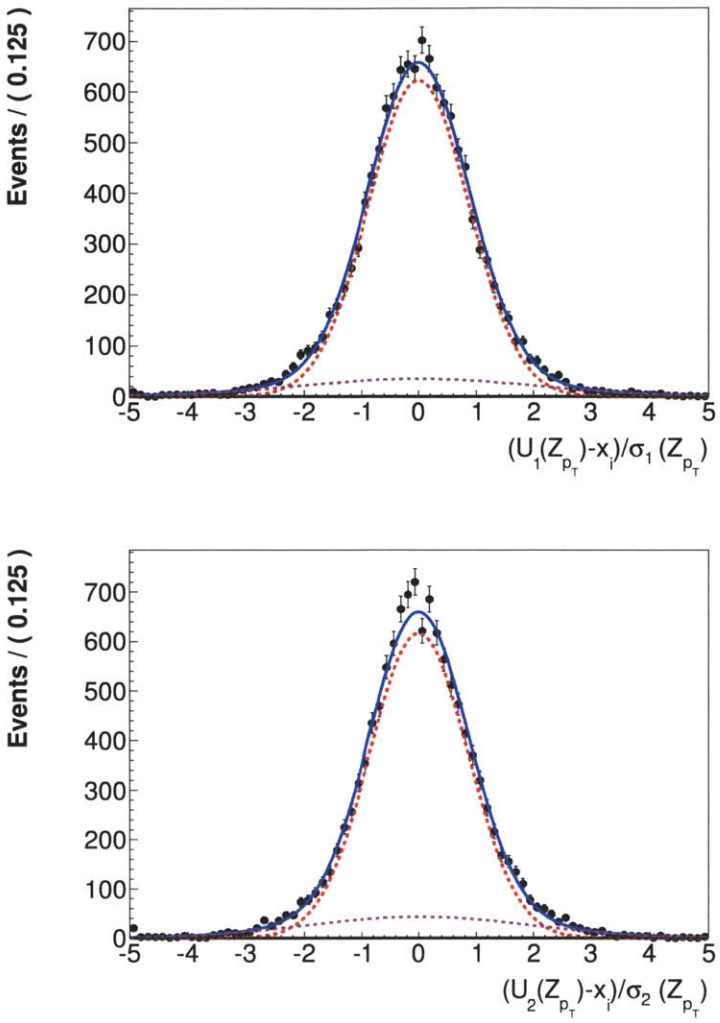

Figure 9-10: Fit to the residuals of the recoil with a double Gaussian on 35.9 pb^{-1} of data for U_1 (top) and U_2 (bottom)

written as:

$$\sigma_{\mathrm{mean}}(p_{\mathrm{T}}^{\mathrm{V}}) = f\sigma_1(p_{\mathrm{T}}^{\mathrm{V}}) + (1-f)\sigma_2(p_{\mathrm{T}}^{\mathrm{V}}) \ , \tag{9.5}$$

where σ_1 is the small Gaussian width, σ_2 is the large Gaussian width, f is the fraction of σ_1 and consequently $1-f$ is the fraction of σ_2. To obtain the two widths of the double Gaussian, a fit for σ_{mean} is performed by applying the unbinned fit and rescaling the fit result by $\sqrt{2\pi}/2$. The two widths of the Gaussian are then determined from a unbinned profile likelihood fit to the the pull variable a_{i}.

A fit to the pull variable in a_{i} is shown in figure 9-10. This distribution has a clear double Gaussian resolution. Taking the two resolution parameters σ_1 and σ_2 from this fit to a_{i} and the average of the two Gaussians, $\sigma_{\mathrm{mean}}(p_{\mathrm{T}})$, we determine the

double Gaussian parameters $\sigma_1(p_{\mathrm{T}}^{\mathrm{Z}})$, $\sigma_2(p_{\mathrm{T}}^{\mathrm{Z}})$, $f(p_{\mathrm{T}}^{\mathrm{Z}})$ through equation 9.5.

9.3.5 Application

Once a parametrization for the Z boson recoil is determined we apply a data/simulation correction to the W Monte Carlo simulated U_1 and U_2 distributions (section 9.4) and recalculate the $\not\!\!E_{\mathrm{T}}$ distribution (using equation 9.1). Figure 9-11 shows the corrected W boson $\not\!\!E_{\mathrm{T}}$ distribution after data/simulation corrections comparing a single Gaussian parametric model of U_1 and U_2 to a double Gaussian parametric model of U_1 and U_2. From the figure, the double Gaussian resolution model determines a $\not\!\!E_{\mathrm{T}}$ distribution less wide and models the distribution beyond 40 GeV better. The uncertainty band given by the red and the blue distributions covers the data along the whole range of $\not\!\!E_{\mathrm{T}}$ beyond 30 GeV. The bottom plot in figure 9-11 represents the closure test whereby the extrapolation to the $\not\!\!E_{\mathrm{T}}$ distribution is performed using the recoil parameters from fitting Monte Carlo simulation. Following the extrapolation all points are within 2% of the true distribution. The difference below the plot is defined as the fractional difference and is given by

$$\text{Frac. Difference} = \frac{N_{\text{data}} - N_{\text{prediction}}}{N_{\text{prediction}}} \ . \tag{9.6}$$

9.3.6 Shape p_{T} Variation Uncertainty

In fitting the pull variable a_{i} for events over the whole p_{T} range , we have implicitly made the assumption that the same double Gaussian resolution shape describes the resolution over the whole range of boson p_{T}. In reality, this resolution function can change with boson p_{T}. To account for variations of the double Guassian shape we apply a small correction.

To apply the correction, we a select events in the region $> 2\sigma_{\text{mean}}$. This creates a sample where the contribution from σ_2 is more than 50 percent. By selecting all events $> 2\sigma_{\text{mean}}$ and fitting a polynomial to $|U_{\mathrm{i}} - U\,(p_{\mathrm{T}})\,|$ in this region, we determine a correction factor $\mathrm{corr}(p_{\mathrm{T}}^{\mathrm{V}})$ to σ_2, which modifies σ_2 by

$$\sigma_{2-\mathrm{Corr}}(p_{\mathrm{T}}^{\mathrm{Z}}) \ = \ \left(\frac{\mathrm{corr}\,(p_{\mathrm{T}}^{\mathrm{Z}})}{\mathrm{corr}\,(p_{\mathrm{T}}^{\mathrm{Z}}(\mathrm{mean}))} \right) \sigma_2 \ . \tag{9.7}$$

Figure 9-12 illustrates the resulting fit.

To correct the full distribution, first note that three parameters describe a double Gaussian resolution. These are constrained by a single equation (equation 9.5) leaving two free parameters. The correction $\mathrm{corr}(p_{\mathrm{T}}^{\mathrm{V}})$ modifies only one of the two free parameters, thus to solve for the corrected shape, we make one of two assumptions:

1. The resolution σ_1 is held constant with respect to σ_{mean} and the fraction of f is recalculated following the correction to σ_2

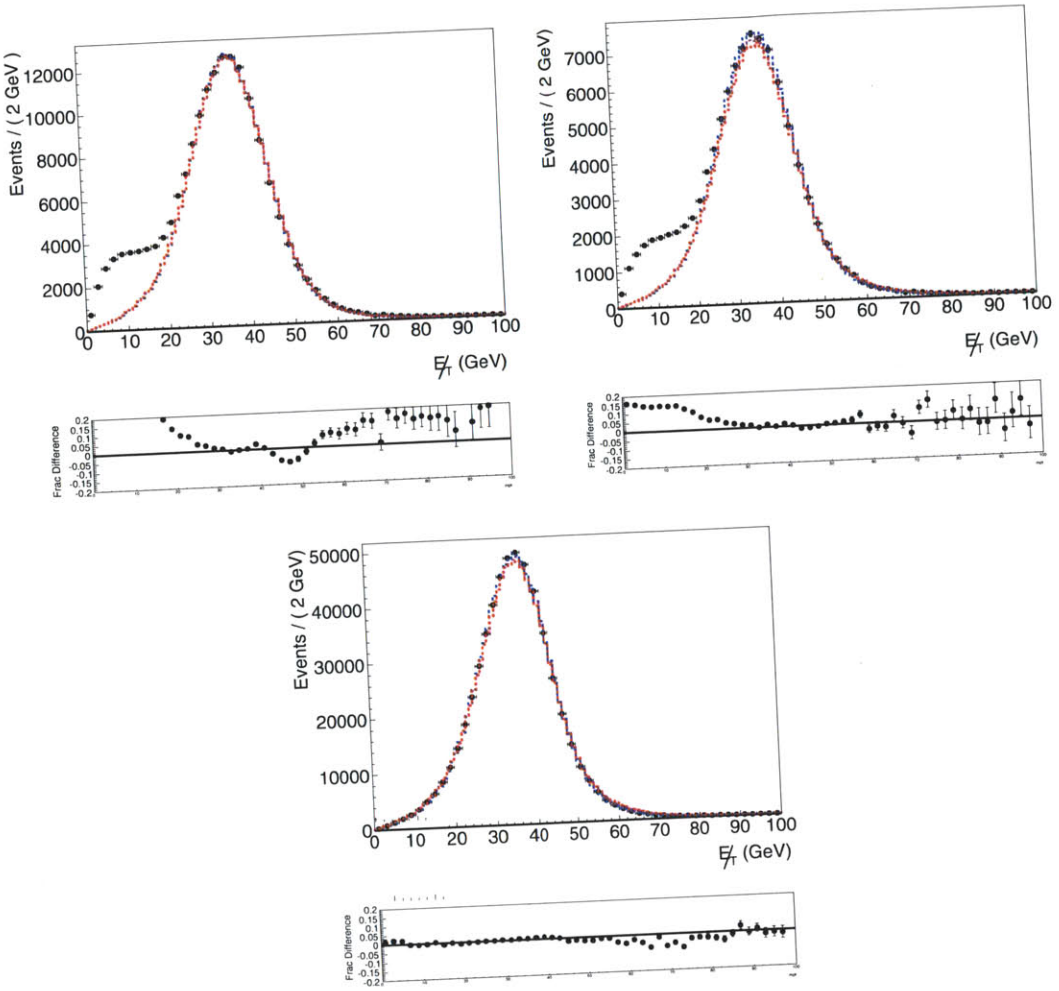

Figure 9-11: Extrapolation of the $\not\!\!E_T$ distribution using Gaussian resolution function (top left) and a double Gaussian resolution function (top right). On the bottom is the Monte Carlo simulated $\not\!\!E_T$ compared to the simulation predicted $\not\!\!E_T$ using the double Gaussian recoil model. The black points below is the residual data/Monte Carlo simulation disagreement.

2. The fraction f is held constant and σ_1 is recalculated following the correction to σ_2

The first assumption yields a model description closer to the predicted truth in simulation and is thus used. A systematic uncertainty, σ is assigned on the value of σ_1 given by the maximum variation of $\sigma_1/\sigma_{\text{mean}}$ for $p_T^Z < 50$ GeV when f is held constant. This systematic uncertainty is propagated into the high and low uncertainty templates of the final double Gaussian shape. The variation of $\sigma_1/\sigma_{\text{mean}}$ is found to be 5% in data and 2 % in simulation.

Applying corr(p_T) of this on the final $\not\!\!E_T$ shape gives an effect on a the final $\not\!\!E_T$ that is negligible; however the systematic uncertainties corresponding to this assumption

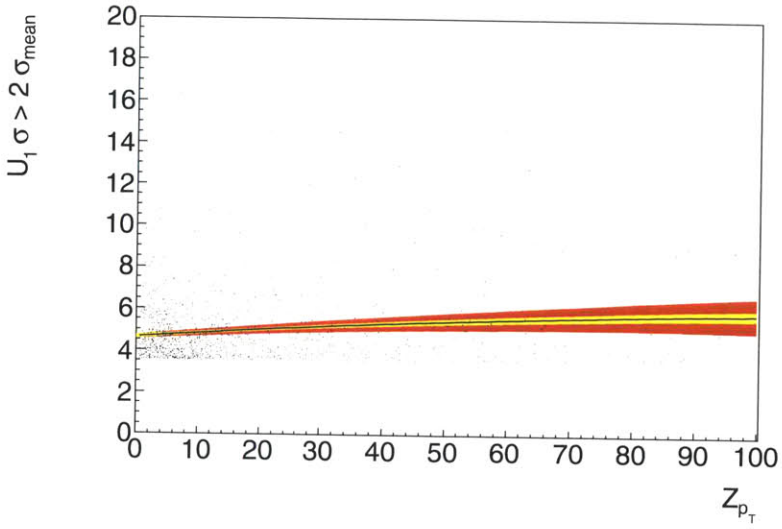

Figure 9-12: Fit to the pull a_i for events $> 2\sigma_{\text{mean}}$

are not. These are thus propagated in with the uncertainties from the fit to determine high and low fluctuated $\not\!\!E_T$ templates.

Figure 9-13, shows the $\not\!\!E_T$ distributions given the application of corr(p_T^V) under two possible assumptions, either fixing f or fixing σ_1. The uncertainty band of both methods cover fluctuations in the data. Also shown is a third correction, where the parameters are not corrected given one of the previous assumptions. The large uncertainty bands in this third plot reflects the large uncertainty from limited sample of events $> 2\sigma_{\text{mean}}$.

9.4 Calculation of the scale factors

The fits described in the preceding section provide response and resolution curves for U_1 and U_2 in Z boson data and simulation. These curves are utilized to determine data/simulation scale factors that are applied to the results of the same recoil fit to W boson simulation. The form of the scale factors is shown in equation 9.4. The application of the scale factors is written as:

$$\sigma_i = \frac{\sigma_Z^{data}(p_T^W)}{\sigma_Z^{MC}(p_T^W)} \sigma_W^{MC}(p_T^W) \ . \tag{9.8}$$

The correction is performed on the small resolution σ_1, the large resolution σ_2, the mean of the two resolutions σ_{mean}, the correction corr to σ_2, and the response parameters $U_i(p_T)$ $(i \in 1, 2)$. This avoids corrections to the relative fraction f, which is recalculated using equation 9.5.

In addition to generating corrected σ_i and U_i, the uncertainties, both statistical

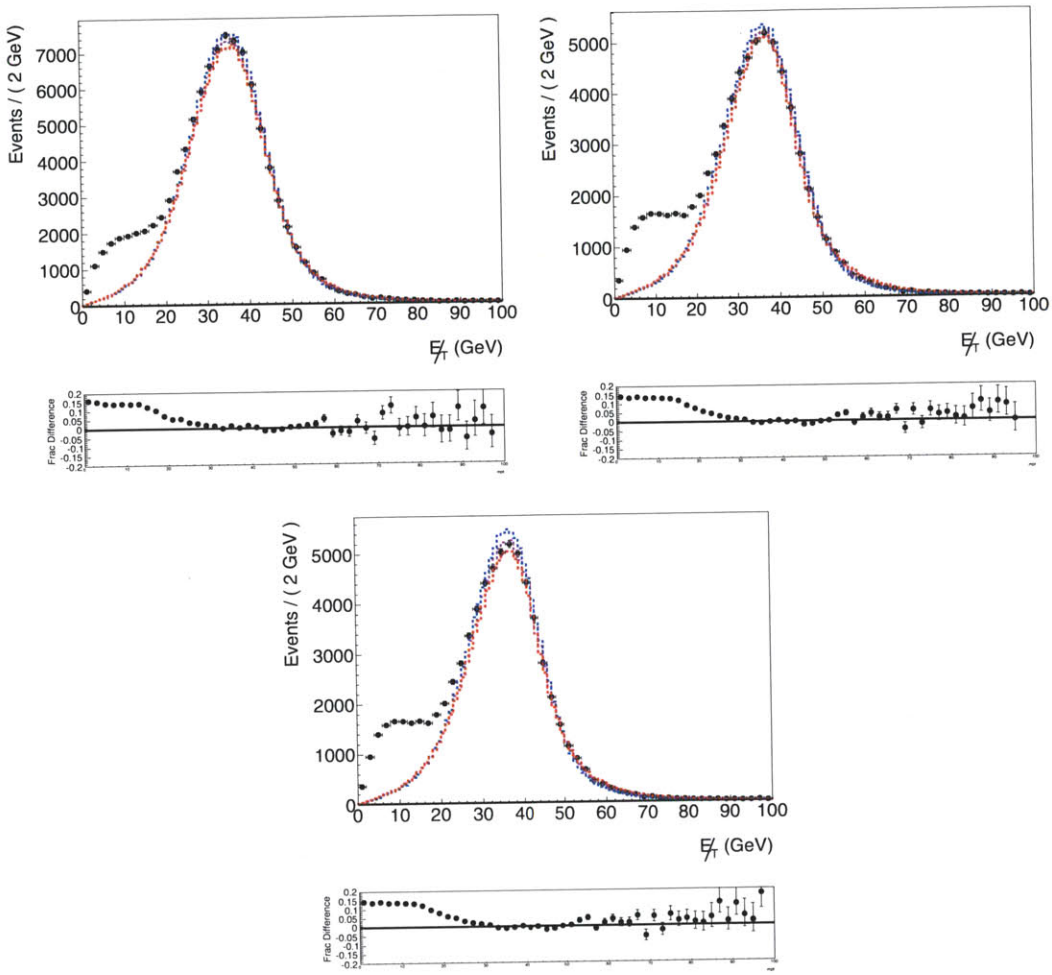

Figure 9-13: Extrapolation of the $\not\!\!E_{\rm T}$ distribution using a double Gaussian where σ_2 is corrected by fixing σ_1 (top left) fixing f (top right) or not further correcting (bottom). The black points below show the residual data/Corrected MC disagreement.

and systematic, are propagated through all of the fit parameters to generate high and low uncertainty templates. The contribution to the uncertainties come fifty percent from the fits to double Gaussian and the resolution parameter $\sigma_{\rm mean}$, and fifty percent from the correction of σ_2.

The full recipe of correction and application to recalculate the $\not\!\!E_{\rm T}$ distribution follows as:

1. Calculate the scale factors data/simulation on all parameters σ_1,σ_2,$\sigma_{\rm mean}$, and corr
2. Rescale the W simulation fit parameters σ_1,σ_2,$\sigma_{\rm mean}$, and corr by multiplying through the scale factors
3. Build the high and low uncertainty templates by propagating the uncertainties

through to get $\pm\sigma$ modified W boson fit parameters

4. Apply the correction on σ_2 given by equation 9.7
5. Calculate the relative fraction f given $\sigma_1/\sigma_{\text{mean}}$ is constant
6. For each U_{i} randomly sample double Gaussian distribution dictated by the rescaled W fit parameters to determine the recoil $\vec{U}$
7. Combine the recoil $\vec{U}$ and the lepton $\vec{\ell}$ back to determine the $\not\!\!E_{\text{T}}$

The fits to determine the resolution in data use the reconstructed p_{T}^{V} in Z boson data, but generated p_{T}^{V} in W and Z boson simulation. Thus, the data/simulation scale factor implicitly includes the resolutions of the lepton reconstructed p_{T} in the fits. The effect of this on the total $\not\!\!E_{\text{T}}$ resolution increases it by about 0.15 GeV, a value well within uncertainties. However, to minimize this effect when calculating the W boson $\not\!\!E_{\text{T}}$ distribution by adding the lepton $\vec{p_{\text{T}}}$ with the corrected recoil $\vec{U}$, we use the generator level lepton $\vec{p_{\text{T}}}$ with the energy scale corrections applied (chapter 7).

In figures 9-14 to 9-18 the various resolution functions and scale factors for Z boson data, W boson simulation, and Z boson simulation are shown. The uncertainties on these plots come from the propagation of the covariance matrix to all polynomial fits combined with the uncertainty from the double Gaussian fit. With the additional pileup simulation inserted in the most recent simulation, the scale factors are all close to unity. Deviations from unity in the scale factor are predominantly a result of the deviations between the Z2 tune and data.

9.4.1 Scale factor variation

An additional systematic uncertainty results from the fact that the scale factor from Z bosons between data and simulation may not be the exact same as the scale factor between W boson data and simulation.

The W and Z bosons have small differences in their production mechanisms. These differences result from differences in the quark composition and the mass difference of the two bosons. In figure 9-14 we plot the resolution parameters for Z boson simulation, W boson simulation, and Z boson data. The resolutions have a 10% discrepancy between W and Z boson simulation. This discrepancy is a direct result of the differences in the W and Z boson production mechanisms. Such a difference in the production mechanisms also leads to a different $\sum E_{\text{T}}$ distribution, plotted in figure 9-19.

In order to mitigate this difference and determine a systematic uncertainty on the scale factor, both the Z boson data and Z boson simulation are reweighted by the ratio of the W boson data $\sum E_{\text{T}}$ distribution to Z boson data $\sum E_{\text{T}}$ distribution. The reweighted data is then fit with the full recoil fit framework determining the resolution parameters and the scale factors. The results of the fit on U_1 are plotted in figure 9-16. The reweighting modifies σ_{mean} to lie on top of the W boson fit parameters. After the reweighting the two double Gaussian resolutions σ_1 and σ_2

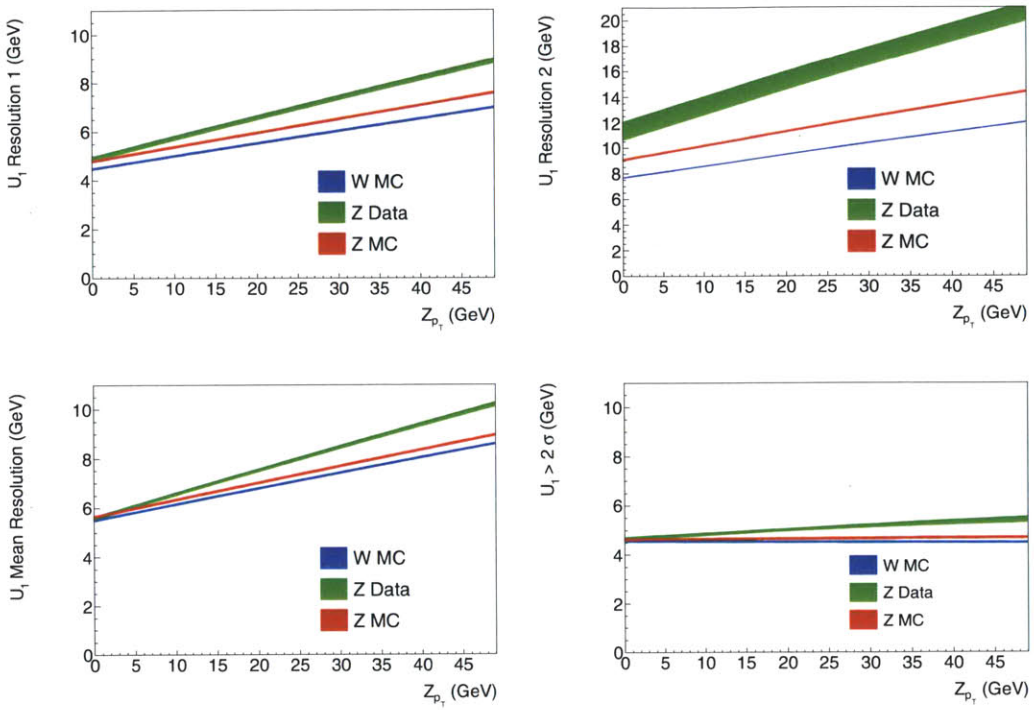

Figure 9-14: Recoil distributions for the various resolutions and correction of U_1 the band on each parameter corresponds to the propagated polynomial and double Gaussian fit uncertainties.

are nearly identical to the respective W boson resolutions. In figures 9-17 and 9-18 the data/simulation scale factors of the reweighted Z boson fits are compared to the original Z boson fits. In order to ensure agreement between the reweighted and the unweighted scale factors the uncertainties are increased on the parameters σ_1, σ_2, and σ_{mean} by a factor of three. This increase is performed in both figures 9-17 and 9-18 leading to the observed agreement. The increase in the uncertainties in these three parameters is taken as an additional systematic uncertainty propagated into the high and low uncertainty templates.

9.5 Corrections at NNLO

In addition to the aforementioned corrections, an additional correction to the $\not\!\!E_{\text{T}}$ distribution is applied to account for the higher order NNLO and NNNLL resummation terms. The correction is determined by calculating the ratio of the boson p_{T} distribution of Resbos to generator level Powheg where both have the appropriate acceptance cuts applied (in the same manner as as done in chapter 8). In figure 9-20, the W boson $\not\!\!E_{\text{T}}$ distribution in Powheg, and Resbos reweighted Powheg are shown. The reweighted distribution improves the data simulation agreement for $\not\!\!E_{\text{T}} > 70$ GeV.

In light of the fact that the Z boson sample is independent to the W boson sample,

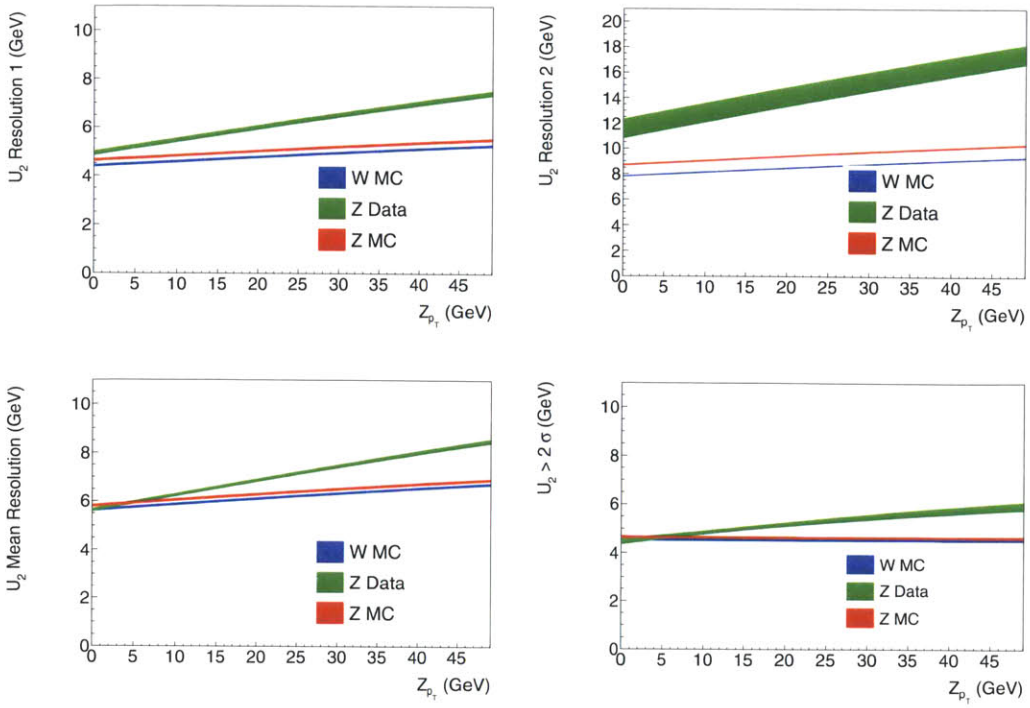

Figure 9-15: Recoil distributions for the various resolutions and corrections of U_2 the band on each parameter corresponds to the propagated polynomial and double Gaussian fit uncertainties.

an additional "data" correction to the sample is performed. To perform this correction the p_{T} dependent weight given by data/(Resbos corrected simulation) scale factor of Z bosons is fit with a fifth order polynomial (shown figure 9-21) determining a weight function in terms of boson p_{T}. This weight function is applied to Resbos reweighted W boson simulation. The result of this distribution is shown in the right of figure 9-20; the change between the Resbos reweighted Powheg $\not\!\!E_{\mathrm{T}}$ distribution and the data reweighted $\not\!\!E_{\mathrm{T}}$ distribution is below one percent over the whole range.

9.6 Additional theoretical uncertainties

The final $\not\!\!E_{\mathrm{T}}$ shape must also incorporate additional uncertainties coming from the theoretical mismodeling of neutrino p_{T} distribution. The two largest contributions originate from the parton distribution function uncertainties and from the uncertainty on the boson p_{T} model.

To determine the uncertainty from the parton distribution functions, the $\not\!\!E_{\mathrm{T}}$ distribution is reweighted by the full CT10 PDF uncertainty sets using the procedure outlined in chapter 8. The sum over all of the PDF uncertainty sets determine an uncertainty band on $\not\!\!E_{\mathrm{T}}$ distribution. The result of this band normalized to the default $\not\!\!E_{\mathrm{T}}$ shape is shown in figure 9-22. The effect of the PDF uncertainties are

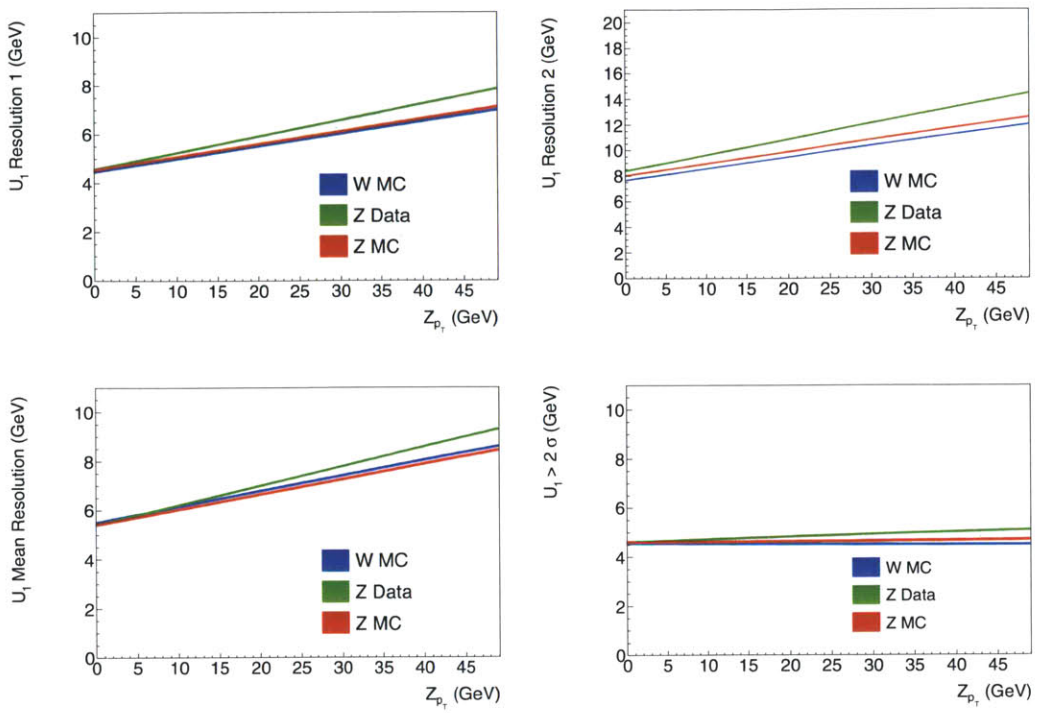

Figure 9-16: Recoil distributions for the various resolutions and correction of U_1 after reweighting the Z boson data $\sum E_{\mathrm{T}}$ distribution to the W boson data $\sum E_{\mathrm{T}}$ distribution. The uncertainty bands on each parameter are artificially suppressed due to the reweighting procedure.

bounded by the $\not\!\!E_{\mathrm{T}}$ uncertainties, thus no additional systematic uncertainties on $\not\!\!E_{\mathrm{T}}$ model are quoted.

The uncertainty on higher order QCD corrections, both NNNLL and NNLO, is determined by performing the cross section measurement before and after the NNLO weighted correction is applied. The overall difference in the cross section measurement is found to be less than 0.08 percent.

9.7 Modified cumulant fit

A final cross check was performed by expanding the moment defined by $|U_{\mathrm{i}}-U_{\mathrm{i}}^{mean}\left(p_{\mathrm{T}}^{\mathrm{V}}\right)|^{n}$ in orders of n. These additional moments in n is written as

$$I_{\mathrm{n}}\left(\sigma_1,\sigma_2,f,....\right) \;=\; \int_{-\infty}^{\infty} dx|x-x_{\mathrm{i}}|^{n}p(x)\;, \tag{9.9}$$

where $p(x)$ is the probability distribution function of the resolution of U_{i}. For $p(x)$ a double Gaussian resolution, an integral over x fixes I_{n} to be a function of the resolution parameters σ_1, σ_2, f, and additional constants. Expanding out to three

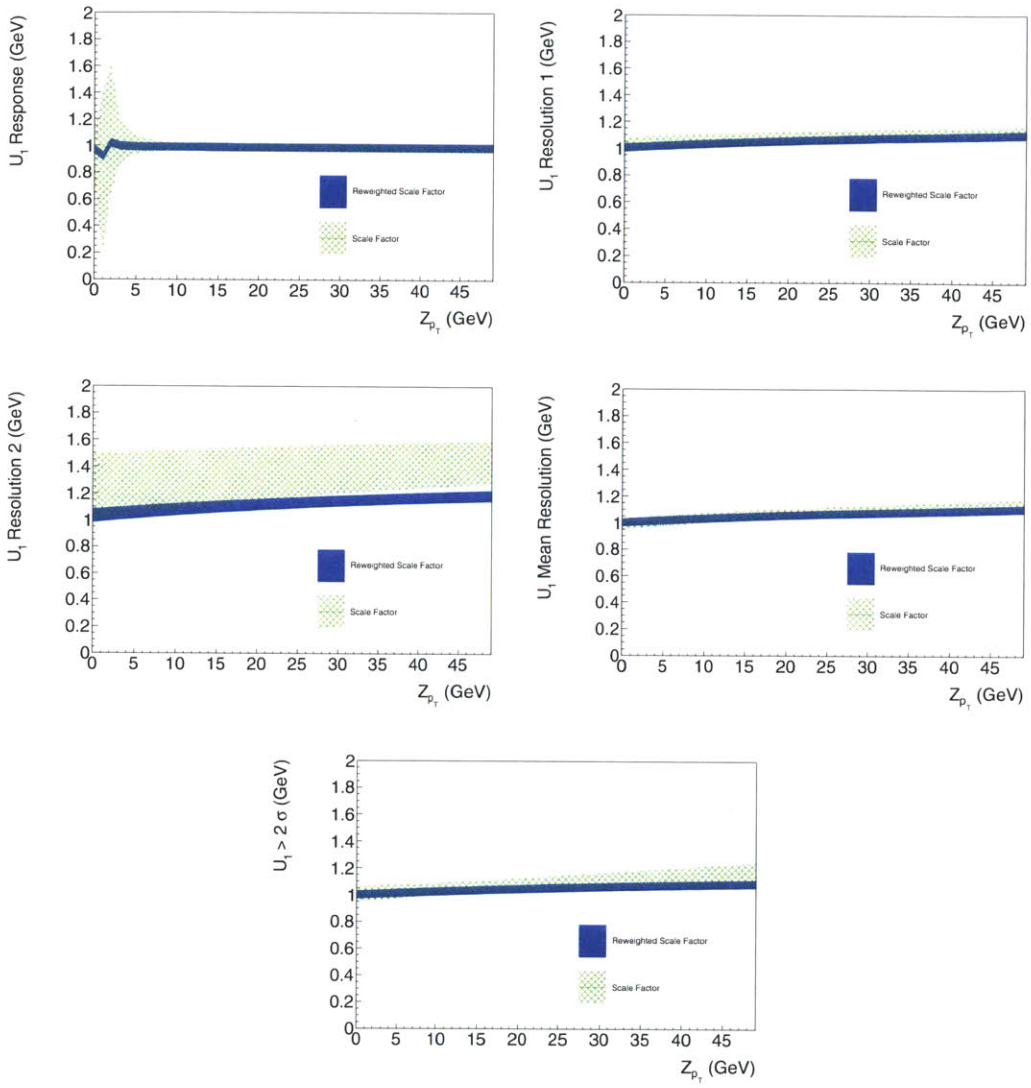

Figure 9-17: Scale factor for the U_1 response and various resolutions. C orrection of U_1 the green band corresponds to the unweighted fit to data and the blue band to a fit on data reweighted by $\sum E_{\mathrm{T}}$ to better approximate W boson data. Excluding the correction parameter (bottom right), the uncertainties on the green band have been inflated by a factor of 3 to force agreement between the two scale factors

orders in the moment n, gives a set of three equations which is used to solve for all the parameters of the double Gaussian. This defines another method for which to determine the double Gaussian parameters.

1. Fit a polynomial to the three forms $|U_{\mathrm{i}} - U^{mean}(p_{\mathrm{T}}^{\mathrm{V}})|^n$ where $n \in 1, 2, 3$

2. Solve for the double Gaussian resolution given the system of equations defining I_{n}

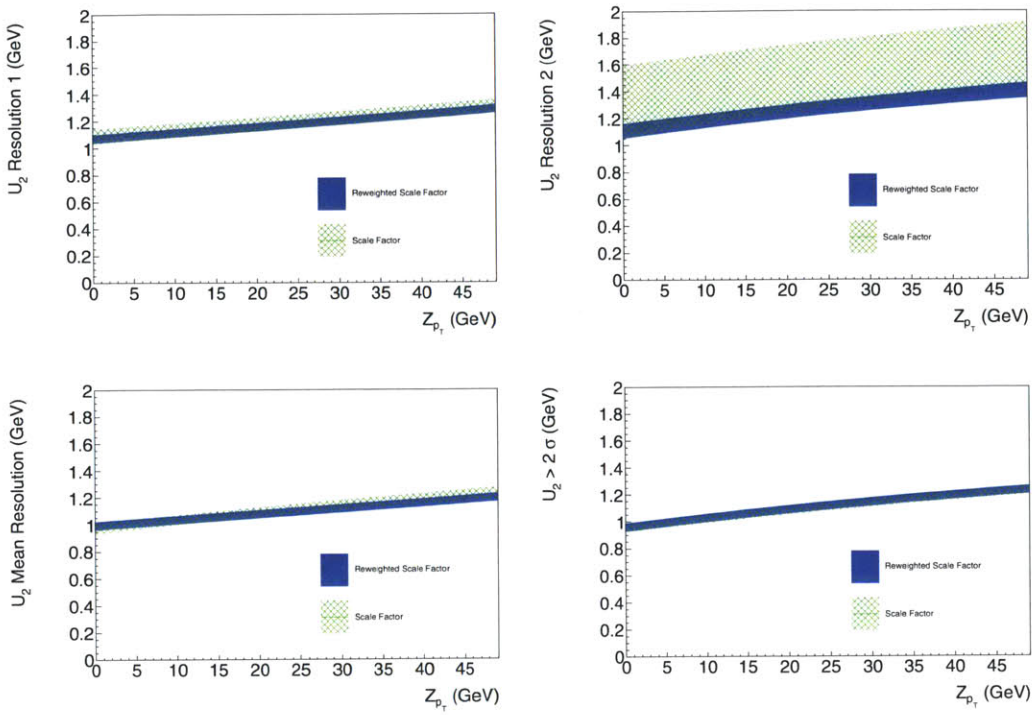

Figure 9-18: Scale factor for the various resolutions and correction of U_2 the green band corresponds to the unweighted fit to data and the blue band to a fit on data reweighted by $\sum E_{\mathrm{T}}$ to better approximate W boson data. Excluding the correction parameter (bottom right), the uncertainties on the green band have been inflated by a factor of three to force agreement between the two scale factors

3. Apply the corrected resolution model to simulation.

This form of expansion is very similar to a cumulant expansion, thus we denote this a modified cumulant expansion. With this method the $\not\!\!E_{\mathrm{T}}$ distribution was reproduced to within three percent for $\not\!\!E_{\mathrm{T}} < 70$ GeV. The uncertainties were not determined with this method due to the complexity of the uncertainty propagation.

9.8 Calculation flow

The full calculation proceeds by

1. Use the unbinned method to calculate the mean of the two resolutions $\sigma_{\mathrm{mean}}\left(p_{\mathrm{T}}^{\mathrm{V}}\right)$
2. Fit the pull of the residuals $(x - x_{\mathrm{i}})/\sigma_{\mathrm{mean}}(p_{\mathrm{T}}^{\mathrm{V}})$ integrated over $p_{\mathrm{T}}^{\mathrm{V}}$ to a double Gaussian
3. Plot the absolute value of the residual $|a_{\mathrm{i}}| = |x - x_{\mathrm{i}}|/\sigma_{\mathrm{mean}}(p_{\mathrm{T}}^{\mathrm{V}})$ for all values where $|a_{\mathrm{i}}| > 2$

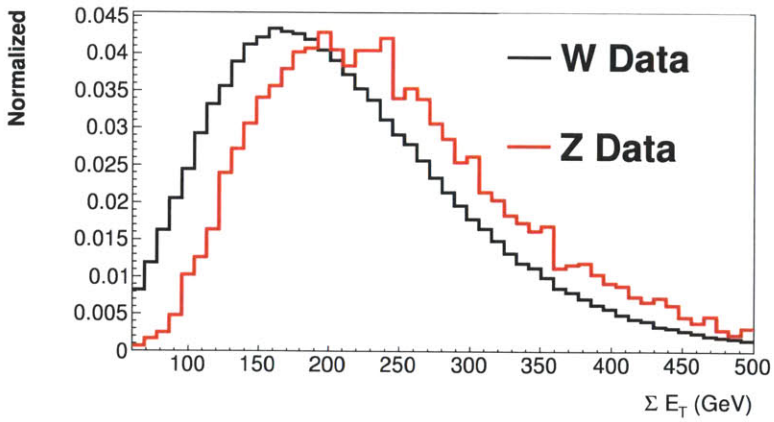

Figure 9-19: W and Z boson ΣE_{T} distributions in data

4. Fit the absolute value of the residuals, where $|a_{\mathrm{i}}| > 2$, to a second order polynomial to determine the function $\mathrm{corr}(p_{\mathrm{T}}^{\mathrm{V}})$

5. Calculate the corrected $\sigma_{2-\mathrm{Corr}}(p_{\mathrm{T}}^{\mathrm{V}})$

6. Calculate the corrected $\sigma_{1-\mathrm{Corr}}(p_{\mathrm{T}}^{\mathrm{V}})$ where the fraction $\sigma_1/\sigma_{\mathrm{mean}}$ is held constant

7. Perform this method for both U_1 and U_2 on Z boson data, Z boson simulation, and W boson simulation

8. Apply the scale factor corrections to the W boson recoil fit parameters

9. Sample from the double Gaussian to construct the modified recoil U_{i}

10. Recalculate the W boson $\not\!\!E_{\mathrm{T}}$ distribution by adding the modified U_{i} and the lepton together

The final step, where we recalculate the $\not\!\!E_{\mathrm{T}}$ distribution, the lepton energy scale is modified to match the fitted energy scale in data. Uncertainties on the lepton energy scale can further be propagated into the $\not\!\!E_{\mathrm{T}}$ distribution, by modifying this lepton energy scale with the assigned uncertainties.

In each method where a fit is applied, an uncertainty associated with that value is propagated through. The uncertainties in the double Gaussian method originate from three different sources.

1. The uncertainties on the polynomial fits of the resolution σ_{mean} and corr

2. The uncertainties on the double Gaussian σ_1 and σ_2

3. Systematic uncertainties

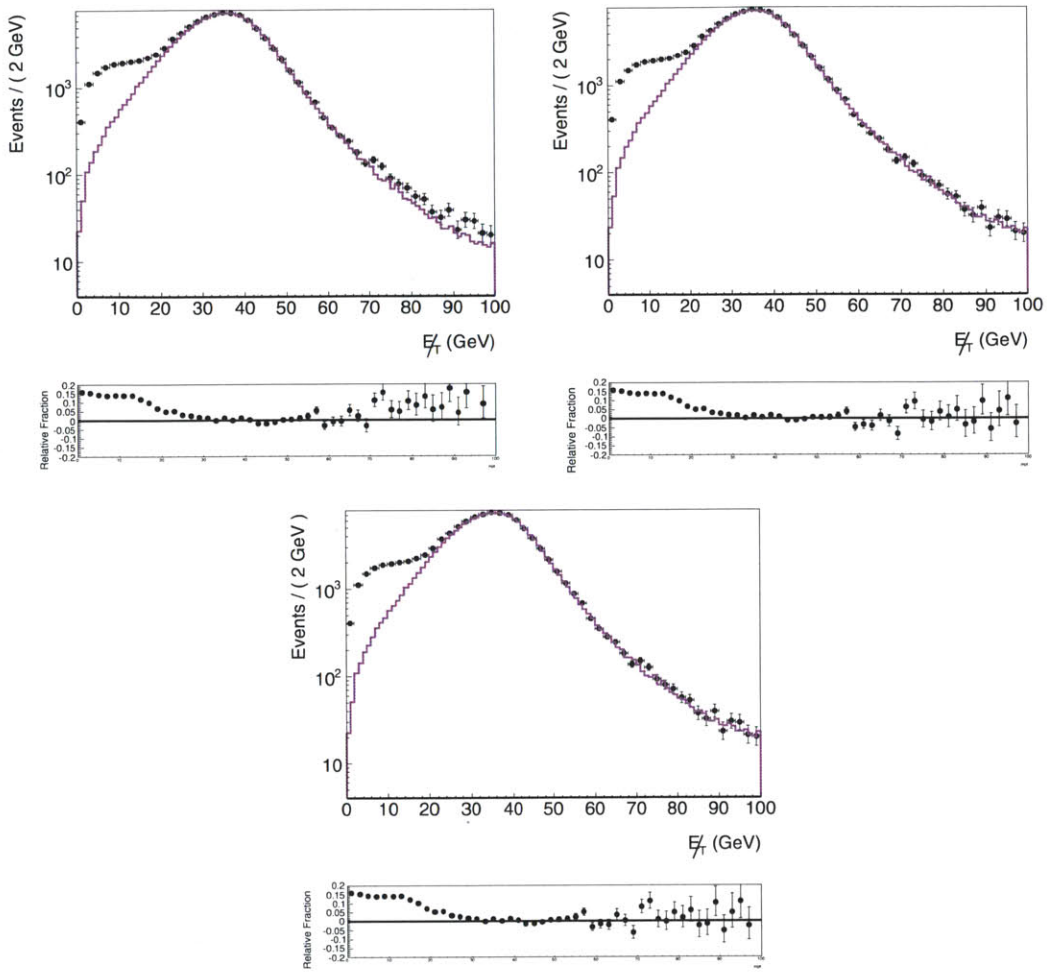

Figure 9-20: $\not\!\!E_T$ distribution before (top left) and after (top right) the Resbos NNLO Corrections, and after data p_T corrections (bottom). The black points below show the residual data/Corrected MC disagreement.

In the first set of uncertainties listed above, we apply a polynomial fit to a series of points. The uncertainties that result from the polynomial fits are propagated through using the full covariance matrix. The second set of uncertainties, those of the double Gaussian fit on σ_1 and σ_2 are obtained from the fit of the double Gaussian to the pull a_i. The final set of uncertainties, the systematic uncertainties, are determined from two different contributions. The first systematic uncertainty comes from the uncertainty on σ_1 given that $\sigma_1/\sigma_{\text{mean}}$ is assumed constant (section 9.3.6). The second systematic uncertainty comes from the difference in the scale factors when Z boson $\sum E_T$ distribution is reweighted to the W boson $\sum E_T$ distribution (discussed in section 9.4.1). This systematic uncertainty requires us to inflate the uncertainties on the three resolution parameters σ_1 σ_2, and σ_{mean} by a factor of three. The final resulting $\not\!\!E_T$ distribution compared with the predicted $\not\!\!E_T$ distribution is shown

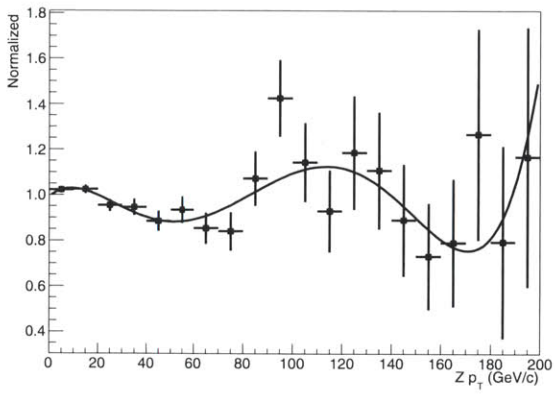

Figure 9-21: Z→ $\mu\mu$ data/Resbos reweighted Powheg simulation p_{T} distribution. The line is a fit to a fifth order polynomial

in figure 9-23 . The deviation from the simulated prediction results mainly from the higher U_1 and U_2 resolutions in data. The uncertainty band on the template is maximized along the falling edge of the W boson $\not\!\!E_{\mathrm{T}}$ distribution near $\not\!\!E_{\mathrm{T}} = 60$ GeV/c. The difference parameter χ below the plots is defined to be

$$\chi \;=\; \frac{N_{\mathrm{central}} - N_{\mathrm{fluctuated}}}{\sqrt{N_{\mathrm{central}}}}\;, \tag{9.10}$$

where N_{central} is the number of events expected in 35.9 pb^{-1} per bin for the central value W boson template and $N_{\mathrm{fluctated}}$ are the high and low uncertainties.

9.9 Summary

In this section we have described a fitting framework that determines the two recoil parameters U_1 and U_2. This fitting framework is then applied to Z boson data, Z boson simulation and W boson simulation. The ratio of the fit results on the Z boson data and simulation are applied to the W boson fit results to come up with a set of corrected recoil parameters which determine the true W boson $\not\!\!E_{\mathrm{T}}$ distribution. The $\not\!\!E_{\mathrm{T}}$ distribution is determined by: taking boson p_{T} kinematics from simulation, determining the recoil distributions for that p_{T}, sampling the recoil distributions, and then adding the sampled recoil distribution to the lepton $\vec{p}_{\mathrm{T}}$ from simulation. Following the $\not\!\!E_{\mathrm{T}}$ determination, a weight factor incorporating Resbos and Z boson data is applied to the W boson p_{T} distribution to determine a corrected $\not\!\!E_{\mathrm{T}}$ distribution. Uncertainties, both systematic and statistical, are propagated through, yielding high and low uncertainty templates.

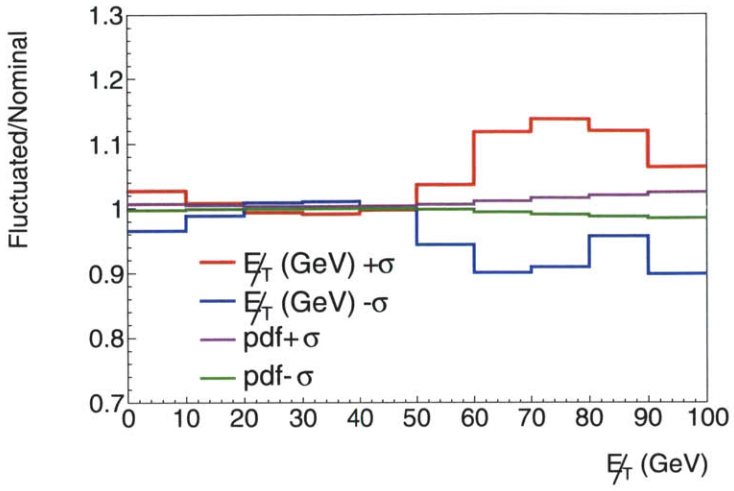

Figure 9-22: Comparison of high (red) and low (blue) uncertainty templates from the recoil prediction normalized per bin by default recoil corrected $\not\!\!E_T$ distribution template with high (purple) and low (green) PDF reweighted uncertainty templates normalized by the default $\not\!\!E_T$ distribution template

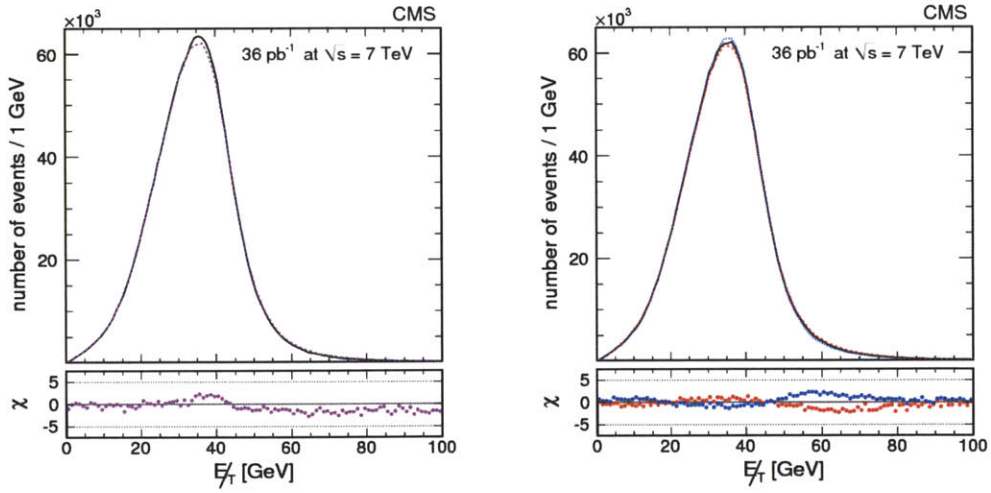

Figure 9-23: Left: Comparison of the recoil corrected $\not\!\!E_T$ template (purple) with the default simulation (black). Right: Comparison of the default template with the high (red) and low (blue) predicted uncertainties from the recoil model.

Chapter 10

Backgrounds

The separation of events in the signal selection into QCD, Electroweak, top, and W boson events is performed by fitting the $\not\!\!E_{\mathrm{T}}$ distribution. This observable is chosen because of its excellent separation power and simplicity in modeling (discussed more in section 10.1.3). The W boson, Electroweak, and top $\not\!\!E_{\mathrm{T}}$ shapes are modeled well by Monte Carlo simulation following corrections to the boson recoil (chapter 9). Thus, we fix the Electroweak and top backgrounds to the W signal template using their predicted NNLO cross section ratios. The QCD background is not modeled well by a Monte Carlo simulation. To model the $\not\!\!E_{\mathrm{T}}$ shape of the QCD, an extrapolation of the non-isolated QCD events into the isolated sample is performed by fitting the $\not\!\!E_{\mathrm{T}}$ distribution to an empirical function and determining the trend in isolation of the function's parameters.

Another observable, transverse mass (m_{T}), is used as a cross check to the $\not\!\!E_{\mathrm{T}}$ distribution. It is defined as the combined lepton plus $\not\!\!E_{\mathrm{T}}$ mass in the transverse plane:

$$m_{\mathrm{T}} = \sqrt{(|\ell_{\mathrm{T}}| + |\not\!\!E_{\mathrm{T}}|)^2 - \left(\vec{\ell_{\mathrm{T}}} + \vec{\not\!\!E_{\mathrm{T}}}\right) \cdot \left(\vec{\ell_{\mathrm{T}}} + \vec{\not\!\!E_{\mathrm{T}}}\right)}\ , \tag{10.1}$$

Transverse mass also has excellent separation power between the W boson signal and the QCD background; however it requires an accurate description of the $\not\!\!E_{\mathrm{T}}$, the angle between the $\not\!\!E_{\mathrm{T}}$ and the lepton, and the lepton kinematics.

10.1 Background composition of QCD

A QCD background process is any process, with the exception of $t\bar{t}$ production, where the main interaction is performed with the strong force. This includes jet production, minimum bias production, and heavy flavor quark production. QCD processes that yield an isolated muon are classified into several specific types of decays:

- Heavy flavor decays: a heavy flavored hadron with either a charm or b quark cascades down to a lighter flavor, producing a muon, neutrino, and lighter flavored hadron (figure 10-2)

- Decays in flight: a light meson with a relatively long lifetime (typically a pion or a kaon) decays into an isolated muon
- Punch through: a very high energy meson (typically a pion) passes through the inner detector, the solenoid, and partially into the muon chambers.

The first two decays comprise the largest source of QCD background. The third process, punch through mesons, are completely eliminated from the selection because of the requirement that each muon have at least two well reconstructed segments [72]. The quark composition of the signal region ($isolation < 0.1$) and regions of slightly more isolation are shown in figure 10-1. For regions where the muon is non-isolated, the heavy flavor fraction contributes to 90 percent of the QCD background events. For isolated muons in the signal region the heavy flavor contribution decreases to 80 percent that of the total QCD background. The variation in the heavy flavor fractional contribution and the ability to model it in data contributes most to the systematic uncertainty on the QCD event yield.

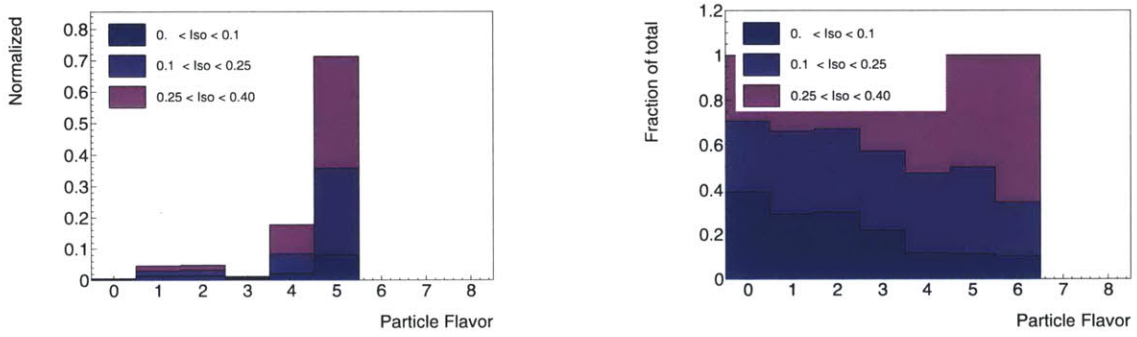

Figure 10-1: Composition of muon decays from tagged QCD events (left) and relative per bin contribution (right) of muon decays from the tagged QCD events passing all muon identification cuts and split into several regions of isolation. The integer on the x-axis denotes the particle composition of the muon decay, which consist of 0-unidentified, 1-up quark, 2-down quark, 3-strange quark, 4-charm quark, 5-bottom quark. 6-top quark

10.1.1 Heavy flavor decays

A typical diagram of a heavy flavor decay that produces muons is shown in figure 10-2. The decay consists of a three body decay of a heavy flavored meson yielding a neutrino, a meson, and a muon. In order for the muon to pass the tight isolation criteria in the signal region ($\chi_{\text{iso}} < 0.1$), the energy of the decaying meson must be low or far away from the muon. In heavy flavor decays, the $\not{E}_{\text{T}}$ varies by large amounts; however, it is biased by the isolation selection to be larger so that the energy deposits from the meson resulting from the heavy flavor decay are small. Due to the

long lifetime of b quarks, heavy flavor muons will, in some instances, decay far away from the primary vertex collision. Thus, further separation of heavy flavor events is performed by cutting on impact parameter. Additionally, heavy flavor production typically appears in $b\bar{b}$ or $c\bar{c}$ pairs, implying the activity of the b(c) quark decaying into a muon is mirrored by another b(c) decay.

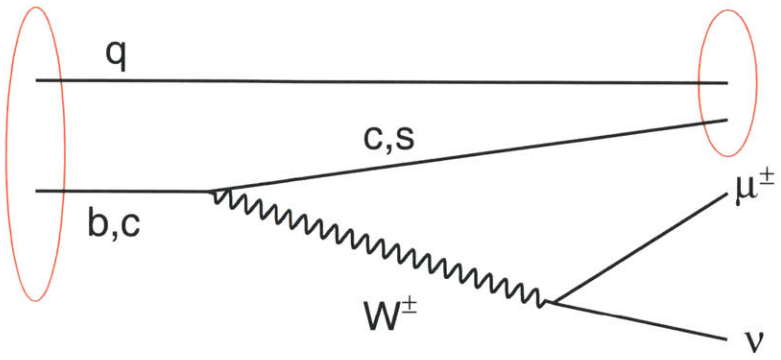

Figure 10-2: Typical heavy flavor decay. The red circles imply the quark (q) and the heavy flavor quark (b, c) are confined together to form a meson

Figure 10-3 shows the variation of the $\not\!\!E_{\mathrm{T}}$ and $\sum E_{\mathrm{T}}$ as a function of isolation for both the full QCD region and a b decay enhanced region applying $d_0 > 0.01$ cm. A linear dependence in both $\sum E_{\mathrm{T}}$ and $\not\!\!E_{\mathrm{T}}$ is present; however, for the region of high impact parameter the variation in the $\not\!\!E_{\mathrm{T}}$ is larger than the equivalent $\sum E_{\mathrm{T}}$ variation. This is because the $\sum E_{\mathrm{T}}$ variation reflects the increased event activity in the b events, whereas the $\not\!\!E_{\mathrm{T}}$ variation reflects both the increased event activity (increasing the resolution) and the increase in missing transverse energy contribution from the neutrino in the heavy flavor decay. This is further justified by figure 10-11, where an increase in the real neutrino energy (simulation level $\not\!\!E_{\mathrm{T}}$) is observed as function of isolation.

10.1.2 Light flavor decays

Muons from light flavor decays result from light mesons (typically π or K mesons) decaying "in flight" to muons. An example decay is shown in figure 10-4. The products of this decay are the exact same as the products of W boson production, which makes it more difficult to separate these events from W boson decays. Separation with W events is originates results from the decay of the light meason, which occurs in the calorimeters. This causes the light meson to be reconstructed in tracker, which implies that the $\not\!\!E_{\mathrm{T}}$ is not from the neutrino in the meson decay, making it small (figure 10-6) and far away from the lepton. This effect causes the m_{T} to be on average larger than the m_{T} distribution of heavy flavor decays (figure 10-5 and figure 10-8) . Light flavor decay muons are additionally found to be prompt, and be non-isolated

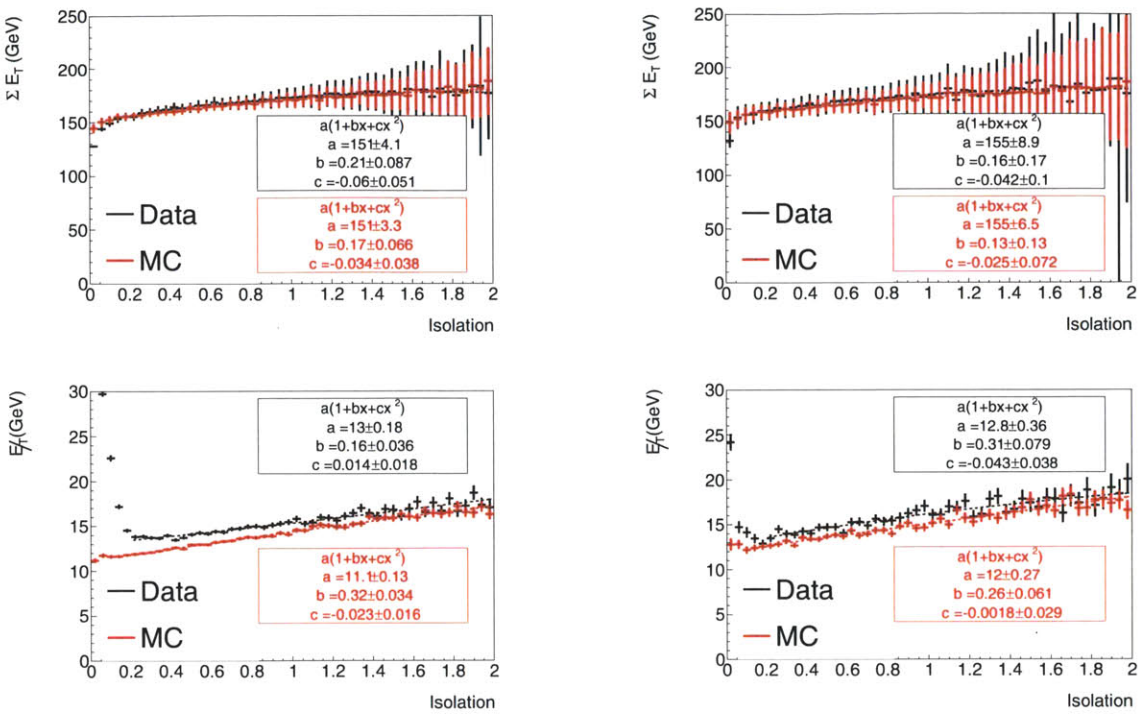

Figure 10-3: Mean $\sum E_{\mathrm{T}}$ (top) and $\not\!\!E_{\mathrm{T}}$ variation as function of isolation for all well identified muons (left) and for muons with $d_0 > 0.01$ cm (right). The boxed off values are the result of a fit of listed form to either data (black) or Monte Carlo simulation (MC)

when selecting on high impact parameter (figure 10-7). The fraction of non-isolated events also differs with that of heavy flavor events, thus using non-isolated events to describe isolated QCD events is made more difficult in that one must account for the differences in the light and heavy flavor shapes.

10.1.3 Comparison in real $\not\!\!E_{\mathrm{T}}$

To understand the $\not\!\!E_{\mathrm{T}}$ trend we separate the QCD background by its generator level $\not\!\!E_{\mathrm{T}}$, where the generator level $\not\!\!E_{\mathrm{T}}$ is defined by the vector sum of the generated neutrinos. This does not include all of the neutrinos coming from K and π mesons, where the neutrino is produced after ther generation step, during simulation.

The composition of large generator level missing energy is dominated by events with heavy flavor decays (figure 10-15) where the neutrino is along the direction of the muon leading to low m_{T} (figures 10-16 and 10-19). Additionally, large reconstructed $\not\!\!E_{\mathrm{T}}$ is strongly correlated with large generator level $\not\!\!E_{\mathrm{T}}$, implying these same heavy flavor decays at low m_{T} contribute to the majority of the large values of the $\not\!\!E_{\mathrm{T}}$ distribution (figure 10-17).

All of these observations imply that the events with large $\not\!\!E_{\mathrm{T}}$, in the region where

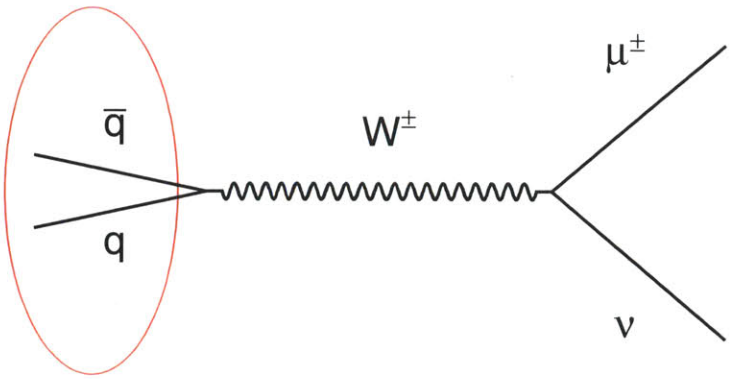

Figure 10-4: Typical light flavor decay. The red circle implies confinement between the quark(q) and the anti quark ($\bar{q}$).

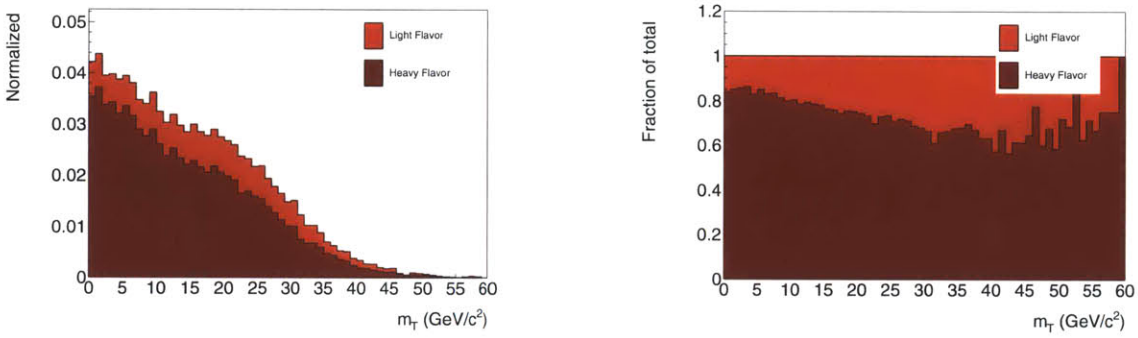

Figure 10-5: Variation in the transverse mass m_{T}(left) and per bin fractional content (right) of muon events in the signal selection originating from light flavor (u,d,s) and heavy flavor (b,c) tagged QCD events

W boson signal is known to be large, result from high energy heavy flavor quark decays. This observation, strongly motivates the choice of using $\not\!\!E_{\mathrm{T}}$ as a selection variable, because heavy flavor decayed muons are both non-isolated and isolated. Thus, it is possible to constrain the large $\not\!\!E_{\mathrm{T}}$ tail by looking at the $\not\!\!E_{\mathrm{T}}$ tail shape in non-isolated events where no W boson signal is present. Inverting the isolation cut for other variables, such as m_{T}, leads to less cerntainty on the shape because the light flavor composition varies with isolation in the critical region where both W boson signal and QCD background is present.

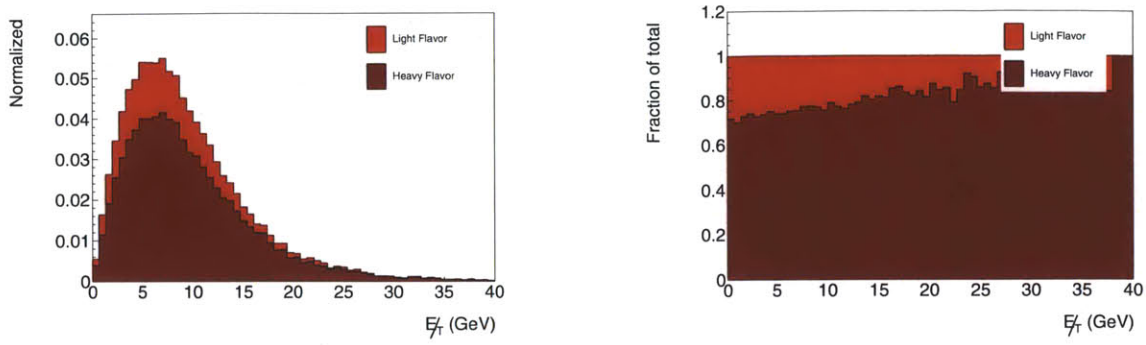

Figure 10-6: Variation in the $\not\!\!E_{\mathrm{T}}$(left) and per bin fractional content (right) of muon events in the signal selection originating from light flavor (u,d,s) and heavy flavor (b,c) tagged QCD events

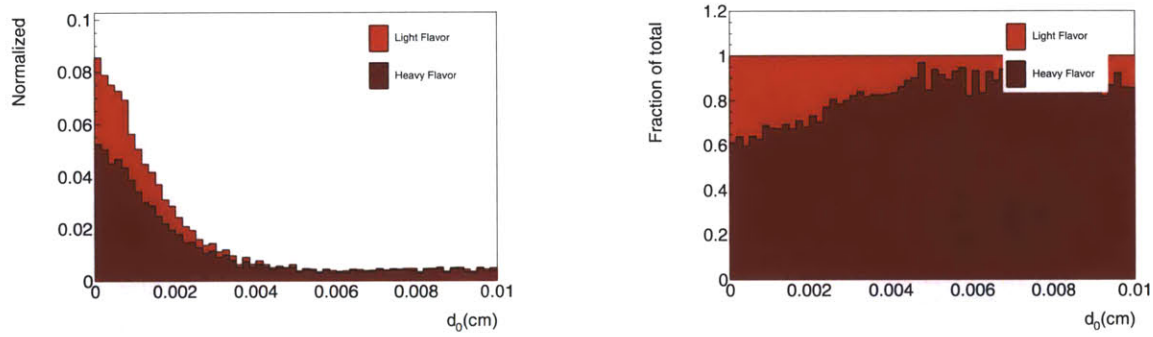

Figure 10-7: Variation in the impact parameter d_0 (left) and per bin fractional content (right) of muon events in the signal selection originating from light flavor (u,d,s) and heavy flavor (b,c) tagged QCD events

10.2 Modeling of the $\not\!\!E_{\mathrm{T}}$

To model the missing transverse energy, we utilize an expression constructed to describe events with a small non zero neutrino $\not\!\!E_{\mathrm{T}}$, a, with probability $P(a)$, which are smeared by a Gaussian resolution function $G\left(\not\!\!E_{\mathrm{T}}, a\right)$. The observed $\not\!\!E_{\mathrm{T}}$ is written as

$$P\left(\not\!\!E_{\mathrm{T}}\right) \;=\; G\left(\not\!\!E_{\mathrm{T}}, a\right) \otimes P(a) \tag{10.2}$$

Typical simulated distributions of $P(a)$ are similar to a Gaussian with a mean of 2-3 GeV. The full convolution gives a complicated form, which closely approximates

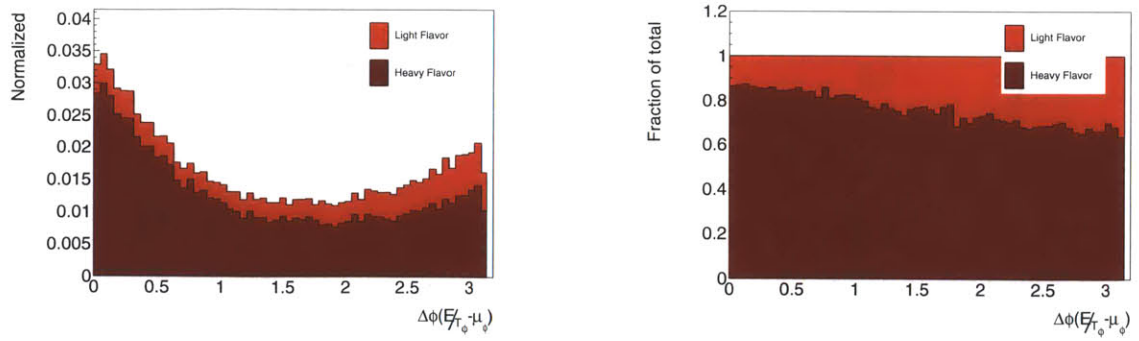

Figure 10-8: Variation in the angle between the lepton and the $\not\!\!E_{\rm T}$ in the transverse plane(left) and per bin fractional content (right) of muon events in the signal selection originating from light flavor (u,d,s) and heavy flavor (b,c) tagged QCD events

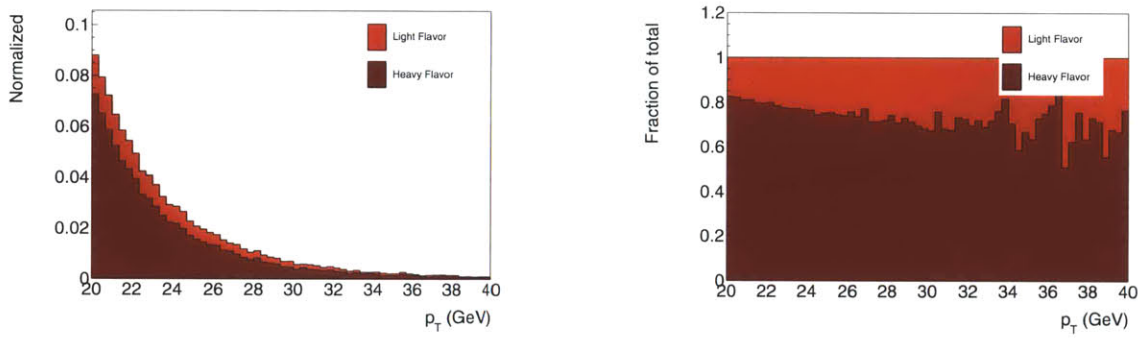

Figure 10-9: Variation in the $p_{\rm T}$ (left) and per bin fractional content (right) of muon events in the signal selection originating from light flavor (u,d,s) and heavy flavor (b,c) tagged QCD events

a Gaussian with a modified resolution

$$P\left(\not\!\!E_{\rm T}\right) = erf\left(\not\!\!E_{\rm T} - x_0\right)\exp\left(-b\left(\not\!\!E_{\rm T}\right)^2\right) , \tag{10.3}$$

$$\approx \exp\left(-\frac{\not\!\!E_{\rm T}^2}{2\sigma^2 + a'\,\not\!\!E_{\rm T}}\right) , \tag{10.4}$$

where x_0 denotes a constant depending on other terms and b is a constant depending on the magnitude of the non zero $\not\!\!E_{\rm T}$ distribution. The final a' is a modified constant that shifts the large $\not\!\!E_{\rm T}$ contribution to the distribution outward to correspond to

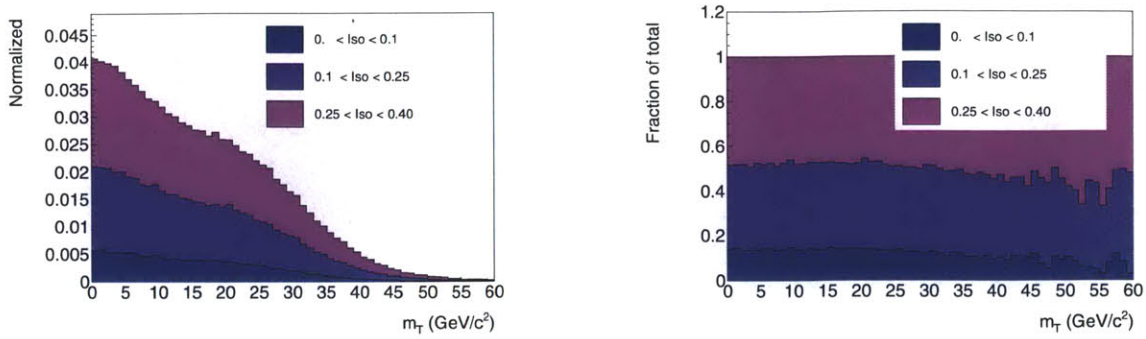

Figure 10-10: Variation in the transverse mass m_{T} (left) and per bin fractional content (right) of muon events in the signal selection originating from QCD events with different levels of isolation

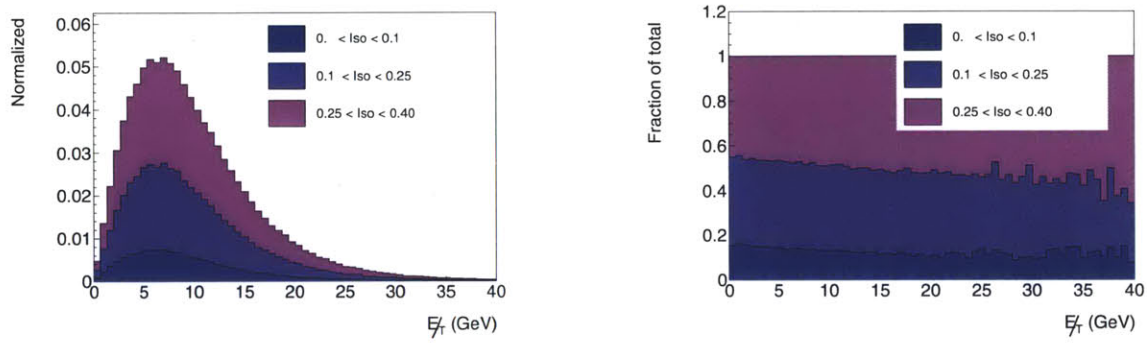

Figure 10-11: Variation in the $\not\!\!E_{\mathrm{T}}$ (left) and per bin fractional content (right) of muon events in the signal selection originating from QCD events with different levels of isolation

events with $\not\!\!E_{\mathrm{T}}$ from neutrinos . Projecting the x and y $\not\!\!E_{\mathrm{T}}$ onto $r = \sqrt{x^2 + y^2}$ gives:

$$f\left(\not\!\!E_{\mathrm{T}}\right) = \left(f\left(\not\!\!E_{\mathrm{T_x}}\right) \otimes P(a)dx\right)\left(f\left(\not\!\!E_{\mathrm{T_y}}\right) \otimes P(a)dy\right) \ , \tag{10.5}$$

$$= \not\!\!E_{\mathrm{T}} f\left(\not\!\!E_{\mathrm{T}}\right) \otimes P(a)dr \ , \tag{10.6}$$

$$\approx N \not\!\!E_{\mathrm{T}} \exp\left(\frac{\not\!\!E_{\mathrm{T}}}{2\sigma^2 + a' \not\!\!E_{\mathrm{T}}}\right) d\not\!\!E_{\mathrm{T}} \ , \tag{10.7}$$

where N is a normalization factor. The projection onto dr space is known as a Rayleigh distribution and describes any quadratic sum of two Gaussians. In order to fully describe the QCD distribution, the resolution σ is modified to have the form $\sigma \to \sigma + b \not\!\!E_{\mathrm{T}}$, this follows from the fact that the missing energy resolution σ scales with $\sqrt{\sum E_{\mathrm{T}}}$, thus one expects an increase in $\not\!\!E_{\mathrm{T}}$ resolution with more $\not\!\!E_{\mathrm{T}}$. Effects consisting of decays of events with non-zero $\not\!\!E_{\mathrm{T}}$ are additionally accounted for by the b term. The full combination yields the generalized QCD probability distribution

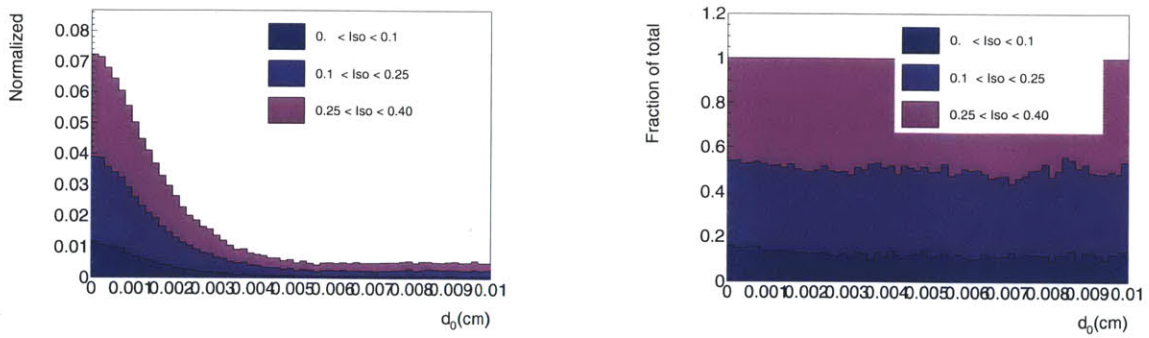

Figure 10-12: Variation in the impact parameter d_0 (left) and per bin fractional content (right) of muon events in the signal selection originating from QCD events with different levels of isolation

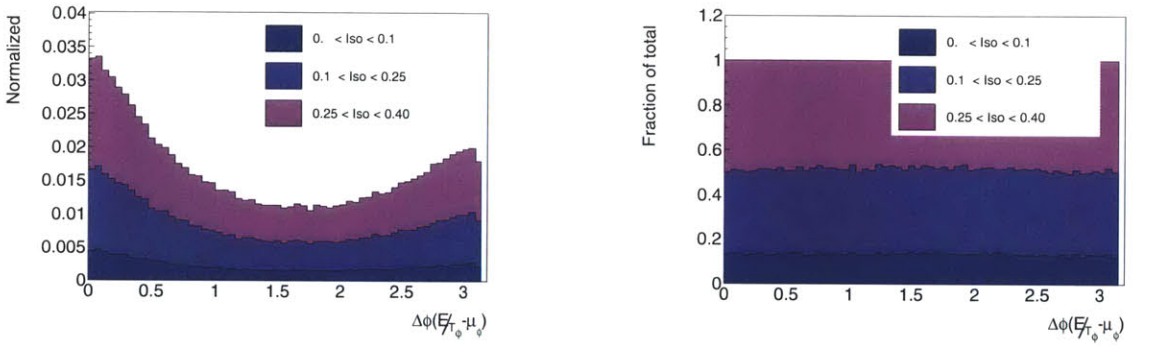

Figure 10-13: Variation in the angle between the lepton and the $\not\!\!E_T$ in the transverse plane(left) and per bin fractional content (right) of muon events in the signal selection originating from QCD events with different levels of isolation

function defined as

$$f\left(\not\!\!E_T\right) \;=\; N\,\not\!\!E_T \exp\left(\frac{\not\!\!E_T}{c + b\,\not\!\!E_T + a\,\not\!\!E_T{}^2}\right) . \tag{10.8}$$

This is sufficient to describe the shape of the missing energy for all regions of isolation, i. A fit to this distribution in both Monte Carlo simulation and data is shown in the figure 10-21. In this figure, a control region defined by $0.3 < isolation < 0.5$ and a signal region (defined by $isolation < 0.1$) for the Monte Carlo simulation are fit. In all cases, the fit describes the shape of the QCD background well, with no systematic deviations of the shape over the range of 0 GeV$<\not\!\!E_T <$ 60 GeV. The parameters a and b are constrained by the high values of the $\not\!\!E_T$ distribution beyond $\approx$ 20 GeV. These two parameters will be referred to as the tail parameters. The parameter c is constrained by the bulk of the $\not\!\!E_T$ distribution for values of $\not\!\!E_T$ below

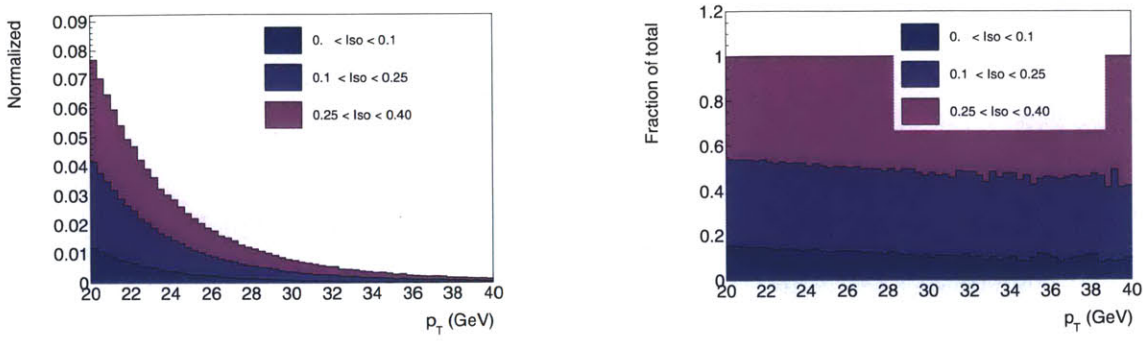

Figure 10-14: Variation in the p_T (left) and per bin fractional content (right) of muon events in the signal selection originating from QCD events with different levels of isolation

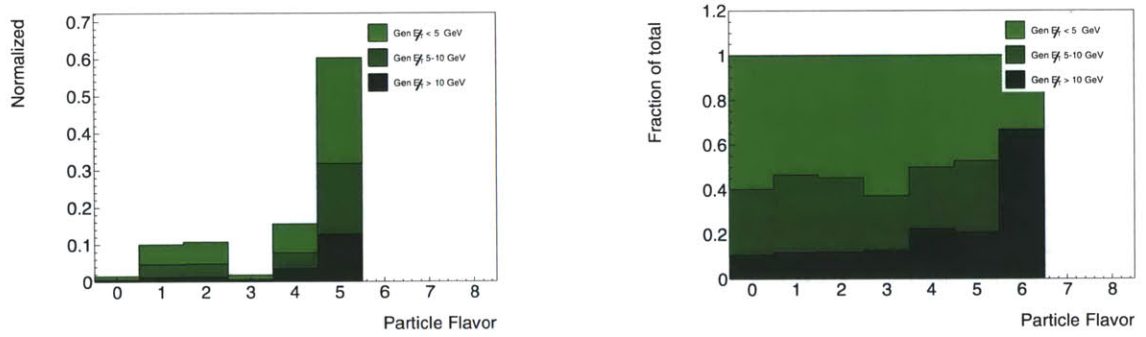

Figure 10-15: Composition of muon backgrounds from QCD decays (left) and relative per bin contribution (right) for QCD events passing all muon identification cuts split into different levels of generator $\not\!\!E_T$ (defined as transverse vector sum of the generator level neutrinos). The integer on the x-axis denotes the originating particle composition of the decayed muon, which consist of (0-unidentified),(1-up quark),(2-down quark),(3-strange quark),(4-charm quark),(5-bottom quark).

20 GeV.

10.3 Extrapolation from non-isolated region

To extrapolate the shape of the QCD $\not\!\!E_T$ into the signal region, defined to be the region where $0 < \chi_{iso} < 0.1$, a fit of the $\not\!\!E_T$ is performed for different regions of isolation. The evolution of the fit parameters is used to extrapolate the fit parameters into the signal region. The extrapolation is determined through both a binned and unbinned fit. The binned fit is performed by selecting eight separate regions of isolation and fitting for the $\not\!\!E_T$ shape in each individual bin. The trend in the resulting parameters

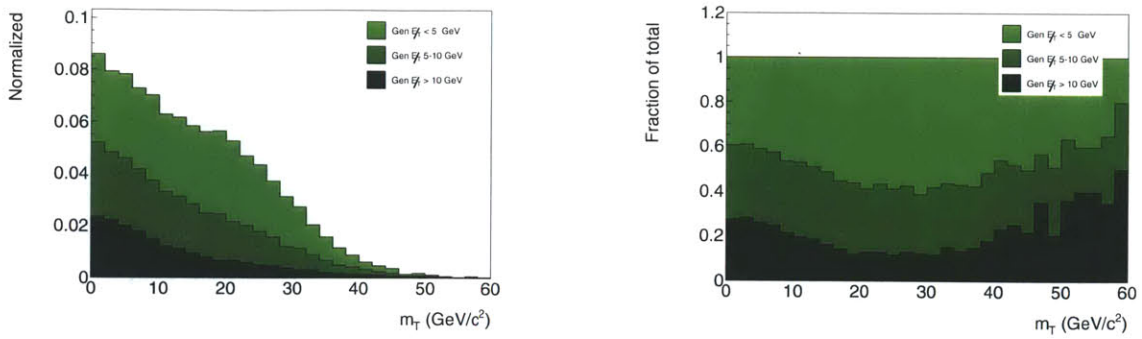

Figure 10-16: Variation in the transverse mass m_{T} (left) and per bin fractional content (right) of muon events in the signal selection originating from muon decays from QCD events with different levels of generator $\not\!\!E_{\mathrm{T}}$ (defined as transverse vector sum of the generator level neutrinos)

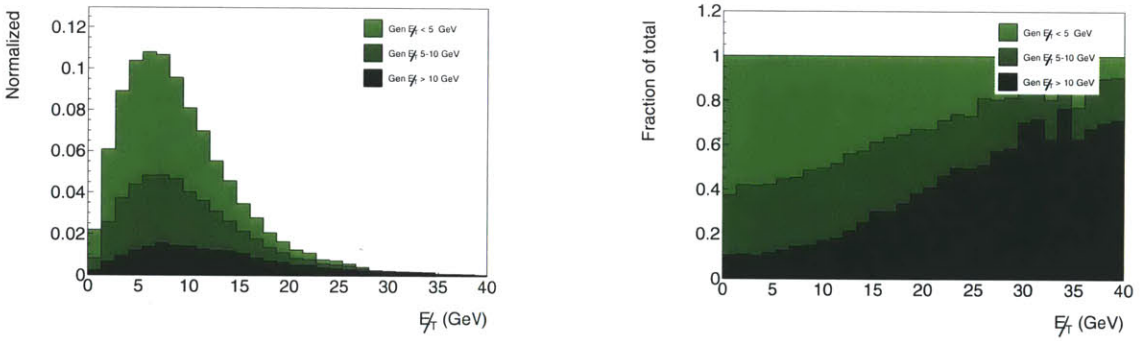

Figure 10-17: Variation in the $\not\!\!E_{\mathrm{T}}$(left) and per bin fractional content (right) of muon events in the signal selection originating from muon decays of QCD events with different levels of generator $\not\!\!E_{\mathrm{T}}$

is fitted and used to extrapolate the parameters in the signal region. The unbinned method fits the two dimensional $\not\!\!E_{\mathrm{T}}$ distribution versus isolation. The unbinned fit function that is minimized is written as (for i the isolation observable)

$$a(i) = a_0 + a_1 i + a_2 i^2 + a_3 i^3 \ , \tag{10.9}$$

$$b(i) = b_0 + b_1 i + b_2 i^2 + b_3 i^3 \ , \tag{10.10}$$

$$c(i) = c_0 + c_1 i + c_2 i^2 + c_3 i^3 \ , \tag{10.11}$$

$$f\left(\not\!\!E_{\mathrm{T}}\right) = N \not\!\!E_{\mathrm{T}} \exp\left(\frac{\not\!\!E_{\mathrm{T}}{}^2}{c(i) + b(i)\ \not\!\!E_{\mathrm{T}} + a(i)\ \not\!\!E_{\mathrm{T}}{}^2}\right) d\not\!\!E_{\mathrm{T}} \ . \tag{10.12}$$

The choice of the cubic terms to describe the trend is motivated by the fact that the binned extrapolations follow a quadratic trend. A cubic variation, thus would cover

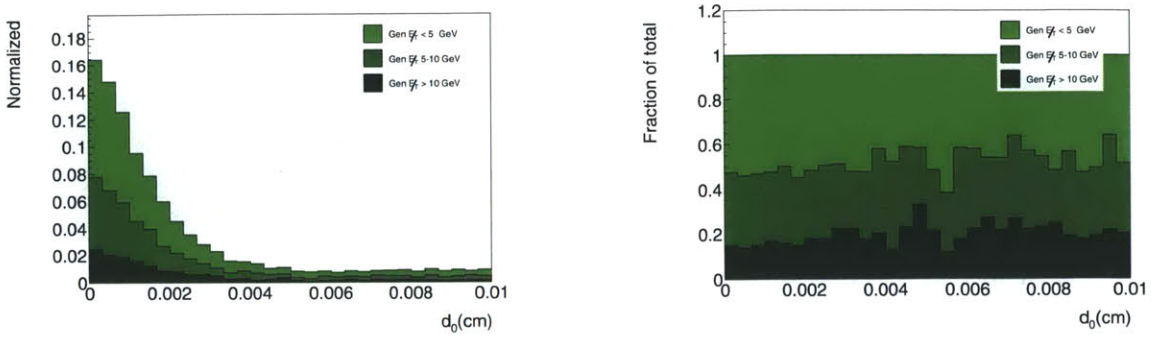

Figure 10-18: Variation in the impact parameter d_0 (left) and per bin fractional content (right) of muon events in the signal selection originating from muon decays of QCD events with different levels of generator $\not\!\!E_{\mathrm{T}}$

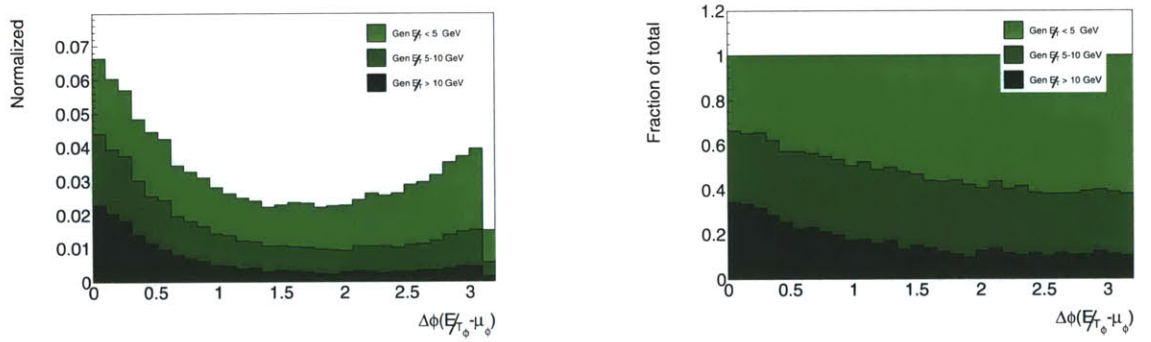

Figure 10-19: Variation in the angle between the lepton and the $\not\!\!E_{\mathrm{T}}$ in the transverse plane (left) and per bin fractional content (right) of muon events in the signal selection originating from muon decays QCD events with different levels of generator $\not\!\!E_{\mathrm{T}}$

any additional small corrections. This choice leads to values consistent with zero in the cubic terms of the fit. The fit is determined by fitting a range in isolation defined by $0.3 < isolation < 1.0$. The choice of this range is motivated by figure 10-3 where a clear upward trend in the mean of the $\not\!\!E_{\mathrm{T}}$ is visible for $isolation < 0.3$. This trend stems from the onset of high $\not\!\!E_{\mathrm{T}}$ events from W boson signal contamination.

Figure 10-22 shows the trend in the parameters for the binned and the unbinned fit. The bands on the unbinned fit correspond to the one σ uncertainties obtained by sampling Gaussians about the eigenvectors of the covariance matrix. The overall trend in the parameters between the binned and unbinned are within one standard deviation in the region of isolation below 0.8. At isolation below 0.3 there is disagreement between the binned and ubinned fits to the data, resulting from signal contamination, which bias the tail parameters a and b high.

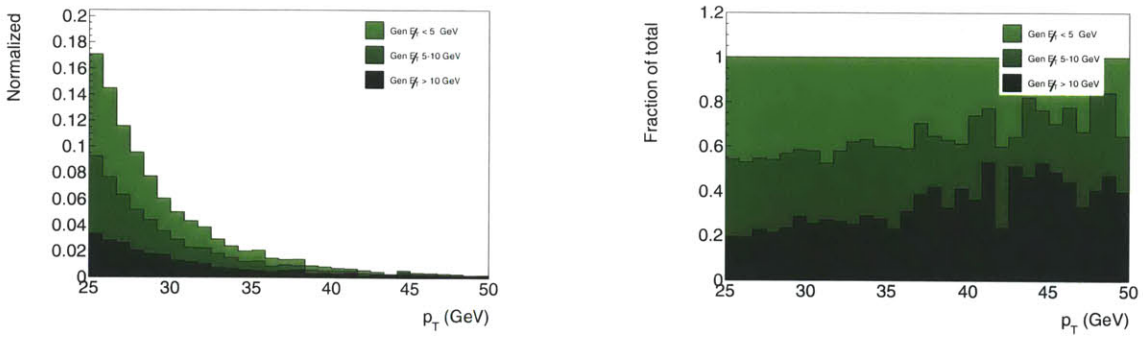

Figure 10-20: Variation in the p_{T} (left) and per bin fractional content (right) of muon events in the signal selection originating from muon decays QCD events with different levels of generator $\not\!\!E_{\mathrm{T}}$

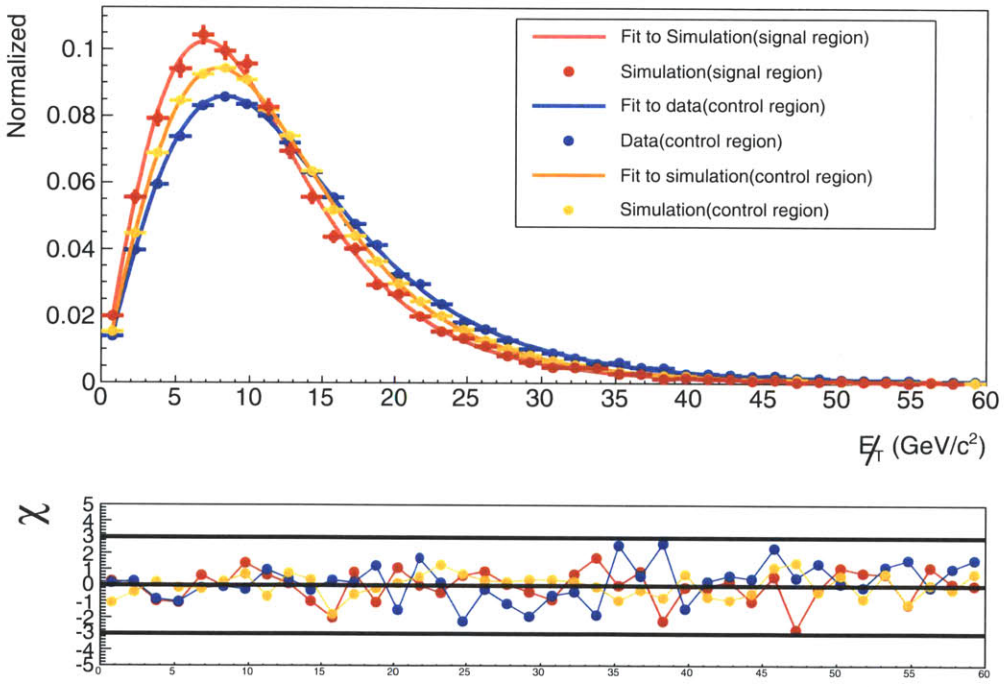

Figure 10-21: Fit (lines) to muons selected from a control region (points) using the modified Rayleigh function (equation 10.8) for a three regions defined by a well identified muon with $0.3 < \chi_{\mathrm{iso}} < 0.5$ on a data selection, $0.3 < \chi_{\mathrm{iso}} < 0.5$ on QCD simulated muon decays, and $\chi_{\mathrm{iso}} < 0.1$ (signal selection) on QCD simulated muon decays

10.3.1 Charge dependence

Muons from QCD processes primarily originate from heavy flavor decays produced in $b\bar{b}$ or $c\bar{c}$ pairs, the yields, and the shapes of the QCD are therefore expected to be

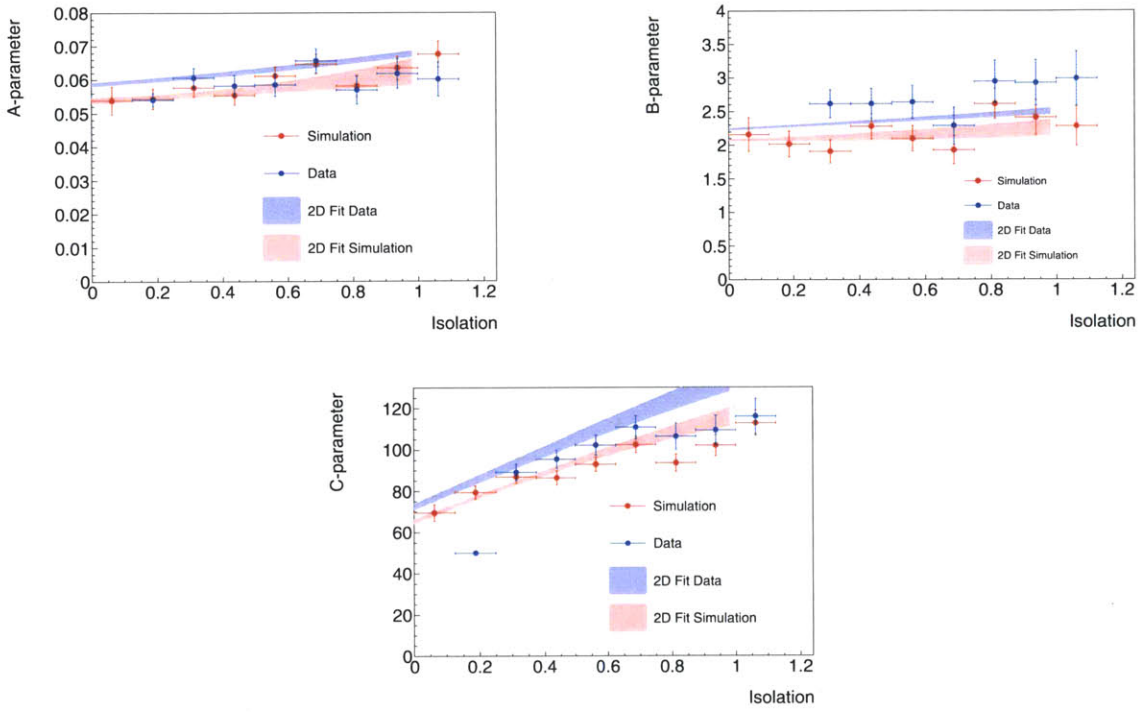

Figure 10-22: Comparison of the three parameters of the QCD $\not\!\!E_{\mathrm{T}}$ fit function (equation 10.8) for data (blue) and Monte Carlo simulation (red). The fit is performed in bins of isolation (points) and in two dimensions: $\not\!\!E_{\mathrm{T}}$ versus isolation (bands) where a parametric form for a,b,c is used (equation 10.12). For the two dimensional data fit, the fit was performed for $0.3 < \chi_{\mathrm{iso}} < 1.0$ and extrapolated to the signal region. The bands are expected to be consistent with the points of the same color. Correlations between the tail parameters a,b lead to small differences between the points and the bands.

symmetric in charge. This is not true where, in the data, the charge dependent η variation in energy scale modifies the shapes and yields of these events.

To determine the difference in the $\not\!\!E_{\rm T}$ shape between charges, fits are applied separately to the positive and negative QCD samples. Figure 10-23 shows the fit parameter trends for the different charges. In data and simulation, the two tail parameters a and b are within uncertainties of each other and additionally within uncertainties of the neutral charge value. The resolution parameter, c is shifted higher for negative leptons in data and slightly lower for negative leptons in simulation.

10.4 Systematic uncertainty

The uncertainty of the QCD model for muons in the signal region results from the uncertainty in the extrapolation of the parameters into the signal region. To compare this, the unbinned fit is performed in the simulation for *isolation* $\in$ 0.3-1.0 and *isolation* $\in$ 0-1.0 The main difference in the fits result from the fraction of light flavor to heavy flavor decays, which increase from around 10 percent for the non-isolated region to 20 percent in the signal region.

To observe a comparable change in the fit, the unbinned fit is performed on the events with $|d_0| < 0.003$ cm. This region has a larger componeision of light flavor QCD events and biases both tail parameters, a and b, low. This bias low in the tail parameters is a result of removing long lived b decays with a large amount of real missing energy coming from a high energy neutrino. The bias low is of similar order to the bias high in the tail parameters a and b when the fit over the whole isolation range is performed. Thus, we take the difference from the fits over two d_0 regions as a systematic uncertainty. This combined with the envelope covering the variation band of the parameters in the signal region ($0 < \chi_{\rm iso} < 0.1$) determines the systematic uncertainty.

Figure 10-24 shows the fitted trends of the simulation for three different $|d_0|$ selections ($|d_0| < 0.003$ cm, $|d_0| < 0.2$ cm, 0.01 cm $< |d_0| < 0.2$ cm) over two different isolation ranges (0-1,0.3-1). The resulting fits have the expected trend in that the difference in the fit where isolation is $\in$ 0.3-1.0, compared with where isolation is $\in$ 0.0-1.0 is small and occurs at the region of low isolation. The difference biases the tail parameter a to be slightly higher. Fitting on the region of low impact parameter $d_0 <$ 0.003 cm decreases the tail contribution and lowers the resolution c. The systematic uncertainty band (defined above) spans the fitted values over the whole range. The high impact parameter selection, $d_0 > 0.010$ cm, is used as a cross check to generate the opposite behavior of the low impact parameter selection, its sensitivity is limited due to the low event yield for $d_0 > 0.010$ cm .

For separate charges, we add the systematic uncertainty band determined from the inclusive fit to the fit uncertainty bands from the individual positive and negative lepton fits. Using the inclusive fit to determine the systematic uncertainty is sufficient for either charge because the choice of systematic uncertainty was determined to cover a physical effect present in both the positive and negative QCD background events.

Figure 10-25 shows the predicted $\not\!\!E_{\rm T}$ shape along with its systematic uncertainty

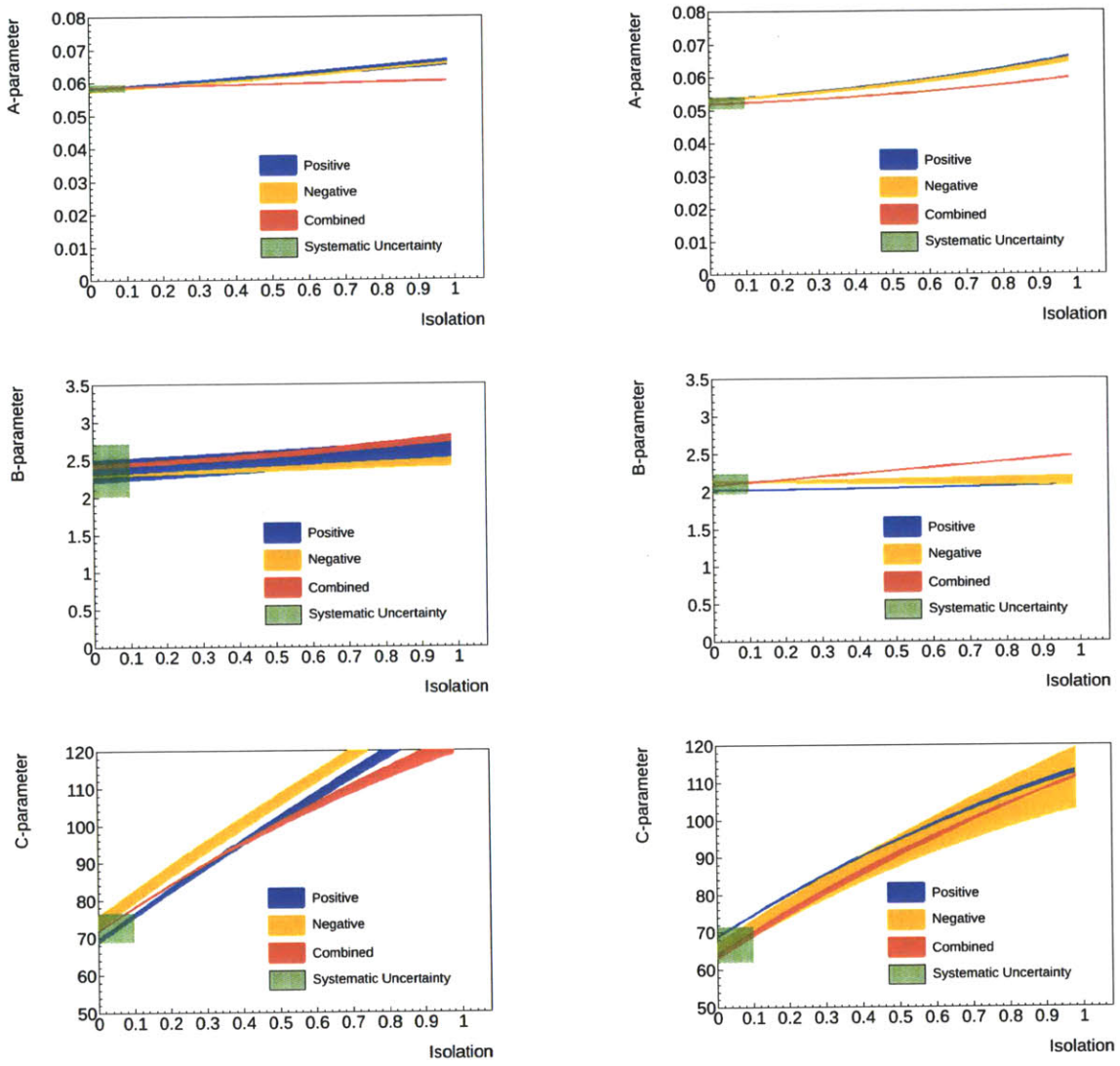

Figure 10-23: Comparison of the two dimensional fit extrapolations of the parameters a, b, and c in the control region for the separate charges for data (left) and simulation (right)

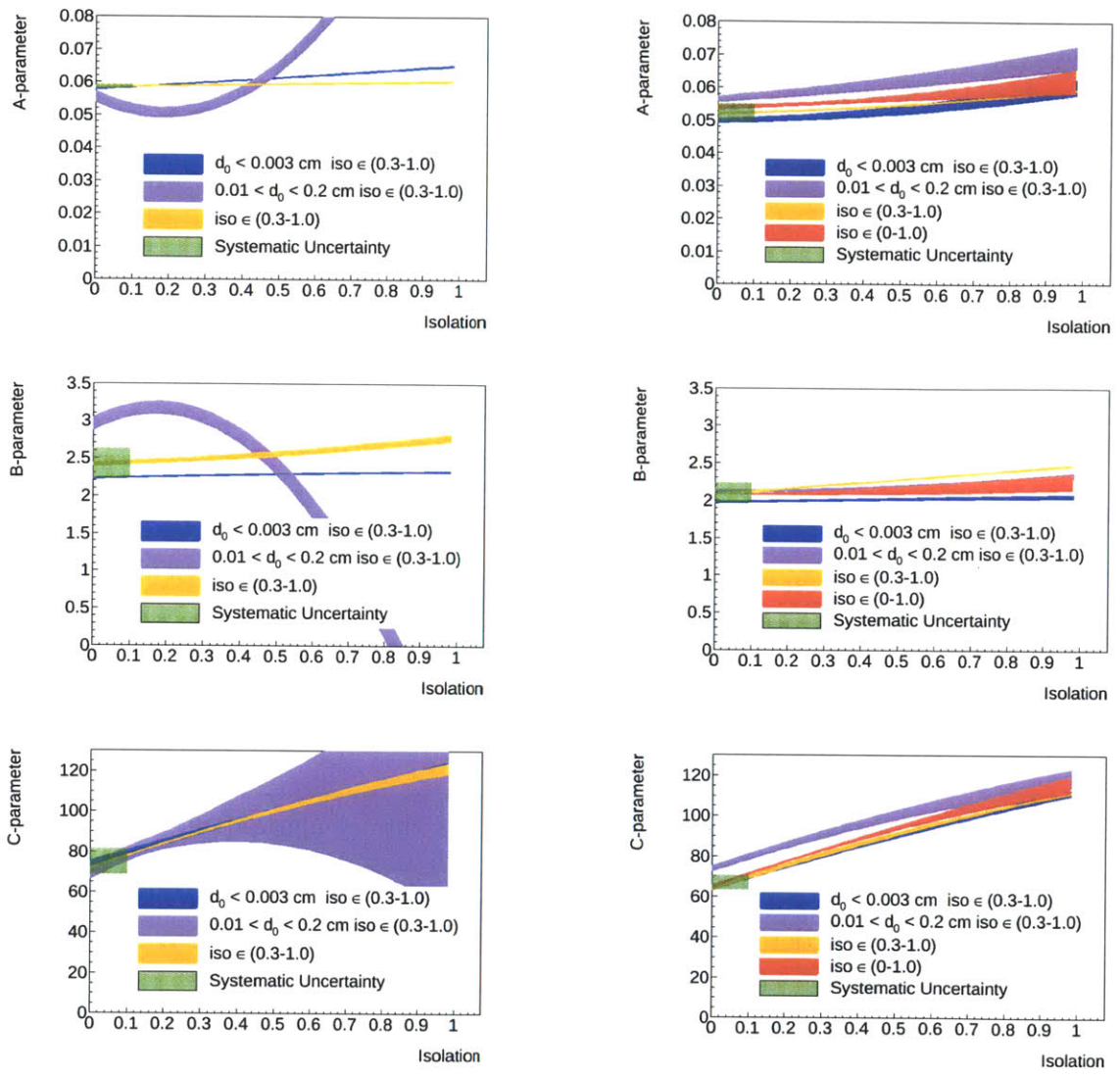

Figure 10-24: Comparison of the two dimensional fit extrapolation of the fit parameter results a, b, and c for the three different control regions defined by the d_0 cut where $0.3 < isolation < 1.0$ for the data (left) and simulation (right). In the simulation, the true fit parameters (given by pink) are also shown.

compared to the true $\not\!\!E_{\mathrm{T}}$ shape from simulation. In the figure, the simulated data is on the edge of the uncertainty band. This ensures coverage by the systematic uncertainties, but may indicate a bias in the fit. The origin of this bias stems mainly from the ten percent variation in the resolution parameter c within the isolation selection. In order to minimize the bias, we float the resolution parameter c and fix the two tail parameters to their predicted values. Figure 10-25 shows the result of floating the c parameter in the fit. We observe that the overall uncertainty band is both reduced, due to fitting, and centered about the QCD background shape.

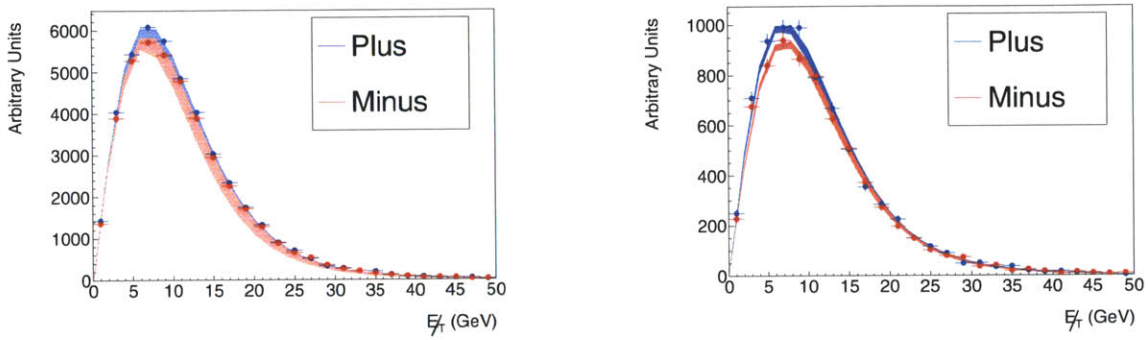

Figure 10-25: Comparison of the true shape (points) versus the predicted band from the two dimensional extrapolation where the band is taken from the systematic uncertainties from all of the variables (left) and for the two tail parameters a and b allowing the bulk resolution c to be floated (right)

This method of floating c and fixing a and b is the fit method used for the W boson yield extraction discussed in chapter 11. For W boson extraction, an additional systematic uncertainty contributes due to the bias on floating c when W boson signal is present. This bias is determined from fits of toy data generated from a W boson and QCD combined shape (discussed later).

10.5 Electroweak backgrounds

The Electroweak backgrounds have two main contributions: W boson tau production decaying to a muon and neutrinos, $\mathrm{W}\rightarrow \tau\nu_\tau \rightarrow \mu\nu_\mu\nu_\tau\nu_\tau$, and Z boson muon production $\mathrm{Z}\rightarrow \mu\mu$. The Z boson background originates from Z events where one muon falls out of the acceptance of the detector. This does not happen frequently because an event is vetoed in the presence of a second muon with $p_{\mathrm{T}} > 10$ GeV/c and $|\eta| < 2.4$. In both the $\mathrm{W}\rightarrow \tau\nu_\tau$ and $\mathrm{Z}\rightarrow \mu\mu$ case, their contribution in the selection region is determined from simulated templates fixed to a W boson signal template by their predicted cross sections in the signal region. The uncertainties on the individual backgrounds are discussed below.

10.5.1 W$\rightarrow \tau\nu$ background

The tau background is determined by fixing the shape predicted by simulation to the W boson template. The uncertainty on the $\not\!\!E_{\mathrm{T}}$ shape is determined by applying the recoil $\not\!\!E_{\mathrm{T}}$ corrections for the W$\rightarrow \mu\nu$ to the W$\rightarrow \tau\nu$ simulated sample. The corrections compared with the simulated prediction are shown in figure 10-26. Use of the recoil corrections and the uncertainty fluctuated templates in the cross section measurement modifies the cross section by less than 0.1%, thus allowing for the simulated sample to be used without modifying the cross section by more than 0.1%.

Additional uncertainties originaties from the tau branching ratio uncertainty and the tau decay simulation. The branching ratio is known to 0.22 % [34]; this value multiplied by the three percent fraction of W$\rightarrow \tau\nu$ events in the signal region yield a negligible uncertainty for this analysis. The tau decay simulation uncertainty modifies the W boson yield. The kinematic simulation of τ decays has been tuned to the percent level using measurments of LEP processes [109]. This equates to a systematic uncertainty below 0.1 percent.

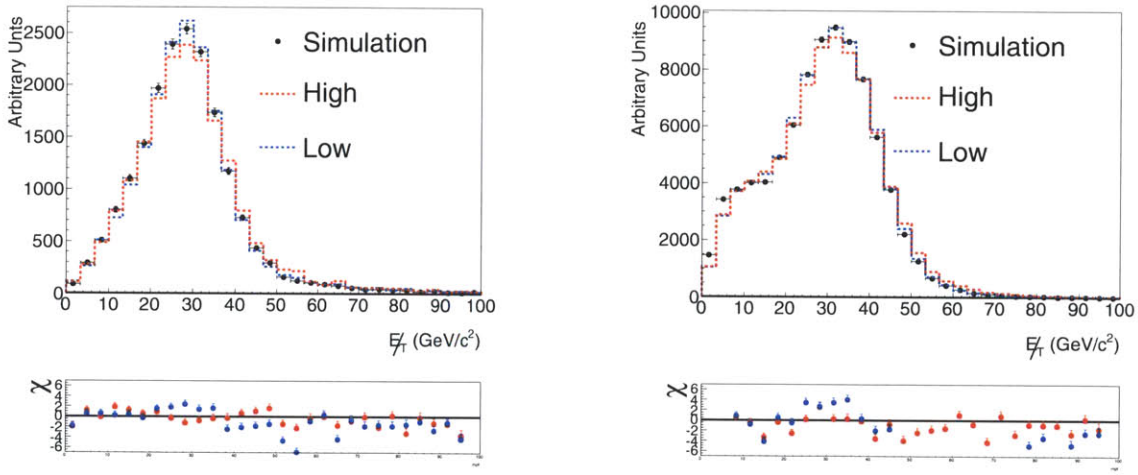

Figure 10-26: Comparison of the recoil corrected high and low $\not\!\!E_{\mathrm{T}}$ distributions compared with the simulated true prediction for W$\rightarrow \tau\nu$(left) and Z$\rightarrow \mu\mu$ events (right). The difference plot below reports the values χ defined in equation 11.53

10.5.2 Z$\rightarrow \mu^+\mu^-$ background

The Z boson background originates from events where the second lepton either falls out of the acceptance range or fails the second lepton veto, leading to a distinctive shape in the missing energy distribution shown in figure 10-26. The low $\not\!\!E_{\mathrm{T}}$ component originates from events where a muon fails the second muon veto, but the missing energy picks up the muon as a track or cluster of tracks. Due to the difficulty of calculating the correct u_1 and u_2 from muon like tracks which may originate from the

Z boson, the $\not\!\!E_T$ correction is imperfect in this low region. Thus, the Monte Carlo simulated shape is taken.

The effect of the $\not\!\!E_T$ uncertainty is evaluated from the uncertainty bands on the corrected shape (which nearly span the Monte Carlo simulation). The uncertainty is found to be $< 0.1\%$.

In addition to the uncertainty on the $\not\!\!E_T$ model, another uncertatinty results from the predicted yield ratio of $Z \rightarrow \mu\mu$ events to the W boson events in the fixed signal prediction. The combination of the $\not\!\!E_T$ uncertainty and the predicted ratio uncertainty yield a systematic uncertainty of 0.1 percent.

10.5.3 Other backgrounds

In addition to the QCD, $W \rightarrow \tau\nu$ and $Z \rightarrow \mu\mu$ backgrounds, additional backgrounds from top pair production and diboson production contribute. The contribution of these events to the cross section is below 0.3 percent. The $\not\!\!E_T$ shape for these events is determined from simulation and fixed to the W $\not\!\!E_T$ template.

10.6 Summary

Table 10.1 summarizes the expected contributions from all of the backgrounds. The overall contribution of the backgrounds in the signal region is on the order of 15 percent. With the exception of the QCD background, the uncertainty on the background shape is on the order of 0.1 percent.

The results from table 10.1 combined with QCD background yield are floated along with the c parameter to determine the individual contributions of the W boson signal and each background.

Background	Acceptance	Cross section (nb^{-1})	Fractional Contribution
$(W^+ \to \tau\nu)_+$	0.0122	6.15	0.0296
$(W^- \to \tau\nu)_-$	0.0127	4.29	0.0318
$(Z \to \mu^+\mu^-)_+$	0.0513	1.633	0.0332
$(Z \to \mu^+\mu^-)_-$	0.0450	1.633	0.0423
$(Z \to \tau^+\tau^-)_+$	0.0085	1.633	0.0055
$(Z \to \tau^+\tau^-)_-$	0.0072	1.633	0.0067
$(t\bar{t})_+$	0.0473	0.157	0.0029
$(t\bar{t})_-$	0.0465	0.157	0.0043
$(W^+W^-)_+$	0.0679	0.043	0.0012
$(W^+W^-)_-$	0.0393	0.043	0.0010
$(WZ)_+$	0.0572	0.0182	0.0004
$(WZ)_-$	0.0035	0.0182	0.0000
$(ZZ)_\pm$	0.011	0.059	0.0002
QCD_+	N/A	N/A	0.0850
QCD_-	N/A	N/A	0.132

Table 10.1: Acceptances, total cross section and contributions of all backgrounds in W events. The underscore denotes the charge for which this background contributes. The large difference between charge in the QCD background fractional contribution results from the different W^+ and W^- cross sections compared to the nearly equal QCD_+ and QCD_- cross sections

Chapter 11

Cross Section and Ratio Measurements

The W boson cross section is determined by fitting the $\not\!\!E_{\mathrm{T}}$ distributions. Fitting determines the yield N, the Electroweak yield N_{EWK}, and the QCD background yield N_{QCD}. This completes the determination of the cross section:

$$\sigma = \frac{N - N_{\mathrm{EWK}} - N_{\mathrm{QCD}}}{a\epsilon\mathcal{L}} \ . \tag{11.1}$$

The acceptance, a, efficiency, ϵ, and integrated luminosity, $\mathcal{L}$, were previously discussed in chapters 6, 8, and 2 respectively.

In performing the fit over $\not\!\!E_{\mathrm{T}}$, we rely on the studies of modeling the $\not\!\!E_{\mathrm{T}}$ distribution (chapter 9) to determine the W boson signal shape and its uncertainties. Additionally, uncertainties on the the energy scale model (chapter 7) are propagated into corrections to the $\not\!\!E_{\mathrm{T}}$ shape yielding another set of systematic uncertainties. The QCD and Electroweak background models and their uncertainties are presented in chapter 10.

In this chapter, we combine the individual studies into the final cross section measurements.

11.1 W boson yield extraction

The choice of fitting the observable, $\not\!\!E_{\mathrm{T}}$, is presented in chapter 10 as a means of minimizing the effects of mis-modeling the QCD background. The final form for the QCD background shape is found to be well modeled by a modified Rayleigh distribution. With the exception of the c parameter, the parameters for the Rayleigh distribution are determined by a two dimensional extrapolation from an non-isolated muon sample into the signal region. The c parameter modifies the QCD shape in the region where the W boson contribution is small, thus it is floated in the fit of $\not\!\!E_{\mathrm{T}}$. This is performed separately for single lepton selections of positive and negative muons.

The result of the final fits is shown in figure 11-1. The $\not\!\!E_{\mathrm{T}}$ distributions are well

Contribution	Yield
$W^+ \to \mu^+\nu$	84723±309
$W^- \to \mu^-\nu$	57346±255
QCD^+	7597±162
QCD^-	7553±149
EWK^+	6072±22
EWK^-	4922±22
$W \to \mu\nu$	142068±361
EWK	10994±31
QCD	15150±220

Table 11.1: Raw yields from the $\not\!\!E_T$ fit for the different components in the signal region. The uncertainties are the statistical uncertainties extracted from the fit. The EWK rows designate the contribution from all background processes excluding QCD (listed in chapter 10). The charge indicates the total yields for positive and negative leptons separately. The absence of a charge indicates the yield for both charges combined.

modeled over the whole range. This is indicated by χ^2 probability between data and the prediction of 0.927 for W^+ bosons and 1.000 for W^- bosons as well as Kolmogorov-Smirnov test value between the data and the prediction of 0.981 for W^+ bosons and 0.985 for W^- bosons. The result of the floated c parameter gives a value of

$$c_+ = 69.4 \pm 3.3 \text{ and} \tag{11.2}$$
$$c_- = 76.1 \pm 3.3 \, , \tag{11.3}$$

which agrees well with the predicted values for the positive and negative QCD background shapes given by the extrapolation:

$$c_+^{\text{predicted}} = 69.2^{+7.4}_{-0.52} \, , \tag{11.4}$$
$$c_-^{\text{predicted}} = 74.1^{+8.5}_{-1.7} \, . \tag{11.5}$$

The agreement between predicted and fitted validate the choice of using separate fits for the positive and negative QCD extrapolation; moreover, the data confirms the trended predictions correctly model the QCD shape.

The composition of the results are summarized in table 11.1. The QCD yields between positive and negative muons are found to be within one percent of each other, which confirms the prediction that both QCD backgrounds is roughly the same.

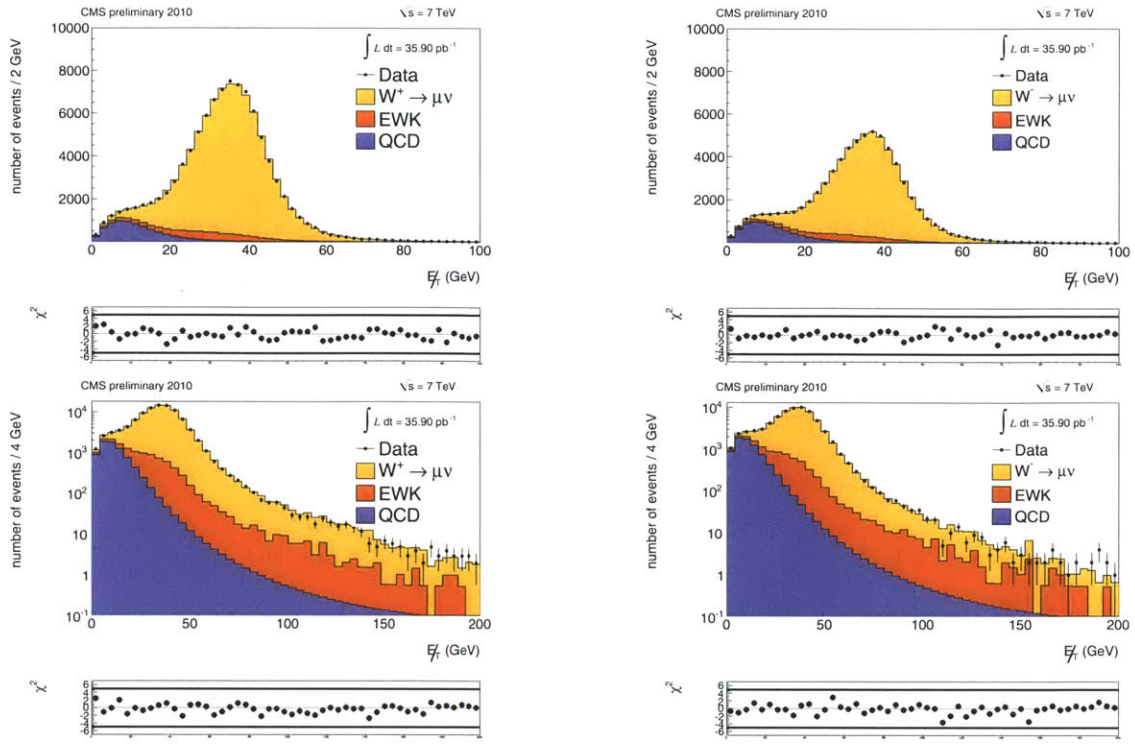

Figure 11-1: $\not\!\!E_{\mathrm{T}}$ distribution taking into account the QCD model, floating the c parameter for positive muons (left) negative muons (right) and extended out to 200 GeV(bottom). The difference plot on the bottom is defined in equation 11.53.

11.2 Uncertainties

The uncertainties that result in the cross sections shape follow directly from the terms in the cross section formula. These are be separated out into

- Luminosity,
- Acceptance (Theoretical uncertainties),
- Efficiency,
- Energy Scale and Resolution,
- $\not\!\!E_{\mathrm{T}}$ modeling,
- QCD modeling, and
- Electroweak and top backgrounds.

Such items are further classified into uncertainties that affect the extraction (*i.e* $\not\!\!E_{\mathrm{T}}$ fit), and uncertainties which correct the W boson cross section. The uncertainties that correct the W boson cross section: the luminosity, acceptance, and efficiency are

propagated through the total cross section calculation. These uncertainties, discussed in the previous chapters, are summarized in table 11.2.2.

11.2.1 Signal extraction uncertainties

The uncertainties on the extraction are determined by propagating the uncertainties into the fit through the Neyman construction[110]. This is performed by generating and fitting a large number of toy data sets to observe trends in the fit bias and fit uncertainties.

An example of the simplest test of the signal extraction uncertainty is the closure test of the fit. To perform this test we :

- Fit the data with default model
- Generate toy data with the same yields produced from the fit with the same signal and QCD shapes determined from the fit
- Fit the toy data and extract the predicted yields and uncertainties
- Repeat this procedure 5000 times (a sufficient number to observe trends)

The results of these "pseudo experiments" determine if there are any biases in the fit. The closure test is particularly important because both the QCD yield and the c parameter are floated in the fit. An average bias in the W boson yield over all the 5000 pseudo experiments would indicate the c parameter over extends or under extends into the W signal region. Figure 11-2 shows the results of the bias in W^+, W^-, and W^+/W^- expressed in terms of the pull variable, p, which is defined for an observable x with fitted central value $\bar{x}$, and uncertainty σ as

$$p = \frac{x - \bar{x}}{\sigma} \ . \tag{11.6}$$

A deviation of the mean of the pull distribution from zero indicates a bias. The shape of the pull distribution determines the true uncertainties of the extracted observable. The fit uncertainty distribution reported assumes a Gaussian. Thus, in this case, the pull distribution is expected to follow a Gaussian distribution with width one. From figure 11-2, we find the three observables have biases less than 0.001 standard deviations less than 0.001 percent of the total cross section. Additionally, the pull distribution is found to be Gaussian with a width consistent with one.

Systematic uncertainty procedure

To extract the systematic uncertainty through the Neyman construction, an uncertainty fluctuated shape (*ie* $\not\!\!E_{\rm T}$ plus σ corrected shape) is treated as the true shape. This shape is then used to generate toy data with yields specified by table 11.1. The resulting toy data is fit with the default fit model. The average bias from the true sampled yield over all of the fits to toy data is quoted as a systematic uncertainty.

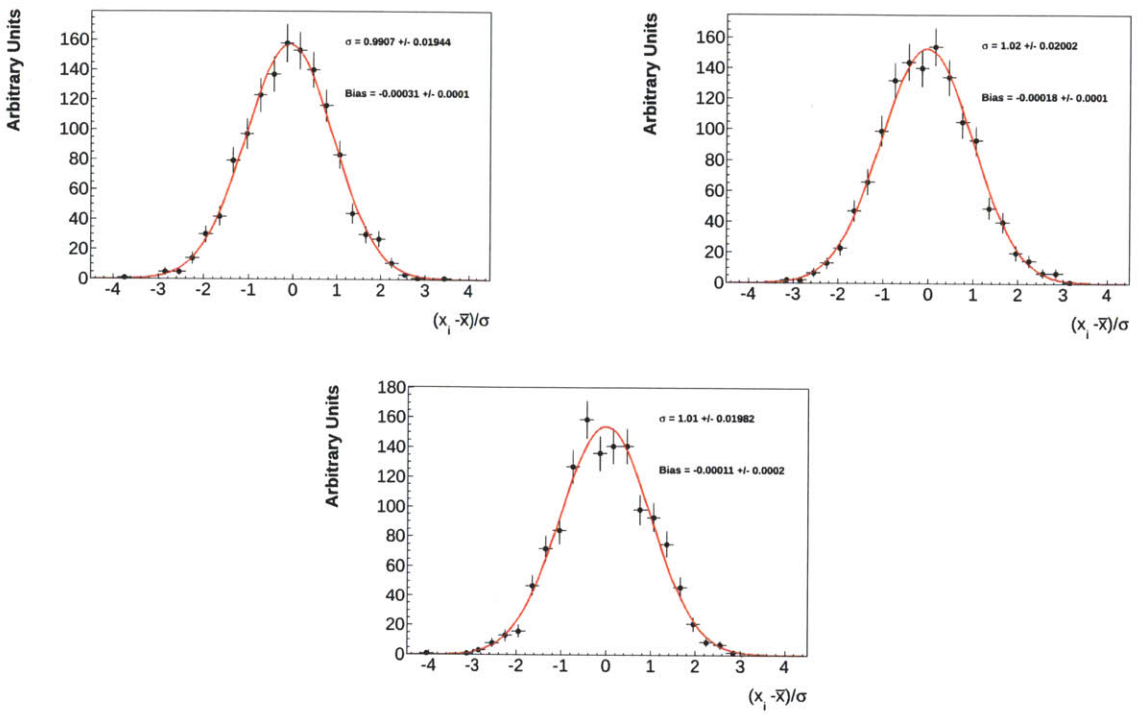

Figure 11-2: Pull distributions for the three observables of the W^+ production (top left), W^- production (top right), and W^+/W^- ratio (bottom). Each distribution is fitted with a Gaussian (red line). The resulting central value of the Gaussian is quoted as the bias and the width of the Gaussian confirms Gaussian uncertainties in the fit procedure.

$\not\!\!E_T$ systematic uncertainty The $\not\!\!E_T$ uncertainty is determined from templates where the $\pm\sigma$ uncertainty on the hadronic recoil is propagated into the corrected $\not\!\!E_T$ distribution to create a high and low uncertainty templates. These templates are treated as truth and used to perform toy data. The bias is determined from fits to the each of the 5000 toy data samples. The systematic uncertainty is found to be:

$$\sigma_{\not\!\!E_T}^{W^+} = {}^{0.20}_{-0.19}\,\% \,, \tag{11.7}$$

$$\sigma_{\not\!\!E_T}^{W^-} = {}^{0.20}_{-0.19}\,\% \,, \tag{11.8}$$

$$\sigma_{\not\!\!E_T}^{W} = {}^{0.20}_{-0.19}\,\% \,, \tag{11.9}$$

$$\sigma_{\not\!\!E_T}^{W^+/W^-} = {}^{0.016}_{-0.009}\,\% \,. \tag{11.10}$$

Lepton energy scale and resolution uncertainty The lepton energy scale is found by recalculating the $\not\!\!E_T$ distribution with corrected leptons fluctuated by sys-

tematic energy scale band, $\pm 0.4\%$ (chapter 7). The result of this gives:

$$\sigma_{\mathrm{ES}}^{\mathrm{W}^+} = {}^{0.11}_{-0.28}\% , \tag{11.11}$$
$$\sigma_{\mathrm{ES}}^{\mathrm{W}^-} = {}^{0.18}_{-0.24}\% , \tag{11.12}$$
$$\sigma_{\mathrm{ES}}^{\mathrm{W}} = {}^{0.14}_{-0.26}\% , \tag{11.13}$$
$$\sigma_{\mathrm{ES}}^{\mathrm{W}^+/\mathrm{W}^-} = {}^{0.0}_{-0.08}\% . \tag{11.14}$$

Additionally, the full cross section measurement starting from the p_{T} cut through to the reconstruction of the templates is repeated given the uncertainty on the muon energy scale is fluctuated high or low by the systematic uncertainty. The resulting differences in the cross section amount to:

$$\sigma_{\mathrm{ES}}^{\mathrm{W}^+} = {}^{0.18}_{-0.07}\% , \tag{11.15}$$
$$\sigma_{\mathrm{ES}}^{\mathrm{W}^-} = {}^{0.0}_{-0.04}\% , \tag{11.16}$$
$$\sigma_{\mathrm{ES}}^{\mathrm{W}} = {}^{0.17}_{-0.06}\% , \tag{11.17}$$
$$\sigma_{\mathrm{ES}}^{\mathrm{W}^+/\mathrm{W}^-} = {}^{0.18}_{-0.0}\% . \tag{11.18}$$

These uncertainties are added in quadrature with the previous energy scale systematic uncertainty measurement. The systematic uncertainty on the energy resolution is determined by smearing the lepton by an additional 0.5 GeV. The result of these uncertainties are below 0.15% (listed below):

$$\sigma_{\mathrm{Res}}^{\mathrm{W}^+} = -0.12\% , \tag{11.19}$$
$$\sigma_{\mathrm{Res}}^{\mathrm{W}^-} = -0.07\% , \tag{11.20}$$
$$\sigma_{\mathrm{Res}}^{\mathrm{W}} = -0.10\% , \tag{11.21}$$
$$\sigma_{\mathrm{Res}}^{\mathrm{W}^+/\mathrm{W}^-} = -0.05\% . \tag{11.22}$$

QCD model systematic uncertainty The QCD uncertainty is determined by generating pseudo data with parameters a, b and c modified by their high and low systematic uncertainties $\pm\sigma$ determined in chapter 10. The systematic uncertainty through this method is found to be

$$\sigma_{\mathrm{QCD}}^{\mathrm{W}^+} = {}^{0.21}_{-0.25}\% , \tag{11.23}$$
$$\sigma_{\mathrm{QCD}}^{\mathrm{W}^-} = {}^{0.32}_{-0.32}\% , \tag{11.24}$$
$$\sigma_{\mathrm{QCD}}^{\mathrm{W}} = {}^{0.26}_{-0.28}\% , \tag{11.25}$$
$$\sigma_{\mathrm{QCD}}^{\mathrm{W}^+/\mathrm{W}^-} = {}^{0.068}_{-0.109}\% . \tag{11.26}$$
$$\tag{11.27}$$

As a cross check to this analysis, toy data is generated with the simulated "truth" QCD distribution. The fit is performed with the default fit function, fixing the parameters a, b from the simulated predictions. The resulting biases are found to

Source	$W^+ \to \mu\nu(\%)$	$W^- \to \mu\nu(\%)$	$W \to \mu\nu(\%)$	W^+/W^- (%)
$\not{E}_T$ modeling	0.2	0.2	0.2	0.0
Energy Scale and Resolution	0.3	0.2	0.3	0.2
QCD modeling	0.3	0.3	0.3	0.1
Total extraction uncertainty	0.4	0.4	0.4	0.2
Efficiency	1.0	1.0	1.0	1.1
Acceptance (Theory)	1.3	1.7	1.1	2.1
Total Before Luminosity	1.7	2.0	1.5	2.4
Luminosity	4.0	4.0	4.0	-

Table 11.2: Systematic Uncertainties on the W boson cross section and related measurements

be

$$\bar{x}_{\not{E}_T}^{W^+} = 0.05\% , \quad (11.28)$$

$$\bar{x}_{\not{E}_T}^{W^-} = 0.12\% , \quad (11.29)$$

$$\bar{x}_{\not{E}_T}^{W} = 0.08\% , \quad (11.30)$$

$$\bar{x}_{\not{E}_T}^{W^+/W^-} = -0.07\% . \quad (11.31)$$

These are well within the systematic uncertainties quoted above.

11.2.2 Combined systematic uncertainties

The systematic uncertainties are summarized in table 11.2.2. Included are the systematic uncertainties on the efficiency measurement, the integrated luminosity and the acceptance, which were previously determined. From the reported high and low uncertainty values in section 11.2.1, the largest of either the high or the low uncertainties are taken and quoted below.

At four percent, the luminosity contributes the largest single uncertainty. The overall uncertainty, excluding the luminosity uncertainty, is near two percent. Of the two percent, the largest uncertainty in all cases comes from the theoretical uncertainty on the acceptance. The second largest uncertainty originates from the efficiency measurement, which is dominated by the statistical uncertainty. The theoretical calculations on the total cross section are known to four percent, thus with slightly improved cross section measurements it is possible to constrain the integrated luminosity measurement beyond its present uncertainty.

11.3 W boson cross section

The predicted value from the NNLO theoretical cross section[79] is determined using FEWZ NNLO with MSTW 2008 NNLO PDF sets. The uncertainties on the cross

section are determined by combining the high order correction (α_s) uncertainties with the PDF variation uncertainties.

Combining the integrated luminosity measurement with the efficiency measurement and the total yield through equation 11.1, the final cross section for W^+ is

$$\begin{aligned} \sigma\left(pp \to W^+\right) \times \mathcal{B}\left(W^+ \to \mu^+\nu\right) &= 6.07 \pm 0.02(\text{stat}) \pm 0.10(\text{sys}) \pm 0.24(\text{lumi}) \text{ nb}, \\ \text{NNLO prediction} &= 6.15 \pm 0.17 \text{ nb}, \end{aligned} \tag{11.32}$$

in excellent agreement with the predicted value. The W^- cross section is

$$\begin{aligned} \sigma\left(pp \to W^-\right) \times \mathcal{B}\left(W^- \to \mu^-\nu\right) &= 4.23 \pm 0.02(\text{stat}) \pm 0.08(\text{sys}) \pm 0.17(\text{lumi}) \text{ nb}, \\ \text{NNLO prediction} &= 4.29 \pm 0.11 \text{ nb}, \end{aligned} \tag{11.33}$$

which is again in very close agreement with the NNLO prediction.

Combining the two charged cross section values gives:

$$\begin{aligned} \sigma\left(pp \to W\right) \times \mathcal{B}\left(W \to \mu\nu\right) &= 10.30 \pm 0.03(\text{stat}) \pm 0.15(\text{sys}) \pm 0.41(\text{lumi}) \text{ nb}, \\ \text{NNLO prediction} &= 10.44 \pm 0.27 \text{ nb}. \end{aligned} \tag{11.34}$$

The ratio of the two cross sections is written as

$$\frac{\sigma_+}{\sigma_-} = \frac{N_{W^+}}{N_{W^-}} \frac{\epsilon_- a_{W^-}}{\epsilon_+ a_{W^+}} \,. \tag{11.35}$$

From the values above, adding in the appropriate systematic uncertainties, we find the cross section ratio to be

$$\begin{aligned} \frac{\sigma\left(pp \to W^+\right) \times \mathcal{B}\left(W^+ \to \mu^+\nu\right)}{\sigma\left(pp \to W^-\right) \times \mathcal{B}\left(W^- \to \mu^-\nu\right)} &= 1.433 \pm 0.008(\text{stat}) \pm 0.016(\text{sys}) \pm 0.030(\text{th.}) \\ \text{NNLO prediction} &= 1.430 \pm 0.010 \,, \end{aligned} \tag{11.36}$$

close to the predicted ratio. Here, the theory uncertainty, (*textrmth*), is separated out because it is very sensitive to the PDFs and quite large. This result provides a new constraint on the theory calculation which will allow this uncertainty to be further reduced.

11.4 Z boson cross section

In order to compute the W/Z boson cross section ratio, we first determine the Z boson cross section. To determine the Z boson cross section, we select two well identified muons with $p_T > 25$ GeV/c and $|\eta| < 2.1$ using the same quality cuts used for muons from the W boson decays (chapter 5). The mass of the combined leptons is required to be within a window of 60 GeV/$c^2 < m_{\ell\ell} < 120$ GeV/c^2. The second lepton selection nearly eliminates the background, thereby allowing the signal extraction to be performed by counting events in the signal region. The full cross section is determined through the procedure:

- Select two leptons with the same identifications used for the single lepton selection in W boson decays (so as to reuse the efficiency measurement)
- Count the total number of events inside the Z mass window
- Subtract the predicted background from the total number of events.
- Correct the efficiency by the scale factors using the same measurement as in the W boson (so that the W/Z ratio cancels out)
- Correct for the acceptance

The choice of using the same kinematic and identification cuts as that of the W boson cancels out the efficiency systematic uncertainty in the W/Z ratio measurement. These kinematic requirements are slightly tighter than optimal for exclusively determining the Z boson cross section.

11.4.1 Selection of events

The total amount of events found in the data with the Z boson selection is found to be 10598±103. The composition of the dilepton selection within the mass window is summarized in table 11.4.1. The total background composition is expected to contribute to 0.36% of the total events in the signal region. The main background comes from $t\bar{t}$, which is well modeled in simulations of this kinematic selection. The next largest background Z→ $\tau^+\tau^-$ and the subsequent diboson production are also well modeled in simualtion; thus, we consider a systematic uncertainty on the background of 50% the total contribution, making the background systematic uncertainty 0.18%.

The uncertainty on the acceptance is determined in the same manner as the W boson uncertainty (chapter 8), where the best resummed, FSR, and NNLO models are compared with the default Powheg Monte Carlo simulation. The uncertainty on the acceptance is found to be

$$a_z = 0.3191 \pm 0.0039(\text{ISR+NNLO}) \pm 0.0042(\text{PDF}) \pm 0.0018(\text{EWK},) \quad (11.37)$$

$$a_z = 0.3191 \pm 0.0060(\text{sys.}) \quad (11.38)$$

The largest difference of these uncertainties when compared with the W boson acceptance uncertainty originates from from the Electroweak (EWK) uncertainties; where different $\mathcal{O}(\alpha)$ corrections contribute in the Z boson channel.

11.4.2 Z boson efficiency correction

The efficiency correction of the muon identification and isolation, track reconstruction, and Stand-Alone muon reconstruction is performed through a scale factor applied to both legs in the event. The correction is written by summing over all bins used in

Background	Expected yield	Acceptance	Cross section (pb^{-1})	Fractional contribution
$Z \rightarrow \mu^+\mu^-$	11111	0.3191	970	0.9963
$t\bar{t}$	13	0.0024	158	0.0012
$Z \rightarrow \tau^+\tau^-$	10	0.0002	1666	0.0009
WZ	9	0.0133	18.2	0.0008
ZZ	5	0.025	5.9	0.0005
WW	3	0.0021	43	0.0003
$W \rightarrow \mu\nu + Jets$	0	0	6152	0.0000
$W \rightarrow e\nu + Jets$	0	0	4286	0.0000

Table 11.3: Acceptances, total cross section and contributions of all backgrounds in dimuon events with a both $p_T > 25$ GeV/c, and a mass window given by $60 < m_{\mu\mu} < 120$.

calculating the efficiencies given as:

$$\epsilon_{\text{data}} = w_Z \epsilon_{\text{simulation}} , \tag{11.39}$$

$$w_Z = \sum_{ij} w_i(\mu_+) w_j(\mu_-) p_{ij} , \tag{11.40}$$

where w_Z is the overall scale factor on Z events, $w_i(\mu_a)$ is the binned scale factor, and p_{ij} is the probability that a given event has a positive muon in the ith bin and a negative muon in the jth bin. This is determined from the tag and probe dataset for a muon in the ith kinematic bin with charge μ_a. The uncertainties on the scale factors are propagated through considering the bin by bin scale factor variations. This follows as

$$\sigma = \sqrt{\sum_i \left(\sum_j \sigma_i w_j p_{ij} \right)^2 + \sum_j \left(\sum_i \sigma_j w_i p_{ij} \right)^2} . \tag{11.41}$$

The systematic uncertainties are taken from the bin by bin systematic uncertainties determined in chapter 6. Taking into account the full bin by bin correlations, these uncertainties are added together giving

$$\sigma_{\text{sys}} = \sum_{ij} p_{ij} \left(\sigma_i^{sys} + \sigma_j^{sys} \right) , \tag{11.42}$$

Summing over all efficiencies with the exception of the trigger, the final result for the scale factor (κ) is

$$\kappa = 0.9522 \pm 0.0049(\text{stat}) \pm 0.0143(\text{sys.}) \tag{11.43}$$

The trigger efficiency correction is determined by considering the probability that both leptons will not fire a trigger. Summing over the positive and negative muon

bins i and j respectively, this is written as

$$\epsilon = \sum_{ij} \left(1 - (1 - \epsilon_i)(1 - \epsilon_j)\right) p_{ij} , \tag{11.44}$$

where in this instance ϵ_i is the trigger efficiency for the ith lepton. Propagating the uncertainties in the same way previously done we have the trigger scale factor

$$\kappa_{trig} = 0.9961 \pm 0.0005 . \tag{11.45}$$

The combined efficiency includes an additional systematic uncertainty of 0.5% originating from the uncertainty on trigger prefire correction. Adding in this uncertainty with the other terms gives:

$$\kappa_Z = 0.9485 \pm 0.0049(\text{stat}) \pm 0.0143(\text{sys}) . \tag{11.46}$$

To determine the W/Z boson ratio, all of the efficiencies for one of the muon legs in the Z boson decay, excluding the trigger efficiency, cancel out (*ie* for W^+ production the efficiency on the positive muon cancels and for W^- the negative muon efficiency cancels out). Propagating the uncertainties for the two legs, an efficiency uncertainty for the W/Z boson ratio is given by

$$\sigma = \frac{\sigma_{W^+}}{\sigma_W}\sigma_\epsilon^- \oplus \frac{\sigma_{W^-}}{\sigma_W}\sigma_\epsilon^+ , \tag{11.47}$$

$$\sigma_{W/Z} = 0.26(\text{stat}) \pm 0.67(\text{sys}) . \tag{11.48}$$

11.4.3 Energy scale uncertainty on Z boson selection

An additional uncertainty comes from the p_T cut threshold on the energy scale. Modifying the energy scale on each leg by its respective uncertainties and recalculating the cross section yields an additional systematic uncertainty of

$$\sigma_{sys}^{scale} = 0.15\% \tag{11.49}$$

11.4.4 Z boson cross section

The Z boson cross section is determined by applying the scale factor κ_Z to the simulated acceptance and efficiency. The predicted background yield is subtracted from the total yield. Taking the yield and combining all of the uncertainties with the integrated luminosity, using equation 11.1, gives the cross section:

$$\begin{aligned} \sigma(pp \to Z) \times BR\left(Z \to \mu^+\mu^-\right) &= 972 \pm 11(\text{stat}) \pm 14(\text{sys}) \pm 18(\text{th}) \pm 39(\text{lumi}) \text{ pb}, \\ \text{NNLO prediction} &= 970 \pm 30 \text{ pb}, \end{aligned} \tag{11.50}$$

which agrees well with the NNLO prediction from FEWZ.

11.5 W/Z boson ratio

The W/Z boson ratio is defined as the ratio of W boson production to Z boson production.

$$\frac{\sigma_{\mathrm{W}}}{\sigma_{\mathrm{Z}}} = \frac{N_{\mathrm{W}}}{N_{\mathrm{Z}}} \frac{a_{\mathrm{W}}}{\epsilon_{\mathrm{W/Z}} a_{\mathrm{Z}}} . \tag{11.51}$$

Taking the uncertainty from equation 11.48, the additional uncertainties on the W boson cross section measurement, plus the theoretical systematic uncertainties, and combining them to give the W/Z production ratio yields:

$$\begin{aligned} \frac{\sigma\left(pp \to \mathrm{W}\right) \times \mathcal{B}\left(W \to \mu\nu\right)}{\sigma\left(pp \to \mathrm{Z}\right) \times \mathcal{B}\left(Z \to \mu^{+}\mu^{-}\right)} &= 10.59 \pm 0.12(\mathrm{stat}) \pm 0.08(\mathrm{sys}) \pm 0.13(\mathrm{th}) , \\ \text{NNLO prediction} &= 10.74 \pm 0.14 . \end{aligned} \tag{11.52}$$

This measured value is slightly lower than the NNLO prediction, but still within uncertainties of the prediction.

11.6 Differential W boson distributions

To check the performance of the cross section measurement, we plot several W boson differential distributions. In these distributions, the QCD distributions are taken from the Monte Carlo simulation normalized to the yields determined by the cross section measurement. This leads to a slightly inaccurate measurement due to the fact that the QCD background shape is only modeled in the $\not\!\!E_{\mathrm{T}}$ variable. To mitigate the influence of the QCD background contribution, we plot both the differential cross sections with the standard acceptance cuts as well as an additional cut of $\not\!\!E_{\mathrm{T}} > 20$ GeV. The signal template has been corrected for the binned variation in the efficiency scale factors and the modified $\not\!\!E_{\mathrm{T}}$ after recoil corrections. Each of the plots shows the $\pm$ uncertainty band determined by taking the W boson signal templates where the $\not\!\!E_{\mathrm{T}}$ and the lepton energy scale is fluctuated up or down. Below each plot is the difference χ defined from the statistical uncertainty as

$$\chi = \frac{N_{\mathrm{data}} - N_{\mathrm{simulation}}}{\sqrt{N_{\mathrm{data}}}} \tag{11.53}$$

Figure 11-3 shows the lepton p_{T} distributions. After the $\not\!\!E_{\mathrm{T}}$ cut is applied, the p_{T} distribution shows excellent agreement along the whole p_{T} range. Before the $\not\!\!E_{\mathrm{T}}$ cut is applied, small disagreement at low p_{T} is present due to the mis-modeling of the QCD background.

Figure 11-4 shows the angle between the $\not\!\!E_{\mathrm{T}}$ and the lepton. This variable reflects the accuracy of the $\not\!\!E_{\mathrm{T}}$ resolution, which is well reproduced by the recoil model. Figure 11-5 shows the m_{T} distribution. The m_{T} is a combination of the three variables the $\not\!\!E_{\mathrm{T}}$, the lepton p_{T}, and the angle between the $\not\!\!E_{\mathrm{T}}$ and the lepton. The excellent

agreement between the three variables is reflected in the m_{T} variable.

We end this section by presenting the W boson p_{T} distribution in figure 11-6. The W boson p_{T} distribution is very sensitive to the theoretical modeling, the $\not\!\!E_{\mathrm{T}}$ model and the of the predicted QCD yield. The signal template used is corrected to Resbos and then further corrected by a data/simulation weight determined by Z bosons. The final p_{T} demonstrates excellent agreement to boson p_{T} beyond 200 GeV/c . In figure 11-6, the performance of the p_{T} shape before Resbos and data/simulation scale factors are applied. Here, a large disagreement is visible for $p_{\mathrm{T}} > 80$ GeV/c. This is a reflection of the necessity of NNLO differential calculations in describing the full boson p_{T} shape.

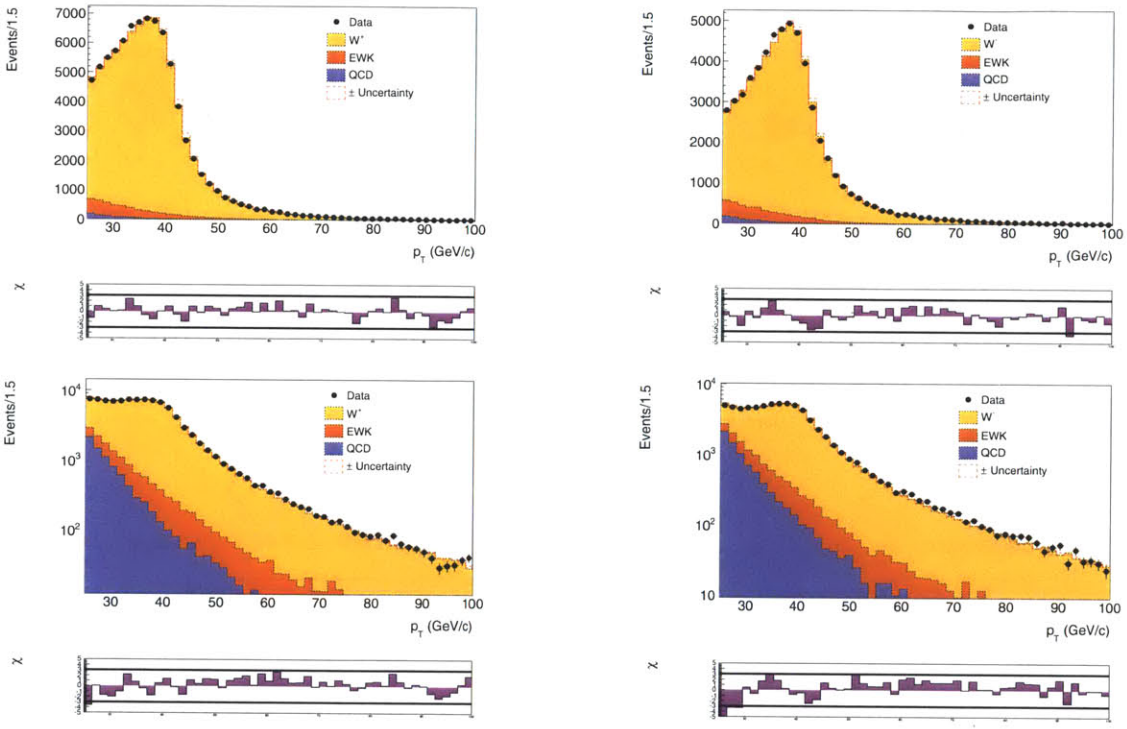

Figure 11-3: p_{T} distribution for positive (left) and negative (right) muons for $\not\!\!E_{\mathrm{T}} > 20$ GeV(top) and inclusive (bottom). Below the plot (purple) is χ, defined in equation 11.53. The black line indicates the values $\chi = \pm 3$.

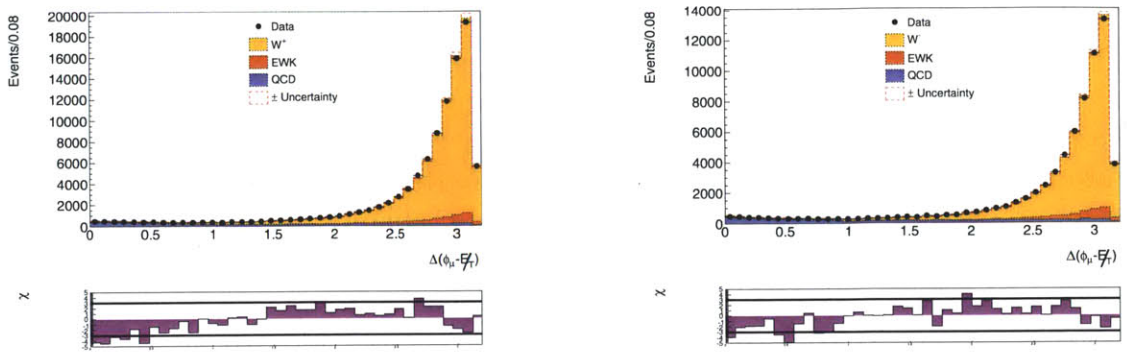

Figure 11-4: Angle between $\not{E}_{\mathrm{T}}$ and the muon for positive muons (left) and negative muons (right). Below the plot (purple) is χ, defined in equation 11.53. The black line indicates the values $\chi = \pm 3$.

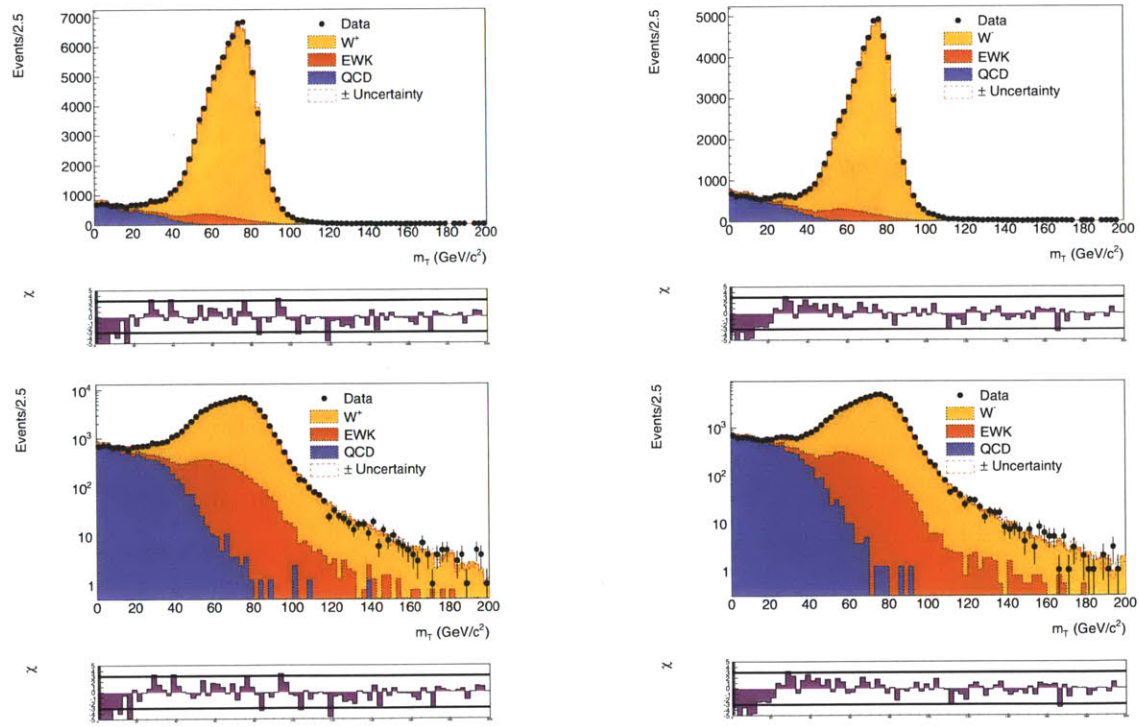

Figure 11-5: m_{T} distribution for positive muons (left) and negative muons (right). Below the plot (purple) is χ, defined in equation 11.53. The black line indicates the values $\chi = \pm 3$.

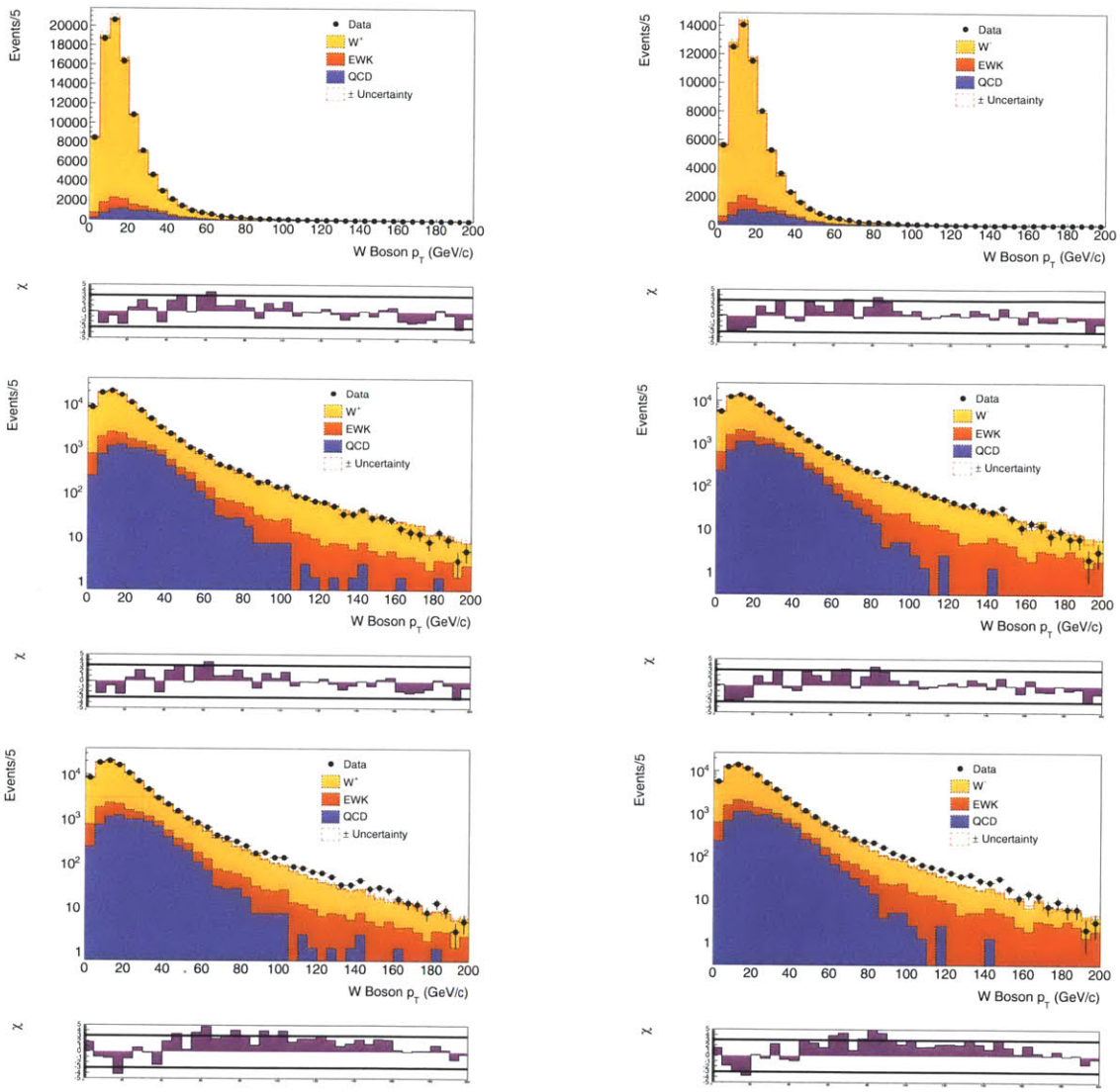

Figure 11-6: W boson p_{T} distribution for positive muons (left) and negative muons (right) with default p_{T} reweighting from data (top two) and without reweighting (exclusively Powheg) (bottom). Below the plot (purple) is χ, defined in equation 11.53. The black line indicates the values $\chi = \pm 3$.

Chapter 12

Conclusions

The precision measurement of the

1. W^+ boson cross section
2. W^- boson cross section
3. W boson cross section
4. Z boson cross section
5. W^+/W^- cross section ratio
6. W/Z cross section ratio

in the muon channel is performed. The results are summarized graphically in figure 12-1.

Events are selected using a quality muon selection requiring tight isolation criteria to remove QCD background. One muon is required for W boson measurements and two muons are required for the Z boson measurements. The efficiency of this selection, determined with tag and probe on $Z \rightarrow \mu^+\mu^-$ events, is found to be near 85 percent with the largest inefficiency originating from the trigger. The final extraction of the efficiency is determined by fitting the $\not\!\!E_T$ observable with a signal template constructed from corrected simulation, a QCD template constructed from a modified Rayleigh distribution, and an Electroweak shape from simulation. Corrections and uncertainties on the simulation of the W boson template and the Electroweak template are performed to incorporate the energy scale variation, the hadronic recoil model, and the boson p_T distribution; all of which are determined from Z bosons. The QCD background templates for each charge are constrained by a two dimensional fit to the $\not\!\!E_T$ as a function of the isolation. The final result is corrected by the acceptance back to the full kinematic phase space. Uncertainties on the extrapolation result from missing NNLO, NNNLL, FSR, and Electroweak corrections in the extrapolation.

Results are summarized in figure 12-1. They are found to be in agreement with the standard model predictions. The largest deviation is in the W/Z cross section ratio, which is still within the one standard deviation of the theoretical prediction.

This measurement establishes a baseline for understanding muon efficiencies, the $\not\!\!E_T$ behavior, energy scale uncertainties, and QCD shape modeling. Deviations in the theoretical modeling have been minimized and a detailed prescription of obtaining these uncertainties has been established.

This measurement is currently the most precise single Electroweak measurement at the LHC.

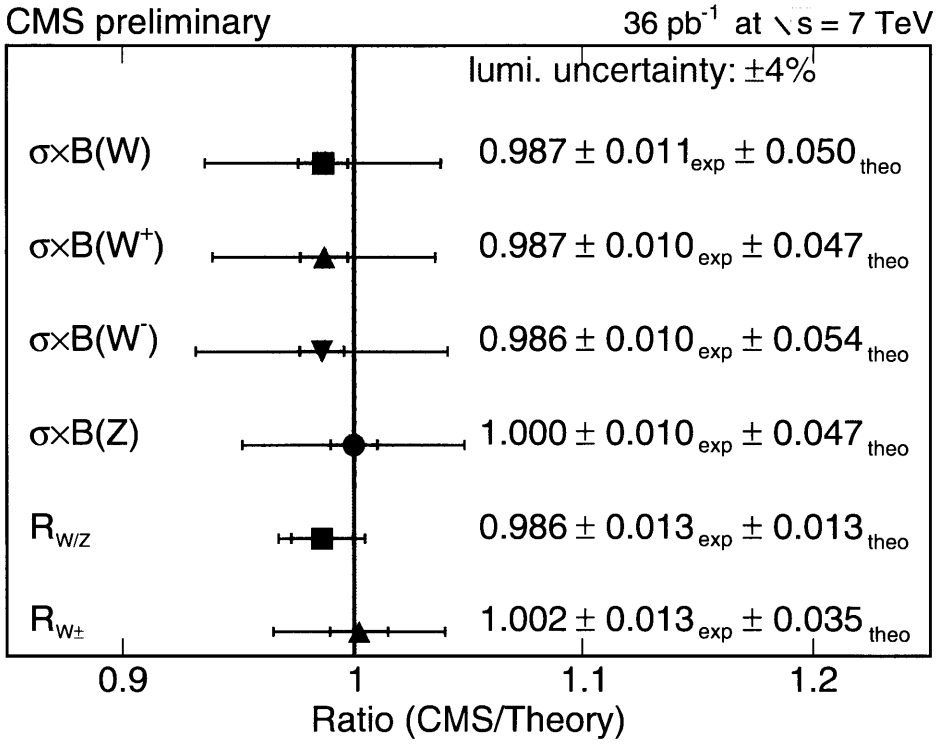

Figure 12-1: Results of the six measurements performed in this thesis compared with the standard model predictions

Bibliography

[1] CMS Collaboration, "Measurements of inclusive W and Z cross sections in pp collisions at $\sqrt{s}$=7 TeV," *JHEP*, vol. 1101, p. 080, 2011.

[2] H. Goldstein, *Classical Mechanics.* Boson, Massachusetts: Addison-Wesley, 1980.

[3] R. Wald, *General Relativity.* Chicago, Illinois: University of Chicago Press, 1984.

[4] M. E. Peskin and D. V. Schroeder, *Introduction to quantum field theory.* Boson, Massachusetts: Addison-Wesley Pub. Co., 1995.

[5] P. Nadolsky *et al.*, "New parton distributions for collider physics," *Phys.Rev.D*, vol. 82, p. 074024, 2010.

[6] Y. Dokshitzer *Sov.Phys.JETP*, vol. 46, p. 641, 1977.

[7] V. Gribov and L. Lipatov *Sov.J.Nucl.Phys*, vol. 15, p. 438, 1972.

[8] G. Altarell and G. Parisi *Nucl.Phys.B*, vol. 126, p. 298, 1977.

[9] A. Martin, W. Stirling, R. Thorne, and G. Watt, "Parton distributions for the LHC," *Eur.Phys.J.C*, vol. 63, pp. 189–285, 2009.

[10] CMS Collaboration, "Qcd effects in the w cross section measurement," *CMS AN2009 183v2*, 2009.

[11] UA1 Collaboration, "Experimental observation of isolated large transverse energy electrons with associated missing energy at $\sqrt{s}$ = 540 GeV," *Phys. Lett. B*, vol. 122, pp. 103–116, 1983.

[12] UA1 Collaboration, "Experimental observation of lepton pairs of invariant mass around 95 GeV/c^2 at the cern sps collider," *Phys. Lett., B*, vol. 126, p. 398, 1983.

[13] Y. Nambu, "Quasiparticles and gauge invariance in the theory of superconductivity," *Physical Review*, vol. 117 (3), pp. 648–663, 1960.

[14] P. Higgs, "Broken symmetries and the masses of gauge bosons," *Physical Review Letters*, vol. 13(16), pp. 508–509, 1961.

[15] The ALEPH, DELPHI, L3, OPAL, SLD Collaborations, the LEP Electroweak Working Group, the SLD Electroweak and Heavy Flavour Groups, "Precision Electroweak Measurements on the Z Resonance," *Phys. Rept.*, vol. 427, p. 257, 2006.

[16] CDF and D0 Collaborations and the Tevatron new Phyiscs working group, "Combined CDF and D0 upper limits on standard model higgs-boson production with up to 6.7 fb^{-1} of data," *arXiv:hep-ex/0001014v1*, 2010.

[17] The LEP Working Group for Higgs Boson Searches, "Search for the standard model higgs boson at lep," *Phys. Lett. B*, vol. 565, p. 61, 2003.

[18] B. W. Lee, C. Quigg, and H. B. Thacker *Phys.Rev.D*, vol. 56, pp. 1519–1531, 1977.

[19] S. M. on Behalf of L3, "Recent results from the l3 experiment," *arXiv:hep-ex/0001014v1*, 2001.

[20] D0 and CDF Collaborations, "Combined cdf and d upper limits on standard-model higgs-boson production," *FERMILAB-CONF-11-354-E*, 2011.

[21] ATLAS Collaboration, "Update of the combination of higgs boson searches in 1.0 to 2.3 fb1 of pp collisions data taken at $\sqrt{s} = 7$ TeV with the atlas experiment at the lhc," *ATLAS-CONF-2011-135*, 2011.

[22] CMS Collaboration, "Search for standard model higgs boson in pp collisions at $\sqrt{s}$=7 TeV and integrated luminosity up to 1.7 fb^1," *CMS PAS HIG-11-022*, 2011.

[23] D. Michael *et al.*, "Observation of muon neutrino disappearance with the minos detectors in the numi neutrino beam," *Physical Review Letters*, p. 191801, 2006.

[24] CMS Collaboration, "Measurement of the Polarization of W Bosons with Large Transverse Momenta in W+Jets Events at the LHC," *CMS-EWK-10-014*, 2011.

[25] R. Hamburg, W. van Neerven, and T. Matsuura *Nucl. Phys. B*, vol. 359, p. 343, 1991.

[26] K. Melnikov and F. Petriello *Phys. Rev. Lett*, vol. 96, p. 231803, 2006.

[27] S. Catani, L. Cieri, G. Ferrera, D. de Florian, and M. Grazzini *Phys. Rev. Lett*, vol. 103, p. 082001, 2009.

[28] CMS Collaboration, "Search for a heavy gauge boson w' in the final state with an electron and large missing transverse energy in pp collisions at *sqrts* = 7 TeV," *Phys.Lett. B*, vol. 698, pp. 21–39, 2011.

[29] L. Evans and P. Bryant, "LHC machine," *JINST*, vol. 3, p. S08001, 2008.

[30] CERN, "http://lhcathome.cern.ch/lhc/lhc.shtml."

[31] G. Arduini and P. Raimondi, "Transverse emittance blow-up due to injection errors," *SL-NOTE*, vol. 99-022, 1999.

[32] S.Bolognesi *et al.*, "Calibration of the CMS magnetic field using cosmic muon track," *Lepton Photon proceedings*, 2009.

[33] J. Jackson, *Classical Electrodynamics*. Danvers, Massachusetts: John Wiley and Sons, 1998.

[34] K. Nakamura *et al.*, "Particle Data Group," *J. Phys. G*, vol. 37, p. 075021, 2010.

[35] H. Bethe *Z. Phys.*, vol. 76, p. 293, 1932.

[36] F. Bloch *Z. Phys.*, vol. 81, p. 363, 1933.

[37] CMS Collaboration, "The CMS experiment at the CERN LHC," *JINST*, vol. 3, p. S08004, 2008.

[38] U. Firenze, "http://hep.fi.infn.it/cms/sensors/siliconpage.html."

[39] CMS Collaboration, *The CMS tracker project : Technical Design Report*. Geneva,CH: CERN/LHCC 98-6, 1998.

[40] CMS collaboration, "Performance of track-corrected missing e_{T} in CMS," *CMS-PAS-JME-09-010*, 2009.

[41] M. Raymond *et al.*, "The cms tracker apv25 0.25μm cmos readout chip," *Sixth Workshop on Electronics for LHC Experiments*, vol. CERN/LHCC/2000-041., 2000.

[42] CMS Tracker Collaoration, "Commissioning and performance of CMS silicon tracker with cosmic ray muons," *JINST*, vol. 5, p. T00308, 2010.

[43] B. Wittmer *et al.*, "The laser alignment system for the CMS silicon microstrip tracker," *NIM A*, vol. 581, pp. 351–355, 2007.

[44] R. Bellan, *Study and Development of the CMS High Level Trigger and Muon Reconstruction Algorithms and Their Effects on the pp$\rightarrow \mu^+\mu^- jjjj$*. PhD thesis, U. Torino, 2007.

[45] CMS Collaboration, *CMS ECAL Technical Design Report*. Geneva,CH: CERN/LHCC 97-33, 1997.

[46] CMS Collaboration, "Performance, calibration and alignment of the CMS preshower detector," *Nucl. Phys. B*, vol. 215, pp. 119–121, 2011.

[47] CMS Collaboration, "Electromagnetic calorimeter calibration with 7 TeV data," *CMS-PAS-EGM-10-003*, 2010.

[48] P. B. Cushman *et al. NIM A*, vol. 387, p. 107, 1997.

[49] CMS Collaboration, "Single-particle response in the CMS calorimeters," *CMS-PAS-JME-10-008*, 2010.

[50] CMS Collaboration, "Jet energy resolution in CMS at sqrt(s)=7 TeV," *CMS-PAS-JME-10-014*, 2010.

[51] CMS Collaboration, *The CMS muon project : Technical Design Report.* Geneva,CH: CERN, 1997.

[52] E. Gatti *et al. Nucl. Instr. and Meth.*, vol. 163, p. 83, 1979.

[53] CMS collaboration, "Performance of muon identification in 2010 data," *CMS-PAS-MUO-10-004*, 2010.

[54] T. Sjostrand *et al.*, "Pythia 6.4 physics and manual," *JHEP*, vol. 05, p. 026, 2006.

[55] G. Corcella *et al.*, "Herwig 6.5," *JHEP*, vol. 0101, p. 010, 2001.

[56] CMS Collaboration, "CMS luminosity calculation," *CMS IN2008 029*, 2008.

[57] CMS Collaboration, "Measurement of CMS luminosity," *EWK-10-004-PAS*, 2010.

[58] CMS Collaboration, "Absolute calibration of luminosity measurement in CMS," *CMS Note*, vol. AN2011 093v1, 2011.

[59] M. Zanetti *et al.*, "Luminosity normalization measurements based on Van Der Meer Scans at CMS," *LHC Lumi Days Workshop Proceedings*, 2011.

[60] CMS Collaboration, "Photon reconstruction and identification at sqrt(s) = 7 TeV," *CMS-PAS-EGM-10-005*, 2010.

[61] CMS Collaboration, "Electron reconstruction and identification at sqrt(s) = 7 TeV," *CMS-PAS-EGM-10-004*, 2010.

[62] B. Mangano *et al.*, "CMS track reconstruction performance," *17th International Workshop on Vertex detectors proceedings*, 2008.

[63] CMS Collaboration, "Description and performance of the CMS track reconstruction," *CMS AN2011 172v2*, 2011.

[64] CMS Collaboration, "Track reconstruction in the CMS tracker," *CMS-PAS-TRK-09-001*, 2010.

[65] W. Erdmann *et al.*, "Offline primary vertex reconstruction with deterministic annealing clustering," *CMS IN-2011/014*, 2011.

[66] W. Adam *et al.*, "Track and vertex reconstruction in CMS," *CMS CR-2006/098*, 2006.

[67] C. Bernet *et al.*, "Important CMS upgrade: Particle-flow event reconstruction." Presenation at CERN EP seminar, April 2009.

[68] CMS Collaboration, "MET performance in pp collisions at sqrts=7 TeV," *CMS-PAS-JME-10-009*, 2010.

[69] G. Salam *et al. JHEP*, vol. 04, p. 063, 2008.

[70] CMS collaboration, "Muon reconstruction in the CMS detector," *CMS AN2008 097v4*, 2008.

[71] CMS Collaboration, "Muon high-level trigger in CMS," *CMS Note*, vol. AN2010 234v2, 2010.

[72] CMS collaboration, "Performance of muon identification in pp collisions at sqrt(s) = 7 TeV," *CMS-PAS-MUO-10-002*, 2010.

[73] D. Green and J. Swets, *Signal detection theory and psychophysics.* New York, NY: John Wiley and Sons, 1966.

[74] F. James and M. Roos, "MINUIT-A system for function minimization and analysis of the parameter errors and correlations," *Computer Physics Communications*, vol. 10, pp. 343–367, 1975.

[75] S.Alioli, P.Nason, C.Oleari, and E.Re, "NLO vector-boson production matched with shower in POWHEG," *arXiv:hep-ph/0805.4802*, 2008.

[76] K. Cranmer, "Kernel estimation in high energy physics," *arXiv:hep-ex/0011057*, 2001.

[77] J. Gaiser, *Charmonium Spectroscopy from Radiative Decays of the J/Psi and Psi-Prime.* PhD thesis, Stanford University, 1982.

[78] CMS Collaboration, "Measurement of tracking efficiency," *CMS-PAS-TRK-10-002*, 2010.

[79] CMS Collaboration, "Measurement of the inclusive W and Z production cross sections in pp at $\sqrt{s} = 7$ TeV," *CERN-PH-EP-2011-107*, pp. CMS–EWK 10–005, 2011.

[80] CMS Collaboration, "Alignment of CMS tracker during comissioning with cosmic rays," *JINST*, vol. 5, p. T03009, 2010.

[81] G.Flucke, P.Schleper, and G.Steinbruck, "CMS silicon track alignment strategy with the Millipede II algorithm," *JINST*, vol. 3, p. P09002, 2010.

[82] V.Karimiki, T.Lampen, and F.P.Schilling, "The HIP algorithm for track based alignment and it application to the CMS pixel detector," *CMS Note*, vol. 018, 2006.

[83] D. Yennie, S. Frautschi, and H. Surra *Ann. of Phys. 13*, p. 13, 1961.

[84] J.Collins and D. Soper, "Parton distributions and decay functions," *Nucl.Phys.B*, vol. 194, p. 445, 1982.

[85] G. Altarelli, R. Ellis, M. Greco, and G. Martinelli *Nucl Phys. B*, vol. 246, 1984.

[86] C. Balazs, *Soft Gluon Effects on Electroweak Boson Production in Hadron Collisions.* PhD thesis, MSU, 1996.

[87] R. Ellis, W. Stirling, and B. Webber, *QCD and Collider Physics.* Cambridge Unversity Press, 2003.

[88] J.Collins, D.Soper, and G.Sterman, "Transverse momentum in Drell-Yan pair and W and Z boson production," *CERN-Re.TH.*, vol. 3923, 1984.

[89] P. Nadolsky, "Resbos and nonperturbative contributions to q_{T} renormalization." W boson workshop, Fermilab, October 2010.

[90] R. Brock, F. Landry, P. Nadolsky, and C. Yuan, "Tevatron run-1 Z boson data and Collins-Soper-Sterman resummation formalism," *Phys. Rev. D*, vol. 67, p. 074015, 2003.

[91] P. Nadolsky and C. Yuan, "Soft parton radiation in polarized vector boson production:theoretical issues," *Nucl. Phys. B*, vol. 666, pp. 3–30, 2003.

[92] D0 Collaboration, "Precise study of Z/gamma* boson transverse momentum distribution in ppbar collisions using a novel technique," *D0 Conference Note*, pp. 6111–CONF, 2010.

[93] R. Ellis and S. Veseli, "W and Z transverse momentum distributions: Resummation in q_{T} space," *Nucl. Phys. B*, vol. 511, pp. 649–669, 1998.

[94] P. Arnold and R. Kauffman *Nucl. Phys. B*, vol. 349, p. 381, 1991.

[95] C. Balazs and C. Yuan *Phys.Rev.D*, vol. 56, pp. 5558–5583, 1997.

[96] G. Ladinsky and C. Yuan *Phys. Rev. D*, vol. 50, p. 4239, 1994.

[97] M. Shatz *Nuclear Physics B*, vol. 224, pp. 218–228, 1983.

[98] R. Field, "Early LHC underlying event data-findings and surprises," *arXiv*, p. 1010.3558, 2010.

[99] N. Adam, V. Halyo, and S. Y. . W. Zhu *JHEP*, vol. 0809, p. 133, 2008.

[100] P. Nadolsky, S. Barge, F. Olness, and C. Yuan, "Transverse momentum resummation at small x for the tevatron and LHC," *Phys.Rev.D*, vol. 72, p. 033015, 2005.

[101] C. C. Calame, O. Nicorsini, and A. Cucini, "Precision electroweak calculation of the charged current electroweak distribution," *JHEP*, vol. 0612, p. 016, 2006.

[102] P. Golonka and Z. Was *Eur. Journal Phys J*, vol. C45, p. 97, 2006.

[103] J. Pumplin, D. Stump, and W. Tung, "Multivariate fitting and the error matrix in global analysis of data," *Phys.Rev.D*, vol. 65, p. 014011, 2001.

[104] P. Collaboration, "PDF4LHC working group interim recommendations," *arXiv:1101.0538v1*, 2011.

[105] P. Nadolsky *et al.*, "Implications of cteq global analysis for collider observables," *Phys.Rev.D*, vol. 78, p. 013004, 2008.

[106] S. Forte *et al.*, "Neural network parametrization of deep-inelastic structure functions," *JHEP*, vol. 062, 2002.

[107] CDF I Collaboration, "Measurement of the W boson mass with the Collider Detector at Fermilab," *Phys. Rev. D.*, vol. 64, 2001.

[108] CDF II Collaboration, "First measurements of inclusive W and Z cross sections from run II of the Tevatron collider," *Phys. Rev. Lett.*, vol. 94, 2005.

[109] Z. Was, "Tauola the library for tau lepton decay and kkmc/koralb/koralz/... status report," *Nucl.Phys.Proc.Suppl.*, vol. 98, 2001.

[110] J. Neyman, "Outline of a theory of statistical estimation based on the classical theory of probability," *Philosophical Transactions of the Royal Society of London A*, vol. 236, pp. 333–380, 1937.